Development of Sustainable Superhydrophobic Surfaces for Water Manipulation

by

Yi Wang

A thesis
presented to the University of Waterloo
in fulfillment of the
thesis requirement for the degree of
Doctor of Philosophy
in
Chemical Engineering

Waterloo, Ontario, Canada, 2023

Examining Committee Membership

The following served on the Examining Committee for this thesis. The decision of the Examining Committee is by majority vote.

External Examiner	Yonghao Ni Professor
Supervisor	Michael K. C. Tam Professor
Internal Member	Yuning Li Professor
Internal Member	Xianshe Feng Professor
Internal-external Member	Kevin Musselman Associate Professor

Author's Declaration

This thesis consists of material all of which I authored or co-authored: see Statement of Contributions included in the thesis. This is a true copy of the thesis, including any required final revisions, as accepted by my examiners.

I understand that my thesis may be made electronically available to the public.

Statement of Contributions

Chapter 2 of this thesis consists of two review papers. One of these review papers was co-authored by myself and my supervisor, Weinan Zhao, Lian Han. I am the first author of this paper. I conceptualized the study and design, performed data collection and manuscript writing. My coauthors reviewed the manuscript and provided feedback on the draft manuscript.
"Yi Wang, Weinan Zhao, Lian Han, Michael KC Tam. Superhydrophobic surfaces from sustainable colloidal systems. Current Opinion in Colloid & Interface Science, 2022, 57: 101534."

The other review paper was co-authored by myself and my supervisor, Weinan Zhao, Mei Han and Dr. Jiaxin Xu. I am the first author of this paper. I conceptualized the study and design, performed data collection and manuscript writing. My coauthors reviewed the manuscript and provided feedback on the draft manuscript.
"Yi Wang, Weinan Zhao, Mei Han, Jiaxin Xu, Kam Chiu Tam. Biomimetic Surface Engineering for Sustainable Water Harvesting Systems. (Nature Water, 2023, 1, 587–601)"

Chapter 3 of this thesis consists of a paper that was co-authored by myself, my supervisor, Mei Han, Lu Guan, Lian Han, Afraz Hemraj. I am the first author of this paper. I wrote the entire manuscript, and planned and executed the experiments, Weinan Zhao planned and executed some of the experiments. My coauthors reviewed the manuscript and provided feedback on the draft manuscript.
"Yi Wang, Weinan Zhao, Mei Han, Lu Guan, Lian Han, Afraz Hemraj, Michael KC Tam. Sustainable Superhydrophobic Surface with Tunable Nanoscale Hydrophilicity for Water Harvesting. Angewandte Chemie International Edition. 2021, e202115238"

Chapter 4 of this thesis consists of a paper that was co-authored by myself, my supervisor, Weinan Zhao, Mei Han, Dr. Jiaxin Xu, Xiaoming Zhou, Wesley Luu, Lian Han. I am the first author of this paper. I wrote the entire manuscript, and planned and executed the experiments, Weinan Zhao planned and executed some of the experiments. My coauthors reviewed the manuscript and provided feedback on the draft document.
"Yi Wang, Weinan Zhao, Mei Han, Jiaxin Xu, Xiaoming Zhou, Wesley Luu, Lian Han, Kam Chiu Tam. Topographical Design and Thermal-Induced Organization of Interfacial Water Structure to Regulate the Wetting State of Surfaces. JACS Au. 2022, 2, 9, 1989–2000."*

Chapter 5 of this thesis consists of a manuscript that was co-authored by myself, my supervisor, Weinan Zhao, Mei Han, Dr. Yebin Lee, Gaili Cao. I conceptualized the study and design, carried out the experiments, collected and analyzed the data, and prepared the manuscript. My coauthors reviewed the manuscript and provided feedback on the draft document.

Chapter 6 of this thesis consists of a manuscript that was co-authored by myself, my supervisor, Weinan Zhao, Dr. Yebin Lee, Dr. Yuning Li. I conceptualized the study, carried out the experiments, collected and analyzed the data, and prepared the manuscript. My coauthors reviewed the manuscript and provided feedback on the draft document.

Abstract

This thesis focuses on the development of functional superhydrophobic surfaces based on green and sustainable materials. Wettability is central to numerous biological processes as well as many engineering and industrial applications, especially for water manipulation. Nature serves as a source of inspiration, as it presents us with a wide range of intriguing wetting properties exhibited by plant and animal surfaces, such as Namib desert beetle, lotus leaf, and tree. These special capabilities are attributed to their intricate hierarchical structures and composition, enabling them to exhibit exceptional water utilization capabilities. Biomimicking their surface morphologies will lead to the development of engineered superhydrophobic surfaces, offering various potential applications, such as water harvesting, emulsion separation and non-loss micro droplet transfer.

In the first study (**Chapter 3**), we presented a unique superhydrophobic surface with tunable nano-scale hydrophilicity via a self-assembled process, where the cellulose nanocrystal (CNC)/wax Pickering emulsion was used to prepare surfaces that display outstanding water harvesting performance. Specifically, the emulsion templated surface engineering described here not only offers a convenient approach to tailor the hydrophilic nanodomain density, but it also imparts superhydrophobicity to the fog-harvesting surface via topography design. These hydrophilic CNC nanodomains act as nuclei to activate the water deposition process, coupled with superhydrophobic features for the manipulation of droplet mobility. Appropriate tunning of the binary cooperative wettability characteristics of the surfaces, our hydrophilic/superhydrophobic pattern surface allowed us to enhance the water deposition rate without sacrificing the water transport rate. Thus, through changing the surface topography, balancing the trade-off between water deposition and transport, and ensuring the surface stability on the resulting hydrophilic/superhydrophobic surface, it could achieve a high-water harvesting flux of 3.402 $L/m^2/h$ with a CNC density of 84.7%. This hydrophilic/superhydrophobic surface allowed the controllable manipulation of droplet nucleation and removal to enhance the water harvesting efficiency.

To enable precise droplet behavior control over wetting behavior, smart surfaces with switchable wettability transitions offer exceptional water manipulation properties that can be triggered by external stimuli, such as temperature. In **Chapter 4**, we studied the temperature-dependent interfacial properties on thermo-responsive surfaces, where the building blocks of surfaces were obtained by grafting two well-known thermo-responsive polymers, poly(N-isopropylacrylamide) (PNIPAM) and poly(oligoethylene glycol)methyl ether acrylate ($POEGMA_{188}$) onto micro-pollen particles. By investigating the assemblies of microparticles grafted with two types of LCST polymers, we demonstrated that the temperature-dependent interfacial properties of the polymer grafted L.SEC particles were associated with the interaction between interfacial water film and apolar/polar groups of the polymer brushes, as revealed by *in-situ* Raman spectra and thermodynamic analysis. The results revealed that above the lower critical solution temperature (LCST), the bonded and free water at the interface partially transformed to intermediate water that

disrupted the ‘water cage’ surrounding the hydrophobic groups. The increased amounts of intermediate water produced hydrogen bonding networks that were less ordered around the polymer grafted microparticles, inducing a weaker binding interaction at the interface and a lower tendency to wet the surface. Combining the roughness factor, the bulk surface assembled by distinct polymer-grafted-pollen microparticles could undergo a different wettability transition for liquid under air, water, and oil respectively. This work identifies new perspectives on the interfacial water structure variation at multiple length scales, which contributed to the temperature-dependent surface wettability transition. It offers inspiration for the application of thermo-responsive surface to liquid-gated multiphase separation, water purification and harvesting, biomedical devices, and various forms of advanced printing technologies.

The development of responsive surfaces with adjustable adhesion properties has significant implications for liquid manipulation in diverse fields, allowing for the tailored interactions with different liquids. In **Chapter 5**, we presented a novel concept for constructing programmable responsive surfaces that exhibit wettability transformation properties, facilitating efficient and rapid droplet manipulation. Sunflower sporopollenin extine shell (SEC) that modified with copolymer shell made of poly (N-isopropylacrylamide (NIPAM)-co-N-tert-butylacrylamide (NtBA)) were used as building blocks to endow the surface with desirable interfacial conformation. By utilizing the pH-responsive shape transformation found in SEC, wherein 3D microspheres with spiky arrays swollen into 2D microsheets under alkaline condition, we constructed pollen-based surface features with adjustable topography under different pH conditions. By harnessing the conformational transformation of polymer shell and hierarchical structures of SECs, the surface exhibited superhydrophilic/superhydrophobic transformation depending on the lower critical solution temperatures (LCSTs). More importantly, the surface under superhydrophobic state could adjust its water attraction and adhesive properties in a controllable manner. As the addition of hydrophobic comonomers (NtBA), the surfaces exhibited lower water attractive forces due to the weak hydrogen bonding network, imparting the SEC0 surfaces with lower adhesive forces. Compared to surfaces fabricated with SEC microsheets, the high-roughness surface produced from SEC microspheres (SEC0) possessed stronger water-repellent pressure endurance due to the air cushion beneath the spiky structures that lowered its adhesive force. Based on this phenomenon, we demonstrated the controllable droplet transferring on programmable wettability sites, together with effective droplet deposition and transport for water harvesting.

Building upon our previous investigation into the switchable wettability transition exhibited by pollen microparticles, we discovered that this distinctive water manipulation property can serve as a "solid gating" mechanism for efficient water transport and evaporation in solar-driven evaporation systems. In **Chapter 6**, we developed a bilayer-structured solar evaporator (SDWEs) by engineering the fluidic flow within two water transport channels. A porous polydopamine (PDA) coating layer served as photothermal section and water supply microchannels, while the thermo-responsive sporopollenin layer on the bottom skeleton acted as a switchable water gating layer. Through

confocal laser microscopy and micro-CT characterization, we demonstrated that this structural design enabled the selective and directional water supply. Noteworthy, this unique fluidic flow could facilitate the continuous supply of thin water layers and reduce the latent heat required for water evaporation. Therefore, the optimized p-SDWE sample achieved a high-water evaporation rate of 3.58 kg m^{-2} h^{-1} using 93.9% solar energy from 1 sun irradiation, and successfully delivered 18–22 liters of purified water per square meter of SDWE per day when treating brine water. This work elucidated the functions of water transport at the interface within the solar evaporator and presented a novel strategy for high-performance solar-driven water generation.

Acknowledgments

This thesis marks a significant milestone in my academic journey and signifies the completion of my invaluable doctoral pursuit. As I write this thesis, I would like to seize this moment to express my appreciation to all the individuals who have supported and assisted me along the way.

First, I would like to express my deepest gratitude to my supervisor, Professor Tam who provided me with strong support, guidance and advice during my Ph.D. study. His invaluable support and guidance have played a pivotal role in shaping my research journey. I have the opportunity to explore diverse research ideas and learned how to be a professional researcher. His guidance and wisdom have not only influenced my research but has also shaped my mindset and problem-solving approach in life. I am truly grateful for his invaluable contributions to my academic and personal growth.

Moreover, I appreciate my Ph.D. thesis examining committee members, including Professor Kevin Musselman, Professor Xianshe Feng, and Professor Yuning Li from the University of Waterloo, and Professor Yonghao Ni as the external examiner from the University of Maine for their valuable time and insights.

I would like to thank all the group members who were always there to help and provide valuable advice on my research endeavors.

I would also like to thank all those lovely close friends that I have made here in Canada. Thanks for all their generous support whenever and wherever I needed.

I would like to give my sincere gratitude to my parents and partner for their unconditional support, encouragement, and love.

I would like to acknowledge the China Scholarship Council for their support in granting me the opportunity to pursue my Ph.D.

Finally, I am deeply grateful for the incredible experience I have had here in University of Waterloo.

Table of Contents

List of Figures

List of Tables

List of Abbreviations

Abbreviation	Definition
4-HBW	4-coordinate hydrogen-bonded water
ACA, θaca	Advancing contact angle
AFM	Atomic Force Microscope
ATRP	Atom transfer radical polymerization
BW	Bound water
C	Hydrophilic nanodomain density
CA	Static water contact angle
CAH	Contact angle hysteresis
CAN	Cerium(IV) ammonium nitrate
CH3	Methyl group
CLSM	Laser Scanning Confocal Microscope
CMC	Carboxymethyl cellulose
CNC	Cellulose nanocrystal
CNF	Cellulose nanofiber
CNT	Carbon nanotube
CT	Computerized tomography
CTAB	Cetrimonium bromide
CVD	Chemical Vapor Deposition
DADMAC	Diallyldimethylammonium chloride
DCAT	Dynamic contact angle measuring instruments and tensiometers
DIC	Differential interference contrast microscopy
DSC	Differential scanning calorimetry
EDS-SEM	Elemental analyses were conducted using the energy dispersive X-ray spectroscopy
EPA	U.S. Environmental Protection Agency
EPTMAC	Glycidyltrimethylammonium
$F_{adhesion}$	Surface adhesion force
FDTS	1H,1H,2H,2H-perfluorodecyltrichlorosilane
FT-IR	Fourier transform infrared spectroscopy
H3PO4	Phosphoric acid
HA	Hydroxyapatite
HI	Hydrophilic surface
HNO3	Nitric acid
IP	Isopropyl groups
IW	Intermediate water
KI	Potassium iodide
KOH	Potassium hydroxide
L.SEC	Lycopodium sporopollenin extine shell
LCST	Lower critical solution temperatures
LPD	Liquid phase deposition

MMA	Methyl methacrylates
MOF	Metal–organic framework
NtBA	N-tert-butylacrylamide
OEG	Oligo(ethylene glycol)
OH	Hydroxyl group
OWRK	Owens, Wendt, Rabel and Kaelble
PDA	Polydopamine
PNIPAM	Poly(N-isopropylacrylamide)
POEGMA188	Poly(oligoethylene glycol)methyl ether acrylate
PSA	Particle size analyzer
RCA, θrca	Receding contact angle
RH	Relative humidity
Rq	Roughness factor
SCA	Sliding angle
SDS	Sodium dodecyl sulfate
SDWE	Solar-driven water evaporator
SEC	Sunflower sporopollenin extine shell
SEM	Scanning electron microscope
SHS-HIm	Superhydrophobic surface with hydrophilic nanodomains
SM	Smooth microparticles
SOCAL	Slippery omniphobic covalently attached liquid surfaces
SS	Smooth surface
STAC	Stearyltrimethylammonium chloride
TEM	Transmission electron microscopes
TEMPO	(2,2,6,6-Tetramethylpiperidin-1-yl)oxyl
TPCL	Three-phase contact line
UV-vis-NIR	Ultraviolet Visible Near Infrared Spectrophotometry
UV	Ultraviolet
WHO	World Health Organization
XPS	X-ray photoelectron spectroscopic

Chapter 1. Introduction

1.1 Overview

Globally, the number of people that lacks access to water is 2.1 billion, while 4.5 billion people have inadequate sanitation and access to clean water source[1]. Clearly, the scarcity of freshwater is a growing concern, more so when the weather is becoming more unpredictable. Many methods have been used to harvest water, such as water desalination, ground water harvesting and rainwater collection and storage. Obviously, for these to work, liquid water must already be available, but when such supplies are limited, harvesting atmospheric water becomes essential. To efficiently harvest water from fog, nature has served as a source of inspiration in fabricating advanced fog collectors, such as the patterned back of fog basking beetles[2], spindle-knots structure of spider silk[3], the conical spine of cactus cluster[4] and many more[5].Those discoveries promote the development of fog-harvesting devices especially on their special wettability surfaces that have attracted increasing attention spanning fundamental research to water-harvesting devices. Due to their excellent water droplet manipulation characteristics, superhydrophobic surface is a key element in the construction of efficient water collectors.

As the principles of superhydrophobicity is better understood, several materials and methods have been developed to fabricate superhydrophobic surface, which is to construct hierarchical air-trapped microstructure on substrates, and coating the surface with low surface energy materials, such as fluoropolymers or organic siloxanes. Although, these surfaces display good performance in water repellency, fluoride-based materials are harmful to the environment and human. Moreover, the fabrication methods have many restrictions and large-scaled production of devices to collect freshwater is challenging. To overcome these issues, it is essential to develop green and sustainable approaches to construct superhydrophobic surfaces using nontoxic and biocompatible materials that are scalable for practical applications.

1.2 Motivation and challenges

The motivation of this research is to develop superwettable surface systems that utilizes sustainable materials and methods for efficient water harvesting and water manipulation. We will explore and exploit the use of sustainable superhydrophobic surface in a continuous water harvesting system to capture or generate freshwater.

For current water harvesting technologies, the research of bio-mimicking natural organisms, such as lotus leave[2], fog basking beetles[25], insect wings[4], etc. has inspired the development of water-collection devices based on their special wettability surfaces and delicate structures. Superhydrophobic systems like lotus leaf possess superior water removal characteristics[5] but they cannot achieve self-capture water vapor from the air, which is unfavorable for water harvesting. Distinct from these superhydrophobic systems, the fog basking beetles found in the desert offers a novel strategy for water collection[6]. Even in an arid environment, they can collect drinking water on their backs from fog-laden wind using their hydrophilic/hydrophobic pattern back, which

captures water and transports to their mouth[7]. Nevertheless, the hydrophilic bumps as micrometer deposition regions are beneficial for capturing droplets but they impede the droplet continuous draining and transport process[8]. Inspiration from nature is only the starting point, while the ultimate goal is to improve surface engineering and material design in order to maximize water collection from fog.

Moreover, a particular interesting research area is to endow the surface with switchable adhesive features capable of manipulating droplet behaviors in response to external stimuli, displaying superior intelligence and control in smart devices.[1] In this regard, temperature, light, or electrically responsive surfaces offer a promising strategy to develop substrates or systems with precise control and low energy consumption.[2] Nevertheless, many studies consistently claimed that the functionalized surface groups could only directly affect the water molecule in contact with or extremely close to (normally 1~2 nm) the interface. Thus, fundamental understanding on how such a short-range interaction influence the macroscopic wettability transition is necessary for the manipulation of bulk surface wettability.

In addition, the delayed response time to external stimuli remains a significant challenge for further improvement of these surfaces. To further advance the development of controllable liquid manipulation surfaces, it is necessary to explore surfaces that have a programmable response range and are highly sensitive to external signals.

More recently, interfacial solar-driven evaporation has emerged as a sustainable method for generating clean water using solar energy. Unlike traditional solar evaporation that requires heating bulk water, interfacial solar-driven evaporation achieves heat localization to achieve improved solar energy utilization. However, the low efficient water-thermal management still hinder the water generation rate in different solar evaporation system.

1.3 Research Objectives

The objectives of this thesis include:

(1) To develop scalable and sustainable superhydrophobic surfaces that enable precise control over droplet manipulation, with a specific focus on enhancing fog harvesting efficiency by optimizing the balance between water deposition and transport.

(2) To investigate and understand the underlying molecular-level conformational transitions that govern macroscopic surface wettability, leading to the development of surface design strategies for achieving switchable wettability transitions on thermo-responsive surfaces.

(3) To study thermo-responsive surfaces with programmable wettability and adhesion transformation properties, aiming to facilitate the advancement of controllable droplet manipulation techniques.

(4) To fabricate a bilayer-structured solar evaporator that enables the continuous thin water supply and efficient thermal energy management. By leveraging the properties of the thermo-responsive layer, the water transport channel can be selectively and directionally activating the water supply.

1.4 Thesis outline

This thesis is structured into seven chapters, each focusing on different aspects of the research. The following is an overview of the contents covered in each chapter:

Chapter 1-Introduction

This chapter introduces the motivation behind each project and presents an outline of the thesis.

Chapter 2-Background and Literature Review

In this chapter, a comprehensive review is presented on the background information related to the development of sustainable superwettable surface systems. Topics covered include surface wettability, design principles for sustainable superwettable surfaces, multiscale water manipulation, and potential applications in water harvesting and treatment.

Chapter 3- Nano-hydrophilic/superhydrophobic Superhydrophobic Surfaces for Fog Harvesting

Chapter 3 focuses on the development of a unique superhydrophobic surface with tunable nano-scale hydrophilicity. The surface was produced through a self-assembled process using CNC/wax Pickering emulsion, and its exceptional water harvesting performance was investigated.

Chapter 4-Thermo-Responsive Surfaces

This chapter explores the preparation of thermos-responsive surfaces by grafting two representative thermo-responsive polymers, PNIPAM and $POEGMA_{188}$, onto pollen microparticles. The water-surface interaction at different length scales was studied, through tunning the morphology and roughness of the surfaces.

Chapter 5-Dual-Tunable Adhesion and Wetting Surfaces for Programmable Water Droplet Manipulation

Based on Chapter 4 investigation of thermo-responsive pollen-derived surfaces, this chapter develops the surfaces with programmable adhesion and wettability for efficient droplet transfer.

Chapter 6-Solar-driven Water Generation gating by thermo-responsive layer

Utilizing the switchable wettability transition properties of pollen particles (studied in Chapter 4 and 5), this chapter develops a novel strategy for high-performance solar-driven water generation.

Chapter 7-Conclusion and Future Directions

The final chapter provides a comprehensive conclusion drawn from the findings presented in chapters 2 to 6. It also suggests future research directions for the advancement of superwettable surfaces and sustainable water harvesting systems.

Chapter 2. Literature Review

2.1 Introduction.

Freshwater scarcity is becoming a global issue due to the changing climatic conditions, which stimulates the development of all-weather water harvesting technologies. Recent advances in regulating surface properties to tailor water capture/release behaviors have attracted increasing attention in water harvesting applications, such as fog/dew harvesting, moisture harvesting, and solar evaporation. This review provides an overview on the design of surfaces and manipulation of active components to tune the behavior of water in different water harvesting systems. Based on inspiration from nature, we present a critical survey on the surface wettability, structures and composition designed by various insects and plants to efficiently utilize water. We summarize the latest progress in developing the desired surface properties and strategies to advance the key processes in water harvesting, such as droplet nucleation, growth and removal, vapor sorption-desorption, and evaporation. The challenges and opportunities to further develop a sustainable water harvesting system, encompassing both fundamental research and practical implementation are highlighted.

2.2 Design of Superwettable Surfaces

2.2.1 Surface Wettability

Contact angle (θ), an important indicator to quantify the surface wettability plays an important role in understanding the interfacial phenomena at the three-phase liquid-vapor-solid surface (**Figure 2.1a**). Young presented an equation to describe this interfacial phenomenon, where a liquid-vapor interface meets a solid surface, and this is the initial method to quantify the surface wettability (Eq. (2.1)).

$$cos(\theta) = \frac{\gamma_{sv} - \gamma_{sl}}{\gamma_{lv}} \qquad (2.1)$$

where γ_{sv} is the solid–vapor interfacial energy, γ_{sl} is the solid-liquid interfacial energy, γ_{lv} is the liquid-vapor interfacial energy. Based on Young's equation, the boundary for the hydrophilic and hydrophobic surface is set to 90°, corresponding to water affinity and repellent characteristics respectively. A surface with a θ value of less than 90° is regarded as hydrophilic, and in particular when θ is close to 0°, it is defined as a superhydrophilic surface where the fluid has a strong affinity for the solid and will spread completely over the surface. In contrast, a surface with a θ value greater than 150° is deemed to be superhydrophobic, where water is highly repelled by the surface and forms a spherical shape on the surface. However, the Young's equation represents an ideal balance of the surface tension, which is only suitable to explain wettability behaviors on flat and smooth surfaces but is not applicable for rough surfaces.

Therefore, improvement to the model were advanced, when in 1936, Wenzel[3] introduced the roughness factor (r) and modified the Young's equation to Eq. (2.2):

$$cos(\theta_r) = r \cdot cos(\theta) \qquad (2.2)$$

where θ and θ_r are the intrinsic and apparent contact angle of the solid surface respectively; r

is the roughness factor of the solid surface, which is defined as the ratio of the actual surface to the geometric surface, and the value of r is theoretically greater than or equal to 1. Therefore, the increase of the solid surface roughness will increase the hydrophilicity or hydrophobicity of the solid surface under the Wenzel model. Rose petal surfaces are a good example of Wenzel state, where they exhibit 'superhydrophobicity' by displaying excellent liquid repellency, while at the same time they are strongly adhesive towards water. Wenzel equation describes the relationship between the apparent contact angle of the rough surface and the intrinsic contact angle. However, in some cases, it is difficult for the liquid to completely penetrate the void of the solid surface, such as in the lotus leaf. In this case, the Wenzel equation is not applicable for rough surfaces comprising of heterogeneous chemical components. In 1944, Cassie and Baxter[4] further extended the Wenzel's theory by adding the surface composition to the Cassie's equation (Eq.(2.3)):

$$cos(\theta_r) = f_1 \cdot cos(\theta_1) + f_2 \cdot cos(\theta_2) \qquad (2.3)$$

where f_1, f_2 are the surface composition of the two components, and the sum of f_1, f_2 is 1, θ_1 and θ_2 are the intrinsic contact angles of the two components respectively. The Wenzel and Cassie model are important improvements to the Young's equation and they also represent an important theoretical framework to describe super-wetting interface systems, in particular the differentiation between high adhesive[5] (**Figure 2.1b**) and low adhesive surfaces[6] (**Figure 2.1c**).

Recently, a wetting transition state called Cassie–Wenzel transition was reported. It is accepted that the Cassie air-trapped wetting regime corresponds to a higher energetic state. Under certain external stimuli, such as pressure or vibration, the Cassie air-trapped wetting state could be converted to the Wenzel state. It is accepted that the Cassie air-trapped wetting regime corresponds to a higher energetic state, and the Cassie–Wenzel transition is irreversible. With further understanding of the surface wettability, the design theory in constructing the surface with special wettability can be tailored through multiscale structural features consisting of surface composition on molecular level and geometric variation on a micro-nanoscale.[7] For example, lubricant-infused slippery surfaces with a rapid liquid transport property can be designed by utilizing the hierarchical structure and the combined interfacial tension difference between lubricant and immiscible liquid phase.[8]

2.2.2 Water Dynamic behavior on superwettable surface

Water will quickly spread and impregnate on the superhydrophilic surface, while water will slide, jump, or adhere to the superhydrophobic surface.[5-6, 8-9] The distinct wettability behaviors of water droplets can be evaluated from different perspectives.

CA hysteresis

CA hysteresis corresponds to the mass-independent measure of the resistance to macroscopic liquid drop movement on an inclined surfaces.[10] It recognizes the role of gravitational force on a liquid droplet to de-pin from a stationary position on a horizontal surface. This triggers it to slide/roll down an inclined surface and the shape of the liquid drop undergoes some deformation. Assuming the solid-liquid contact area remains constant or experiences a relatively insignificant change, this

deformation from its typical spherical dome/cap shape results in an increase in the droplet's liquid-vapor interfacial area. The energy associated with this increase represents the activation energy barrier to liquid drop motion down an inclined surface. From the initial horizontal position (at θ_r), the drop begins to move when its CAs at the front and back ends are capable of advancing, and receding, respectively.

Tensile adhesion experiment is a complementary method to characterize liquid repellency. In an adhesion experiment, a small drop of liquid is brought into contact with a super liquid-repellent layer, which is then gradually withdrawn in a normal (vertical) direction. The drop of 5 μL (as an example) is held in a metal ring, a disk, or at the end of a capillary. The force required to pull the droplet from the surface, i.e. the pull-out or adhesion force is measured in a microelectromechanical balance, usually a tensiometer. When the water drop first touches the surface, the attractive force during this wetting step was measured as the "snap-in" force. The adhesion force between the water droplet and the surface was measured as the "pull-out" force when the water droplet separates (retracts) from the surface. The snap-in force is shown to decrease monotonously as θ_r decreases and becomes zero at θ_r >150. The excellent correlation is not unexpected due to the similarity between the wetting and the "snap-in" process. Liquid repellency is correlated with a low adhesion force. Alternatively, the force between a super-amphiphobically coated microparticle and a liquid was recently measured using the colloidal probe technique.[11]

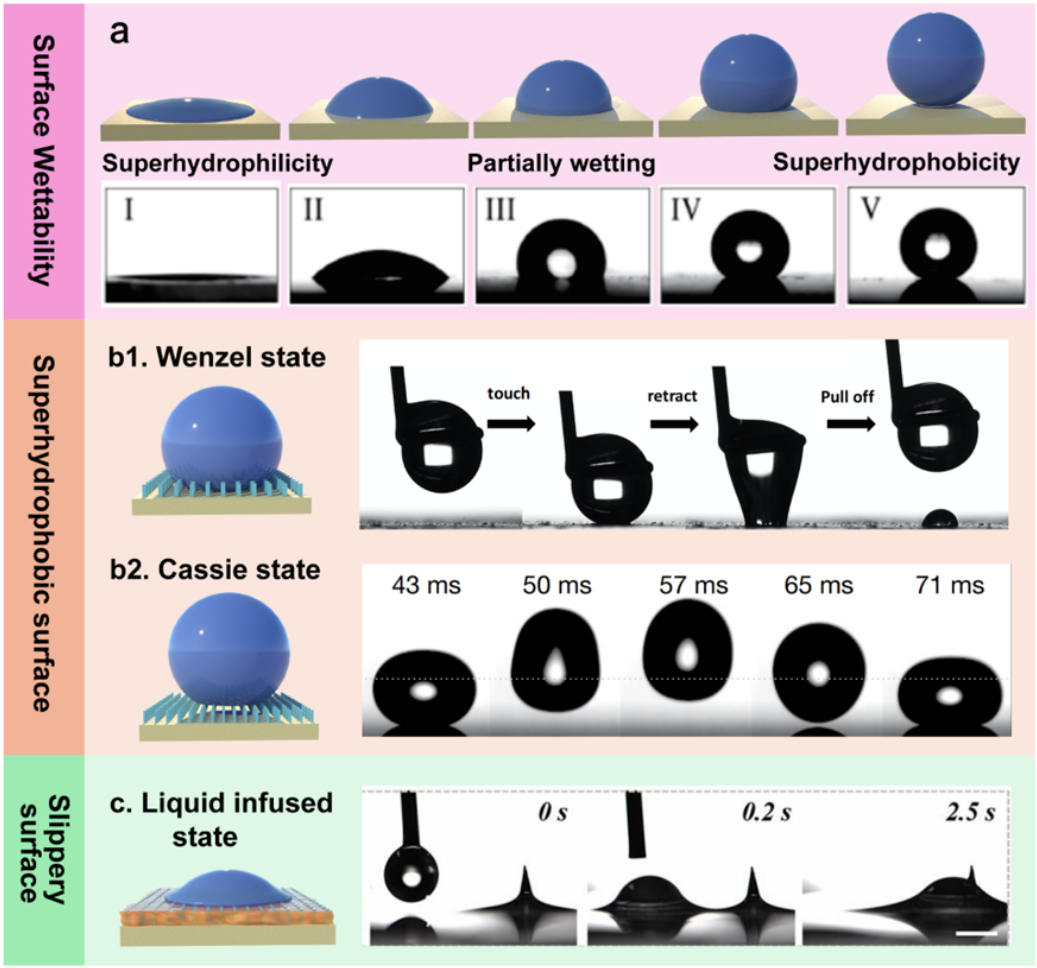

Figure 2.1 The wettability of a surface. a. Surface wettability characterization. Reproduced with permission from ref.[9], Copyright 2017, Springer Nature, b. Two models of superhydrophobic surfaces: b1. Wenzel state characterized by adhesive force. Reproduced with permission from ref.[5], Copyright 2022, Wiley-VCH, b2. Cassie state characterized by dynamic behaviors of droplet. Reproduced with permission from ref.[6], Copyright 2015, Nature Publishing Group, c. slippery surface. Reproduced with permission from ref.[8], Copyright 2019, PNAS.

The apparent contact angle is usually observed by eye or with a low-resolution microscope. To understand the water behavior on a surface, one can image the impalement dynamics in three dimensions by laser scanning confocal microscopy. While the drop evaporates from a pillar array, its rim recedes via a stepwise depinning from the edge of the pillars. Before depinning, finger-like necks form due to adhesion of the drop at the pillar's circumference. Once the pressure becomes too high, or the drop becomes too small, the drop will slowly impale the texture. As soon as the water-air interface touches the substrate, complete wetting proceeds within milliseconds. This visualization of the impalement dynamics will facilitate the development and characterization of superhydrophobic surfaces. Moreover, Berger et al.[12] reported that the lateral adhesion force between a liquid drop and a solid can also be divided into a static and a kinetic regime, which can be measured by AFM. They built an instrument to measure liquid-solid friction between a drop of

liquid and a solid substrate, where a capillary is positioned at the center of the drop. The substrate with the drop is moved sideways against the capillary at a constant velocity. When the capillary reaches the edge of the drop, it sticks to the drop, and consequently, the motion of the substrate is accompanied by a deformation of the drop as well as a deflection of the capillary.

2.3 Bioinspired Surface Design for Water Management

Many biological surfaces in plant and animal kingdoms have unique topographies and constituents to control their interaction with various states of water that sustain them in diverse geographical locations and environmental conditions. By mimicking natural organisms, the principles necessary for water sorption, capture, transport, and release were identified. Herein, we highlight examples from natural species with unique water-handling capabilities, which are adapted for manipulating the water behaviors based on the construction of smart surfaces.

Tiny droplets collection

In regions with extreme daytime temperatures and low rainfall, the condensed dew droplets and wind-driven fog are the main water sources for natural organisms. For instance, the Namib beetle has a unique surface structure for capturing fog from air (**Figure 2.2a)**. Its droplet water-producing system works by a combination of wax-coated hydrophobic and non-waxy hydrophilic elytra. Induced by the low surface energy barrier, the droplet water lands on hydrophilic domains, grows rapidly covering the whole hydrophilic island. Once a critical size is reached, large water droplets are transported along the waxy hydrophobic crevices, achieving the passive droplet collection for beetles.[13] Cactus commonly survives in highly arid regions, and their special conical spine system plays a vital role in water collection process during foggy weather. The water droplets are initially deposited on the hydrophobic tips of the spine (deposition), where they coalesce, grow and are transported along the gradient grooves towards the less hydrophobic base as shown in **Figure 2.2a**. The surface wettability and geometric gradient are the main external forces propelling the water drops toward the base of the cactus and absorbed via strong capillary force. Additionally, some grass species have similar structures on their prickle hairs, like Stipagrostis sabulicola and green bristlegrass.[14] They have micro-scale platelet-like wax structures to prevent the premature shedding of small droplets. Simultaneously, the presence of grooves parallel to the long axis of leaves facilitates the large droplet transport that enhances the fog collection efficiency.

Dew forms via phase transition, where the water vapor in air is transformed into liquid when it contacts a surface, particularly in the morning or night. Spider silk fibers are highly efficient in gathering dew droplets, benefitting from their surface structure of hierarchical spindle knots as shown in **Figure 2.2b**[15]. A directional collection of dew droplets occurs around the spindle-knots promoted by the combined surface energy gradient between the spindle-knots and the Laplace pressure difference generated between the low-curvature region (spindle-knot) with a high-curvature region (joints). As one type of insect-trapping plant, the operculum of Nepenthes is covered with large amounts of trichomes necessary for the condensation of dew droplets.[16] The

condensed droplet would initially wet the smaller inside base channels forming a thin water film. The dew droplets would slide on the top of the thin film and confine within larger microchannels yielding an ultrafast water transport velocity due to Rayleigh instability. Interestingly, the collected dew droplets would wet the peristome of Nepenthe, generating "slippery surfaces" for trapping insects. Except for plants, amphibians can regulate their body temperature to condense dew droplets on their skin, where water is absorbed through their skins.[17] For instance, tree frogs have granular skin with numerous grooves and microchannels and a complex capillary system for water sucking, allowing frogs to more efficiently absorb water compared to smooth skin.

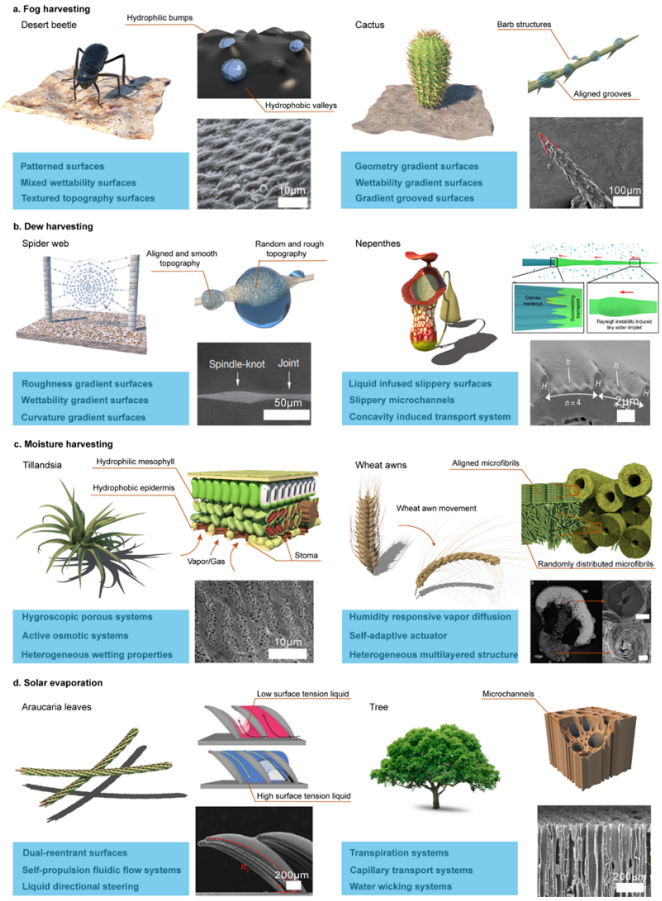

Figure 2.2 Water harvesting devices inspired by the hierarchical structures of natural creatures: **a.** Fog harvesting: dessert beetle, The SEM image is reproduced with permission from ref.[18], Copyright 2001, Springer Nature, and cactus, the SEM image is reproduced with permission from ref.[19], Copyright 2020, Elsevier and Reproduced with permission from ref.[20], Copyright 2022, Springer Nature, **b.** Dew harvesting: spider silk, the SEM image is reproduced with permission from ref.[15], Copyright 2010, Springer Nature, and Nepenthes, the SEM image and illustration are Reproduced with permission from ref. [16], Copyright 2018, Springer Nature, **c.** Moisture harvesting: Tillandsia, the SEM image is reproduced with permission from ref.[21], Copyright 2008, The Royal Society of Chemistry, and wheat awn, the SEM images are reproduced with permission from ref.[22], Copyright 2008, Elsevier, **d.** Solar evaporation: Araucaria leaf, the SEM image and illustration are Reproduced with permission from ref.[23], Copyright 2021, Science Publisher, and tree, the SEM image is reproduced with permission from ref.[24], Copyright 2019, Elsevier.

Moisture concentration and release

In nature, moisture concentration process normally occurs on the surface of plants trapping water from the atmosphere. For instance, the Tillandsia species possess hygroscopic leaves with porous apertures (< 2 μm) capable of trapping moisture from the atmosphere (**Figure 2.2c**). The liquefied water aggregates on the superhydrophilic leaf surface guided by the directed transport of water from the outermost tissues to the interior network via an osmotic process. The well-established tissue systems can hold the absorbed water and regulate the leaf transpiration for sustainable growth. Some plant tissues, like wheat awns have complex and unique structures that interacts with moisture under different RH generating propulsion (hygroscopic motion) that force their seeds into the soil to promote germination. This interaction is associated with the controllable hydration/dehydration process of double-layer cellulose microfibrils that are aligned and distributed within the inner cap and randomly orientated on the outer ridge of wheat awn (**Figure 2.2c**).[22] The difference in the swelling between the two structures induces the wheat awn to contract and expand at higher and lower RH respectively. Besides, the nano-scale plywood architecture of the awns endows the cell wall with sensitive moisture sorption-desorption process (swelling/deswelling) under mild humidity changes.[25] This can be attributed to the hydroscopic expansion of their highly anisotropic arrangement when water molecules enter the structure, creating new nano-sized gaps that increase both the rate and capacity of absorption. A similar moisture absorption transport mechanism is found in pinecones that have a similar double-layer structure like wheat awns.

Liquid water management

Typically, a living tree is constantly circulating water from the ground up by relying on the wood mesostructures (**Figure 2.2d**). The unique hierarchically aligned porous structure of natural hydrophilic wood ensures the continuous supply of water from the bottom to the upper evaporative surface via capillary transport.[24] Moreover, the tree crown not only provides a large surface area for evaporation but also minimizes the loss from radiation and convection. In addition to trees, mushrooms have also inspired smart biomimetic structural designs for solar evaporation.[26] It has a designed diameter ratio between its umbrella-shaped black pileus and fibrous stipes, which can provide a thermal concentration structure and suppress the heat conduction loss to bulk water. Besides, the ratio of surface to the projection area for pileus can simultaneously achieve a large evaporation area and a reduction of heat loss from radiation and convection. The Araucaria leaves have an unexpected liquid steering behavior based on their three-dimensional (3D) ratchets design as shown in **Figure 2.2d**.[23] Different from the conventional 2D liquid transport, this surface structure will impart asymmetric contact line pinning, enabling a directional guiding and rapid transport of liquids with different surface tensions in a well-controlled manner. Besides, the transpiration system of water lilies provides inspiration to researchers. The floating surface is supported by lacunae (air chamber) at the bottom of the leaf in contact with water.[27] Its vascular bundles provide liquid water transport for confined water to spread over the evaporation surface for

vapor generation.

2.4 Preparation of Sustainable Superhydrophobic surfaces

The superhydrophobic surface has attracted intense interest both in academia and industry due to its unique characteristics, such as water-repelling, self-cleaning, and anti-fouling, where these properties can be adapted to many applications, such as water harvesting, windshields, and oil/water separation.[27] In this section, the basic understanding of superhydrophobicity is discussed, including contact angle, theoretical model, and contact angle hysteresis. In addition, this section will provide a detailed analysis of the principles for the use of sustainable colloidal nanomaterials to prepare superhydrophobic surfaces.

Structural Design

The hydrophobicity of a material can be evaluated by the water contact angle and surface energy, which is dependent on their functional groups and morphologies. When the water contact angle is greater than 90°, the corresponding material is defined as hydrophobic. Some hydrophobic groups, such as silane group (-R_3Si), ester group (-RCOOR), amide group (-$CO{=}NH_2$), ether group (-R–O

A wide variety of methods to fabricate superhydrophobic surfaces have been introduced in recent years. In general, the principle of preparing a superhydrophobic surface is by incorporating a micro-nanoscale structure with low energy surface tension materials onto a substrate. The combination of the fabrication methods and low surface energy materials determine the roughness structure and surface energy respectively, which further determine the hydrophobicity of the surfaces. Thus, the superhydrophobic surface fabrication methods and materials are described below, and the advantages and disadvantages are briefly discussed. With the advancement of technologies, there are the many types of processing tools, such as plasma, laser, chemical etching, photolithography electrospinning, and sol-gel coatings which can be used to roughen solid substrates to generate a superhydrophobic surface[50].

Etching methods

McCarthy et al. [51] reported the plasma polymerization to a heptafluoroacrylate film on the surface of ethylene phthalate, and the contact angle of the surface with water was 173°. They also used radio frequency plasma to etch biaxially oriented polypropylene film and added polytetrafluoroethylene to fluorinate the surface of polypropylene (**Figure 2.3d**). The control of the roughness and degree of fluorination of the polypropylene surface was performed by adjusting the time. Bico et al. [52] described a rough surface with micron-level needle, hole and strip-like structures that were prepared on a substrate. The contact angles of the surface and water after fluorination treatment were 167°, 131° and 151°, respectively. Interestingly, Kim et al. [53] reported that a specific doubly reentrant structure that enables a very low liquid-solid contact fraction can render the surface of any material super-repellent via etching method, which can be superomniphobic and bounce off all available liquids, including perfluorohexane. The same superomniphobicity is further confirmed with identical surfaces of a metal and polymer. Free of any hydrophobic coating, the

superomniphobic silica surface also withstands temperatures exceeding 1000°C and resists biofouling.

Electrohydrodynamics/Electrospinning.

Electro-hydrodynamics (EHD) technique is a conventional and feasible method to produce micro- and nanostructures, such as fibers and particles. Using the EHD technique, Jiang et al. [54] fabricated a low-cost superhydrophobic PS film consisting of porous microspheres and nanofibers. Microspheres and nanofibers contributed differently to the stable superhydrophobicity, that is, increasing surface roughness by microspheres and binding the porous microspheres by a 3D nanofibers network (**Figure 2.3a**). They have synthesized a class of spin-coated films of PMMA and fluorodecyl POSS using hydrophobic polyhedral oligomeric silsesquioxane (POSS) molecules with re-entrant surface curvature. These surfaces display extreme resistance to wetting from a number of liquids with low surface tension, including alkanes such as decane and octane.

CVD methods

Furthermore, Deng et al. [55] described an easy-to-fabricate oil- and water-repellent coating produced from soot encased in a silica shell via chemical vapor deposition (CVD) (**Figure 2.3c**). The coating is sufficiently oil-repellent to induce the rebound of impacting drops of hexadecane. Even low surface-tension drops of tetradecane roll off easily when the surface was tilted by 5°, carrying impurities along with them. The surface maintained its super-amphiphobicity after being annealed at 400°C. The coating is transparent and can be applied to a variety of heat-resistant surfaces, such as aluminum, copper, or stainless steel. Based on the previous studies on soot-templated super-amphiphobic surface, and recently[56] they combined this method with rough substrates by photolithography and fabricated the robust superhydrophobicity structuring surfaces at two different length scales, with a nanostructure design to provide water repellency and a microstructure design to provide durability (**Figure 2.3f**). The microstructure is an interconnected surface frame containing 'pockets' that house highly water-repellent and mechanically fragile nanostructures. This surface frame acts as 'armour', preventing the removal of the nanostructures by abradants that are larger than the frame size. This transparent, mechanically robust, self-cleaning glass could help to negate the dust-contamination issue that resulted in the loss of efficiency in solar cells.

Coating methods

Dip-coating is the also most common method to fabricate a superhydrophobic coating on paper or cotton substrates. It typically requires at least three separate processing steps, which include dipping in the coating slurry, drying, and curing. Typically, the coating slurry contains organic solvent, components that increase the coating roughness, e.g., nano-/micro- particles, and binding component. In addition, the coating slurry may contain hydrophilization agents, or the hydrophilization treatment can be performed separately after the dip-coating process. Many superhydrophobic coatings fabricated by dip-coating showed surprisingly good mechanical durability due to the strong binders and hierarchical roughness of the coating. Haag et al. [57] described a simple and efficient dip-coating approach to fabricate highly hierarchical surface

coatings with superamphiphobic properties for a broad range of materials based on a mussel-inspired dendritic polymer (MI-dPG). Zhang et al. [58] prepared a superhydrophobic PMMA-SiO_2 nanocomposite film with micro/nano hierarchical structures on glass slides in the absence of low surface-energy compounds. The PMMA-SiO_2 nanocomposite films possessed a static water contact angle greater than 162°.

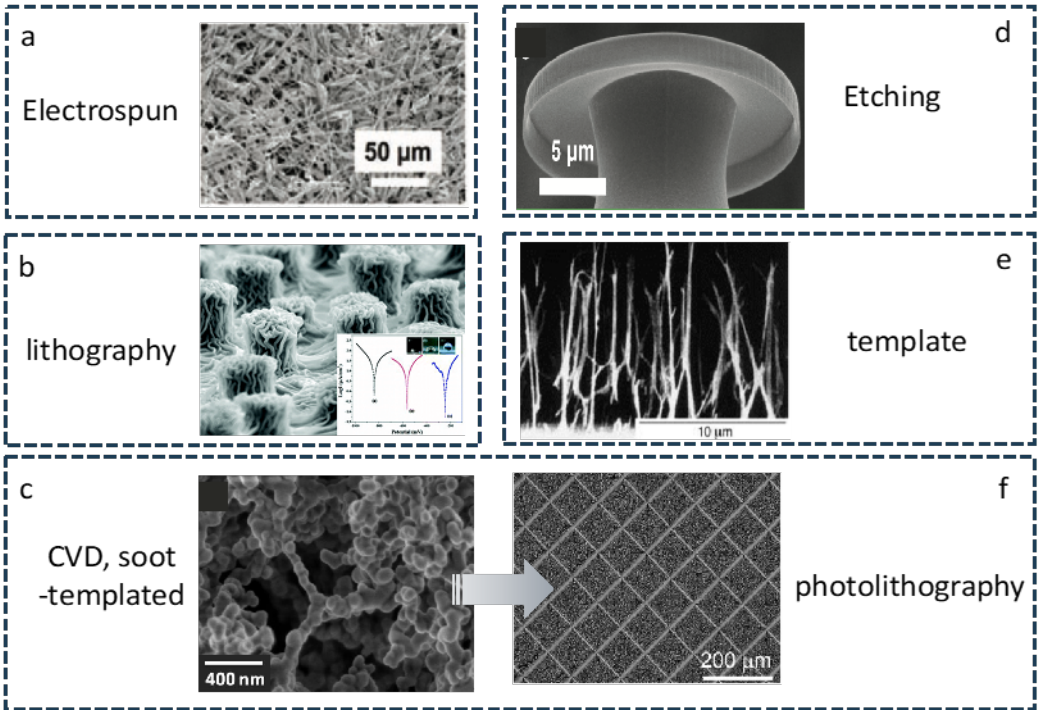

Figure 2.3 The typical fabrication methods of superwettability surfaces[54]-[59]

Materials Selection and Modifications

The most controversial issues in fabricating superhydrophobic surfaces are the hydrophobicity level of the materials. Low surface energy materials, such as siloxanes or fluoropolymers are widely used to impart hydrophobic characteristics on engineered superhydrophobic surfaces. A close examination of the surface by SEM shows that the surface consists of a complex micro- and nanoscopic architecture, and the entire surface is covered by a low surface energy wax[41]. However, in light of environmental concerns and the imperative for sustainability, our focus should be directed towards natural materials and sustainable processes that have a lower potential environmental footprint. Additionally, this will address the environmental concerns of perfluorinated compounds, and the process is deemed to be ecofriendly to sustain large-scale fabrication of the system.

Preparation of Hydrophobic Colloidal Particles

As a large amount of hydroxyl and amino may be present in the cellulose, chitin, chitosan, and lignin colloidal systems, they possess hydrophilic characteristics that hinder their applications in some sectors. Thus, surface modification to enhance colloidal stability, impart hydrophobicity with the desired characteristics is often required.

The abundance of surface hydroxyl groups on the surface of CNC, nanochitin, and nanochitosan

offers an excellent platform for surface modification with hydrophobic groups (**Figure 2.4a and 2.4b**). Detailed modification techniques are illustrated in **Figure 2.4** and they are classified under two broad classes: chemical modification and polymer grafting. Through chemical modification, such as silylation, esterification, acetylation, amidation, urethanization, and etherification [15], CNCs can be directly modified by the covalent attachment of molecules on the CNC surface, making the surface hydrophobic as analogous to nanochitin and nanochitosan. For instance, Wang et al. reported the preparation of hydrophobic CNCs via the esterification of 10-undecenoyl chloride on the CNC surface resulting in enhanced hydrophobicity, while retaining the rod-shaped morphology of the CNC [16]. Notably, Beaumont and co-workers described a unique acetylation reaction on the surface of nanomaterials that was mediated by surface-confined water. In comparison to dry acetylation, surface-confined water elevates the reactivity by 8 times and increases the reaction rate of the surface acetylation on the cellulose with N-acetylimidazole. This study demonstrated a feasible approach of modifying nanomaterials that is sustainable and it outperforms reactions occurring in organic solvents from the perspective of efficiency and environmental consideration [17]. Chen et al. reported on the synthesis of highly alkynyl-functionalized cellulose nanocrystals by introducing hydrophobic alkynyl groups consisting of 4-oxo-4-(prop-2-in-1-acyloxy) butanoic anhydride on CNCs. The alkynyl-modified cellulose nanocrystals (ACNC) possessed a higher contact angle (56.8°) compared to pristine CNC (30.2°), where the surface energy decreased from 68.0 to 28.2 mJ/m^2 [18]. Similar hydrophobic modifications were demonstrated for nanochitin and nanochitosan [19][20].

Grafting polymers onto cellulose is also an excellent approach to modify the chemical and physical properties of the systems. Polymer-nano composites were synthesized via atom transfer radical polymerization (ATRP), free radical polymerization, reversible addition-fragmentation chain transfer (RAFT), and ring-opening polymerization, by coupling the reactive end groups of the polymer to the hydroxyl groups of CNC, nanochitin, and nanochitosan. A wide range of hydrophobic polymers was explored and reported, (e.g., polypropylene oxide, polystyrene, poly(lactic acid), and poly(ε-caprolactone)) [7,15].

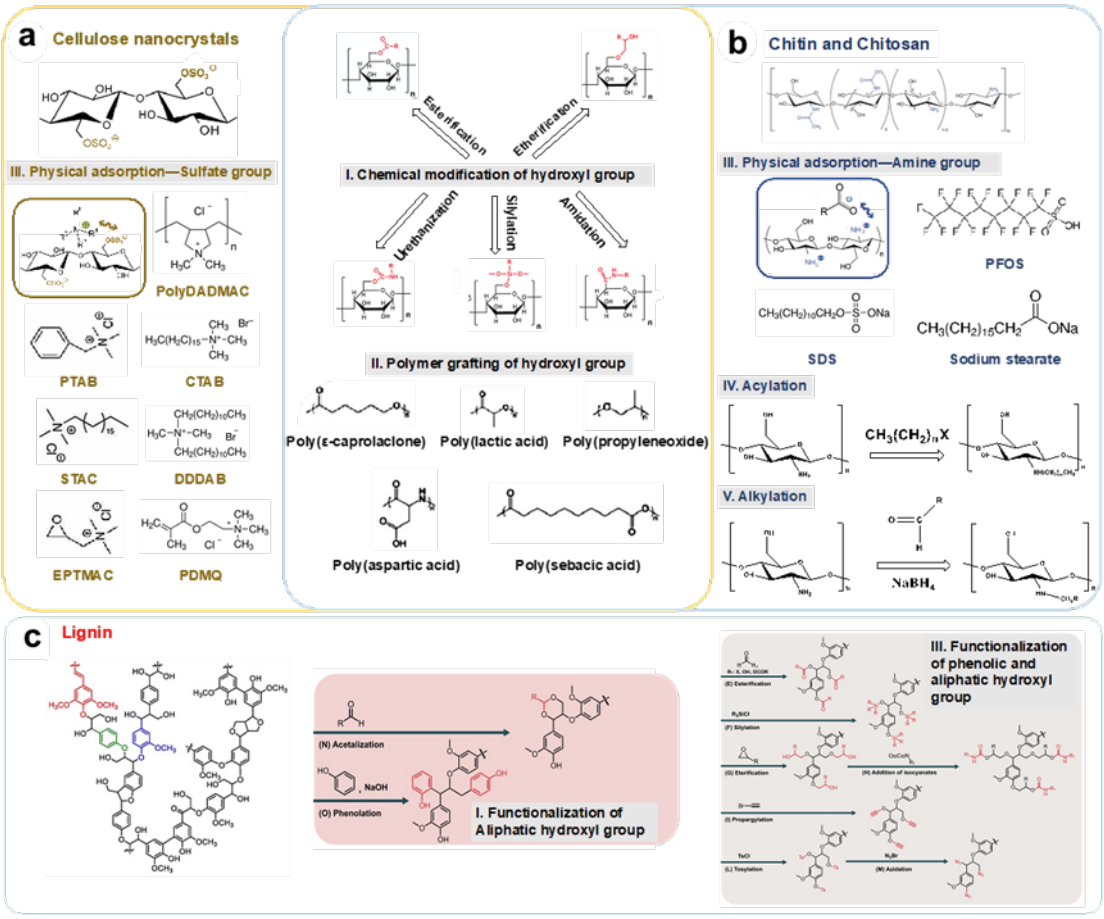

Figure 2.4 The hydrophobic modification of colloidal particles. a. cellulose nanocrystal, b. nanochitin and nanochitosan c. lignin nanoparticle. Images are reprinted with permission from ref. [6,11,15,18].

The modification on CNCs occurs on the hydroxyl groups, for example, CNCs are decorated with negatively charged sulfate groups via sulfuric acid hydrolysis. Adsorption of cationic amphiphilic compounds on the surface will enhance the hydrophobicity of the CNC. Quaternary ammonium salts consisting of hydrophobic and hydrophilic moieties would bind to the negative CNC surface via electrostatic interaction and disrupt the hydrogen bonds between the hydroxyl groups and water molecules. Cetrimonium bromide (CTAB) is a good candidate for the adsorption to CNCs, while polydiallyldimethylammonium chloride (polyDADMAC), stearyltrimethylammonium chloride (STAC), and epoxypropyl trimethylammonium chloride (EPTMAC) can be used to enhance the hydrophobicity of CNCs via physical adsorption. Salajková et al. developed an environmentally friendly method for the surface modification of cellulose nanocrystals (CNCs) via the adsorption of quaternary ammonium salts in an aqueous solution. The C18 alkyl chains modified CNCs displayed a large increase in the water contact angle (71°) compared to unmodified CNCs (12°) [21]. Gicquel et al. investigated a fast and irreversible electrostatic adsorption of thermo-responsive block copolymers onto anionic TEMPO-oxidized CNC, where the quaternized block copolymer comprised of cationic poly(2-(dimethylamino)ethyl methacrylate) (PDMAEMA) and a thermo-

responsive poly(di(ethylene glycol) methyl ether methacrylate) (PDEGMA). The functionalized CNCs not only became more hydrophobic but also achieved the hydrophilic/hydrophobic transition controlled by temperature [22].

Similarly, chitosan can undergo similar reactions as the hydroxyl groups, such as esterification, etherification, urethane formation, cross-linking with polyfunctional reagents, and graft copolymerization to enhance the hydrophobicity via the reduction of the surface energy to less than 30 mJ/m^2. Due to the presence of primary amino groups, which are more reactive than hydroxyl groups, many more attractive pathways for chemical modification are possible, such as acylation, alkylation, formation of Schiff bases, and other NH_2-specific reactions. Specifically, the modified groups (acyl and alkyl groups) produced via acylation and alkylation are hydrophobic, following the reaction schemes described in **Figure 2.4b** IV and V. Furthermore, the amino groups are protonated in an acidic environment to yield positively charged ammonium groups, which offers an alternate route of hydrophobic modification via physical adsorption of anionic compounds. Carboxylates are the most common surfactants consisting of carboxylate salts, such as sodium stearate. Other amphiphilic compounds, such as sodium dodecyl sulfate (SDS) and carboxylate-based fluorosurfactants (perfluorooctanoate (PFOA), perfluorooctanesulfonate (PFOS)) can be used to impart hydrophobic character via physical sorption.

Owing to the complex structure and intrinsic tendency of lignin to form strong intra- and intermolecular bonds, it is more difficult to modify lignin compared to CNC, nanochitin, and nanochitosan. There are four different reported approaches (**Figure 2.4c**) to chemically modify lignin: (1) lignin depolymerization or fragmentation, using the lignin as a carbon source or to cleave lignin into small fragments with aromatic rings; (2) modification of lignin by synthesizing new chemically active sites; (3) chemical modification of the hydroxyl groups presents on the lignin structure; and (4) production of graft copolymers.

Surface functionalization possibilities stem mainly from the reactivity of the aromatic rings of guaiacol, as well as phenolic and aliphatic OH groups present along the lignin backbone. Silylation, esterification, amidation, urethanization, and etherification are commonly performed to introduce various functional groups to transform the hydroxyl groups of lignin into hydrophobic groups [23]. In addition to targeting lignin's aromatic rings, other post-modification methods have been reported, where the lignin's hydroxyl groups were converted to leaving groups for subsequent substitution reactions, such as tosylation, azidation, and propargylation reaction [11, 24].

An important set of reactions (e.g. phenolation and acetalization) could be used to further tailor the hydrophobicity and solubility of lignin. Phenolation reactions on the α and γ hydroxyl groups can effectively add phenolic groups to the lignin side chain, which increases the number of aromatic reactive sites. In addition, Lan and co-workers observed that the solubility of the resulting lignin could be manipulated by functionalizing the lignin with aldehyde groups using an acid catalyst to transform the α and γ hydroxyl groups of the β–O–4 linkage into acetals, making them soluble in

many different solvents [25, 26].

Fabrication of superhydrophobic surface

In the following section, we will present the latest advances in superhydrophobic coatings produced from natural, biodegradable, and nontoxic food or medical grade materials. Processes and fabrication techniques that utilize ecofriendly or water-borne solvents, chemical steps and even solventless casting systems will be discussed.

Cellulose and Its Derivatives

Cellulose is an attractive green and sustainable biomass material, one of the most important natural polymers, and a key source of industrial-scale renewable materials. Cellulose nanomaterials (CNs) encompassing cellulose nanofibrils (CNFs), cellulose nanocrystals (CNCs), and bacterial cellulose (BC), are low-cost, abundant, and biocompatible nanomaterials that have received increasing attention in recent years. CNC, a rod-like shape, possessing length from 200 – 1000 nm and diameters of 5 – 15 nm, in particular is well known for its versatile properties, such as large surface area (~250 m^2/g), high dispersibility and high elastic modulus (145 GPa)[59].

Among them, cellulose nanocrystals (CNCs) originated from the sulphuric acid that the surfaces have large number of sulfates groups ($-OSO_3^-$) and hydroxyl groups (-OH), are excellent candidates for modification. It would be easier to modify CNCs, transforming them from hydrophilic to hydrophobic materials and thus providing the possibility for functionalization. Additionally, cellulosic chemistry includes a large number of surface hydroxyl groups, which readily form hydrogen bonds with water molecules, enabling water to spread over the surface. Cellulose is also capable of absorbing water since it is a hydrophilic and hygroscopic material by nature, and hence is an ideal candidate for atmospheric water harvesting. Geissler et al. [60] fabricated a robust, superhydrophobic, and self-cleaning film using micro/nano structured cellulose fatty acid esters (cellulose stearoyl ester, CSE), which was prepared via nanoprecipitation. The superhydrophobic films could be coated on diverse surfaces with nonuniform shapes via distinct coating techniques. The CSE had a degree of substitution of 2.95, indicating that almost all hydroxyl groups on the cellulose backbone were substituted by stearoyl groups, making it soluble in a variety of organic solvents. Following this work, cellulose nanocrystals (CNCs) are used as a framework material to prepare a necklace-like CNC/SiO_2 nanostructure (referred to as CNC/SiO_2 rod) via in-situ growth of SiO_2 as building blocks to prepare superhydrophobic coatings[61]. The CNC/SiO_2 superhydrophobic coatings could also be prepared by spraying or smearing the CNC/SiO_2 rods onto substrates treated with a commercial spray adhesive. Pradeep et al. [62] demonstrated a simple strategy to develop a multifunctional waterproof paper from chemically modified CNF building blocks via the fabrication of fluoroalkyl functionalized CNFs in aqueous medium. Shimizu et al. [63] adsorbed different alkyl quaternary ammonium salts on the surface of TONC and prepared a hydrophobic and transparent CNP (**Figure 2.5**), and its mechanical properties, and air permeability could be controlled by using various quaternary ammonium salts.

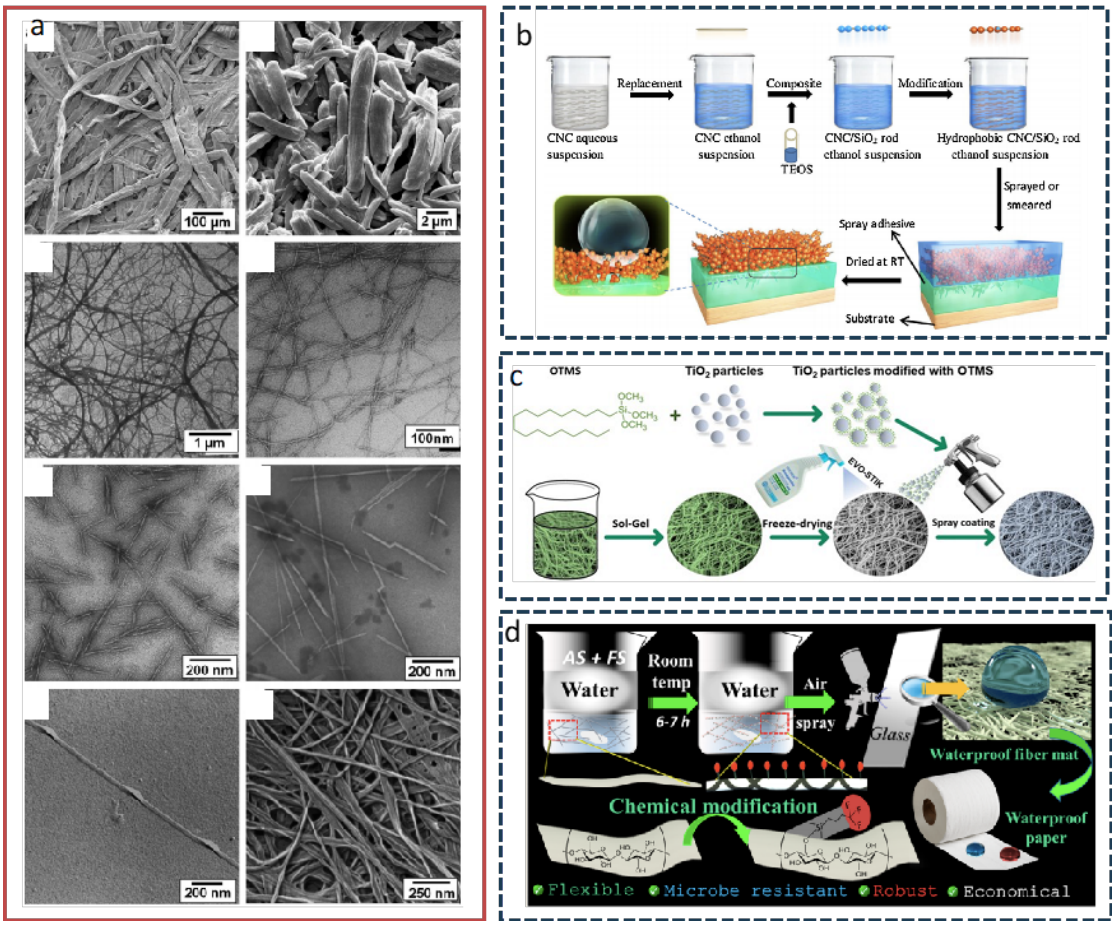

Figure 2.5 Fabrication of cellulose-derived superhydrophobic surfaces. a Scanning Electron Microscopy (SEM) and Transmission Electron Microscopy (TEM) images of cellulose nanomaterials[64], b, c & d Superhydrophobic surfaces designed by cellulose and its derivatives[61]-[63]

Natural Waxes

Surfaces of leaves, stems, or fruits of higher plants are covered with microscopic layers of lipids that are known as epicuticular waxes. Chemically, plant waxes are composed of a large number of different compounds, mostly long-chain aliphatics, which can be further classified according to their structure, substitution, and the distribution of their homologues. Liu et al[65] developed a food container that has micro- and nano-roughness hydrophobic surface to reduce the wastage of liquid foods (**Figure 2.6a**). The superhydrophobic coating was prepared using edible candelilla wax and rice bran wax in hot ethanol through a one step of spraying onto a polypropylene (PP) substrate. The coated PP could maintain excellent super hydrophobic properties after exposure to a high temperature aqueous solution (about 70°C) or 1200 repetitive bends, thus, it was found to have excellent heat resistance and flexibility. Miljkovic et al. [66] reported on the development of environmentally friendly and economical superhydrophobic coatings using naturally abundant sepiolite nanoparticles functionalized with naturally extracted fatty acids from cinnamon and myristica (**Figure 2.6b**). They coated the material on a variety of metallic and nonmetallic surfaces

by dip-coating it with aluminum, absorbent fabrics, glass, and even paper.

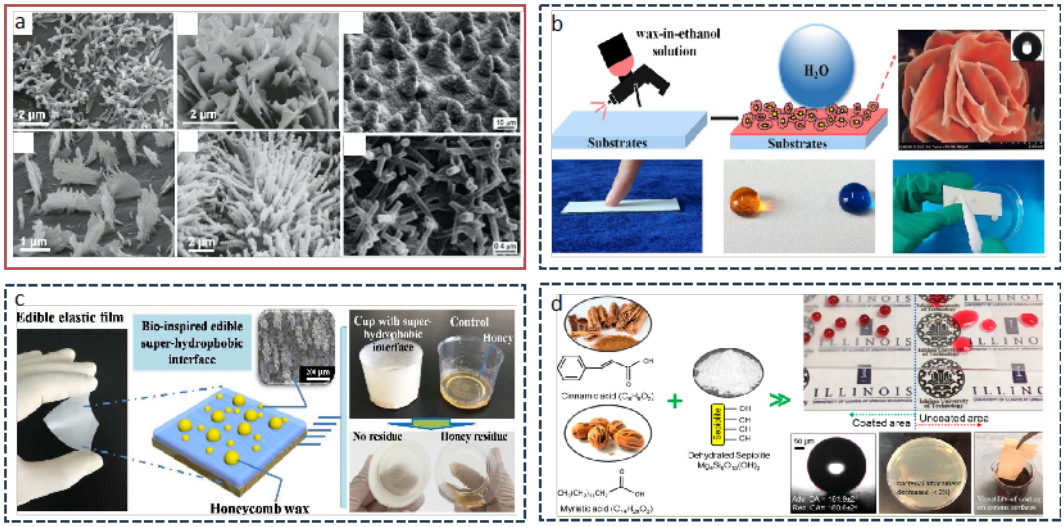

Figure 2.6 Fabrication of paraffin-derived superhydrophobic surfaces. a Scanning Electron Microscopy (SEM) images of waxes[65], b, c & d Superhydrophobic surfaces designed by natural wax and its derivatives[67]–[69]

Pollen and Its Derivatives

A novel plant-based material, pollen derived from ground pine, are roughly 1-250 μm in size and somewhat spherical in shape, it also features small ridge-like structures protruding from their periphery[70]. The spores are intrinsically hydrophobic and have been used to prepare liquid marbles. They are protected by a remarkably complex and robust double-layered wall, consisting of an inner wall layer called *intine*, which is mainly composed of cellulose and several polysaccharides. The outer shell, *exine*, consists largely of sporopollenin, one of the most resistant natural organic materials known. Due to their unique spiky structure, the application of pollen in superwettability studies have been reported[71].

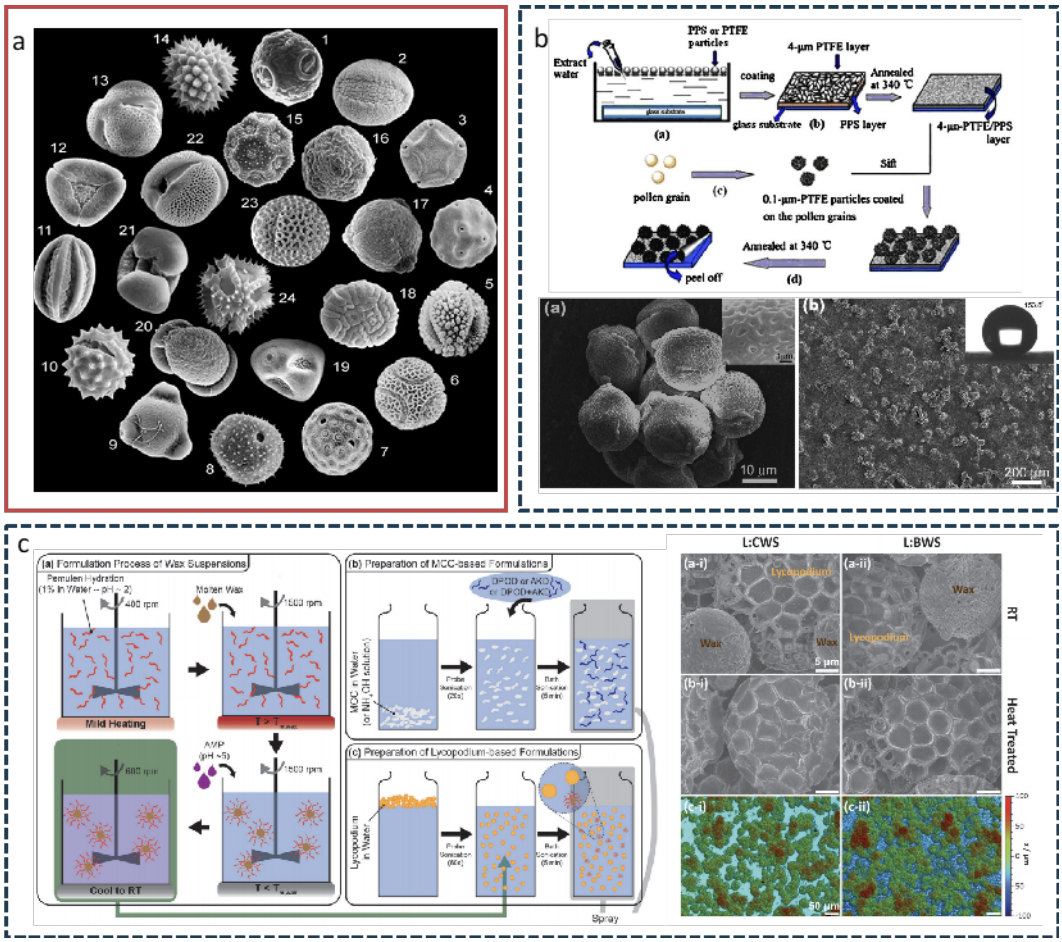

Figure 2.7 Fabrication of pollen-derived superhydrophobic surfaces. a. Scanning Electron Microscopy (SEM) and Transmission Electron Microscopy (TEM) images of various pollen[74], b. pollen modified with PTFE c. Superhydrophobic surfaces designed by pollen and its *derivatives*[72], [73]

Milionis et al. [72] first demonstrated this by fabricating superhydrophobic composite coatings using lycopodium and a thermoplastic starch (**Figure 2.7b**). However, those coatings were sticky (i.e., rose petal effect) and were sprayed from a chloroform-based solution. After that, Morrissette et al.[73] presented an economical method to prepare fluorine- and silane-free emulsion coatings from plant-based filler materials; viz. microcrystalline cellulose (MCC) and lycopodium spores (LS) (**Figure 2.7c**). The wettability of the coated surface was regulated by adjusting the filler/ polymer mass ratio (φ). The results showed that LC-based spray-coatings featuring carnauba wax or beeswax followed with post-heat treatment at 70–100 °C displayed the greatest superhydrophobicity. The study also showed that only the LC-based coating displayed self-cleaning property due to the enhanced surface roughness.

2.5 Design of Functional Superhydrophobic Surfaces

Recently, the study of superhydrophobic surfaces has generated more interest in various applications, where surfaces can be designed to possess different properties in addition to the original water repellent property. In practical application, the superhydrophobic surfaces should possess many

different properties to fit the requirements of the application. In addition, the development of superhydrophobic surfaces tends to simple, robust, sustainable, and multifunctional.

To enable the surfaces to possess specific properties, the modification of different types of materials and the morphology of substrates have been considered. Firstly, stable and robust superhydrophobic surfaces are gaining more attention. For example, Zhu et al. [75] fabricated a carbon nanofiber arrays prepared through thermal pyrolysis of nanostructured polyacrylonitrile (PAN) film, while the as-prepared films showed superhydrophobic property over the whole pH range with the water CA greater than 150° for acidic and basic liquids. Additionally, the optical properties are important in electronic devices, however the surface roughness necessary for superhydrophobicity often results in a reduction in the surface transparency due to light scattering. Lee and co-workers[76] reported on a new antifogging coating design that imparts superhydrophobicity. The system contains a silica nanoporous layer assembled on the polymeric reservoir containing CHI and CMC in order to increase the transmittance and also facilitating the spreading of the condensed water to improve the "wet-style" antifogging property. In addition, the nanoscale roughness provided by the silica nanoporous layer allows for the independent pattern transfer of low-surface-energy PFPE pillars with mechanical durability via a two-step lithography. Also, Nogi and co-workers[77] reported on a foldable, low-CTE, and optically transparent nanofiber paper by smoothing the surface to prepare functional transparent cellulose sheets.

Stimuli-Responsive surfaces

In addition to the properties described above，smart superhydrophobic surfaces are growing rapidly, where switchable and programmable properties have been demonstrated. Stimuli-responsive materials are sensitive to changes in the external environmental conditions, and they can be incorporated with superhydrophobic surfaces to control the surface wettability. The special configuration of functional molecules on surface could be manipulated by external stimuli, and surface wettability would correspondingly change. Since the range of the wettability transition is very limited on a flat surface, roughness structure on superhydrophobic surfaces can act as an effective way to amplify the transition range of wettability. The following sections will describe different responsive materials used to prepare superwettability surface.

Photo-Responsive Superwetting Surfaces

Among the different external stimuli, light can be used to reversibly change the geometric and electronic structures of photo-responsive molecular materials in solutions, crystals, and gels. It is a convenient way to achieve non-contact control of the surface wettability due to the benefit of light sensitive trigger of the surface to achieve precise control of tunable direction, illumination area, and irradiation intensity. The change in the wettability mechanism of these photo-responsive materials is consistent with the mechanism of photocatalysis, i.e., electrons and holes photogenerated by light irradiation and absorption by the water molecules.

The typical photo-responsive materials are including inorganic oxides (TiO_2) and organic compounds such as azobenzene, malachite green and spiropyran. As early as 1997, Fujishima and

co-workers[54] first reported their new discovery on the UV-generated superamphiphilicity on titanium dioxide surfaces. Water droplets and oil could quickly spread on these surfaces after UV irradiation, and the hydrophobicity would recover after long term storage in the dark. Following this concept, many organic materials have been explored, such as azobenzene, which could form cis and trans isomers under ultraviolet and visible irradiation respectively. An azobenzene monolayer on a laser etched rough substrate exhibited a transition from superhydrophobic to superhydrophilic when subjected to UV irradiation. When the azobenzene monolayer was modified on the surface of SiO_2 inverse opal, the structural color and the wettability response could be controlled by the size of the ordered monodispersed structure. A similar phenomenon also was observed by Picraux et al. [56] on the photoinduced isomerization of spiropyran-containing monolayer on the substrate of random silicon nanowire.

Thermal-responsive Superwetting Surfaces

Temperature-responsive polymers have been widely studied, such as poly(N-isopropylacrylamide) (PNIPAAm), polycaprolactone (PCL) and poly-oligo(ethylene glycol) methacrylate (POEGMA) , while these polymer chains often exhibit a conformation change in response to external stimuli.

Jiang et al. [75] deposited a poly(N-isopropylacrylamide) (PNIPAAm) thin film by grafting from a smooth silicon substrate via surface-initiated atom-transfer radical polymerization (SI-ATRP). The surface possessed a hydrophilic state with a CA of 63.5° when temperature was set at 25 °C, and the surface became hydrophobic with a CA of 93.2° at 40 °C. Based on the above results, they also obtained a reversible surface alternating between superhydrophobicity at low temperature and superhydrophilicity at high temperature by coating poly(e-caprolactone) [64] onto a rough substrate. This was caused by the orientation of the polymer chain between the crystalline/amorphous phase transition. In addition, rapid reversibility and excellent stability of thermally switching were observed by Lopez et al.[76] for PNIPAAm-grafted porous anodic aluminum oxide (AAO) membranes. Zareie et al.[77] reported a reversible surface wettability on self-assembled monolayers of oligo-(ethylene glycol) tethered on gold substrates. Additionally, Cao et al.[78] report a versatile strategy to reversibly control the mobility of spherical microdroplets of water on the surface from rollable to pinned state by controlling the temperature. Unlike previous reports on CA switchable surfaces, this study describes the water mobility switching, and furthermore, the static CAs before and after switching are all in the superhydrophobic range. The superhydrophobic surface with switchable water mobility was prepared by simply spin-coating a side-chain liquid crystal polymer (SCLCP), PDMS-4OCB, on an optimized rough silicon wafer.

pH-Responsive Reversibly Tunable Wetting Surfaces

Furthermore, the work environment of superwettability surface is also a key point in many applications, and pH-responsive surfaces have attracted increasing attention as they could be applied to many applications, such as drug delivery, separation, and biosensors. There are many organic compounds that possess the sensitive pH responsive property, such as poly(tert-butyl

acrylate)(PtBA), poly(2-(dimethylamino)ethyl methacrylate) (PDMAEMA), Polyvinylpyrrolidon (PVP), 2-(11-mercaptoundecanamido)benzoic acid (MUABA) and many others.

Uhlmann et al. [79] demonstrated a stimuli responsive binary polymer brushes obtained by "grafting-to" and "grafting-from" approaches. The reversible switching systems obtained through a polymer brush comprised of a hydrophilic and a hydrophobic polymer treated with a non-selective and selective solvents for both polymers. In good solvents, the inter chain repulsion dominates and the polymer chains exist in stretched conformation and for a poor solvent, the repulsion between polymer and solvent dominates causing the chain to collapse yielding a coiled polymer conformation. Hence, when the brush is treated with a selective solvent for the polymer, it becomes hydrophilic and when it is treated with a non-selective solvent, the surface becomes hydrophobic. In addition to molecular mechanism studies, Lu et al. [80] investigated the changes in the surface wettability using pH-responsive polymers. For example, a superhydrophobic PANI-PAN coaxial nanofiber film was prepared by a combination of electrospinning and polymerization. By simply tunning the acid-base and redox properties of the probe solution, this nanofiber film exhibited a pH-reversible conversion between superhydrophobicity and super-hydrophilicity characteristic.

Multi-responsive Superwetting Surfaces

As described previously, many smart surfaces that can switch between superhydrophilicity and superhydrophobicity have been fabricated using the combination of responsive materials and surface roughness. However, most of these surfaces are responsive to only one type of external stimuli, restricting their applications in complex environments that require multi-responsive characteristics.

Jiang et al. [81] reported on a dual-responsive rough surface coated with polypeptide that displayed the switching between superhydrophilic and superhydrophobic states. The surface originated from the unfolding/aggregation of the poly-L-lysine (PLL) in response to pH and temperature, and also the micro-/nanocomposite structure. At pH lower than the pKa of PLL (∼11.0), the rough surface was in a superhydrophilic state due to the PLL random coil conformation. At pH greater than the pKa, the surface became hydrophilic, arising from random to R-helix conformation. Further increase in the temperature will induce the PLL chains to adopt the aggregated β-sheet structures leading to the superhydrophobic state. By decreasing the pH and temperature simultaneously, the surface could be transformed from the superhydrophobic to superhydrophilic states.

Zhou et al.[58] reported multi-responsive coating, where PNIPAM and poly(dimethylamino)ethyl methacrylate (PDMAEMA) were co-grafted from initiator-modified anodized alumina substrates with irregular micro-/nanoscale surface structures. The as-prepared copolymer coatings exhibited highly unusual superhydrophobicity. The changes in the temperature, pH, and electrolytes could reversibly switch the surface between a low and high adhesive state for spherical water/acid/alkali/salt droplets.

2.6 Multiscale Manipulation of Droplets on Wettable Surface

Water management mechanism and design theory

From the fundamental process of water harvesting, one can see that the key design considerations to improve the performance are (i) promoting water capture, (ii) facilitating coalescence and growth of water droplets, and (iii) accelerating water transport. We will introduce these key steps following the sequence of water management using a combination of surface chemistry at a molecular scale and surface topography in micro-nano scale. From the aspects of molecular scale, the higher water affinity (e.g., hydrophilic/superhydrophilic, high surface adhesion, large water contact angle hysteresis) regions contributes to water capture due to the low surface energy barrier required for water deposition or nucleation. For example, water vapor crosses an energy barrier to form micro-droplets on the surface below the dewpoint in dew harvesting/condensation process, typically promoted by a hydrophilic surface. The nucleation process is controlled by the wetting behavior of the surface. Besides, the growth of the droplets leads to coalescence to larger droplets that slide on a vertical surface resulting from the lower water affinity of the surface (e.g., hydrophobic/ superhydrophobic, low surface adhesion, small water contact angle hysteresis). Since the micro-nano scale structure on a surface, conical or triangular geometry and longitudinal grooves are common characteristics of the surface design, the droplets' transport are usually driven by the Laplace pressure difference, surface energy gradient and capillary force .

Water Capture

Surface free energy: This has been recognized for many years in wetted surfaces by the well-known Young equation, where the wetting is favored by low interfacial free energy, high solid surface free energy and low liquid surface free energy. The surface free energy is an important factor in the determination of wettability for a liquid as it plays a critical role in capturing water from the air onto a surface. Fowkes et al.[28] suggested that the total free energy (γ_s) at the surface consisted of various inter-molecular attractive forces at the interface that are divided into both polar and dispersive components, which could be treated independently. The surface free energy of the three surfaces was estimated based on the contact angle data and fitted according to the Owens, Wendt, Rabel and Kaelble (OWRK) method as shown in Eq. (2.4).

$$1 + cos\,\theta = 2\sqrt{\gamma_s^d}\left(\frac{\sqrt{\gamma_l^d}}{\gamma_{lv}}\right) + 2\sqrt{\gamma_s^p}\left(\frac{\sqrt{\gamma_l^p}}{\gamma_{lv}}\right) \qquad (2.4)$$

where θ refers to the contact angle of liquids, γ_{lv} is the free energies of the liquid and solid against their saturated vapor, γ_l^d and γ_l^p corresponds to the free energy of the liquid, where the superscripts p and d are the polar and dispersion force components respectively. and γ_{lv}, γ_l^d *and* γ_l^p have been reported in many references for different liquids.[29] It is evident that high energy, and highly wetting surfaces are generally easier to attach water droplets compared to low energy surfaces. The nucleation process is also strongly controlled by the wetting behavior of the surface. When water nucleates on the surface, the free energy barrier ΔG is related to contact angle θ determined by the surface wettability based on Volmer's classical nucleation theory (Eq. (2.5)),

$$\Delta G = \frac{\pi\sigma_{lv}r^2(2-3cos\theta+cos^3\theta)}{3} \qquad (2.5)$$

where σ_{lv} is the liquid-vapor surface energy and r is the critical radius of the water droplet. According to Kelvin's classical equation, the critical radius is given by $\ln(p/p_\infty) = 2\sigma_{lv}/n_l kTr$, where p is the vapor pressure over a curved interface of radius r, p_∞ is the equilibrium vapor pressure above a flat surface of the condensed phase at temperature T, n_l is the number of molecules per unit volume of the liquid, and k is the Boltzmann constant (Eq.(2.6)).

$$J = J_0 \exp\left(-\frac{\Delta G}{kT}\right) = J_0 \exp\left(\frac{\pi\sigma_{lv}r^2(2-3cos\theta+cos^3\theta)}{3kT}\right) \quad (2.6)$$

The nucleation rate J can be computed by the inverse exponential of ΔG divided by kT, where J_0 is a kinetic constant. Therefore, the contact angle θ, which correlates to surface wettability, significantly controls both ΔG and water nucleation rate.

Water Transport

The nucleation or deposition of water on the substrate surface will result in the subsequent coalescence and growth of water the droplets. Various surface geometry and structural engineering and wettability manipulation have been investigated on different materials to achieve efficient droplet transport in water harvesting system.

*Surface energy gradient***:** Droplet transport on a solid surface is generally subjected to an external force. A wettability gradient force (F_{chem}) will be generated when the roughness gradient exists on the surface along the direction of motion from A to B (Eq.(2.7)),

$$F_{chem} \sim \int_A^B \gamma(cos\theta_m - cos\theta_l)dl \quad (2.7)$$

where γ is the surface tension, θ_l and θ_m are the contact angles of the less and more hydrophobic side of a droplet respectively. From Eq. (2.7), it can be deduced that when a droplet is placed on wettability gradient surface, the droplet will move from the less wettable region to the more wettable region under the action of wettability gradient force.

Laplace pressure: On a geometric gradient surface, the Laplace pressure difference is the main driving force for droplet transport. A Laplace pressure (ΔP) will be generated by a curved liquid surface pointing towards the curvature center, which can be calculated by Eq. (2.8),

$$\Delta P = \frac{2\gamma}{R} \quad (2.8)$$

where R is the radius of curvature of the circle. From Eq. (2.8), it can be inferred that a smaller radius of curvature will generate a larger force. The Laplace force acting on a conical object drives the droplet from regions of smaller radius to a larger radius provided the Laplace force is greater than the adhesion force. During this droplet transport, new droplets may be deposited along the path and coalesce to form a large volume that increase the transport velocity. In most cases, the transport of a droplet is subjected to the contact angle hysteresis resistance due to the surface inhomogeneity. This force is generated from the difference between the advancing contact angle (θ_a) and the receding contact angle (θ_r) of the droplet as described by Eq. (2.9),

$$F_{res} \sim \pi r_0 \gamma(cos\theta_r - cos\theta_a) \quad (2.9)$$

where r_0 is the contact radius. As a matter of fact, smaller hysteresis resistance contributes to the directional transport of the droplet. Recent studies reported the dynamic transport of water droplets

on slippery surfaces promoted the rapid coalescence and removal necessary for efficient water harvesting, as reported by Wong et al.[30]

When the droplet is released at the minor side of a wedge shape, the droplet is pressed by the margins of the trapezoid resulting in a minor rear curvature radius (R_1) and a large front curvature radius (R_2). According to Eq. (2.10), the Laplace Pressure difference (ΔP_t) produced by the two opposite sides can be described by Eq. (2.10),

$$\Delta P_t \sim \gamma\left(\frac{1}{R_1} - \frac{1}{R_2}\right) \quad (2.10)$$

Driven by the ΔP_t, the droplet on the trapezoid platform can achieve spontaneous and directional transport from the minor radius side (R_1) to the large radius side (R_2). The wedge-shaped surface provides a width gradient along the longitudinal direction, while the cone structure provides a radius gradient by varying the length. Due to the asymmetry of the conical geometry, there is also a Laplace pressure difference on two opposite sides of the droplet, which is described by Eq. (2.11),

$$\Delta P_c \sim -\int_{R_S}^{R_L} \frac{2\gamma}{(R+R_0)^2} sin\alpha dz \quad (2.11)$$

where R is the local radius, R_0 is the drop radius, α is the half-apex angle of the cone, and dz is the integrating variable along the diameter of the cone. The Laplace pressure on the high curvature site (small radius R_S) is larger than that on the low curvature site (large radius R_L). This difference in the Laplace pressure can drive droplets to move from the small radius to the large radius along the cone.

2.7 Potential Applications of Sustainable Superhydrophobic Surfaces

2.7.1 Water Harvesting Applications

Freshwater is essential to sustain all aspects of human activity, however, the scarcity of freshwater is a growing concern, more so when the weather is becoming more unpredictable. Additionally, the uneven distribution of freshwater resources is problematic, leading to the decline of health and quality of life, triggering severe infectious diseases and conflicts. To this end, various water collection and purification technologies have been developed to address the challenges associated with the anticipated water scarcity.[31] In coastal and developed regions, desalination has been widely adopted since it is one of the most efficient technologies to provide reliable and high-quality water.[32] On the other hand, in rural and arid regions with unfavorable climatic/geographic conditions coupled with high investment cost in transportation and energy, an alternative strategy is warranted.[33] Thus, the development of all-weather, portable and adaptable water harvesting devices to alleviate the freshwater scarcity in water-stressed countries is critically needed.

One emerging technology that holds promise is atmospheric water generation that can be adapted to geographical and climatic regions with abundant and clean atmospheric water. Depending on the relative humidity in these regions, freshwater can be harvested from atmospheric water via three processes, i.e. fog harvesting, dew harvesting/condensation, and moisture harvesting.[34] Specifically, fog harvesting, an inexpensive and low-maintenance technology, is particularly suitable in mountainous and foggy areas with higher annual relative humidity (>80%).[35] Dew harvesting could be implemented in areas where its efficiency is associated with the dew point and

ambient temperature.[36] Moisture harvesting represents a portable and scalable process to extract atmospheric water from an arid climate (~40%), powered by abundant and freely available solar energy. [37] For water-rich regions like coastal cities, solar evaporation is a promising technology to generate freshwater due to its low environmental impact.[38] Thus, there is a compelling motivation to develop sustainable and environmentally friendly water harvesting technologies that can be decentralized to provide clean and fresh water to communities with limited access to traditional water sources. These technologies should satisfy the criteria of low-cost, energy-efficient, potable, off-grid and minimal environmental footprints. (**Figure 2.8**)

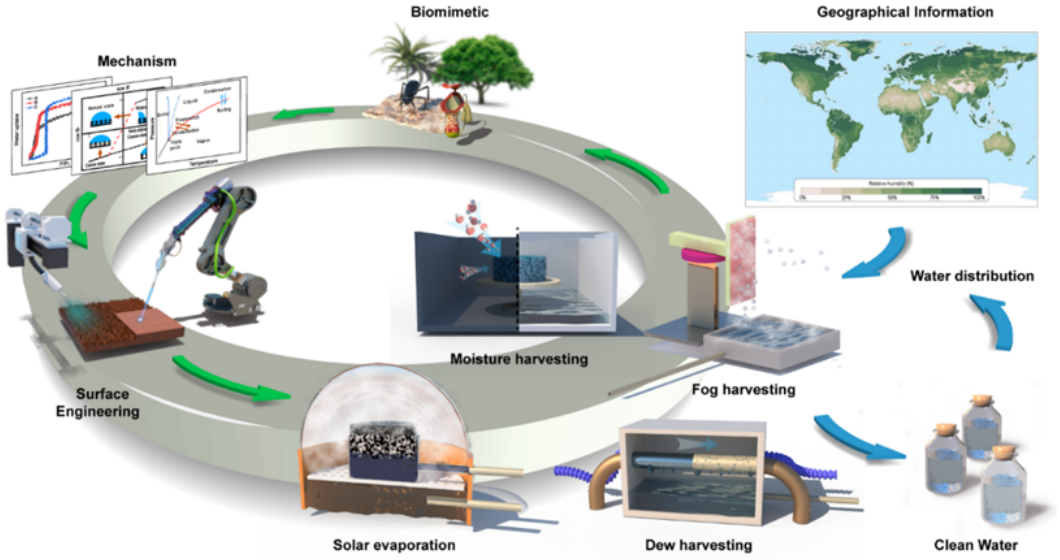

Figure 2.8 Nature-Inspired Water Harvesting Technologies: Innovative Approaches for Sustainable and Decentralized Water Management. Schematic showing the biomimetic surface engineering for various water harvesting devices for clean water production, depending on the relative humidity and geographical information in different regions better reflect the content to be discussed in this thesis. Inspiration from nature creatures, their unique water manipulation strategies offer insights into these surface design and efficient water management process. With the advancements in biomimetic surface engineering, innovative and sustainable approaches to decentralize water management have been developed to utilize atmospheric water (i.e. fog harvesting, dew harvesting, moisture harvesting) and seawater (i.e. solar evaporation). These sustainable and environmentally friendly water harvesting systems can provide clean and fresh water to communities with limited access to traditional water sources, thereby addressing water scarcity and safety concerns for these communities.

In particular, the discipline of bioinspired surface engineering has attracted increasing attention in water harvesting systems.[39] Nature is an important source of inspiration as many living systems are proficient in utilizing water resources to survive. Drawing from the physical principles embedded on the surfaces, researchers designed and integrated water harvesting technologies with

favorable water manipulation capabilities to achieve the precise water management at multiple scales.[40]

In this section, we explore key components of freshwater generation systems being developed for a broad range of applications. We will focus on understanding the mechanisms of manipulating droplet, vapor, or liquid water at interface and utilizing these principles to achieve controllable water management in four water harvesting systems.

Water Management Theories

The different sustainable water harvesting techniques are associated with interfacial phenomenon. We will introduce the water management theories generated at the interface, and the interaction behavior between the surface and various water states.

Fog and dew harvesting: Fog harvesting and dew harvesting with dropwise collected modes enable the rapid on-site water production involving similar fundamental processes: nucleation (**Figure 2.9a**), growth and coalescence (**Figure 2.9d**), and droplet removal (**Figure 2.9f**). Therefore, they are mainly governed by surface wetting mechanism, where there are minor differences between fog and dew harvesting in nucleation.[35a] In fog collection, the tiny droplets land on the target surfaces, and to prevent re-entraining into the air, the surface requires higher water affinity. (**Figure 2.9b**) For a smooth and defect-free surface, this water affinity can be described by the intrinsic contact angle (θ_i) via the Young's equation. Typically, the higher water affinity will lower the contact angle, and by modifying the surface structure, the wettability of the surface can be tuned to capture the droplet in its quasi-static state on the surfaces (Wenzel, Cassie, Wenzel-Cassie-transition and liquid-infused slippery wetting state, omniphobic liquid-like surface).[41] (**Figure 2.9e**) Dew harvesting relies on the condensed nucleus formed on a sufficiently cooled surface below a critical temperature. As such, a phase-change process (condensation) will initially occur and a new solid-liquid interface is generated by the working fluid, producing a free energy barrier that must be overcome.[42] During condensation, the critical droplet size is only a few nanometers at atmospheric pressure based on the classical nucleation theory, where the energy barrier and heat transfer are independent of surface roughness and dependent on the intrinsic surface properties (i.e. heat transfer coefficient, intrinsic contact angle) (**Figure 2.9c**).[42] Once the droplets are nucleated on a supercooled surface, the heat transfer is controlled by wettability, conduction from the droplet morphology and wetted area on the surface. If a rough surface favors Wenzel wetting state, an initial nucleus will continuously grow into a Wenzel droplet that aids in the heat transfer process. Instead, Cassie droplets exhibit lower heat transfer as they insulate the surface and are more conducive to droplet transport and nucleus generation. Therefore, the surface wettability, which correlates to contact angle and wetting state controls both the free energy barrier, water nucleation rate and heat transfer.[43]

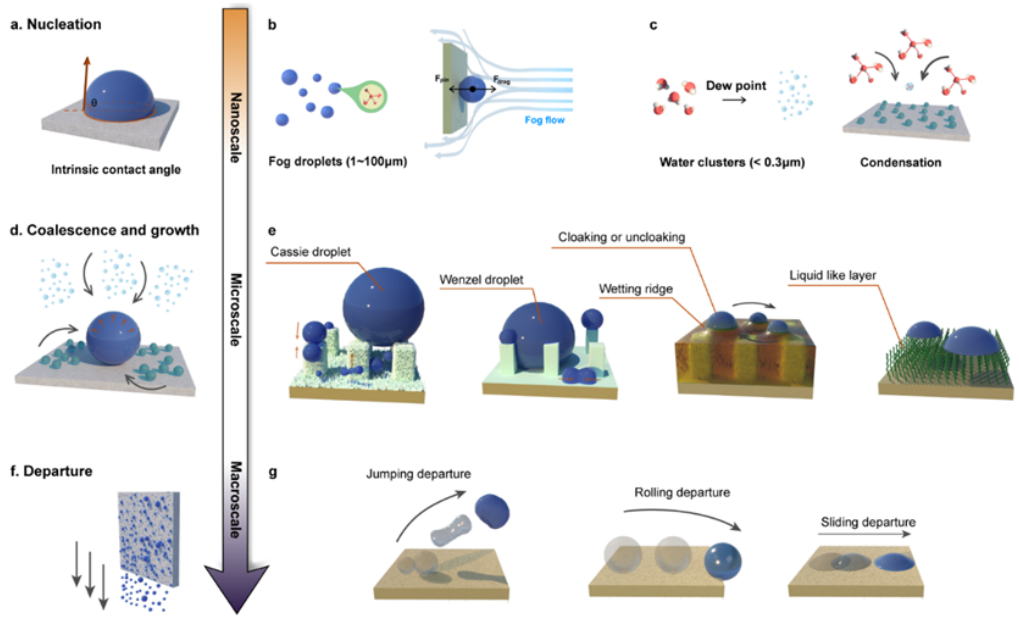

Figure 2.9 Water management mechanisms for fog and dew harvesting: a. Droplet nucleation occurs on the surfaces determined by intrinsic contact angle (θ) of the surface (nanoscale), Illustration of the state of water: b. The existence of water in fog harvesting as tiny droplets with a diameter of 1-100 μm, c. The existence of vapor in dew harvesting or condensation while the dew nucleus generated as a water cluster (<0.3 μm), d. Droplet growth and coalescence (microscale), e. Water droplet behaviors during the coalescence stage: droplet bouncing, coalescence and suspending on textured surface with Cassie assisted mode, droplet merge and coalescence on textured surface with Wenzel assisted mode, droplet slide and growth on lubricant-infused slippery surfaces, droplet slide and suspend on slippery omniphobic covalently attached surface, f. droplet detachment from the surface (macroscale), g. droplet transport modes including jumping, rolling, and sliding depending the initial nucleated phase and surface free energy.

The nucleation or deposition of water on the substrate surface will result in the subsequent droplet growth and coalescence. In most cases, droplet movement that occurs spontaneously can be induced by various factors, such as inhomogeneity in surface composition on superhydrophobic surfaces,[13] asymmetric surface topographies on conical or wedge-shaped surfaces,[44] liquid meniscus on lubricant-infused surfaces,[45] and surface energy gradient on slippery omniphobic covalently attached liquid (SOCAL) surfaces.[46] (**Figure 2.9e**) During droplet transport, they may collect and merge with other droplets along the way, forming larger droplets that increase the speed of transport. Ultimately, droplets will detach from surfaces through gravity-induced sliding or jumping, which depends on the surface wettability. Lowering contact angle hysteresis can facilitate droplet detachment at smaller sizes, leading to a more effective dropwise condensation process.

Moisture harvesting: For the sorbent-based moisture harvester, the first step is spontaneously extracting and concentrating the water molecule from air. (**Figure 2.10a**) Then the accumulated

vapor in the harvesters can be released and condensed by utilizing an additional active or passive condenser, depending on the types of energy input.[47] Thus, the moisture harvesting on the target surface depends primary on the sorption-desorption mechanism.(**Figure 2.10b**) Vapor enrichment can be achieved by either absorption or adsorption, and the main driving forces in absorption are the osmotic effect-based physical absorption and chemical potential gradient-driven absorption.[48] Thermodynamically, the moisture uptake process for absorption proceed into the matrix, such as hygroscopic salts or polymeric gels. For adsorption, the solid surface possesses surface free energy due to the inbalanced residual adhesion force for water molecules that promotes the moisture enrichment process. (**Figure 2.10c**) At the vapor-solid or vapor-liquid interfaces, the adsorption can be divided into two categories, intermolecular induced physical adsorption (i.e. van der Waals forces) and chemical bonding and adsorption (i.e. hydrogen bonding, coordination effect and electrostatic forces).[37b] With increasing surface area (higher quantity of monolayer vapor molecule on the surface in physisorption) of adsorber and enhanced vapor-surface interaction (stronger water affinity in chemisorption), moisture capture capability is enhanced. Conversely, when the vapor molecule gains sufficient energy to overcome the activation-free energy barrier due to a temperature or pressure swings, desorption occurs.

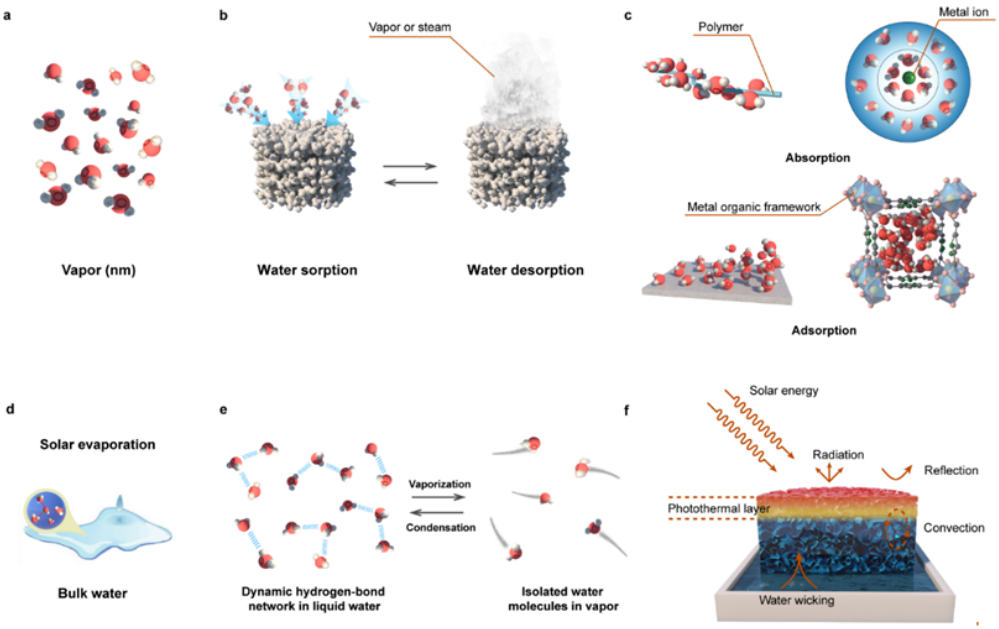

Figure 2.10 Water management mechanism and design theory for moisture harvesting and solar technologies, **a.** The existence of vapor in moisture harvesting, **b.** Illustration of the water management mechanism: sorption-desorption process, **c.** vapor concentration theories at interfaces: hydration shell around metal ions, water molecule absorption around polymer chain, physical and chemical adsorption at the interface, water molecule filled the pore of metal organic framework, **d.** Illustration of the state of water: solar evaporator is conducted to wick liquid water and tune the water into vapor (evaporation), **e.** Illustrations of changes in the hydrogen-bond network during evaporation. The multiple hydrogen bonds break to produce isolated water molecules in gaseous

water after absorbing the latent heat, **f.** Illustration of the solar interfacial evaporators including the light absorber, substrate, and bulk water, as the detailed energy conversion and management including solar radiation, reflection evaporation, radiation, conduction, convection.

Solar evaporation: Solar evaporation technology can directly harvest solar energy, wicking water and generate collectible fresh vapor via evaporation from various resources, like brine and contaminated wastewater. Efficient thermal management is crucial in improving the overall performance of evaporation systems, which can be achieved by minimizing thermal loss caused by conduction, convection, and radiation.(**Figure 2.10d**) Recently, the interfacial solar evaporation system has attracted increasing attentions as it is capable to heat the evaporative portion of water rather than the entire body, localizing the heat at the liquid surface.[49] Typically, a floating liquid-transport structure spontaneously wicks and supplies liquid water to the evaporation layer and achieves a continuous operation with the receding air-liquid interface. (**Figure 2.10f**) Surface wettability plays a vital role in the floating system, especially in liquid water transport and structural stability. On the one hand, hydrophobicity helps to float the structure, minimize unnecessary energy loss and improve the durability by reducing contamination. On the other hand, the capability of water transport to the evaporation structure depends on surface hydrophilicity. In other words, a lower apparent contact angle can increase the water transport via the capillary-wicking effect. However, excess hydrophilicity leads to a water supply surplus at the evaporation surface, resulting in heat loss and salt formation. Thus, researchers have focused on optimizing the surface structure, morphology and materials to achieve the balance between water wicking and supply.[50] In an open ambient environment, water evaporation occurs simultaneously since the partial pressure of water in air is lower than the saturated vapor pressure. (**Figure 2.10e**) This process can be accelerated via the effective control of surface property. For instance, the tunning of surface topography minimizes heat loss and enhances the utilization of latent heat, boosting the heat concentration and recovery, and increasing the evaporation area.

Advanced Development of Water Harvesters

We will discuss water management strategies for water harvesting performance and outline recent progress in material and structural engineering approaches in guiding the design of sustainable water harvesters.

Progress in Fog and Dew Harvesting

Systematic Strategies: Many attractive strategies have been developed to enable controllable water management on demand from bioinspired surface designs. For example, beetle-inspired biphilic surfaces could be considered as critical features to enhance nucleation, evolving single physical interception applied by conventional fog/dew harvester into synergistic physical and chemical capture.[51] The harvester simulated from periodic-spindled fibers of spiderwebs, have been incorporated in the design yielding continuous condensation and efficient droplet coalescence.[52] Noticeably, the droplet coalescence process influences the transport rate and surface flooding, that

can be further enhanced by adjusting the density and spacing of nucleation domains, surface wettability gradient/potential.[53] Studies on the cactus structure-function relationship in water collection systems provide an effective strategy to enhance directional droplet removal and rapid surface renewal.[54] Likewise, pinning-free transport is also a key factor determining the durability of water collectors. Inspired by the multicurvature structures on pitcher plants, slippery surfaces with superior droplet mobility were developed to enhance the removal rate.[55] One pioneering strategy involves creating a hydrophilic directional slippery rough surface, which can facilitate rapid droplet removal and significantly reduce droplet pinning.[56] (**Figure 2.11a**) It's worth to mention that the trade-off between water nucleation and transport efficiency arouse particular requirements for designing the harvesting surfaces. For instance, the dual- or triple-integrated bioinspired water harvesting surfaces were fabricated to separately manipulate the water-surface interaction behaviors using the function-decoupling mechanism.[57] (**Figure 2.11b**) Another advanced approach is replenishing hydrophilic nanodomains on superhydrophobic surfaces by one-step colloidal assembly to reinforce the nucleation without sacrifice transport efficiency.[58]

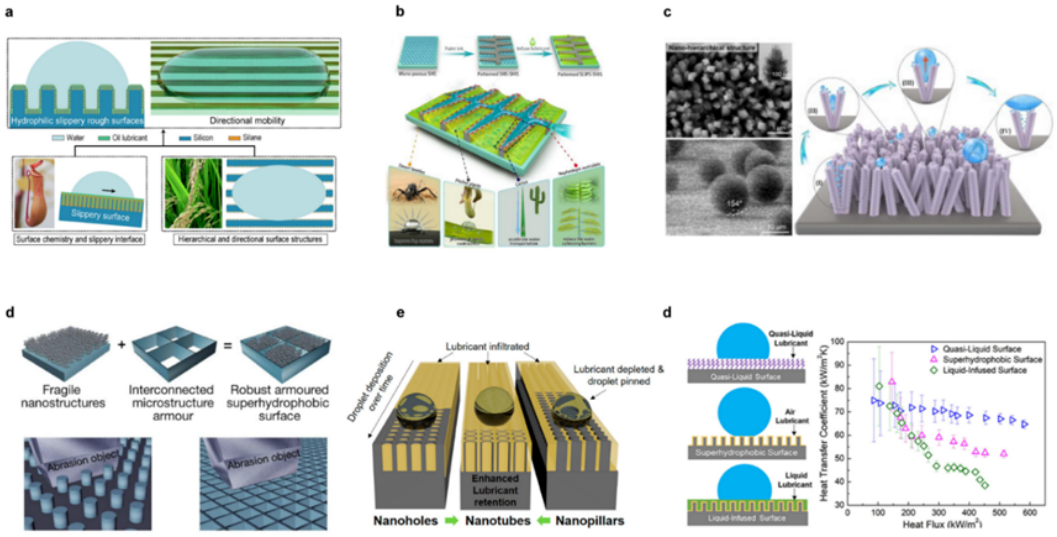

Figure 2.11 Strategies for the design of fog and dew harvesting surfaces: a. Schematic showing directional droplet mobility on a hydrophilic rough-slippery surface. Reproduced with permission from ref.[56], Copyright 2018, AAAS publications, b. Illustration of a quadruple-biomimetic surface for fog harvesting. Reproduced with permission from ref.[57a], Copyright 2021, Elsevier, c. Branched Nanorod Surface for inhibiting condensation-induced droplet wetting. Reproduced with permission from ref.[59], Copyright 2023, Elsevier, d. Schematic showing the strategy for designing superhydrophobic surface within a protective microstructure 'armour'. Reproduced with permission from ref.[60], Copyright 2020, Springer Nature, e. Schematic showing lubricant retention in nanotubes in comparison to nanopillars and nanoholes. Reproduced with permission from ref.[61], Copyright 2021, American Chemical Society, f. Schematic showing the heat transfer coefficient at varying heat flux on quasi-liquid surfaces, superhydrophobic surface and liquid-infused surface. Reproduced with permission from ref.[62], Copyright 2022, American Chemical Society

The surface modified through biomimetic engineering has greatly optimized the manipulability of water droplets. However, one current challenge is the retention of liquid repellency over extended periods, particularly in humid conditions where surfaces are susceptible to degradation or contamination after prolonged use. To ensure efficient and continuous water harvesting, it is important to maintain durable and robust surfaces that can withstand the demands of sustainable water management practices. Dropwise collection on superhydrophobic surfaces derived the design from cicada wing have emerged as effective modes owing to the rapid droplet onset departure, compared to conventional filmwise collection.[59, 63] (**Figure 2.11c**) However, the irreversible destruction of micro/nano structures remains a major concern as it can cause flooding for many superhydrophobic surfaces. Recent progress has showcased practical approaches to enhance the long-term durability of superhydrophobic surfaces, such as the integration of "armour" microstructure,[60](Figure 5d) self-healing surface, or elastic skin layer[64]. Lubricant-infused surfaces, another viable water harvesting surfaces, also encounter similar issues that is lubricant depletion or degradation in condensation process.[65] Strategies such as appropriate lubricant selection, self-replenishing structural design, and the incorporation of intermediate linkage layers have been proposed to minimize these issues.[61, 66](**Figure 2.11e**) Moreover, a promising alternative in the form of slippery omniphobic covalently attached liquid surface (SOCAL) was introduced, which displayed sustained, long-term and efficient dropwise condensation that minimized the air/lubricant loss issues.[41c] These SOCAL surfaces possessed ultra-low surface energy via covalent-bonded flexible polymer brushes or alkyl monolayers capable of preventing “condensation-induced blistering” ensuring interface stability.[67] As the dynamic chain nature of grafted flexible polymers imparts solid surfaces liquid-like properties, the surface with ultralow contact angle hysteresis could achieve the pinning-free and rapid droplet removal.[68] Combined with their ultrathin homogenous coatings, these surfaces display heat transfer enhancement in condensation with good performance in steam condensation (**Figure 2.11f**).[62] Future research efforts should therefore focus on the engineered lubricant-infused surfaces with improved long-term stability, and self-sustaining or self-healing properties.

As large-scale fog/dew harvesting devices are intended to operate in outdoor environments, it is crucial to address the damage caused by sunlight irradiation, wind, dust, and bacteria attacks. Therefore, the design of the next generation of water harvesting surfaces should incorporate multifunctional features, such as improved chemical and mechanical durability, self-healing capability, and resistance to UV radiation and bacteria. Besdies, a well-designed water collection system can maximize the water harvesting performance of the surface, reducing energy consumption, increasing long-term cycling capacity and improving the quality of the collected water. For example, the newly devloped bio-inspired hydrogel membrane for interfacial solar steam generation and fog collection bi-functional working modes represents an efficient prototype to

achieve all-day water harvester.[69] (**Figure 2.12a**) Recent progress in passive dew harvesting assisted by radiative cooling that worked continuously via radiative dissipation to reduce the temperature of the surface, showed remarkable cooling enhancement for water collection without additional energy input.[70] (**Figure 2.12b**) Several attempts have been made to enhance the energy efficiency by incorporating metal additive manufacturing [71](**Figure 2.12c**), waste heat recovery, and multistage heat exchangers in harvesting devices. These techniques have the potential to greatly improve both the economic and environmental benefits of the upcoming generations of sustainable harvesters.

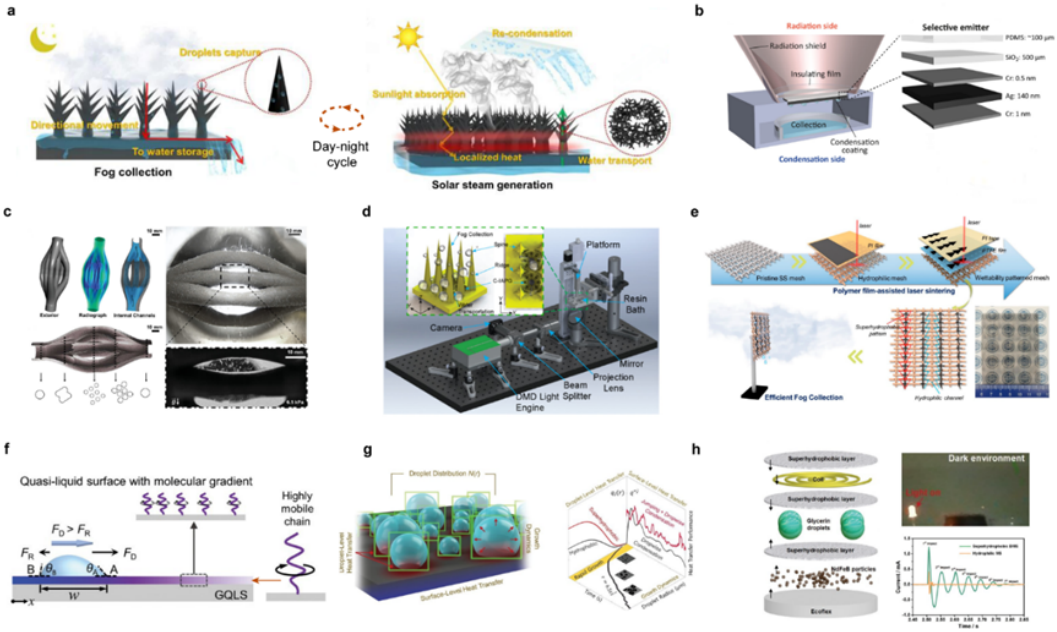

Figure 2.12 Design Strategies for Long-term Cycling Fog and Dew Harvesting Systems: Energy Management and Materials Optimization: **a.** Schematic illustration of the microstructured hydrogel membrane for all-day fresh water harvesting, including fog harvesting during nighttime and solar water generation during daytime, Reproduced with permission from ref.[69], Springer Nature, **b.** Working principle with separated radiation and condensation, Reproduced with permission from ref.[70], Copyright 2021, AAAS publications, **c.** Illustration of jumping droplet condensation on a metal additive manufacturing condenser. Reproduced with permission from ref.[71], Copyright 2022, Wiley-VCH, **d.** Schematic showing 3D-printed fog collector. Reproduced with permission from ref.[72], Copyright 2021, American Chemical Society, **e.** Schematic showing the preparation of wettability-patterned mesh via polymer film-assisted laser sintering. Reproduced with permission from ref.[73], Copyright 2022, American Chemical Society. **f.** Schematic showing droplet motion on the quasi-liquid surface. Reproduced with permission from ref.[74], Copyright 2021, Wiley-VCH. **g.** Schematic showing deep learning of the thermofluidic process of condensation. Reproduced with permission from ref.[75], Copyright 2021, Wiley-VCH, **h.** Schematic illustration of simultaneous electricity generation and water collection from flowing fog. Reproduced with permission from

ref.[76], Copyright 2020, Wiley-VCH.

Material Selection and Structural Design

The production and processing of surfaces for sustainable water harvesting systems should be cost-effective and environmentally friendly. To meet these requirements, the fabrication of superhydrophobic surfaces should minimize the use of hazardous materials and solvents, reduce waste, conserve resources and energy. One way to create these surfaces is by replicating biomimetic structures such as cactus spine-like conical structures and Nepenthes-like grooved structures using 3D printing technology or replica molding.[72] (**Figure 2.12d**) Alternatively, fibers with spindle-knot structure can be synthesized via microfluidic techniques to achieve periodical wettability.[44] Polydimethylsiloxane (PDMS), chitosan, and sodium alginate are commonly utilized in these technologies to determine the wettability characteristics and mechanical strength of the fabricated structures. Moreover, to achieve highly delicate and intricate structure geometries, advanced fabrication techniques such as photolithography and plasma etching are regarded as highly versatile methods. Compared to conventional etching techniques, these methods offer faster etching rates and enable more precise fabrication, thus reducing waste and promoting the efficient use of resources during surface construction.

Due to the requirement of heat transfer for dew condenser, metallic surfaces like copper, aluminum, and steel, are ideal for condenser designs. Recently, surface texturing techniques such as laser ablation and laser direct writing have gained popularity for creating textured surfaces on metal.[73] (**Figure 2.12e**) These methods enable the construction of specific surface patterns with ultrafast and precise processing, without the need for solvents. In addition, efforts are being made to fabricate thin coatings (<100 nm) that are durable and highly thermally conductive to enhance condensation heat transfer. Inorganic materials such as metals, alloys, ceramics, and oxides are preferred substrates in condenser fabrication due to their higher mechanical strength, temperature stability, adhesion, and thermal conductivity compared to organics or organometallics. Recently, chemical vapor deposition (CVD) has gained popularity in the fabrication of condenser surfaces due to its ability to create ultrathin conformal polymer coatings while minimizing waste and emissions.

Additionally, superhydrophobic coatings can be produced through simple and cost-effective methods such as colloidal assembly, deposition, spray-coating, and spin-coating, utilizing patterned structures. Hydrophilic building blocks such as silicon dioxide (SiO_2), silicon carbide, and cellulose nanomaterials can be used, while non-toxic materials such as fatty acids, biopolymers, or long-chain alkanes can be used to conduct the hydrophobic functionalizing instead of long chain fluorine-based materials.

Functional designs of slippery liquid-infused surfaces on various textured substrates have been reported to enable the surface longevity. Infusion of lubricant is an integral part of the manufacturing process of slippery coatings, which could be accomplished by dip-coating, gravimetric draining, and solvent exchange methods. Concerning SOCAL surfaces, the quasi-liquid layers can be

prepared by grafting flexible polymers with an ultralow glass transition temperature, like PDMS, alkyl monolayer, and polyethylene glycol (PEG).[77]A recent strategy of introducing siloxane-silane coating on surfaces via initiated chemical vapor deposition through the grafting of PDMS[77b], or sol-gel SiO_2[78] yielded reproducible coating thickness even on metallic surfaces. By tethering flexible polymer grafting density, a durable quasi-liquid gradient surface were developed that enable the spontaneous droplet transport.[74] (**Figure 2.12f**) In future research, theoretical modelling tools could be incorporated to accelerate the discovery of new flexible and biodegradable materials and predict the relationship between surface wettability properties and chain flexibility.[75] (**Figure 2.12g)** Furthermore, the droplet collection process integrated with functional energy conversion systems can be applied to harvest energy as well.[76, 79] (**Figure 2.12h**)

Progress in Moisture Harvesting

Systematic Strategies The working performance of moisture harvester is strongly dependent on the sorption-desorption processes, as well as freshwater productivity. In principle, this sorbent-assisted harvester requires a high-water sorption capacity under low humidity conditions. Although conventional hygroscopic salts feature water uptake properties, they could not be used alone in water harvesting due to particle agglomeration. Thus, various techniques have been devised to improve the water molecule uptake capacity of newer sorbents.[80]

Several biomimicry studies reported similarity of creatures on dry land on the auto vapor sorption and release using the porous structured skin or leaf and a self-actuated system. Inspired by their hygroscopic vapor diffusion system, the novel sorbents endowed with porous structure were developed to enhance the water molecule sorption-desorption cycling capacity, such as hygroscopic salt-imbedded membrane or polymeric gels.[81] (**Figure 2.13a**) However, vapor desorption of hygroscopic salt-based sorbents is still challenging because of the extensive energy input required for regeneration.

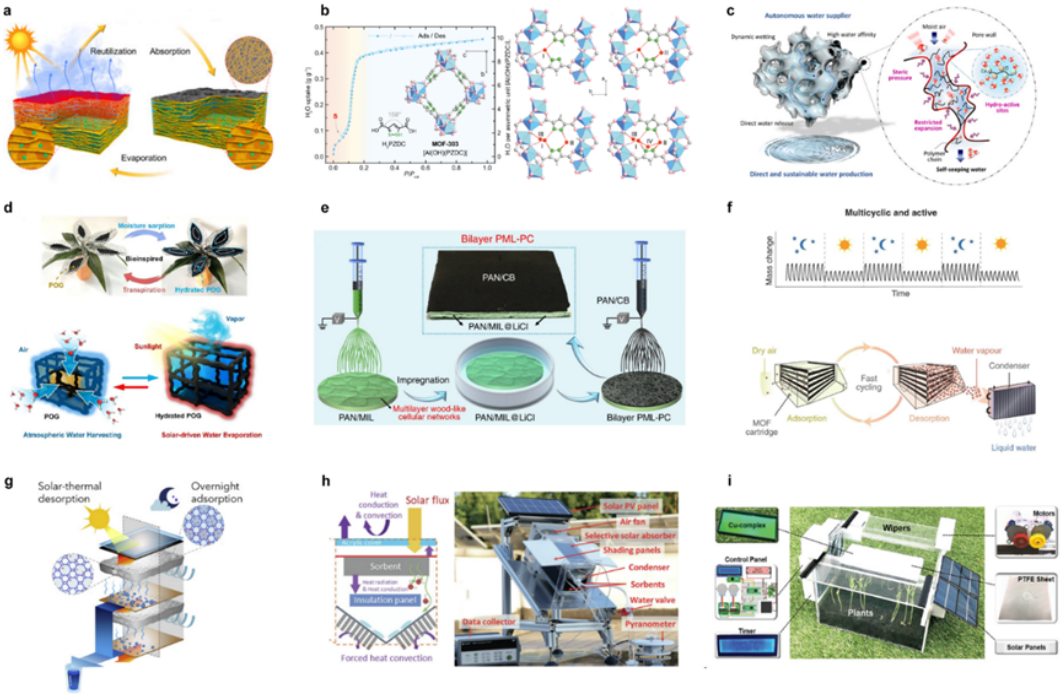

Figure 2.13 Design strategies for moisture harvesting systems: **a.** Illustration of atmospheric water harvesting by a solar-powered nanostructured biopolymer hygroscopic aerogel. Reproduced with permission from ref.[81], Copyright 2021, Elsevier, **b.**Water sorption isotherm and crystal structure of MOF-303. Reproduced with permission from ref.[82], Copyright 2021, AAAS publications, **c.** Illustration of autonomous atmospheric water seeping MOF matrix Reproduced with permission from ref.[83], Copyright 2020, AAAS publications, **d.** Illustration of absorbing water from air by a tillandsia-inspired hygroscopic photothermal organogel. Reproduced with permission from ref.[84], Copyright 2020, Wiley-VCH, **e.** Schematic illustration of the fabrication of biomimetic bilayer via electrospun and salt immersion. Reproduced with permission from ref. [85], Copyright 2020, Springer Nature, **f.** Illustration of the water harvesting cycle. Reproduced with permission from ref.[86], Copyright 2019, American Chemical Society, **g.** Schematics of the Dual-Stage Atmospheric Water Harvesting Device. Reproduced with permission from ref.[87], Copyright 2021, Elsevier. **h.** Schematics of the rapid-cycling continuous water harvester. Reproduced with permission from ref.[88], Copyright 2021, Royal Society of Chemistry, **i.** SmartFarm devices Reproduced with permission from ref.[89], Copyright 2020, Wiley-VCH.

Metal-organic frameworks (MOFs) are promising candidates for achieving an effective vapor sorption-desorption cycle due to their exceptionally high porosity and hygroscopic nature.[90] These materials not only facilitate energy-efficient water release with minimal temperature or pressure changes, but also offer a higher water capacity due to their larger pore volumes. However, as the pore volume increases, the hydrophilicity of the pores decreases, leading to potential structural instability and hindered heat transfer.[34] To optimize the efficiency of passive temperature-actuated water harvesting, it is imperative that future research addresses this inherent limitation. A newly developed aluminum-based MOF-303 [Al(OH)(1H-pyrazole-3,5-dicarboxylate)] has shown

promise in achieving high water productivity through precise modulation of the water molecule adsorption sequence, while allowing for the tunable regeneration temperature and enthalpy.[82](**Figure 2.13b**) Additionally, incorporating metal–organic frameworks (MOFs) with three-dimensional polymeric networks offers a promising solution to achieve sustainable water production, enhancing sorption/desorption kinetics and enabling spontaneous water oozing.[83] (**Figure 2.13c**) Another attractive alternative is the use of a thermal-responsive moisture harvesting device with switchable hydrophilic/hydrophobic surface capable of inducing water sorption/release with a sustainable power source. A flexible strategy based on the Tillandsia-inspired solar-powered moisture harvesting system using hygroscopic photothermal organogel has recently been developed for the synergistic enhancement of moisture sorption and release.[84] (**Figure 2.13d**)

Material Selection and Structural Design Hygroscopic salt-imbedded composites have been fabricated through encapsulation or deposition of hygroscopic salts (for example, LiCl, $MgCl_2$) into fibers or other porous substrates to accelerate water diffusion and sorption.[91] For example, a wood-inspired moisture pump has been reported, where the nanofibrous membrane serves as a good support that is coordinated with the hygroscopic salt via a simple soaking process.[85] (**Figure 2.13e**) MOF materials in moisture harvester can be used as powders or an additive in composites. To optimize MOF materials for use in moisture harvesting, cost-effective synthetic methods were preferred for fabricating MOF powders. Some novel methods like electrochemical synthesis[92], solvent free approach and water-based synthesis[93] are the most likely strategies to succeed in becoming economically and environmentally feasible for future production. Besides, various synthetic methods for supported MOF membrane or composites, such as spin-coating onto films, or cross-linking with polymeric gels, have been developed to further sustain water sorption-desorption cycling process and stability.

Different chemical or physical cross-linking methods were employed to fabricate hydrogel-based moisture sorbents.[80, 94] The fabrication methods such as solvent replacement, in-situ encapsulation, casting methods, the fabricated polymeric hydrogels with hygroscopic salts were proposed to optimize the moisture sorption properties by tailoring the water-polymer interaction.[95] Additionally, the thermo-responsive polymers (e.g. poly(N-isopropylacrylamide), poly(oligoethylene glycol methacrylate)) are commonly used as hydro-active accelerator in enabling water desorption to obtain stimuli-responsive moisture sorbents.[96]

Currently, the most significant challenges in moisture harvesting technology are limitation of vapor sorption-release efficiency, recyclability of sorbents and regeneration of energy consumption. Material design has been primarily focused on improving the maximum one-cycle sorbent capacity, while overlooking the impact of recycling methods and frequency on the feasibility of sorbent-based materials. In future research, the flexible or switchable bonding with water molecules and the hydrolytic stability of the sorbents should be considered in the design. Moreover, for the development of next-generation water harvesting systems, it is important to consider designing a prototype that can operate multiple adsorption-desorption cycles per day to meet the daily water

requirements of humans. A pioneering concept has been proposed to expedite the desorption process in a packed MOF bed through forced convective heating.[86] (**Figure 2.13f**) Nonetheless, it is important to recognize the significance of implementing energy-efficient methods in the upcoming active harvesters to enable sustainable water production. For example, utilizing low-grade energy sources (i.e. solar energy or waste heat) is a good choice to autonomously release water from the sorbent.[87] (**Figure 2.13g**) Other innovative strategies such as radiative cooling condensers, and photovoltaic modules,[88](**Figure 2.13h**) could be introduced in moisture harvesting devices to further improve their performance. Besides, the structural design of a moisture harvester should also take into account its anti-fouling and antibacterial capabilities, as these are crucial factors affecting the quality of the captured water. Once the air pollutants (dust, bacteria, acidic gases, volatile organic compounds) and microorganisms are adsorbed on the surface or the interior, removal of the sorbent is difficult, and this will impact the quality of produced water. By optimizing the integrated device design, a fully automated and self-sustainable solar-powered SmartFarm device has recently been designed to irrigate the plants utilizing harvested water.[89] (**Figure 2.13i**)

Progress in Solar Evaporation

Systematic Strategies Improvement in the thermal efficiency of solar absorbers with the solar-to-thermal efficiency exceeding 90% was achieved by thermal localization in a confined space.[97] Further improvement of the solar evaporator's performance can be achieved by optimizing the water transport, thermal management of evaporation, and and collected apparatus.

An important demand for solar evaporation is anti-gravity water transport from the ground up. Nature-inspired aligned porous structures provide important scientific principles through the rational desgin of water channel, such as vertical water channels, tortuous water channels containing 3D porous, 2D lamella, and 1D columnar structures to facilitate water transport.[98] A newly developed 3D fabric evaporator with vertical aligned yarns produced a multi-scale pore structure that achieved continuous water supply with an ultra-efficient evaporation area.[99] (**Figure 2.14a**) Moreover, the heat demand in the evaporation process, and thermal insulation of the solar evaporator should be maintained to avoid inefficient thermal management. One pioneering design is via the heat localization method by floating the solar absorber at the air/liquid interface, thereby minimizing the heat losses to the bulk liquid. By separating the thermal insulation from the water transport, 1D and 2D water channel constructed using low thermal conductivity materials could mitigate the heat losses efficiently.[100] Despite the efficient water transport and good thermal insulation, interfacial properties, especially its wetability, is an equally important factor to rapidly generate interfacial steam. Some proposed principles are applied to enhance the heat transfer at the interface, i.e. (i) reducing the interfacial thermal resistance via the improvement of wetting characteristics, and (ii) enhancing the heat transfer coefficient through the introduction of surface roughness. By adjusting the geometry of the water pathways, or the ratio of hydrophobic/hydrophilic regions, the efficiency of the system could be optimized with increased water transport rates and reduced vaporization enthalpy.[101] (**Figure 2.14b**)

Even though a water-wicking structure is critical for continuous water supply, it generates an extra transport resistance for salt diffusion such as clogging or crystallization. The salt accumulation occurs on the heating surfaces will result in a reduced light absorption and blocked water flows. Physical removal or backwashing can address the salt blockages, however, it interrupts the continuous production and may damage the surface structures. Some novel strategies such as (i) fluid convection enhancement,[102] (ii) salt backflow (**Figure 2.14c**),[103] and (iii) spatially isolating salt crystallization, [104] (iv) liquid pumping[105] from evaporation, have been implemented in wicking devices to address the salt blockages under continuously operation. However, ensuring the durability and long-term cycling capabilities of the new solar evaporator still requires a proper balance between salt rejection and heat loss.[106] Inspired by superfast water transportation of the Nepenthes peristome surface, a new biomimetic 3D bridge-arch solar evaporator was proposed to induce free-flowing water film with directional Marangoni convection for eliminating salt accumulation.[107](**Figure 2.14d**)

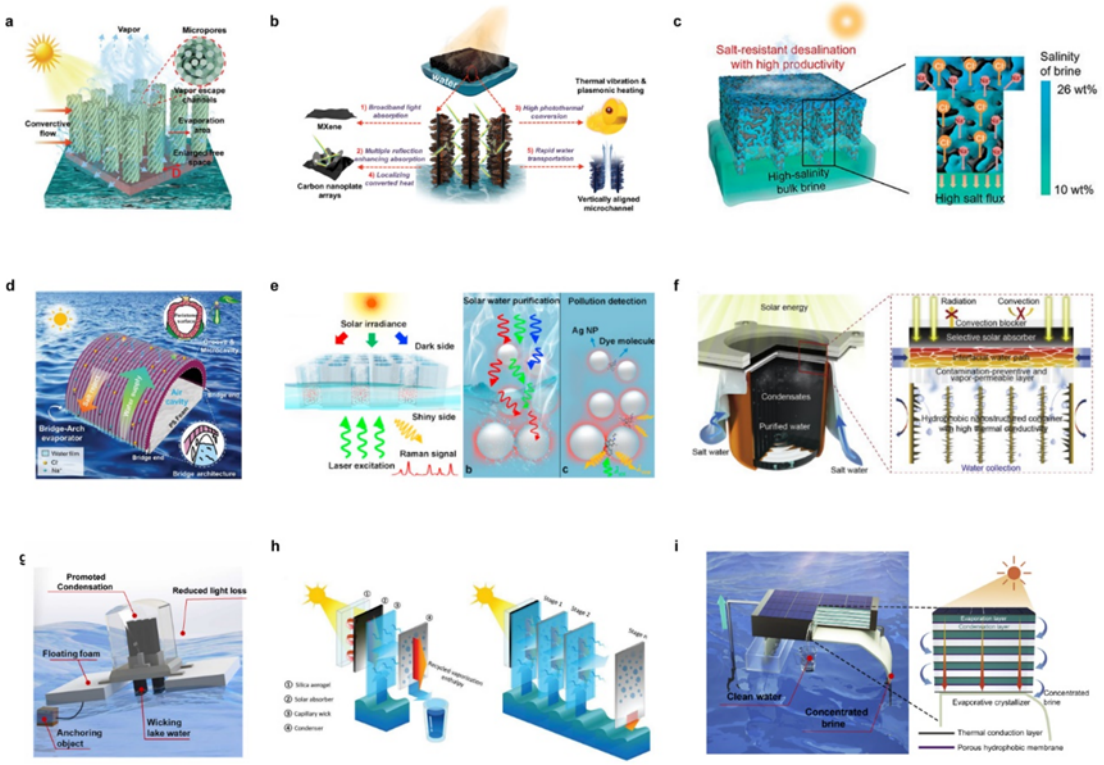

Figure 2.14 Design strategies for solar evaporation systems: **a.** Schematic of all-in-one 3D fabric evaporator with vertical array structure. Reproduced with permission from ref.[99], Copyright 2021, Wiley-VCH, **b.** Schematic of the hierachical design for MXene-Based solar absorber. Reproduced with permission from ref.[101a], Copyright 2020, Wiley-VCH, **c.** Schematics showing solar evaporators with different salt transport fluxes for a photothermal desalination. Reproduced with permission from ref.[108], Copyright 2022, American Chemical Society, **d.** Schematic showing Marangoni-effect-induced salt rejection of biomimetic bridge-arch solar evaporator. Reproduced with permission from ref.[107], Copyright 2021, Wiley-VCH, **e.** Schematic showing the solar purifier with integrated dual-functional asymmetric plasmonic structures for enhanced light absorption and pollution detection. Reproduced with permission from ref.[109], Copyright 2018, Elsevier**, f.** Schematic of the invert-structured solar water purifier. Reproduced with permission from ref.[110], Copyright 2021, Elsevier, **g.** Schematic diagram of water wave vibration-induced solar evaporation. Reproduced with permission from ref.[111], Copyright 2022, Elsevier, **h.** Schematic of the thermally-localized multistage solar still's device architecture. Reproduced with permission from ref.[112], Copyright 2020, Royal Society of Chemistry, **i.** Schematic showing the integrated PV-membrane distillation-evaporative crystallizer device. Reproduced with permission from ref.[113], Copyright 2021, Elsevier.

Material Selection and Structural Design Despite the solar-absorbing materials being explored, the compatible structural design or materials choice of the water transport layer, thermal insulation, and salt rejection is crucial to boost the purified water yield per unit time. In water pathway design, the manufacturing techniques of multi-channeled porous structures have been investigated to tune the structure of water channels, such as freeze casting[114], femtosecond laser processing[115]. Natural

wood can be directly used as base substrates, owing to its hierarchically aligned porous structure and good hydrophilicity.

Furthermore, materials with low thermal conductivity, such as fibrillated cellulose, porous filter paper, or polyurethane sponge, are typically favored as suitable matrices to enhance thermal insulation in the water-wicking section design.[116] Several salt-rejecting structures have been developed based on different operating principles. These structures are designed in unique ways to prevent salt accumulation, such as by drilling millipores or micropores into wood, creating conical structures using 3D printing or molding, or producing Janus polymeric films through electrospinning. In addition to salt fouling, the other contamination factors in the water source could also affect the surface properties, leading to a shorter lifespan and lower yield of clean water. [117] One promising concept is to modify the water channel with plasmonic nanoparticles, carbon-based materials or metallic nanoparticles that facilitate the detection of pollutants as the water is continuously being purified.[109] (**Figure 2.14e**)

The device design of the solar evaporator, including vapor condensation, collection module, seawater supply module, requires further consideration in order to ensure long-term operation of the system.[118] In previous studies of solar vapor generation, the process of vapor condensation and water collection has often been overlooked. Recently, a new concept to avoid heat and optical loss during the evaporation-condensation process was introduced by a new design comprising of an inverted-structure solar water purifier that drives the condensed vapor downwards.[110] (**Figure 2.14f**) Several attempts have also been made to reduce light occlusion in vapor condensation modules, including shaping the condensation cover, integrating vacuum pumps or fan-reinforced vapor evacuation apparatus. Although these efforts have improved the efficiency of the evaporation cycle, they have also increased the energy consumption. Another novel design that uses water wave vibration to promote solar evaporation utilized a vibrating cantilever beam to promote vapor flow that enabled selective condensation on the chamber's side surfaces, achieving high water productivity without additional energy input. (**Figure 2.14g**)[111] Besides, the bioinspired condensation surfaces (i.e. SOCAL surfaces) elucidated previously could be incorporated. Their ultrathin coating layer, efficient water condensing, and removal capabilities could be implemented to address the challenges in vapor collection and optical attenuation.

In addition, the dissipated latent heat and condensation-induced vapor pressure difference need to be further considered in the future design. One innovative prototype that has been developed utilized interfacial solar heat localization and vaporization enthalpy recycling to generate a localized multistage thermal solar still resulting in an ultrahigh solar-to-vapor conversion efficiency (**Figure 2.14h**).[112] Additionally, a PV-assisted solar distiller was developed based on waste heat utilization that exhibited promising results in enhancing freshwater yield (**Figure 2.14i**).[113] Moreover, this technology could be integrated with thermoelectric modules to store and recycle steam enthalpy as thermal energy, which can be further converted to electricity.

2.7.1 Other Advanced Water Manipulation Applications

During the past few decades, many different synthetic strategies have been developed to fabricate functional surfaces with superwettability that are suitable for various types of applications. Among them, perfluorinated compounds have been widely used in superhydrophobic coating formulations, but due to environmental and health concerns, their continual use is in doubt. In this thesis, we will discuss the fabrication of superhydrophobic surface using sustainable colloidal nanomaterials via a green process that possess a lower environmental footprint. In addition, the potential applications of these biobased superhydrophobic surfaces in biomedical, self-cleaning, oil-water separation, food package, water harvesting, and other emerging fields will be addressed. Among these applications, the development and large-scale utilization of sustainable colloidal nanomaterials into useful superhydrophobic coatings will usher the era of resource utilization that will significantly reduce the carbon footprint.

Biomedical

Biofouling is a significant challenge in biomedical devices caused by the continuous deposition and growth of bacteria on medical devices, which poses a high risk of infection. Hence appropriate rectification must be developed to address this. Sustainable superhydrophobic materials play a critical role in addressing these challenges, particularly their environmentally friendly, low cost and self-cleaning characteristics. However, only a few superhydrophobic coatings are suitable for biomedical applications because of the toxicity of chemicals used in the coating systems. We will examine and discuss the superhydrophobicity and related aspects that are necessary for the development of biocompatible superhydrophobic coatings for applications, biomedical diagnosis and instrument [44] and cell culture [45].

Ishikaw et al. produced nanometric composite rods consisting of cellulose nanocrystals (CNCs) and hydroxyapatite (HA) using a simplified simulated body fluid [46]. Nanosized composite rods of ~300 nm in length and ~20 nm in width were produced by the deposition of 22–77 wt% of c-axis-oriented hydroxyapatite (HA) on cellulose nanocrystals (CNCs). The characteristics of CNC–HA nanocomposites were manipulated by controlling the nucleation and growth process. Water-resistant thin transparent coatings were successfully prepared via the evaporation-induced assembly of CNC–HA nanocomposites. The composite coatings exhibited improved mechanical strength compared to crustacean exoskeletons, demonstrating the potentials for bone regeneration. Chitin and chitosan are good candidates as additives for preparing sustainable superwettable coatings for biomedical applications due to their biocompatible, biodegradable, and antibacterial characteristics. Song et al. reported on the synthesis of 3,6-O-di-tertbutyldimethyl silyl chitosan (SC) film using a phase separation process. The SC polymer was fabricated by chemical modification through the amine groups, permitting the control of the surface chemistry and wettability. Following the fabrication of the SC film, an extreme water-repellent SC film over the pH range of 1–14 that displayed topography with organization that yielded a three-level hierarchical roughness. This not only improves the stabilization of chitosan-based films but also demonstrated the possibility of producing

polysaccharide-based superhydrophobic surfaces for use as anti-bacterial substrates in tissue engineering, food packaging, and other biomedical applications [47].

Oil-water separation

The treatment of oily wastewater from industries, such as petrochemical, paper making, mining, and metal finishing, is urgently needed due to the environmental pollution that has created a global social and health challenge. Various approaches, such as gravity separation, floating, and skimming, have been used for oil-water separation. However, the surfactant stabilized oil-in-water emulsion was difficult to be separated due to the stable oil-water interface. At present, superhydrophobic based materials, including membrane, foam [48], aerogel, mesh, and fabric, offer a promising approach for oily wastewater purification, which reduces the wastewater treatment cost and secondary pollution。

Altaf et al. designed a robust methyltrimethoxysilane modified CNC-CNT-PU superhydrophobic paper (MCCP) for water-in-oil emulsion separation. Due to the surface superhydrophobicity and lipophilicity, the MCCP would adsorb the oil while the water would pass through the superhydrophobic paper under vacuum-assisted filtration. As shown in **Figure 2.15b**, the thick Span80 stabilized W/O emulsion was transformed into a transparent liquid after permeating through the MCCP superhydrophobic paper. Besides, the addition of CNT endowed the MCCP with photothermal conversion capability that potentially can be used in water removal. Under NIR, the surface of MCCP paper would increase from an ambient temperature to 48°C within 20 min, which enhanced the volatilization of water. Consequently, in the water removal study, about 30g of water would be volatilized in about 10 min and this evaporation rate remained constant for a period of 20min, highlighting the stability of the coating layer.[35] Yang et al. developed a lignin-based superhydrophobic xerogel for oil-water separation. Due to the high porosity (75.1%), 3D interconnected structure and superhydrophobic surface, a small piece of xerogel could adsorb n-hexane in an underwater spill in several seconds, with a rapid oil recovery capability. Yagoub et al. developed a complex poly(ethylene terephthalate) (PET) fabric membrane coated with cellulose nanocrystal (CNC), chitin nanocrystal, and chitosan (CH) for oil-water separation [49]. CH imparts hydrophobicity and the prepared CNC/ChiNC/CH/PET complex membrane could directly separate water-in-oil emulsion. For the oil/water separation process, oil would easily spread on the surface and consequently form a continuous oil layer on the surface, which reduces the contact area between the membrane and water droplet. Thus, the water droplet would be repelled by the surface, achieving under oil superhydrophobicity, while the oil would pass through the membrane, leading to the separation of oil from the oil-water mixture. The separation efficiency approached 99.2% at a water/oil ratio of 10:120, and the efficiency remained at 96.5% even when the water/oil ratio was reduced to 1/120.

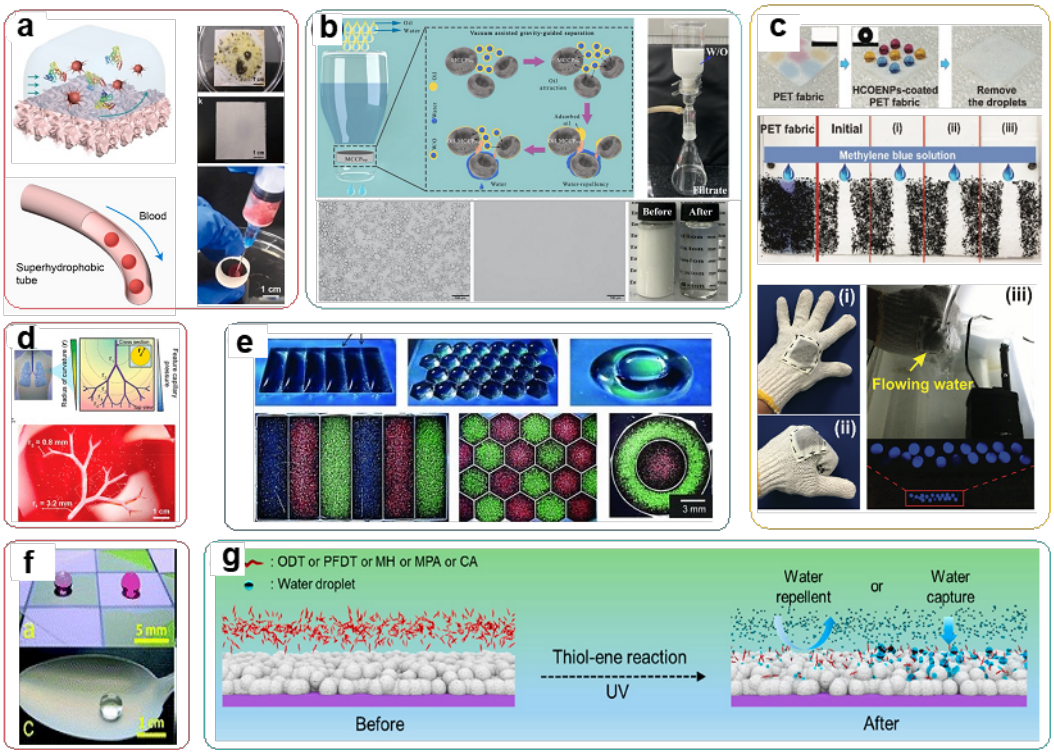

Figure 2.15 Potential applications of superwettable surfaces. a. Scheme illustration of all-natural superhydrophobic surface applied for biomedical devices, b. Oil/water separation conducted by CNC/ChiNC/CH/PET complex membrane, c. wearable all-fabric-based TEG fabricated using hydrophobic cellulose oleoyl ester nanoparticles (HCOENPs) for energy harvesting, d. 3D biofabrication of bacteria nanocellulose films, e. Illustration of different cells culturing in micropatterned superhydrophobic surface, f. Food package coating prepared from cellulose stearoyl ester, g. Schematic of cellulose-based superhydrophobic surface employed on water harvesting application. Electron microscopy images are reprinted with permission from ref. [40-45,52,53]

Food packaging

Food residual waste is becoming a human challenge, and it has taken a huge toll on our society. One of the efficient and environmentally friendly approaches to reduce such waste is to utilize sustainable and superhydrophobic food packaging. Such a system can be applied to a variety of industries by introducing water/food repellency and self-cleaning characteristics to the packaging materials to reduce food waste.

Geissler et al. reported robust, semitransparent, superhydrophobic, and self-cleaning films prepared via the nanoprecipitation of cellulose stearoyl ester (CSE) yielding morphologies consisting of branch-like nanostructures (100–200 nm) decorating the micropapillae (sizes of 5–9 μm) [50]. The superhydrophobic films could be applied to a broad range of substrates (hydrophobic and hydrophilic surfaces) with non-uniform shapes via specialized coating techniques. High contact angles (155.6°) with small contact angle hysteresis were reported when the surfaces were prepared using different coating techniques. The advantage of these films in comparison to films fabricated

from other materials is that they are produced from non-toxic and biodegradable cellulose and fatty acids. (**Figure 2.15f**). Wang et al. described a simple method to fabricate lignin nanospheres (HT-LNS) via solvent exchange and they were then cross-linked via a hydrothermal treatment in water [51]. Furthermore, the HT-LNS can be employed for the preparation of superhydrophobic coatings, yielding water contact and sliding angles of 151.9 ± 1.4 and 9.4 ± 0.5° respectively. This study provides a simple and effective technology platform to construct superhydrophobic coatings using environmentally friendly nanoparticles that are ideal for food packaging instead of silane, or fluorine-based compounds. El-hadi reported a biocomposites film comprising of poly (3-hydroxy butyrate) (PHB), cellulose nanocrystal (CNC) and a plasticizer (TBC) that were blended with PLLA to increase the elongation at break, which meets the specifications for food packaging system [6].

Biofabrication and On-chip Microreactor

The unique water droplet manipulation on superhydrophobic surfaces provides a new route for the formation of spherical superparticles, nano or micro polymeric gel, as well as biofilms, with important applications in synthetic biology, drug delivery, polymer science and engineering.

Greca et al. exploited the three-dimension (3D) biofabrication of bacteria nanocellulose films at superhydrophobic interfaces. The biofabricated replicas were hollow comprising of seamless nanofibrous objects with a controlled morphology that was controlled by wetting, incubation time, and nutrient availability (**Figure 2.15d**). This work provided a novel sight in the general field of synthetic biology, and microbiology [54]. Tian and co-workers developed an efficient and green strategy to prepare porous magnetic chitosan (PMCS) particles via a special superhydrophobic effect of a porous fluorinated polyimide (PFPI) fiber mat with a petal effect. Through the electrospinning method, the spindle bead-fiber structure of the PFPI fiber mat was fabricated, and it displayed high-adhesion superhydrophobicity. By controlling the fiber morphology and porous structures on the fiber surface, the water contact angle on the fiber mat could reach as high as 155.3°. The results suggested that the obtained PMCS particles exhibited excellent Cu(II) adsorption capacity and reusability [55].

Moreover, the superhydrophobic/superhydrophilic transition can be achieved by stimuli-responsive surfaces that can detect the characteristic of liquid deposited on the surfaces. Such systems could be deployed for blood detection and microreactor. Li et al. reported smart superhydrophobic surfaces fabricated via a facile "glue + powder" strategy. A thin layer of commercialized polydimethylsiloxane (PDMS) acted as the glue to bind the chitosan powders, while the as-prepared surfaces possessed remarkable water-repellent and pH-responsive characteristics. The chitosan-based hydrophobic surface was pH-responsive and it could be used to control the contact angle of liquids on its surface. The neutral droplet on the surface (1 M sodium chloride) remained spherical for more than 20 min, whereas in acidic (1 M hydrochloric acid) and alkali (1 M sodium hydroxide) conditions, water droplets gradually spread within 10 min. More interestingly, the pH-sensitive superhydrophobic surface could be used to visually identify the pH value of droplets without the loss of the liquid [56]. Jana et al. introduced a common and robust chemical approach to preparing

chemically reactive, tunable adhesion and stimuli-responsive superhydrophobicity, where a chitosan-covalent cross-linked material possessed dual chemical reactive functionality [57]. The chitosan polymeric material was synthesized following a facile 1,4-conjugate addition reaction between amine and acrylate groups, which provided a facile basis for both single and dual post-functionalization using a wide range of chemical moieties. The embedded pH-responsive superhydrophobic surface was expanded to prepare self-cleaning prints using water-soluble dye. These materials could be adapted for various potential applications, such as patterned wettability, smart microfluidic devices, and customized drug delivery systems.

Energy Harvesting-Piezoelectric/Triboelectric Generator

The impact dynamics of liquid drops on the superhydrophobic surface is of great importance in a variety of industrial processes, such as energy transfer and storage, precision solder-drop dispersions in microelectronics, or deposition of pesticides on leaves [58]. Xiong et al. described a wearable all-fabric-based triboelectric generator (TEG) fabricated using hydrophobic cellulose oleoyl ester nanoparticles (HCOENPs). The superhydrophobic HCOENPs-coated fabric displayed excellent performance in water harvesting in addition to self-cleaning and antifouling characteristics (**Figure 2.15c**). It could be used to harvest both electrostatic and mechanical energy of water, achieving a maximum instantaneous output power density of 0.30 $W \cdot m^{-2}$. The HCOENPs-coated fabric possessed excellent breathability, washability, and being environmentally friendly, it offers promise in the wearable self-powered system [59].

Chapter 3. Sustainable Superhydrophobic Surface with Tunable Nanoscale Hydrophilicity for Water Harvesting Applications

3.1 Introduction

Freshwater is an essential element for society to sustain all aspects of human activity. However, current freshwater sources are severely impacted by man-made pollution and climate change, leading to a scarcity of water to meet the growing demand for this vital resource. Several water collection and purification technologies have been developed to augment the increasing demand for water resources. Particularly, water harvesting from air has emerged as a promising strategy due to the abundance of clean atmospheric water, which accounts for up to ~10% of freshwater sources.[1] For current water harvesting technologies, the research of bio-mimicking natural organisms, such as lotus leave,[2] fog basking beetles,[3] insect wings,[4] etc. has inspired the development of water-collection devices based on their special wettability surfaces and delicate structures. Superhydrophobic systems like lotus leaf possess superior water removal characteristics but they cannot achieve self-capture water vapor from the air, which is unfavorable for water harvesting.[5] Distinct from these superhydrophobic systems, the fog basking beetles found in the desert offers a novel strategy for water collection.[6] Even in an arid environment, they can collect drinking water on their backs from fog-laden wind using their hydrophilic/hydrophobic pattern back, which captures water and transports to their mouth.[7] Nevertheless, the hydrophilic bumps as micrometer deposition regions are beneficial for capturing droplets but they impede the droplet continuous draining and transport process.[8] Inspiration from nature is only the starting point, while the ultimate goal is to improve surface engineering and material design in order to maximize water collection from fog.

Several attempts have been reported for improving the water harvesting performance of surfaces from different perspectives. A beetle-inspired micro-hydrophilic/hydrophobic pattern surfaces reported by Moazzam et al.,[9] achieving a water collection rate of 0.97 L/m^2/h. Although hydrophilic patterns contribute to droplet capture and coalescence, the formation of micro hydrophilic pattern reduces droplet mobility and leads to surface flooding since droplets nucleate within the surface textures. Mishchenko et al.[10] developed a bottom-up fabrication approach by depositing nano hydrophilic polymers and particles on the tips of superhydrophobic surface to achieve a spatial control over the uniform nucleation, growth, and coalescence of water droplets without surface flooding. However, the surface durability[8] is still limited by the fragile structure, where the hydrophilic polymers could potentially be destroyed or contaminated after prolonged use. Zhang et al.[11] presented a slippery surface comprising of hollow hydrophilic hydrogel bump arrays and a lubricant infused inverse opal film to efficiently control and manipulate the droplets. Even though the surface displayed high-water collection rate of 49 mg/cm^2/min, the complicated fabrication method, restricted lubricant types[12] largely impeded its practical applications.

In this study, we present a unique superhydrophobic surface with tunable nano-scale

hydrophilicity via a self-assembled process, where the CNC/wax Pickering emulsion was used to prepare surfaces that display outstanding water harvesting performance. Specifically, the emulsion templated surface engineering described here not only offers a convenient approach to tailor the hydrophilic nanodomain density, but it also imparts superhydrophobicity to the fog-harvesting surface via topography design. These hydrophilic CNC nanodomains act as nuclei to activate the water deposition process, coupled with superhydrophobic features for the manipulation of droplet mobility. Appropriate tunning of the binary cooperative wettability characteristics of the surfaces, our hydrophilic/superhydrophobic pattern surface allows us to enhance the water deposition rate without sacrificing the water transport rate. Thus, through changing the surface topography, balancing the trade-off between water deposition and transport, and ensuring the surface stability on the resulting hydrophilic/ superhydrophobic surface, it could achieve a high water harvesting flux of 3.402 L/m^2/h with a CNC density of 84.7%.This study not only offers a practical strategy for the water-stressed community to ease the growing shortage of clean water but also provides scalable manufacturing techniques to tailor the surface topology with patterned micro/nanostructures and heterogeneous wettability.

3.2 Materials and method

Cellulose nanocrystals (Celluforce, Inc.), amine terminated polystyrene (Sigma-Aldrich, average M_n = 5000 Da), paraffin wax (Sigma-Aldrich), Ethanol (Sigma-Aldrich), 1H,1H,2H,2H-Perfluorodecyltrichlorosilane (Sigma-Aldrich). All chemicals were used without additional purification, unless stated otherwise. Milli-Q water (resistivity of 18.2 MΩ·cm) was used to prepare the aqueous dispersions.

Synthesis of CNC/wax emulsion particles

The pristine CNC aqueous solutions with different concentrations (1.0, 3.0, 5.0 7.0 10.0 mg/mL) were obtained by dispersing CNC powder in deionized water followed by ultrasonic treatment for 1 h. A certain amount of amine-terminated polystyrene (PS-NH_2), with a constant ratio of 10:1 to CNC, was dissolved in the paraffin wax at 70°C in the oven. For the synthesis of the Pickering emulsion, the mixture of oil and water phase was homogenized using an ultrasonic probe (Misonix-Microscon-XL2000) for 5 min at 65°C, where the CNC solution and paraffin wax were used as the water and oil phase at volume ratio of 4:1 respectively. Then, the O/W Pickering emulsion was obtained and placed at room temperature for further preparation of hydrophilic/superhydrophobic surface.

Preparation of the hydrophilic/superhydrophobic patterned surface

The as-prepared CNC/wax emulsion particles were added dropwise into ethanol and kept stirring overnight in a glass vial before coating the substrates. Then the emulsion solution was uniformly sprayed onto the cleaned substrates (e.g., glass, mesh) with a spray gun under 0.5 MPa N_2 gas. The final hydrophilic/superhydrophobic surfaces were obtained after the solvent completely evaporated, which were recorded as SHS-HI_m for varying CNC concentrations (m=1.0, 3.0, 5.0, 7.0, 10.0

mg/mL).

3.3 Characterization

3.3.1 Interfacial behavior characterization

Interfacial tension The interfacial tension measurement was conducted using a tensiometer DCAT 11(Dataphysics). To measure the interfacial tension between water phase and oil phase, a Wilhelmy plate was thoroughly cleaned and attached to a balance with a thin metal wire. The forces on the plate due to wetting with different liquids were measured using a tensiometer and used to calculate the interfacial tension.

Interfacial coverage A pendant water droplet containing CNC was placed in the liquid wax solution with a syringe connected to a blunt needle, where the volume was recorded as V_F. During equilibration of the droplet in the oil phase for 10 to 20 min, the interfacial tension was measured. At equilibrium, the volume of the drop was reduced by withdrawing the fluid with a syringe, and the interfacial area would decrease until the wrinkling and buckling of the assembled CNC occurred. The volume of the buckling in the droplet was recorded as V_J, and the interfacial coverage (C) was calculated from the values of V_F and V_J.

Wetting characterization

The water static contact angle and dynamic contact angle measurements were performed using an OCA 15 (Dataphysics).

Static contact angle To measure the static contact angle, a sessile drop (5 μL) was dispensed onto the test surface with an auto-dosing system with a 500 μL needle, and a side-view image was captured with the camera when the droplet stabilized. To obtain an accurate value of the static contact angles, the captured image was further measured by Image J analysis software.

Dynamic contact angle Slide angles were measured as follows: a droplet (5 μL) was dispensed by the auto-dosing system onto the test surface and aligned with the tilting axis of the stage. The stage was then tilted at a specific angle and stopped once the droplet started rolling on the surface.

Advancing contact angle and receding contact angle The dynamic mobility of the droplet on the surfaces was tested via the sessile-drop goniometry. A drop deposited on the measured surface and the volume was increased from 3 to 10 μL, and the value of the ACA was obtained from the advancing contact line. For the RCA, the volume of the drop was reduced to 3 μL, and the value of the RCA was obtained from the receding contact line[1] recorded by the experimental snapshots using a high-speed camera.

Tensile measurement In the adhesion experiment, a small drop of liquid was brought into contact with a super liquid-repellent layer and then gradually withdrawn in the normal (vertical) direction. The drop of typically 5 μL was held in a metal ring, a disk, or at the end of a capillary. The force required to pull the drop off the layer, the pull-off or adhesion force, was measured in a tensiometer (DCAT11).

Water jet impact experiment To characterize the effect of water wetting induced by abrasion of the surface, we used the water jet with a constant volume velocity of 10 mL/min to impact the

surface at a specific incident angle (~ 35°). The nozzles have nominal diameters of 0.25 mm. The water jet's impact on the substrates was recorded with an IDS high-speed camera fitted with a macro lens at a frame rate of 3,000 fps. The incident and deflected angles were determined by Image J analysis software.

3.3.2 Water Harvesting experiment

The experimental setup is shown schematically in **Scheme 3.1** and **Figure 3.12.** The as-prepared surfaces were secured onto a holder, and a simulated fog flow (300 mL/h) was produced by a humidifier and used to evaluate the water harvesting performance of different surfaces. The experiment was conducted under the same environment at 25°C and RH=80%. To quantify the droplet dynamic (r=12 μm) on the surface during nucleation and detachment state, the water droplet nucleation weight was measured continuously by high sensitivity load cell connected to the glass substrates (**Figure S9**), while the water weight was determined by collecting the water using a measuring vial weighed on an electronic balance at intervals of 5 seconds for a duration of 1h.

3.3.3 Other characterizations

The emulsions captured in optical microscopic images and videos were carried out using the Nikon LV ND microscope and Photron SA5 high-speed camera. The particle size was measured using the particle size analyzer (Anton Paar 1190). The surface topography and characteristics were determined using a scanning electron microscope (SEM), energy dispersive X-ray spectroscopy (EDS) analysis, Confocal optical microscope (Olympus LEXT ols5000) and XPS (Escalab 250XI, Thermo Scientific, USA).

3.4 Result and discussion

3.4.1 Synthesis of CNC/wax emulsion particles and preparation of the hydrophilic/ superhydrophobic patterned surface

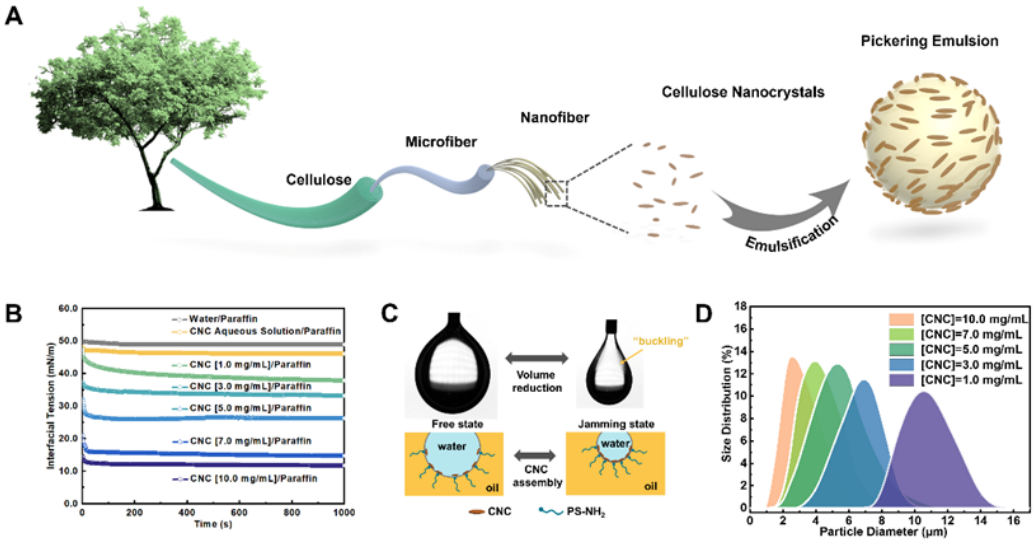

Figure 3.1 A. The schematic of CNC/wax Pickering emulsion formation, B. Time evolution of interfacial tension between CNC aqueous solution and liquid wax dissolving PS-NH2, C. Interfacial

surface coverage of CNC on the emulsion droplets, D. The dependence of emulsion particle size on CNC concentration

The formation of CNC/wax Pickering emulsion as illustrated in **Figure 3.1A**, where the constituents comprised of CNC and paraffin wax. Specifically, CNC rod-like nanoparticles derived from biomass were good candidates as emulsifier to stabilize the Pickering emulsion due to its sustainability, hydrophilicity, and negative surface charge.[13–16] Pristine CNC can assemble on the O/W interface to form stable Pickering emulsions when the negative surface charge is screened by materials with positive surface charge. We fabricated stable oil-in-water (O/W) Pickering emulsion by homogenizing a mixture consisting of an aqueous dispersion of pristine CNCs and liquid paraffin wax solution of amine-terminated polystyrene (PS-NH_2) in a one-step process[17,18]. Herein, the electrostatic repulsion between CNC particles at the interface can be effectively overcome through the cooperative interaction of CNC and positive charge polymer[19], e.g., PS-NH_2 (**Figure 3.2**). Owing to the irreversible assembly of CNC and PS-NH_2 at the interface, a stable Pickering emulsion was produced (**Figure 3.3**).

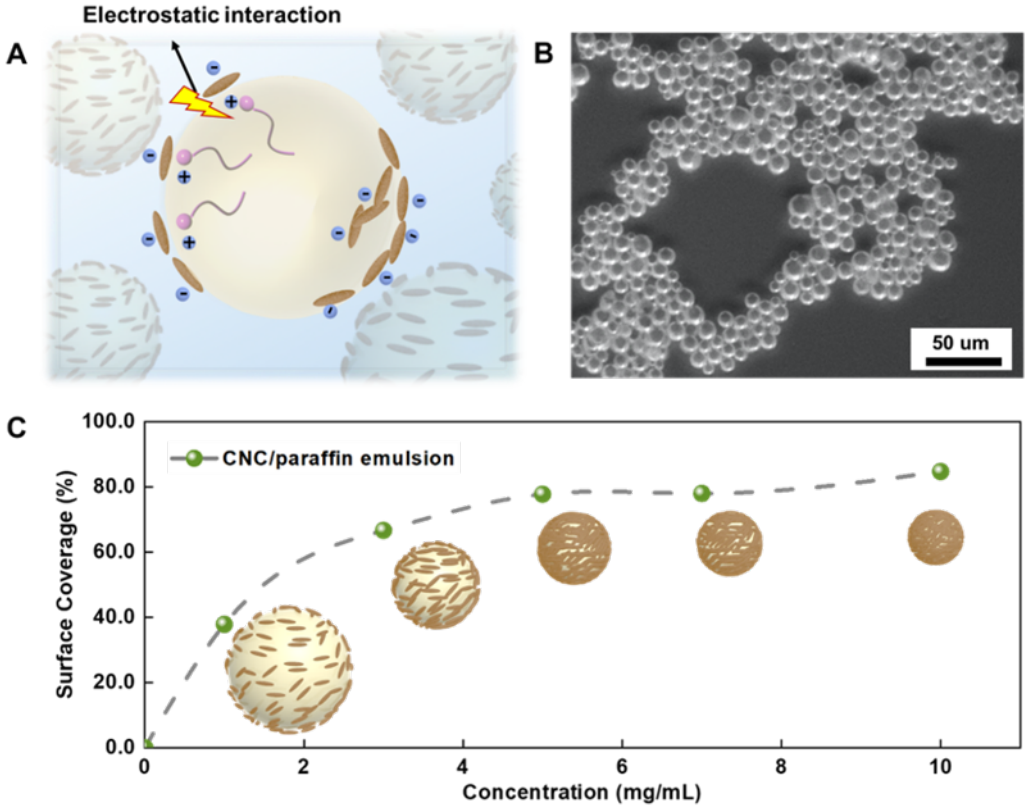

Figure 3.2 A. The mechanism illustration of forming stable CNC/wax Pickering emulsion via electrostatic interaction, which the negative charge on CNC outer surface interacting with positive charge polymer (PS-NH_2), B. Optical microscopic image of CNC/wax Pickering emulsion at [CNC]=1.0 mg/mL C. Surface coverage of CNC/paraffin emulsion varying in different concentration.

The interfacial kinetics of CNC/wax was conducted by the Wilhelmy plate method to investigate

the emulsion formation, assembly, and jamming at the water–oil interface.[20] Pristine CNCs were well-dispersed in water but they could not pack tightly at the oil–water interface owing to the electrostatic repulsion from negatively charged CNC. As a result, the equilibrium interfacial tension (γ) between pure CNC aqueous solution and liquid wax was about 46 mN/m, which is close to the pure water–wax system (48 mN/m). However, when the PS-NH_2 was added to the oil phase, the protonated polymer amine groups (NH_3^+) induced strong electrostatic interactions with deprotonated sulfates groups ($-OSO_3^-$) on the CNC surface under acidic condition (pH=4.0), causing the simultaneous arrangement at the interface that reduced the oil-water interfacial tension. As shown in **Figure 3.1B**, at lower CNC concentrations ranging from 1.0, 3.0, 5.0 7.0 mg/mL, a continuous reduction in γ with time was observed and the final equilibrium interface tensions were 36, 32, 26 and 15 mN/m, respectively. Further, at the CNC concentration of 10.0 mg/mL, a faster equilibrium state was achieved at the water/oil interface and the interfacial tension decreased to as low as 12 mN/m. These results demonstrated that the change in the interfacial tension was attributed to the assembly of CNC and PS-NH_2 at the interface, which could be controlled by the CNC concentration in the aqueous solution.

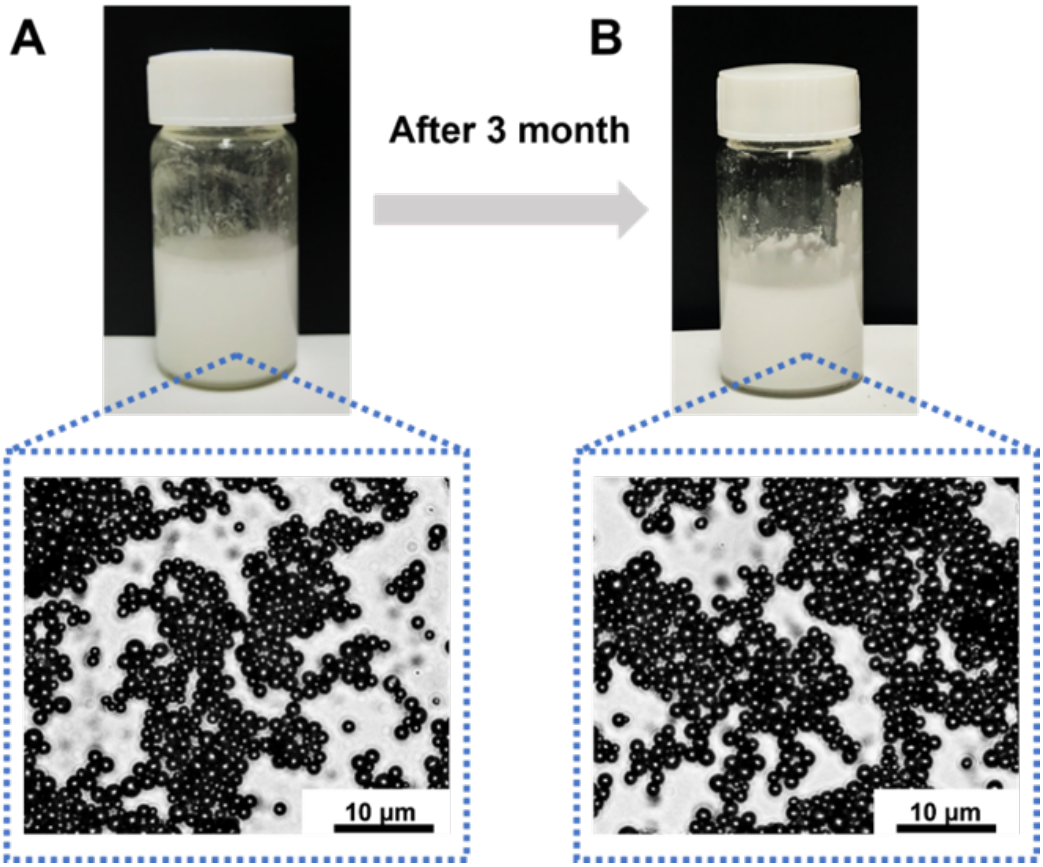

Figure 3.3 The stability of CNC/wax Pickering emulsion: A. original CNC/wax Pickering emulsion, B. CNC/wax Pickering emulsion stored after three months.

With regards to the adaptive structure of CNC/wax emulsion, the packing density of CNC at the interface was adjusted and evaluated by monitoring the interfacial coverage (C) via the pendant drop tensiometer. The schematic of the interfacial coverage measurement is displayed in **Figure 3.1C**. A pendant water droplet containing CNC was suspended in the liquid wax, where CNC were uniformly distributed over the area of the interface (termed the "free" state).[19] During equilibration of the droplet in oil phase, the dispersed CNC nanoparticles interacted with the PS-NH_2 in oil, and assembled and packed at the interface.[21] When the volume of the drop was reduced by withdrawing fluid at a certain rate, the interfacial area diminished and the buckling of the assembled CNC occurred on the drop surface (termed as the "jammed" state). Thus, the interfacial coverage can be calculated by $C = S_J/S_F$, where S_J and S_F were regarded as surface areas correspond to the volume of jammed and free (initial) states, respectively. As shown in **Figure 3.1C**, the buckling phenomenon occurred when a large volume reduction occurred at the CNC concentration of 1.0 mg/mL, indicating the insufficient assembly of CNCs at the interface (C~37.8%). However, when the concentration approached 3.0 mg/mL, the emulsion droplets possessed an interfacial coverage of 66.6% with an increase in the buckling onset volume. As the concentration of CNC was increased to 10.0 mg/mL, more CNC partitioned and assembled to form a monolayer film at the interface with the interfacial coverage approaching 84.7%. However, because of the geometry and irregularity of the shapes of the CNC, the rod-like nanoparticles would jam in a non-close-packed state, where further increase in the interfacial coverage was inhibited by the assembly constraints at the interface (since the coverage should be less than 100%). Notably, the emulsion droplets coated with a monolayer of CNC particles possessed increasing surface coverage of 37.8% to 84.7% when the CNC concentration was increased from 1.0 mg/mL to 10.0 mg/mL. The results showed that the interfacial packing behavior of the CNCs could be manipulated by the CNC concentration, which will further influence the morphology and stability of the emulsion particles.

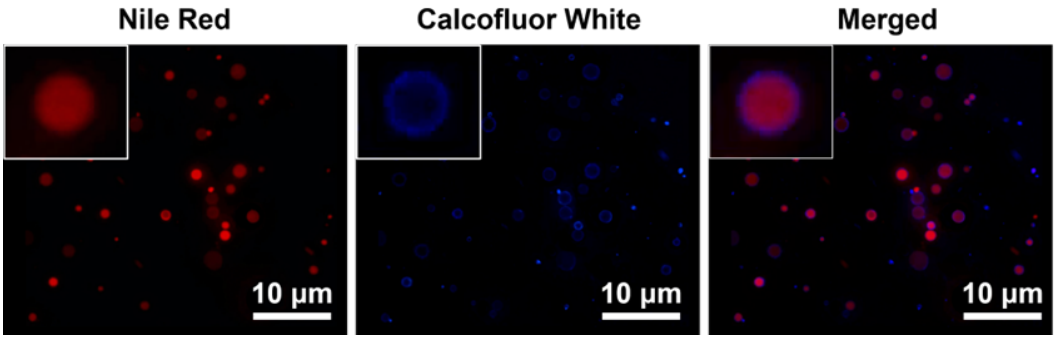

Figure 3.4 Fluorescent micrographs of CNC/wax Pickering emulsions stabilized with CNC at concentrations of 10.0 mg/mL. The left, middle and right rows correspond to the stained oil phase, dyed CNC, and the merged images, respectively. Prior to observation, the oil phase was stained with Nile red, and CNCs were dyed with Calcofluor white.

The morphology of emulsion particles was preliminary observed in an optical microscope and

fluorescence optical microscope (**Figure 3.4**),[22] while the emulsion particles size was determined by the particle size analyzer (PSA) in **Figure 3.1D**. A low CNC concentration (1.0 mg/mL) was sufficient to produce stable Pickering emulsion particles with a mean size of about 10.9 μm. With increasing CNC concentration, the particles size distribution shifted to smaller diameter due to the enhanced surface coverage. If the CNC concentration was increased to 10 mg/mL, the high surface coverage produced a "jamming state" on the outer surface of the emulsion particles, and the particle size decreased to 2.45 μm. The results showed that the size of emulsion droplets could be manipulated by changing the concentration of CNC, where the emulsion dimensions were inversely proportional to the interfacial coverage. Depending on the amount of CNC emulsifier at the interface, the oil droplet will coalesce to minimize the specific surface area and interfacial free energy that is sufficient to stabilize the Pickering emulsions.[23] Consequently, the higher CNC concentration normally generated smaller emulsion particles, which is caused by the closely packed CNC at the interface, while larger emulsions were produced at low CNC concentration. A series of emulsion droplets with size ranging from 10.9 μm to 2.45 μm was produced by progressively increasing the concentration of CNC.

Scheme 3.1 described the preparation of a hydrophilic/ superhydrophobic surface templated by Pickering emulsion. At the beginning of preparation process, Pickering emulsion was added dropwise into the ethanol suspension, and the emulsion particles with a swollen outer layer (formed by hydrogen bond and repulsive force) shrunken and aggregated, and self-assembled into microaggregates.[24] When applied to the surface via spray coating, a thin coating with porous hierarchical structure was constructed (**Figure 3.5**), where the microaggregates self-organized into micropillars. Such microstructure could be prepared on various types of substrates, such as glass, mesh, ceramics. These surfaces for water harvesting contained varying emulsion particles (designated as SHS-HI_m), were prepared where m corresponding to the CNC concentration (ranging from 1.0, 3.0, 5.0, 7.0, 10.0 mg/mL). To obtain a deeper understanding on the influence of surface topography on the water harvesting performance, the HS-$HI_{10.0}$ surface were prepared directly from the Pickering emulsion without solvent exchange and completely hydrophilic surface (denoted as HI) were also prepared respectively (**Figure 3.6**).

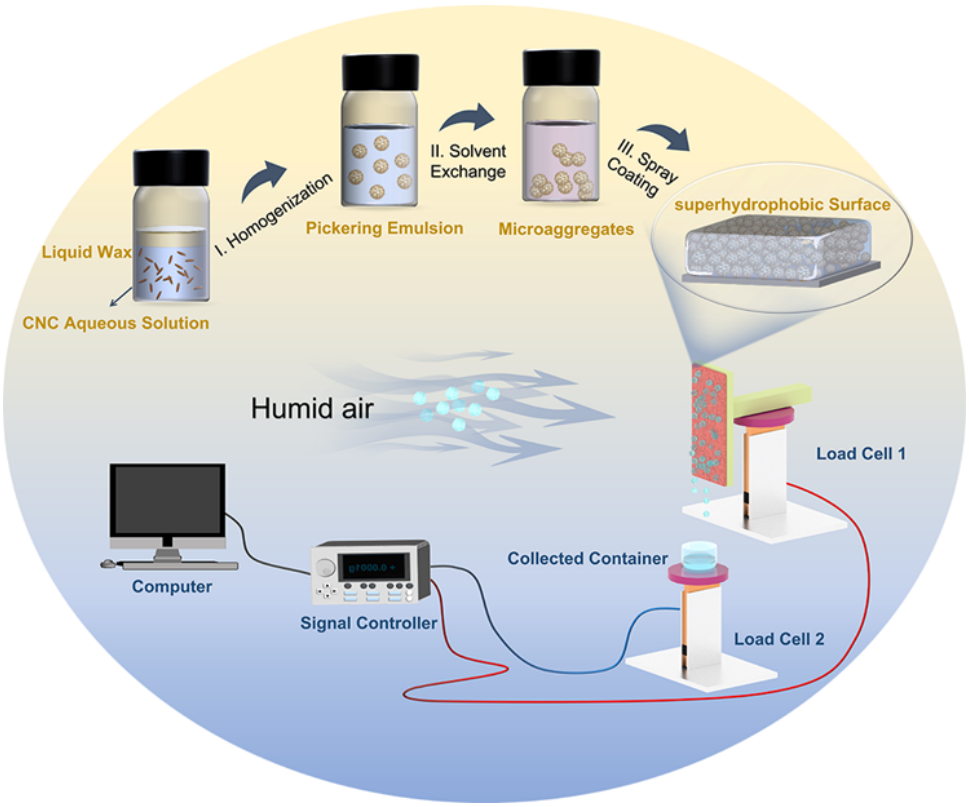

Scheme 3.1 Schematic representation of the fabrication procedure of hydrophilic/superhydrophobic surfaces via spray coating and (down) Diagram shows the water harvesting performance testing on hydrophilic/superhydrophobic surfaces recorded the deposition weight and collection weight with time evolution by using the load cell 1,2.

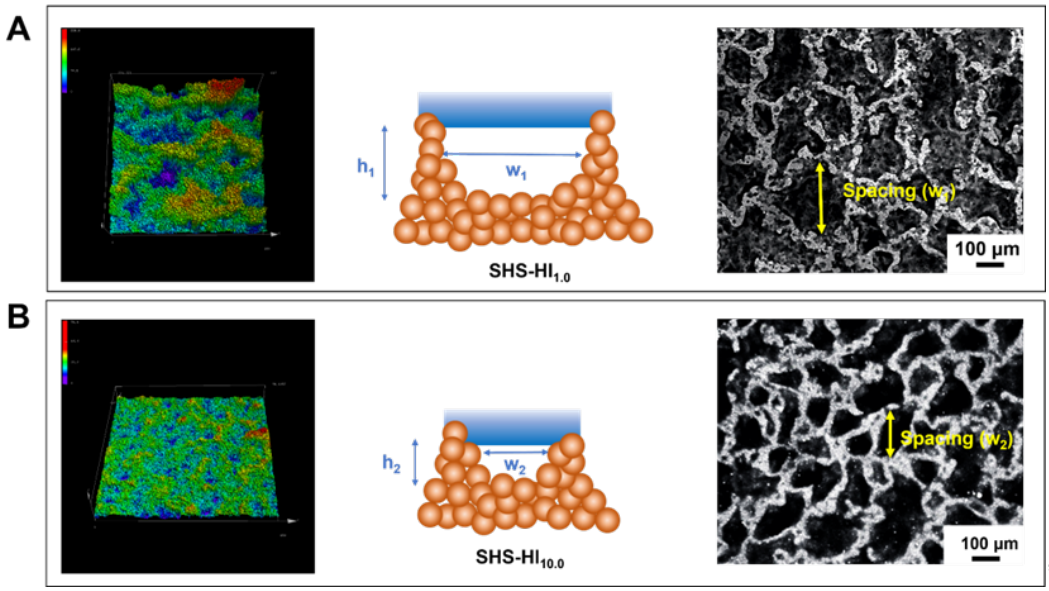

Figure 3.5 A. The topography of SHS-$HI_{1.0}$ surface was observed through confocal optical microscope (right) and the superficial structure was demonstrated by optical microscope(left), where the simplified model of micropillars constructed on SHS-$HI_{1.0}$ that labeling the spacing (w_1) and height (h_1) between two adjacent pillars, B. The topography of SHS-$HI_{10.0}$ surface was observed

through confocal optical microscope (right) and the superficial structure was demonstrated by optical microscope (left), where the simplified model of micropillars constructed on SHS-$HI_{10.0}$ that labeling the spacing (w_2) and height (h_2) between two adjacent pillars.

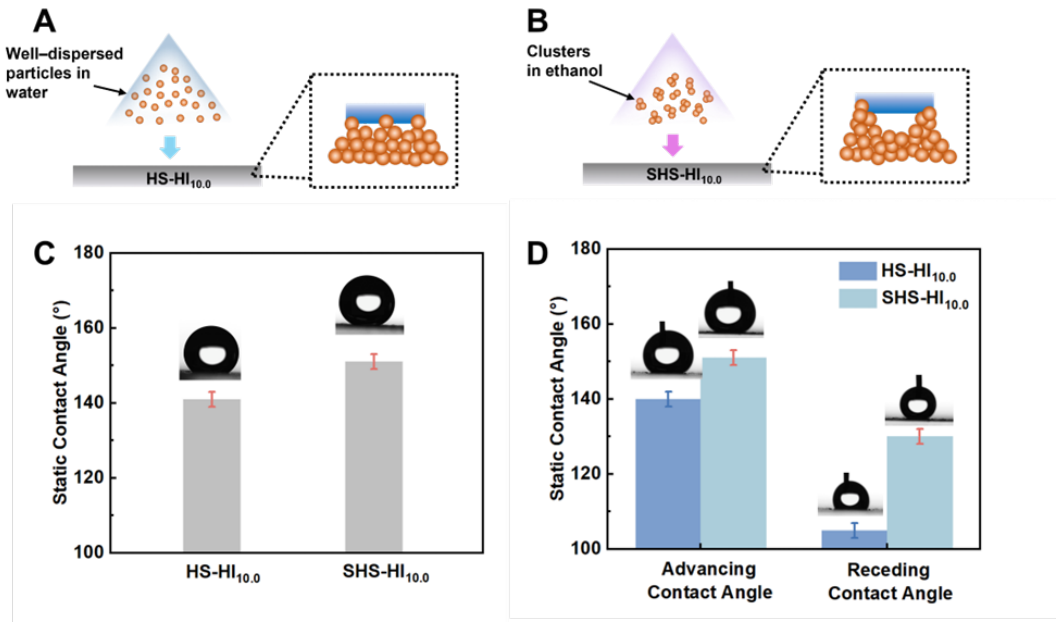

Figure 3.6 Illustration of the construction and surface topography of CNC/wax-based surfaces: A. HS-$HI_{10.0}$, B. SHS-$HI_{10.0}$, C. Static contact angles on SHS-$HI_{10.0}$ and HS-$HI_{10.0}$, D. Dynamic contact angles on SHS-$HI_{10.0}$ and HS-$HI_{10.0}$.

3.4.2 Droplet mobility on hydrophilic/superhydrophobic surfaces

The formation of the hierarchical structures on the surfaces were first observed by optical microscopy (**Figure 3.5**). The micropillars at the micron levels was identified from the lighter regions in the microscope images indicating the presence of porous network structures, while the darker regions corresponded to the spacing between the micropillars. Notably, the pillars on the surface produced with smaller emulsion droplets (2.45 μm) possessed lower height and a larger spacing yielding a smoother structure (SHS-$HI_{10.0}$) compared to SHS-$HI_{1.0}$ surface constructed with 10.9 μm emulsion particles. The topography of the coating layer was measured via confocal optical microscope as well, where the structural roughness gradient was indicated by color bar. Obviously, SHS-$HI_{1.0}$ surface possessed more roughness than SHS-$HI_{10.0}$ surface. Moreover, the surface morphology of these microscale hierarchical coatings was further examined using a scanning electron microscope (SEM). **Figure 3.7A** shows the structure of SHS-$HI_{1.0}$, which possessed aggregated emulsion clusters comprising of emulsion particles. The roughness of the micro and nanoscale structures were clearly evident in the enlarged images (**Figure 3.7C**). On the SHS-$HI_{1.0}$ surface, the emulsion particles consisted of micron-sized spheres, and the surface of the sphere was decorated with CNC nanoscale wrinkles, forming the micro-nano hierarchical structure. A similar

morphology was observed for the other SHS-HI_m surfaces. When the emulsion particle size of SHS-HI_m was increased, such as SHS-$HI_{10.0}$ surface, each sphere was covered with higher amount of CNC compared to SHS-$HI_{1.0}$. The results indicated the CNC nanostructure at the interface was affected by the interfacial coverage of the emulsion particles, and the surface's topmost layer containing hydrophilic nanodomains were in the order of SHS-$HI_{1.0}$ <SHS-$HI_{3.0}$< SHS-$HI_{5.0}$<SHS-$HI_{7.0}$<SHS-$HI_{10.0}$. However, without the solvent exchange step, the as-prepared HS-$HI_{10.0}$ surface was smoother than SHS-$HI_{10.0}$ at the same CNC coverage, and its roughness factor (R_q) decreased significantly from 6.3 μm to 2.8 μm (**Figure 3.7**).[25]

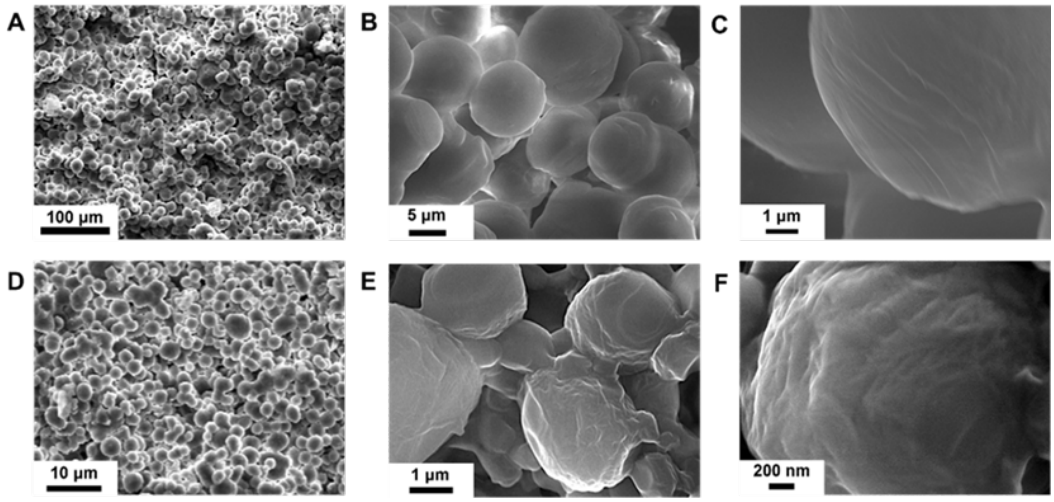

14

Figure 3.7 SEM images of the surface morphology: A & B. the microscale structure of SHS-$HI_{1.0}$ surface, C. enlarged SEM image of SHS-$HI_{1.0}$ surface towards wrinkle nanostructure on one emulsion particle outer surface, D&E. the microscale structure of SHS-$HI_{10.0}$ surface, C. enlarged SEM image of SHS-$HI_{10.0}$ surface towards wrinkle nanostructure on one emulsion particle outer surface.

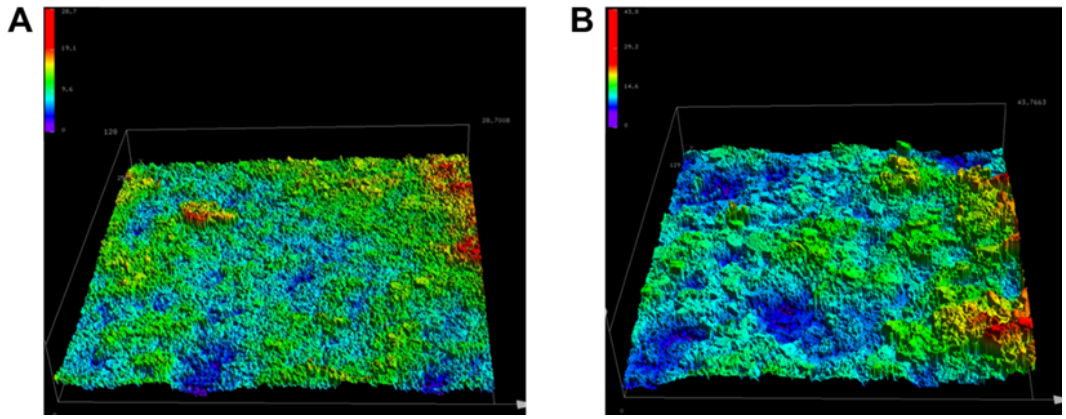

Figure 3.8 Surface topography by confocal microscope (100X): A. HS-$HI_{10.0}$, B. SHS-$HI_{10.0}$.

These hierarchical structures with disparate roughness would have a major impact on the hydrophobicity of the surfaces, which could be evaluated by measuring the static water contact

angle (CA) and contact angle hysteresis (CAH). A water droplet placed on the SHS-$HI_{1.0}$ surface displayed a CA of 160±2° and possessed a rolling-off angle (RA) of around 5°, demonstrating the high superhydrophobicity of the surface (**Figure 3.9B**). Besides, this extreme water repellency was further confirmed by the low CAH (the difference between the advancing and receding contact angles of a moving droplet) of the surface (**Table 3.1**).[26] However, smaller emulsion particles had a corresponding increase in the hydrophilic nanodomain density on the SHS-$HI_{3.0}$, displaying a CA about 158±2°, which was slightly lower than the SHS-$HI_{1.0}$. Furthermore, the static CA of the other three surfaces displayed a downward trend (155±1°, 153±2°, 151±2°) corresponding to the SHS-$HI_{5.0}$, SHS-$HI_{7.0}$ and SHS-$HI_{10.0}$ surface, respectively. The superhydrophobic characteristic was caused by the hierarchical structure of the surface, with numerous entrapped air pockets (hydrophobic medium between micropillars beneath the water) imparting an upward force to hold the water suspended on the structure without touching the bottom structure.[27]

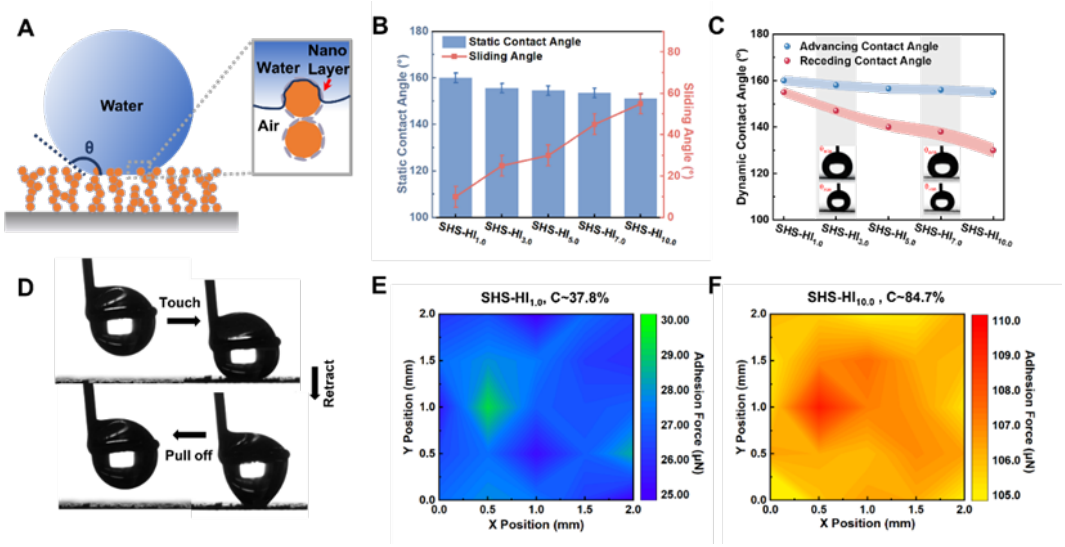

Figure 3.9 A. Schematic of a sessile liquid drop on a hydrophilic/superhydrophobic surface made of highly porous aggregates of microspheres. The schematic illustrates the definition of the static contact angle. The term "edge" is used to distinguish the formation of three-phase contact line (TPCL) between nanostructure and microstructure, B. The static contact angles and sliding angles of different surfaces, C. The advancing contact angles and receding contact angles of different surfaces, D. Tensile adhesion testing procedure on SHS-$HI_{1.0}$, E. The surface adhesion mapping of SHS-$HI_{1.0}$, F. The surface adhesion mapping of SHS-$HI_{10.0}$.

Table 3.1 Wettability characteristics of SHS-HIm including surface adhesion (Fadhesion) and contact angle hysteresis (CAH), where CAH was calculated by advancing contact angle (θaca) minus receding contact angle (θrca)

Surfaces	$F_{adhesion}$	CAH	θ_{aca}	θ_{rca}
SHS-$HI_{1.0}$	27.6 μN	9±2	160±2	152±2
SHS-$HI_{3.0}$	48.4 μN	13±2	158±2	145±2
SHS-$HI_{5.0}$	59.5 μN	15±2	155±2	139±2
SHS-$HI_{7.0}$	66.7 μN	18±2	153±2	136±2
SHS-$HI_{10.0}$	107.6 μN	21±2	151±2	130±2

As discussed previously, the CA displayed a decreasing trend as the size of emulsion particles was reduced. This behavior could be explained further be examining the three-phase contact line of water droplet on the surface as shown in **Figure 3.9A**. The micropillars of SHS-$HI_{1.0}$ possessed larger spacing compared to the other four surfaces formed with smaller particles (SHS-$HI_{3.0}$, SHS-$HI_{5.0}$, SHS-$HI_{7.0}$ and SHS-$HI_{10.0}$), which could trap more air and water would only adhere the topmost surface of the micropillars and partially wet the CNC nanostructure. Due to the higher CNC nanodomain density covering the micropillars of SHS-$HI_{10.0}$, this surface possessed more water affinity domains when the water molecules could adhere to the hydrophilic CNC particles on the wax microdomains. According to the Cassie-Baxter model[2], the increased liquid-solid contact line combined with the reduction in the air pocket beneath the water would contribute to a lower CA of the surface. Although the CAs showed a slight downward trend from 160±2° to 151±2°, all the SHS-HI_m surfaces possessed superhydrophobic characteristics due to microscale structure.[28] If the surface had insufficient structural roughness, like HS-$HI_{10.0}$, the excess hydrophilic region with less air pockets would lead the change of the wetting state from Cassie-Baxter to Wenzel state, resulting a much lower CA and the loss of its superhydrophobicity (only 141±2°).

To further investigate the dynamic wettability of the hydrophilic/superhydrophobic surface with different morphologies, the CAH values were calculated to determine the sliding effect on a surface. Clearly shown in **Figure 3.9C,** large advancing contact angle (ACA, 161±2°) with a receding contact angle (RCA) of 152±2° was achieved for SHS-$HI_{1.0}$, indicating a low CAH (10°). When the CNC nanodomain density increased from 66.6 and 77.7 to 78.2%, the receding contact angle decreased significantly, leading to the enhanced CAH of SHS-$HI_{3.0}$, SHS-$HI_{5.0}$ and SHS-$HI_{7.0}$ of 13±2°,15±2° and 18±2°, respectively. As the surface coverage was further increased to 84.7% (SHS-$HI_{10.0}$), with the highest density of hydrophilic nanostructured CNC, the RCA decreased to 130±2° and CAH approached 21±2°. Moreover, the variation of the CAH values on these surfaces with sliding angle was in good agreement (**Figure 3.9B**). Since the water droplet would easily wet the hydrophilic nanostructure on the outer surface of the microparticle and bridged their neighbouring pillars during the ACA measurements, the solid-liquid contact area was increased resulting in a large adhesion force. When the droplet surface contact line began to retract from the neighbouring pillars, the droplet needed to overcome a large energy barrier for surfaces with high density of hydrophilic domains.[29] In other words, nonwetting state over the large micro-grooves would increase the advancing contact angle, whereas the impregnation of water on the nano-grooves would delay the

receding contact angle. Notably, the hydrophilic nanodomains on the pillar's outer surface reduced the receding contact angle, resulting in a pronounced hysteresis.[30] However, the droplet on HS-$HI_{10.0}$ surface would wet the whole hierarchical structure (both the nano-grooves and micro-grooves surface) due to the lower superhydrophobic character of the surface. During the RCA measurement, the receding line motion would induce a large energy barrier, which would reduce the RCA. Thus, the water droplet behavior on the SHS-HI_m and HS-$HI_{10.0}$ were attributed to the combined effects of the hierarchical microscale and nanoscale structure. This characteristic was harnessed to determine the threshold of the self-departure droplet size during the water harvesting process.

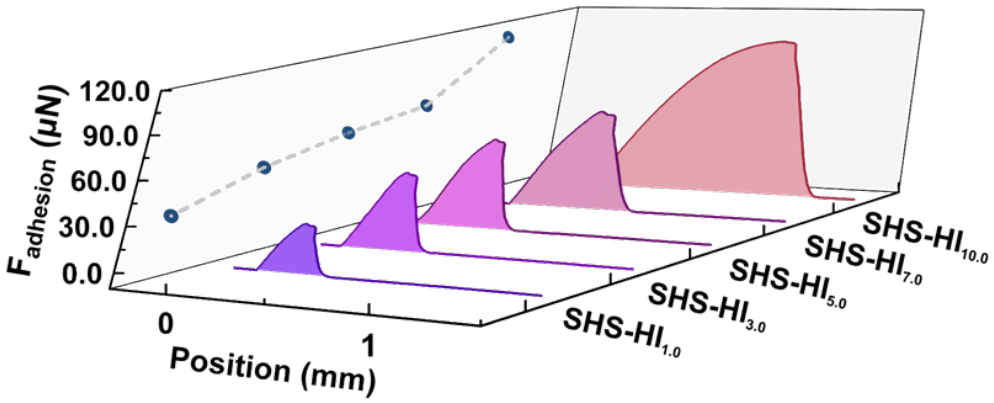

Figure 3.10 The average surface adhesion of SHS-HI_m that showing the adhesion force change with position during the tensile measurement.

In addition, the surface adhesion force ($F_{adhesion}$) towards droplets in the vertical direction was conducted via the tensile adhesion experiments (**Figure 3.9D**), allowing for the determination of the pinning effect of water on the surface.[31] The surface adhesion force was obtained through the touch-sensitive approach, where the force accompanied the water shape deformation as the water touched and retracted from the surface was recorded. **Figure 3.9D** showed the surface adhesion force measurements on the SHS-$HI_{1.0}$ surface, which revealed a slight droplet shape stretching as the droplet was separated from the surface. We measured the surface adhesion force on different regions of the 2-D surface, and the results is shown in **Figure 3.9E.** Surface adhesion mapping[32] revealed that the edges displayed lower values than the inner regions with differences of less than 5 μN, demonstrating the SHS-$HI_{1.0}$ possessed fairly uniform surface adhesive force of 27.6 μN over the whole surface. For the SHS-$HI_{3.0}$, SHS-$HI_{5.0}$ and SHS-$HI_{7.0}$ surfaces, the results revealed that the surface adhesive forces were in the order of 48.4 μN, 59.5 μN and 66.7 μN as shown in the **Figure 3.10**. In comparison, the shape of the water droplets deformed significantly when the water was withdrawn from the SHS-$HI_{10.0}$ surface, revealing the water repellent characteristics in different regions as illustrated in **Figure 3.8F** with an average adhesion force of 107.6 μN. It is worth noting that the surface adhesive forces displayed the same trend with CAH and sliding angle (SCA), where more hydrophilic nanodomains produced a larger $F_{adhesion}$, CAH and SCA that led to the water pinning effect. This was a result of the Cassie-impregnated state of our surfaces, where the water

droplets on an incline surface impregnated into the hydrophilic nanoscale apertures that hinder the separation of the water droplet from the surface. With the reduction of the nanodomain density on the surface, the gaps between nanodomains increased resulting in a lower water affinity on the nanoscale structures that enhanced the capacity to maintain a thin air pocket layer in the nanoscale apertures.[33] On the other hand, the HS-$HI_{10.0}$ would generate large adhesion force with residual water left on surface after testing, possibly due to the Wenzel state of the surface (**Figure 3.10**) as the water droplet could not be completely detached from the surface. Thus, the surface wettability characteristics of the hydrophilic/superhydrophobic surface could be easily tuned by the topography design using the Pickering emulsion containing varying amounts of CNC nanoparticles.

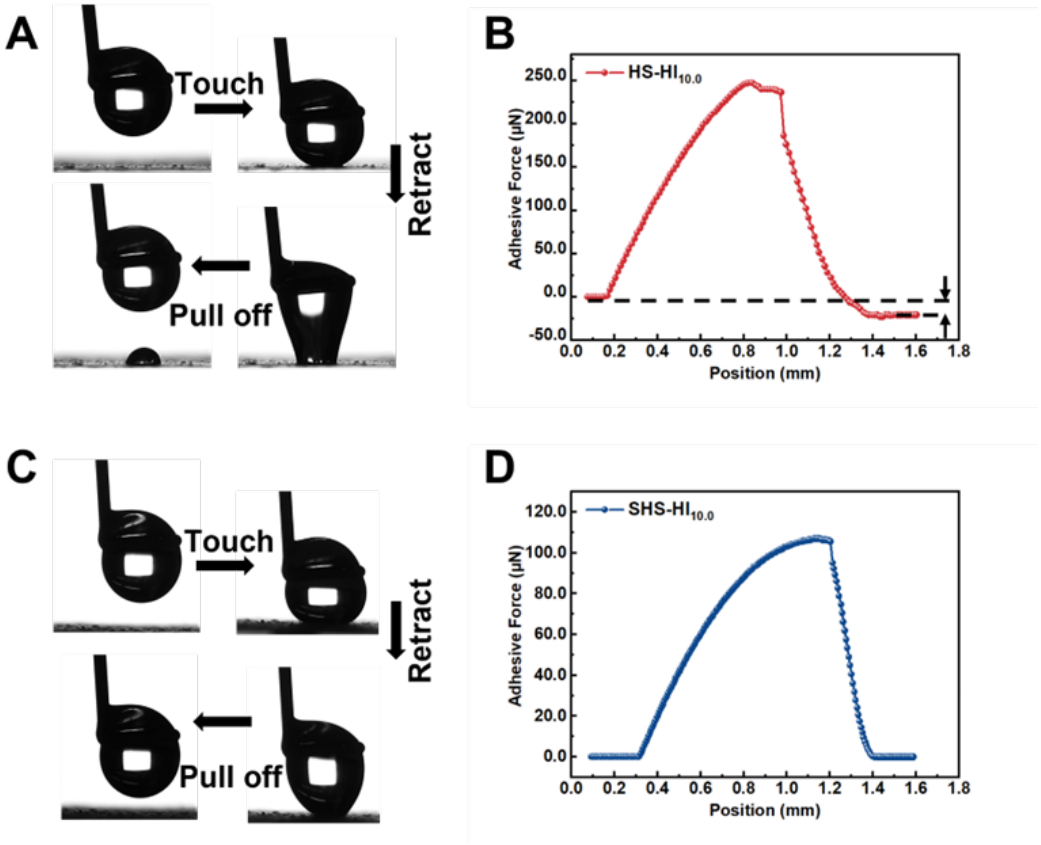

Figure 3.11 Tensile adhesion that showing the adhesion force change with position during the tensile measurement: A. and B. HS-$HI_{10.0}$, C. and D.SHS-$HI_{10.0}$.

3.5 Water harvesting behavior

3.5.1 Cyclical droplets capture on hydrophilic CNC nanoscale structures

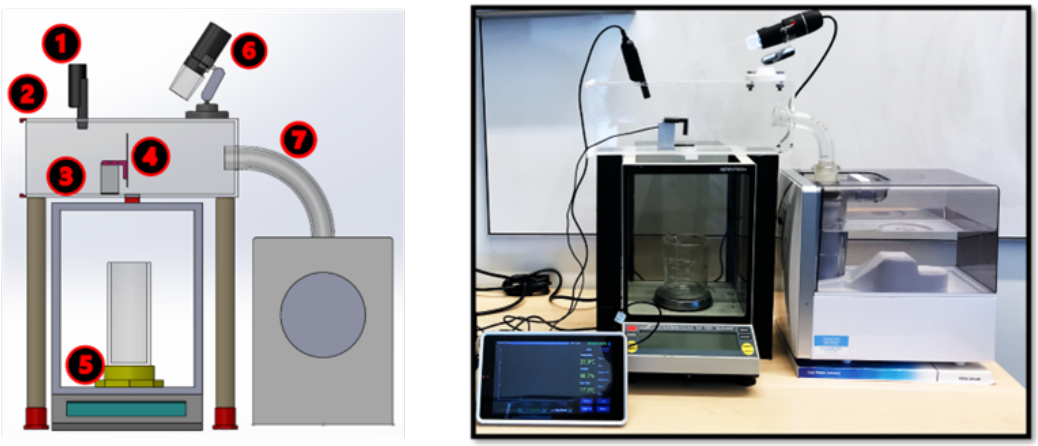

Figure 3.12 A. The model of water harvesting equipment, B. The homemade water harvesting setup.

The water harvesting experimental setup shown schematically in **Scheme 3.1** and **Figure 3.12** and the water capture/release dynamics on the hydrophilic/superhydrophobic surface were demonstrated by the experimental snapshots via the optical microscope (**Figure 3.13A**). Firstly, we recorded the water droplet behaviors on SHS-$HI_{10.0}$ during the water harvesting process. In contrast to the water adhesion on the macro/microscale hydrophilic structures, we observed that the hydrophilic CNC nanodomains could continually capture water from the humid air and nucleate tiny water droplets on the SHS-$HI_{10.0}$ surface (t=0~150 s). The presence of water nucleating sites was attributed to the abundance of surface hydroxyl groups on CNC, which induced the formation of hydration layers of individual cellulose nanocrystal. Owing to the strong cellulose–water interactions, there was surface-confined water generated on the surface of CNC under ambient humid conditions. This presence of confined water on nanocellulosic materials was observed by Beaumont and coworkers.[16] After the deposition of water droplets on the surface, the droplets interacted with nearby droplets that grew into large droplets at 260 ~280s (**Figure 3.13A (c-d))** via a process called static coalescence. With the droplet growth and coalescence, the merged droplet migrated to the surface (t=360s~365s), and continued to grow to reach a critical size, where the gravitation force ejected them from the surface, leaving behind a water-free area with no liquid residual (t=800s). Then, small droplets in the air re-deposited on the "refreshed" surface as shown in the panel h at 860s.

Accordingly, the droplet dynamic behaviors on hydrophilic/superhydrophobic surfaces during water harvesting process could be separated into two stages: deposition and transport**.**[34] The main mechanism that limit the efficiency of fog collectors was the trade-off between the deposition and transport stage, which corresponds to aerodynamic collection efficiency (η_p), deposition efficiency (η_a) and shedding efficiency (η_b).[35] These three parameters directly influenced the overall water harvesting efficiency (η) of the system, which was in proportional to water collection flux (V) (Eq. (3.1):

$V \sim \eta = \eta_p \cdot \eta_a \cdot \eta_b$ (3.1)

Specifically, we characterized the percentage of water droplets in the vapor stream colliding with the capture surface. This was related to the permeability of the collector, η_p was assumed to be unity since the substrate characteristics was not considered in this study. In terms of shedding efficiency, η_b was related to the ratio of the amount of collected water in the container to the total amount of captured water on the surface over a given time interval. From the observation of droplet behavior at transport phase, η_a was affected by the convective loss of deposited droplets during the transport process that was depended on two aspects: re-entrainment phenomena and residual water on the surface.[34] The re-entrainment was caused by the aerodynamic drag force (F_{drag}) that detached the captured water droplets from the surface and re-entrain them into the air flow before they reach a critical droplet size and fall into the container driven by gravity. The force balance acting on the deposited droplet on horizontal orientation was conducted as shown by the schematic on the droplet force analysis (**Figure 3.13B**), where the competition between the aerodynamically induced detachment force F_{drag} (Eq. (3)) and surface induced pinning force F_{pin} (also referred as horizontal adhesion force). When the small droplet collided with the surface, the water droplet adhered on the hydrophilic portion of the exposed sphere. F_{pin} below the droplet generated by capillary effect, was described by Equation (3.2)[36]:

$F_{pin} = 2\pi\gamma r_{drop} sin^2(\frac{\theta_{rec}}{2})$ (3.2)

$F_{drag}=\frac{1}{2}\upsilon^2\rho_{air}C_DA$ (3.3)

where γ was water surface tension, r_{drop} was the radius of droplet, θ_{rec} was receding angle, υ was air flow velocity, ρ_{air} was humid air density, C_D was drag coefficient, A was the projected area of droplet. The initial droplet size captured from the vapor (r_{drop}=12 μm) only received little resistance that corresponded to a small F_{drag}~ 0.14 μN. On SHS-$HI_{10.0}$ surface, before the droplet size increased to ~5.4 mm **(Figure 3.13C)**, the pinning force exceeded the drag force on the deposited water,[36] and re-entrainment of the droplet could be minimized when the $F_{drag} < F_{pin}$. Otherwise, droplet re-entrainment was expected in the region when the drag force $F_{drag} > F_{pin}$. According to Equation (3.2), receding contact angles as a key parameter influenced the F_{pin} values and further determined the droplet re-entrainment region. To avoid adverse impact of convective loss of deposited droplets during the transport process, the surface wettability should be tuned to accelerate the droplet transport which further reduce the critical droplet self-removal size (r_c).

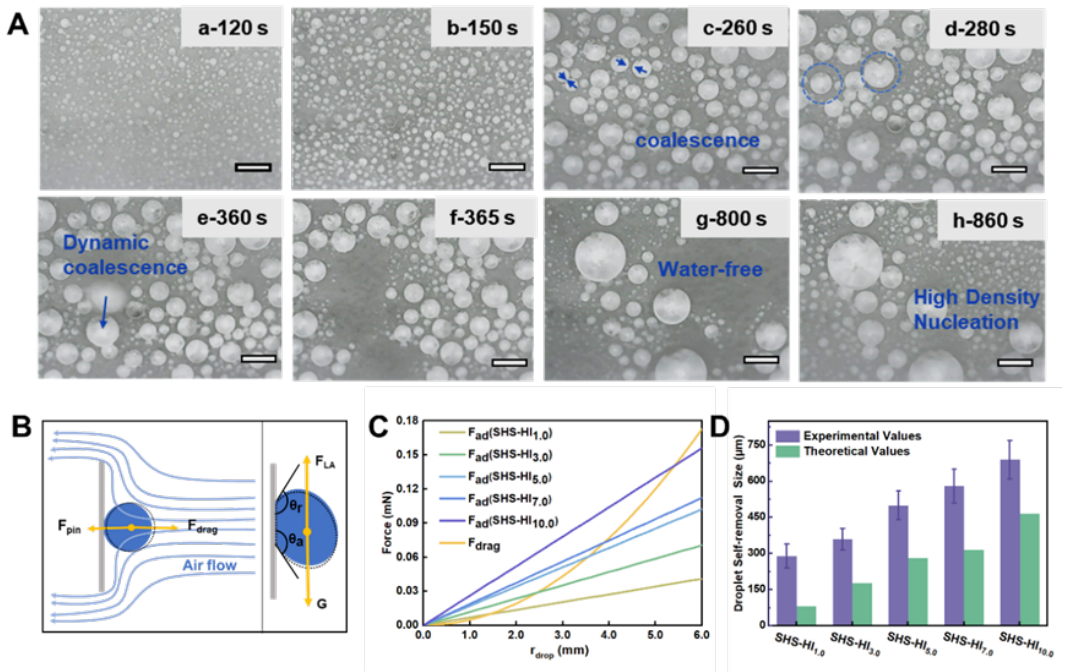

Figure 3.13 A. droplet dynamic behaviors on SHS-$HI_{10.0}$ surface at different time interval (scale bar=200 μm), B.(left) The force analysis of droplet on horizontal orientation induced by drag force and pinning force, (right) The force analysis of droplet on vertical orientation induced by lateral adhesion force and gravitational force, C. The balance between drag force and pinning force varied by the collected droplet size, D. The droplet self-removal size was observed by optical microscopy compared with the theoretical values.

In this study, the superhydrophobic surface decorated hydrophilic nanostructure was used to address this problem. According to the vertical force balance (**Figure 3.13B right**), the lateral adhesion force (F_{LA}) and gravitational force (G) were the dominant force for droplet dynamics on the substrate. In particular, the lateral adhesion force represented the force that hindered the movement of the droplet, which was attributed to the contact angle hysteresis.[37] The superhydrophobic surface enhanced the droplet dynamics by controlling the critical droplet self-removal size since the superhydrophobic surface with low CAH reduced the resistance for sliding. The gravitational force counteracted the lateral adhesion force and accelerated the droplet motion[38] as described by Eqs. (3.4) and (3.5).

$$G = \rho_{drop} g V \quad (3.4)$$

$$F_{LA} = \frac{24}{\pi^3} \gamma r_{drop} (\cos\theta_{rec} - \cos\theta_{adv}) \quad (3.5)$$

where ρ_{drop} was the density of water, g was the constant of gravity, V was the volume of the spherical cap-shaped water droplet, and γ was the surface tension (γ= 0.0728 N m^{-1} for water). If the lateral adhesion force was smaller than the gravitational force, the droplet would drain off from the surface, leading to a fresh unoccupied area for the next water deposition cycle. We could estimate the threshold of the critical droplet self-removal size (r_c) from the balance of these two

forces (Eq. (3.6)),

$$r_c = \sqrt{12\gamma(\cos\theta_{rec} - \cos\theta_{adv})/\pi\rho_{drop}gB(3+B^2)} \quad (3.6)$$

The theoretical r_c values of SHS-HI_m surfaces were all smaller than r_{drop} for each of the surface, ranging from 66 μm ~ 217 μm, which suggested that the water droplet adhered to the surface and grew rapidly into the critical droplet suitable for self-removal before the drag force drawn the droplet back into the air (**Figure 3.13D**). Compared to experimental images, the real critical droplet self-removal size displayed a slight fluctuation but possessed a similar trend as the theoretical results for r_c ranging from 120 μm ~ 650 μm. Thus, the shedding efficiency could be assumed to be 1 for our SHS-HI_m surfaces, while the water deposition performance played a key role in influencing the overall water harvesting efficiency ($\eta \sim \eta_a$).[39] However, the HS-$HI_{10.0}$ with insufficient surface topography design would lead to surface flooding phenomenon after prolonged water harvesting (**Figure 3.14**). The water stains on the surface generated a lower shedding efficiency (<1) compared to SHS-HI_m , further influencing the water harvesting efficiency.

The mass of water collected was recorded for three comparative surfaces, where the mass of water collected profiles described the water collected on the surface and water transport to the container respectively. Firstly, the slope of water deposition on HS-$HI_{10.0}$ was smaller than SHS-$HI_{10.0}$ surface, indicating that the water deposition rate was lower. This is attributed to the lower nucleation sites on the HS-$HI_{10.0}$ compared to the SHS-$HI_{10.0}$ surface. The water collection profile in **Figure 3.14 A1** demonstrated the SHS-$HI_{10.0}$ surface possessed many water nucleating sites compared to the other two surfaces, which agreed with the sharp slope of the water collected profile. Additionally, the droplet collected on the SHS-$HI_{10.0}$ surface displayed as spherical shape (**Figure 3.14 A2)** due to its superhydrophobicity, while non-spherical droplets **(Figure 3.14 B2)** were present on HS-$HI_{10.0}$ surface and the water droplets spread on the HI surface **(Figure 3.14 C2**). Thus, the SHS-$HI_{10.0}$ surface could accommodate large amounts of tiny spherical droplets in same area. Following the growth of the water droplets on the surface, more spherical water droplets were deposited on the surface that generated the largest water collection mass (0.93 g) compared to the HS-$HI_{10.0}$ surface (0.58 g) and HI surface (0.39 g). The water droplets rapidly coalesced with the neighbouring droplets on the SHS-$HI_{10.0}$ surface due to the high droplet surface coverage and grew into a large critical size. Then the droplets were removed from the SHS-$HI_{10.0}$ surface and new nuclei were generated on the same area as shown in **Figure 3.14 (A2**, **B2 and C2)**. In contrast to SHS-$HI_{10.0}$ surface, the water droplets took a long time to grow into a critical size on the HS-$HI_{10.0}$ surface and HI surfaces. In addition, the wetting state on the HS-$HI_{10.0}$ and HI surface would produce water stains on the surface after the water droplets were detached form the surface. As the water harvesting progressed, the water droplet collection would change into a film collection, which led to a low water harvesting efficiency.

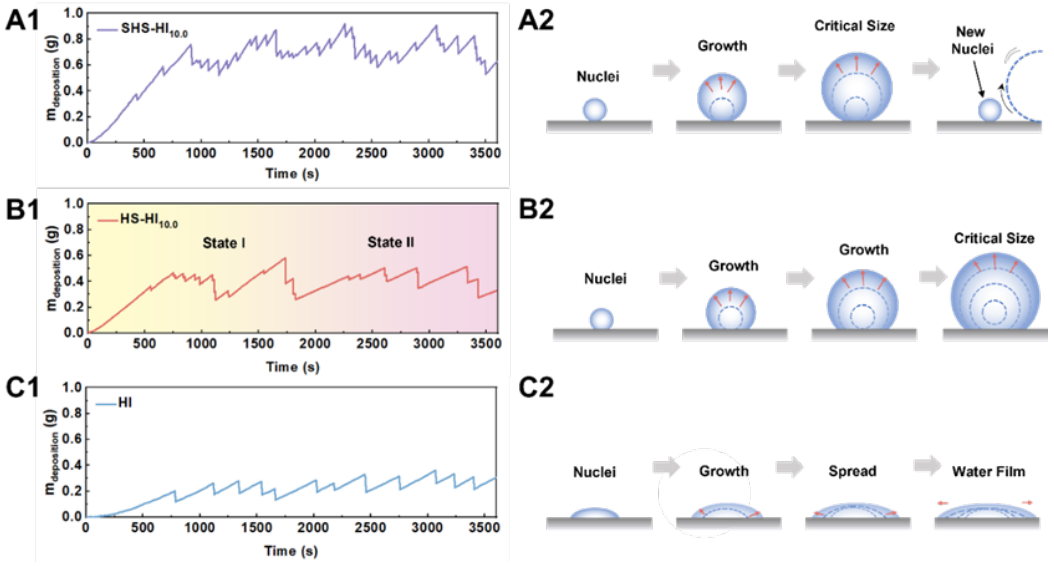

Figure 3.14 Water deposited on the surface recorded by mass of water collected over time: A1. SHS-$HI_{10.0}$, B1. HS-$HI_{10.0}$, C1. HI; Droplet dynamic behavior during water deposition process: A2. SHS-$HI_{10.0}$, B2. HS-$HI_{10.0}$, C2. HI.

The deposition efficiency, a key parameter to evaluate water deposition performance defined as $\eta_a = A/A_0$, where A_0 was the water collection area and A was the area occupied by the water droplets. Furthermore, the deposition rate (V_d) was another parameter that described the efficient water deposition mass change on the surface at a certain time interval, indicating the water capturing capability of each surface. This parameter represented as $V_d = m_d/t_d$, where m_d was the mass of efficient deposited droplets and t_d was the time interval.

With regards to the water harvesting mechanism on our surfaces, the droplets deposition process has a significant impact on the water harvesting efficiency. Herein, the hydrophilic nanodomains acting as the nucleation sites activated the small droplet formation during the deposition process. To promote the water harvesting efficiency on the SHS-HI_m, we investigated the influence of CNC nanodomains wettability and density working on the droplet movements on each surface.

3.5.2 Tunning CNC nanodomain hydrophobicity

Here, we investigated the influence of hydrophobicity of the nanostructure during the deposition process. The spray-assisted surface engineering offered a convenient approach to tailor the nanoscale hydrophobicity. The morphology of CNC/paraffin emulsion particles was previously described, depicting the coating of hydrophilic CNC particles on the surface of micron-size paraffin spheres. Thus, the hydrophobicity of CNC nanodomains covering the outer surface can be regulated by the fluorine modification before spray coating. In this study, the emulsion droplets were treated with 1H,1H,2H,2H-perfluorodecyltrichlorosilane (FDTS) via a liquid phase deposition (LPD)[40] to coat the rod-like CNC with fluorine molecules for preparing F-emulsion particles (**Figure 3.15A**). The deposited fluoroalkyl groups could be clearly resolved on SHS-$HO_{10.0}$ via the significantly

strong F peak in the XPS spectra (**Figure 3.15B**).[41] Using these two emulsion particles with distinct hydrophobic nanodomains, the hydrophilic/superhydrophobic surface (SHS-$HI_{10.0}$) and superhydrophobic surface (SHS-$HO_{10.0}$) were constructed using the spray coating process.

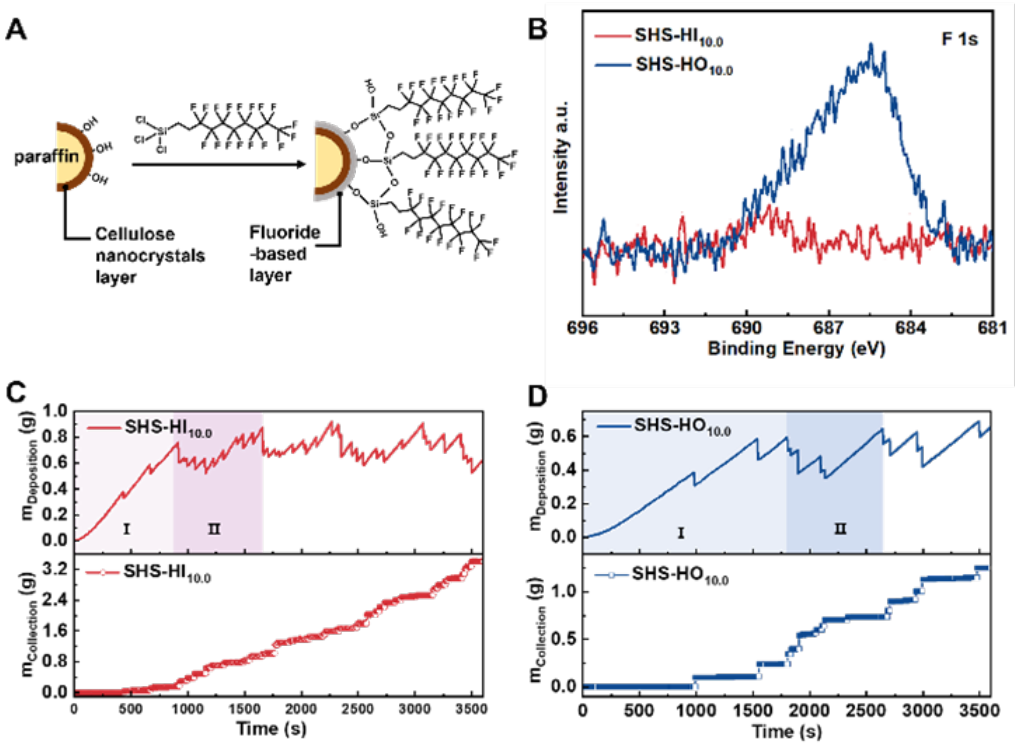

Figure 3.15 A. Fluoride modification on SHS-$HI_{10.0}$ via a liquid phase deposition, B. F characteristic XPS spectra for the layers of SHS-$HI_{10.0}$ and SHS-$HO_{10.0}$, C. SHS-$HI_{10.0}$ surface and SHS-$HO_{10.0}$ surface: water deposition weight on the tested surface showed on top figure and water collection weight gathered in the tank showed on bottom figure.

To examine the water harvesting performance, the droplet behaviors on SHS-$HI_{10.0}$ and SHS- $HO_{10.0}$ surfaces were recorded in an optical microscope at three representative stages, droplet deposition, growth and coalescence, transport stage, under the same testing conditions (ambient temperature was 25°C and relative humidity was 80%) (**Figure 3.15C**). In the initial deposition stage, the water droplet transported by air flow approached the vertical surface, where some of the droplets collided and deposited on the surface. The snapshots revealed that the droplet number grew incrementally at a rapid rate on SHS-$HI_{10.0}$ from the start to 200s compared to SHS-$HO_{10.0}$. This was caused by the enhanced surface free energy of SHS-$HI_{10.0}$ surface (**Table 3.2** and **Figure 3.16**) that generated strong interaction force with the small water droplets via hydrogen bond that minimized kinetic energy barrier for droplet nucleation process.[42–44] At that time, the low surface energy of SHS-$HO_{10.0}$ surface (**Figure 3.15D**) delayed the water deposited onset times, since the droplet cannot adhere to the surface owing to its excellent water repellent characteristics.

Table 3.2 Components of Surface Energy for SHS-$HI_{10.0}$, SHS-$HO_{10.0}$ and Paraffin wax surfaces

Surfaces	Contact Angle (°)		Surface Free Energy (mJ/m²)		
	Water	Methylene iodide	γ_s^d	γ_s^p	γ_s
SHS-$HI_{10.0}$	151	68	29.5	8.5	38.0
SHS-$HO_{10.0}$	163	109	7.2	2.3	9.5
paraffin wax	108	66	25.4	0	25.4

Fowkes[43] suggested that the total free energy (γ_s) at the surface was composed of various inter-molecular attractive forces at the interface that comprised of both polar and dispersive components, which could be treated independently (the polar-dispersive interaction can be neglected). The surface free energy of the three surfaces was estimated based on the contact angle data and fitted according to the Owens, Wendt, Rabel and Kaelble (OWRK) method as shown below (the calculation detail was added to the supporting information).

$$1+\cos\theta = 2\sqrt{\gamma_s^d}\left(\frac{\sqrt{\gamma_l^d}}{\gamma_{lv}}\right) + 2\sqrt{\gamma_s^p}\left(\frac{\sqrt{\gamma_l^p}}{\gamma_{lv}}\right)$$

where θ referred to the contact angle of liquids, γ_{lv} referred to the free energies of the liquid and solid against their saturated vapor, γ_l^d and γ_l^p referred to the free energy of liquid, where the superscripts p and d were the polar and dispersion force components respectively. and γ_{lv}, γ_l^d and γ_l^p were published in many references of different liquids[44-45].

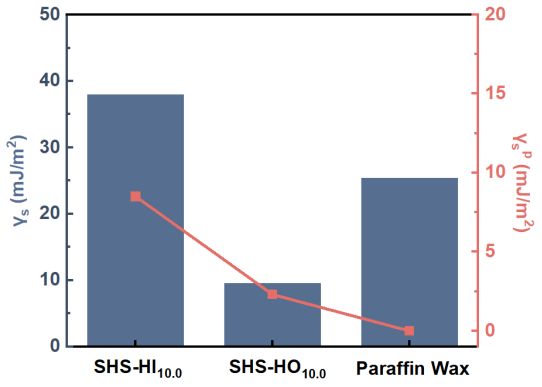

Figure 3.16 Surface free energy and dipolar-dipolar interaction force of different surfaces.

As can be seen from the calculated results summarized in **Figure 3.17**, SHS-$HI_{10.0}$ showed a higher static contact angle (CA~151°) but the overall surface free energy was much larger (38.0 mJ/m^2) compared to pure wax surface (25.4 mJ/m^2). This could be attributed to the increased dipole-dipole interaction between solid and liquid (from 0 mJ/m^2 to 8.5 mJ/m^2). In this test and our study, the

dipole-dipole interaction was mainly derived from the hydrogen bonding between the solid and water droplet. For the SHS-$HI_{10.0}$, the CNC coated on wax particle would generate strong interaction with the small water droplet via hydrogen bond, resulting in a high nucleation density. Besides, the enhanced surface free energy of SHS-$HI_{10.0}$ surface also reduced the kinetic energy barrier for the droplet nucleation process. Nevertheless, if the surface functional groups were changed from -OH to -CF_3 by grafting FDTS, a large reduction was observed for SHS-$HO_{10.0}$ both in the polar and dispersive energy due to the stable -CF_3 covalent bond, causing a low molecular attraction during water harvesting. Thus, the deposition rate would become slow due to the large kinetic energy barrier needed to be overcome on the SHS-$HO_{10.0}$ surface. All these results demonstrated the important role of hydrophilic CNC on the high-water harvesting performance. The tremendous hydrophilic domains could offer the large density of nucleation sites with higher surface free energy during water harvesting, which increased the water harvesting performance.

When the droplet approached and collided with the surface, the drag force would transport the droplet to the air stream before they could attach on the low adhesion superhydrophobic surface.[36] Repeated collisions led to continuous deposition, followed by droplet growth and coalescence in the second stage. After the initial deposition stage, the SHS-$HI_{10.0}$ surface was covered with high-density small water droplets that acted as nucleation sites caused by the water affinity of CNC nanostructure. Compared to the SHS-$HI_{10.0}$ surface, there were some sporadic water droplets scattered on SHS-$HO_{10.0}$ surface, which did not promote droplet growths. **Figure 3.17C and 3.17D** described the time evolution of droplet coverage (P(x)) on these two surfaces, where it was evident that the droplet coverage on SHS-$HI_{10.0}$ was higher with a greater increase than on SHS-$HO_{10.0}$, where the maximum P(x) was 62%. When the droplets grew larger, the neighbouring water droplets merged and coalesced that was continuously triggered by the exclusion of numerous mobile droplets from the surface. In the meanwhile, the average droplet size deposited on the SHS-$HI_{10.0}$ surface increased from 100 s to 300 s, while it only displayed a slight increase for the SHS-$HO_{10.0}$ surface. This confirmed that the deposited droplet density had a large impact on the second droplet deposition and coalescence process. The results demonstrated that SHS-$HI_{10.0}$ with hydrophilic nanodomains could continuously trapped water from humid air while the deposited water was re-entrained to the vapor phase.[37] However, the high affinity for capturing water could adversely affect the transport process, which hindered the water droplet sliding from the surface. The critical droplet self-removal size on SHS-$HI_{10.0}$ surface was 650 μm, which was larger than for the SHS-$HO_{10.0}$ surface (502 μm), due to the lateral adhesion force of the surface. Although the critical droplet self-removal size was reduced, the onset time for the droplet sliding from the surface occurred earlier than SHS-$HO_{10.0}$ surface, due to the rapid droplet growth into the critical onset size. Overall, the hydrophilic nanodomains on the surface displayed excellent water capture characteristic and enhanced water deposition efficiency. In comparison, the low lateral adhesion force of SHS-$HO_{10.0}$ possessed a high droplet mobility that generated a large nucleation barrier. Thus, the durable water harvesting necessitated the balance of contrasting wetting features and the deposition enhancement and water

transport.

To quantify the water collection rate on the surface, the water droplet weight change deposited on the surface and collected in the container was continuously measured. **Figure 3.17A and 3.17B** presented the effect of nanodomains hydrophobicity of water harvesting surfaces (SHS-$HI_{10.0}$ and SHS-$HO_{10.0}$) by examining the weight of water collected as a function of time. There was an initial growth period signifying the deposition and capture of water droplets (Region I), where SHS-$HI_{10.0}$ displayed a shorter (435 s) to achieve the initial deposition phase before the sliding stage commenced. The deposition rate for the weight of deposited water droplets was determined from the slope of deposited mass, which is summarized in **Figure 3.15C and 3.15D**, where the deposition rate of SHS-$HI_{10.0}$ was 3.168 L/h larger than SHS-$HO_{10.0}$, demonstrating the SHS-$HI_{10.0}$ was more efficient in capturing water on its surface. This is due to the hydrophilic CNC layer being shielded by the fluorine molecules with ultra-low surface energy on SHS-$HO_{10.0,}$ a surface that impeded the droplets' interaction and nucleation on the surface.[45]

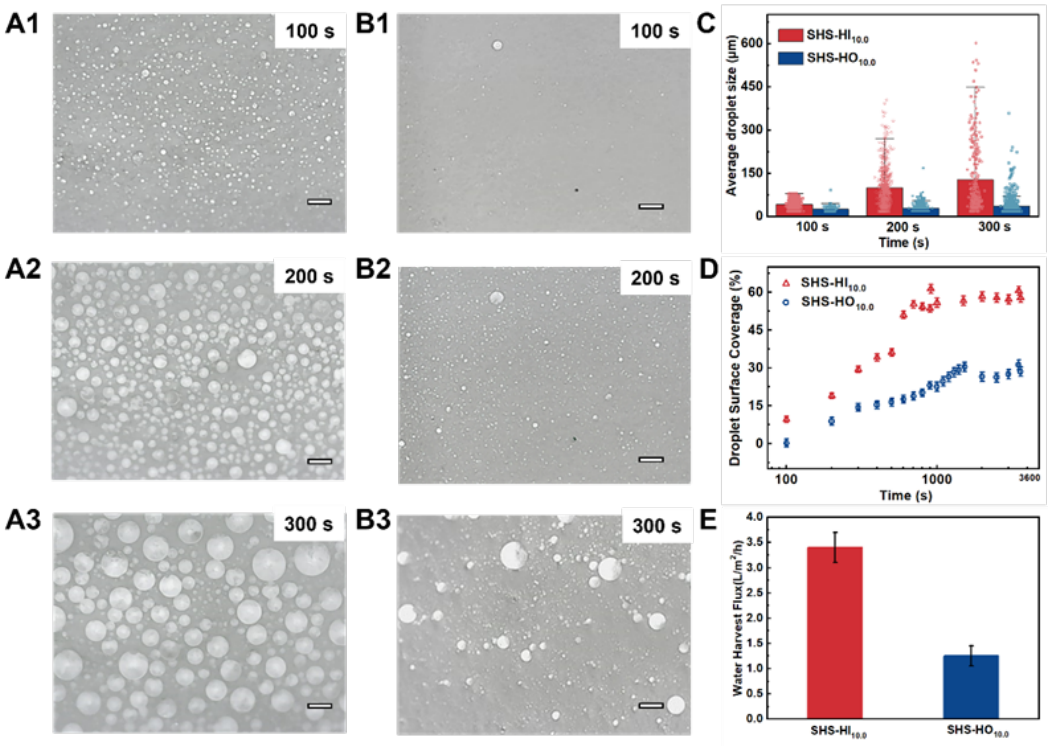

Figure 3.17 A. water droplet deposited on SHS-$HI_{10.0}$ surface (scale bar=200 μm), B. water droplet deposited on SHS-$HO_{10.0}$ surface (scale bar=200 μm), C. Average Droplet size on two surfaces, D. The droplet surface coverage on two surfaces during water harvesting with time evolution, E. Water harvesting flux of SHS-$HO_{10.0}$ surface and SHS-$HI_{10.0}$ surface

As for the water transport process, the water leaving the surface was followed by a cyclically re-deposition process, where the droplet merged and coalesced (Region II). The cycling time was associated with the water harvesting rate, and it reflected on the surface's capability for nucleation and re-nucleation of the water droplets. In comparison, the cycling time of SHS-$HO_{10.0}$ was approximately two-times longer than SHS-$HI_{10.0}$, reflecting its lower efficiency resulting from the

trade-off between the water nucleation and removal process.

Moreover, the maximum nucleation content of the water droplet was a key parameter to evaluate the water harvesting rate, because it provided the information on droplet surface coverage and nucleation density during the whole process (**Figure 3.17D**). It showed the maximum nucleation mass of SHS-$HI_{10.0}$ was 0.93 g while the maximum droplet surface coverage was 62%, confirming that the hydrophilic CNC nanodomains on surface could enhance the nucleation density and further improve the water harvesting rate.

Furthermore, the water harvesting capability was demonstrated by the amount of water collected in the tank. SHS-$HI_{10.0}$ possessed a water collection flux of 3.402 L/m^2/h, which was about 3 times greater than SHS-$HO_{10.0}$ of 1.25 L/m^2/h. The results demonstrated that the combination of a superhydrophobic hierarchical surface with hydrophilic nanoscale domains led to an enhanced performance in water collection (**Figure 3.17E**). Through the comparisons in the water nucleation/detachment stages which showed that the hydrophobicity of nanodomains strongly influenced the water nucleation rate, indicating that the cyclical water capture could be predominately managed via controlling the contrasting wetting patterns.

3.5.3 Tunning hydrophilic CNC nanodomain density

The superhydrophobic surface with contrasting wettability nanodomains enhanced the water harvesting performance, where the hydrophilic nanostructure played a key role in accelerating the deposition rate.[46] To elucidate the underlying physics of droplet nucleation dynamics on a surface with hydrophilic nanostructure, we investigated the correlation between deposition rate and the hydrophilic nanodomain density. The emulsion templated surface engineering proposed in this study offers a convenient approach to tailor the hydrophilic nanodomain density on the surface and the corresponding microstructure geometry, which can be regulated by tunning the concentration of CNC in the synthesis of Pickering emulsion particles.[47] Different hydrophilic nanodomain density led to a substantial variation of water droplet behaviors on the surface during the water harvesting process. For the as-prepared hydrophilic/superhydrophobic surface (SHS-HI_m) constructed by the emulsion particles covered with different density of hydrophilic nanostructure, we compared their water droplet deposition/transport performance under the same environmental conditions (**Figure 3.18**).

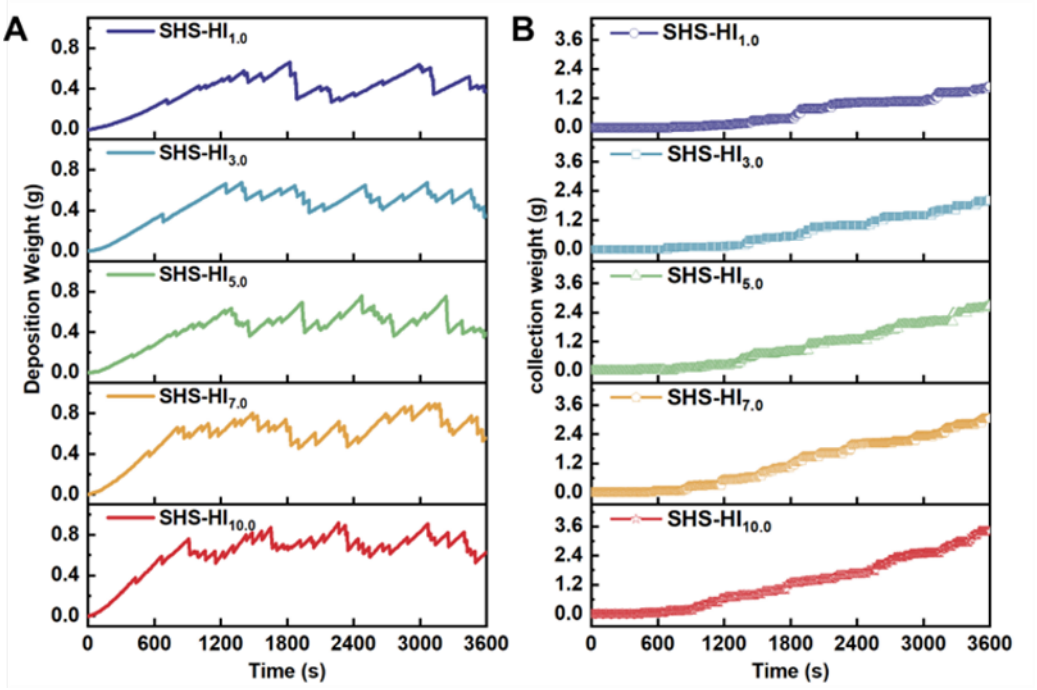

Figure 3.18 A. The weight change of water depositing on SHS-HI_m surfaces during 1 h water harvesting process, B. The weight change of water transport from surface to the collected container during 1 h water harvesting process.

To optimize droplet nucleation dynamics on a surface with contrasting wettability, we investigated the correlation between the fraction of droplet coverage and the hydrophilic nanodomain density (C). As shown in **Figure 3.18**, water droplets deposited on the surface and the mass accumulated showed a higher increase for the SHS-$HI_{10.0}$ surface. After the deposited water droplets growth and coalescence, the deposition mass could achieve a maximum value of 0.93 g with a corresponding droplet coverage of 62%. **Figure 3.19A** illustrated the maximum deposition mass of the other four surfaces was in order of SHS-$HI_{3.0}$ (0.68 g) <SHS-$HI_{5.0}$ (0.74 g) <SHS-$HI_{7.0}$ (0.88 g) <SHS-$HI_{10.0}$ (0.93 g), while the deposited droplet coverage proportion showed similar increasing trend from 32% to 62%. The results implied that m_d was proportional to P(x) because all the droplet possessed spherical morphology on the superhydrophobic surface, where the same mass droplet corresponded to a similar size. In addition, the droplet shape affected the carrying capacity of the same surface area and critical removal size of the surface.[48] Thus, these two parameters could describe the capturing water capability of the surfaces, where the SHS-$HI_{10.0}$ possessed high density droplet coverage. Combined with the deposited mass, the SHS-$HI_{10.0}$ possessed extraordinary water capture performance compared to the other four surfaces with high density droplet coverage and fast deposition rate. Interestingly, the density of hydrophilic nanostructure on SHS-HI_m surfaces displayed the same trend for the deposition rate where the large amounts of hydrophilic nanodomains on the surface accelerated the deposition rate. The results were assumed to be related to the increased droplet deposition sites and improved surface adhesion on the surface generated by

the hydrophilic CNC nanostructure. Since the hydrophilicity of the nanodomains possessed high surface energy and water affinity, the droplet deposited nuclei tended to capture and adhere on the surface when water vapor collided with the surface.[24,49] Thus, with increasing hydrophilic nanodomain density, the water droplets could be easily intercepted by the hydrophilic/superhydrophobic surface and scattered closer on the surface, leading to a fast deposition rate.

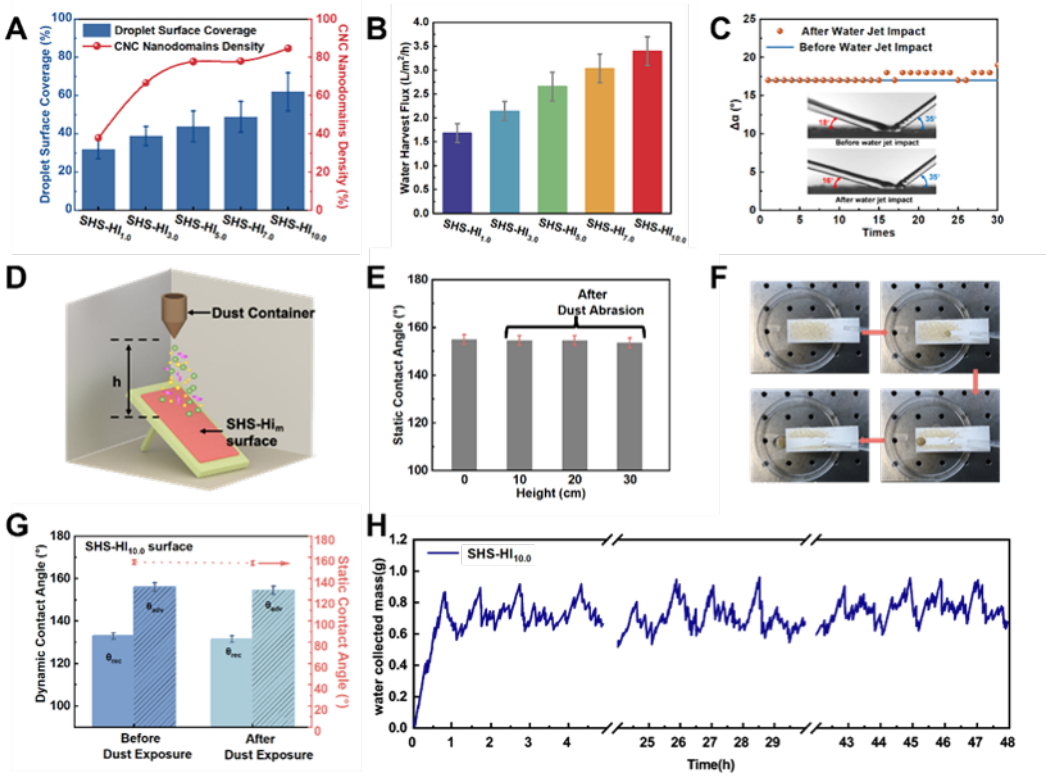

Figure 3.19 A. The relationship between droplet surface coverage and CNC nanodomain density, B. water harvesting flux on SHS-HI_m surfaces, C. high-speed water jet impact measurement: the change of angle (Δα) when the water jet (at a flow velocity of 10 ml/min) was deflected by the superhydrophobic surfaces before and after water jet impact ($\Delta\alpha = \alpha_{incident} - \alpha_{deflected}$), D. Dust abrasion measurement, E. Static water contact angle of SHS-HI10.0 surface before and after dust abrasion from different height, F. Self-cleaning characteristic of SHS-HI10.0 surface characterized by dust removal measurement, G. Changes in the dynamic contact angles and static contact angles before and after dust exposure, H. long-time (48 h) water harvesting durability test of SHS-HI10.0 surface.

Based on the water harvesting experimental observations, the droplets were re-deposited on the refresh area after water transport. Thus, the cyclical water harvesting time could be reduced by accelerating the droplet transport stage. The critical droplet self-removal size suggested that SHS-$HI_{1.0}$ with rapid water refreshing rate favored droplet self-removal at 120 μm, showing the same trend with the theoretical self-removal size. While the surface adhesive kept increasing to 107.6 μN,

the critical self-removal size was observed at 650 μm on SHS-$HI_{10.0}$ that the transport onset time of each droplet was delayed. However, the SHS-$HI_{10.0}$ still showed excellent water harvesting efficiency because its transport performance was negated by high density re-nucleation rate on the water-free regions. Owing to its superhydrophobicity, SHS-$HI_{10.0}$ successfully maintained dropwise collection rather than filmwise collection (e.g., HS-$HI_{10.0}$, HI). The presence of the hydrophilic nanodomains did not significantly hinder the droplet transport and instead, only slightly delayed the starting collection time (**Figure 3.20**). Moreover, the droplets swept away all adjacent droplets along their path and exposed the water-free area towards vapor, increasing deposition/re-deposition efficiency and further enhanced the overall water harvesting efficiency of SHS-$HI_{10.0}$.

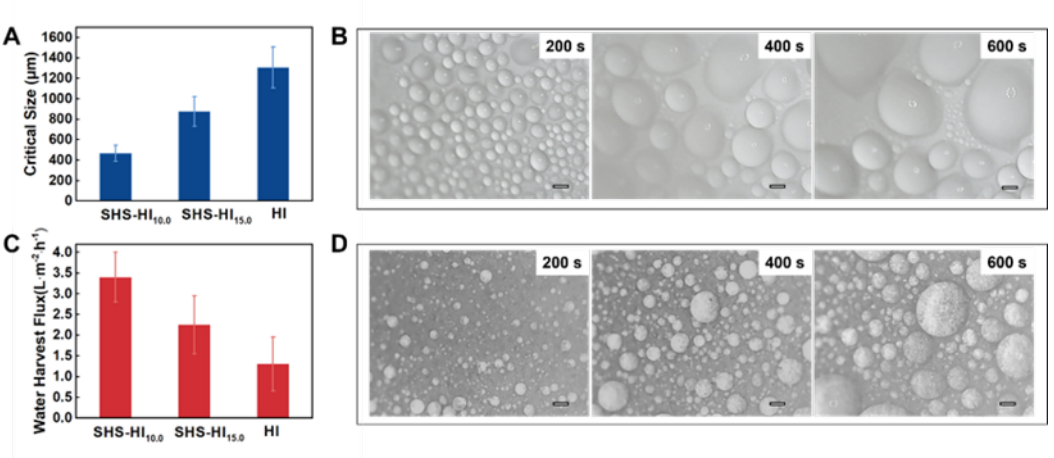

Figure 3.20 The controllable water harvesting experiment on hydrophilic surface (HI) and SHS-$HI_{15.0}$ surface: A. The droplet self-removal size on HI, SHS-$HI_{10.0}$, SHS-$HI_{15.0}$ surfaces, B. The droplet dynamic behaviors on HI surface during water harvesting process (t=200 s, 400 s, 600 s), C. Water harvest flux on HI, SHS-$HI_{10.0}$, SHS-$HI_{15.0}$ surfaces, D. The droplet dynamic behaviors on SHS-$HI_{15.0}$ surface during water harvesting process (t=200 s, 400 s, 600 s).

Therefore, for efficient water harvesting, the hydrophilic area fraction needed to be tailored to balance the droplet pinning and sliding effects. The water harvesting experiments performed on the HS-$HI_{10.0}$ (**Figures 3.21**) and SHS-$HI_{15.0}$ surface (**Figure 3.20**) were used as the reference to investigate their water harvesting performance. Although the same hydrophilic nanodomain density (C) was present on each building blocks, the lower roughness and surface area of the HS-$HI_{10.0}$ surface impeded the generation of water nuclei. Besides, the HS-$HI_{10.0}$ surface possessed a large RCA and CAH that gave rise to a large F_{pin} and F_{LA} that increased the resistance to the droplet mobility resulting in the residual water on the surface after the water droplet was detached from the surface. SHS-$HI_{15.0}$ possessed fast deposition rate, which was even higher than SHS-$HI_{10.0}$, because the hydrophilic nanodomains greatly increased the water affinity. However, the hydrophilic spots had strong affinity for the water droplets and hindered the droplet mobility, which delayed the water removal from the surface. Unlike HS-$HI_{10.0}$ and SHS-$HI_{15.0}$ with low deposition efficiencies and insufficient water transport characteristics, SHS-$HI_{10.0}$ decorated with the moderately hydrophilic

nanodomains could balance the trade-off between deposition enchantment and sustain a stable high water transport efficiency.

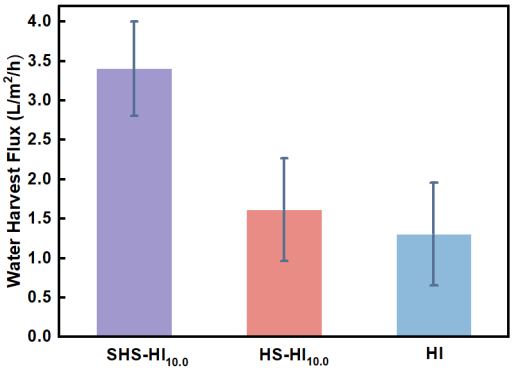

Figure 3.21 Water harvest flux on the surface: SHS-$HI_{10.0}$, HS-$HI_{10.0}$ and HI.

3.6 Surface durability for Water Harvesting

Durable water harvesting required tunning contrasting wetting features to strike a balance between nucleation enhancement and water transport efficiency. The hydrophilic/superhydrophobic surface of SHS-$HI_{10.0}$ exhibited excellent water harvesting efficiency. Besides surface chemistry, the robustness of the surface and physical characteristics of the substrates were two critical criteria that ensured its scalability for practical applications.

Owing to the phase change and adhesion properties of paraffin wax, the sprayed molten wax particles when cooled to solid particles would adhere strongly to substrates after the solvent removal and the robust surfaces were obtained. The mechanical robustness of our superhydrophobic surfaces was demonstrated by the high-speed impact of water jet (**Figure 3.19A**).[27,32] The water jet impact was tested for the durable water harvesting characteristics without water-flooding phenomenon may hinder the reuse of the substrate in high humidity environment.[32] As shown in **Figure 3.19B**, the surfaces maintained a static contact angle greater than 150° and the change of angle (Δα) remained constant even after 30 water jet colliding cycles. The SHS-$HI_{10.0}$ maintained its superhydrophobicity under extremely harsh conditions,[51] such as UV irradiation (**Figure 3.22A**), dust pollutants (**Figure 3.23 and 3.24**) and temperature difference (**Figure 3.22 B and C**). We further conducted the dust abrasion experiment and anti-soiling test as shown in **Figure 3.19D-G**. The results showed that the surface topography and wettability was not destroyed after dust abrasion, and it was reusable due to its self-cleaning characteristic. It suggested that the surface maintained a stable water harvesting efficiency confirming that it could be used for fog harvesting in outdoor environment.

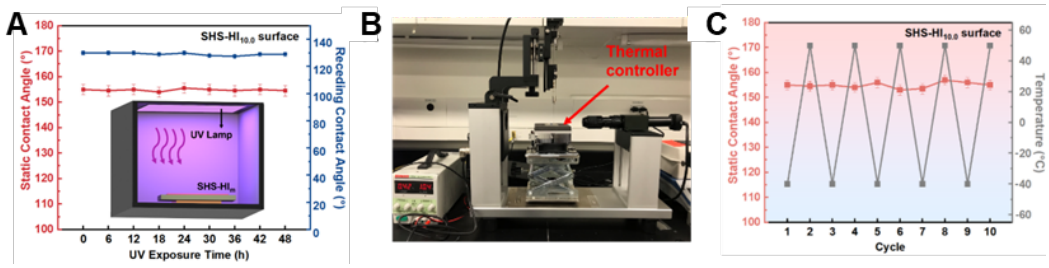

Figure 3.22 A. The static contact angle and receding contact angle of SHS-$HI_{10.0}$ surface exposed to UV light. Thermal stability of SHS-$HI_{10.0}$ surface: B. Illustration of water contact angle measurements controlled by a temperature controller, C. The static contact angle measured over many cycles of temperature change of -40 to +50 ºC.

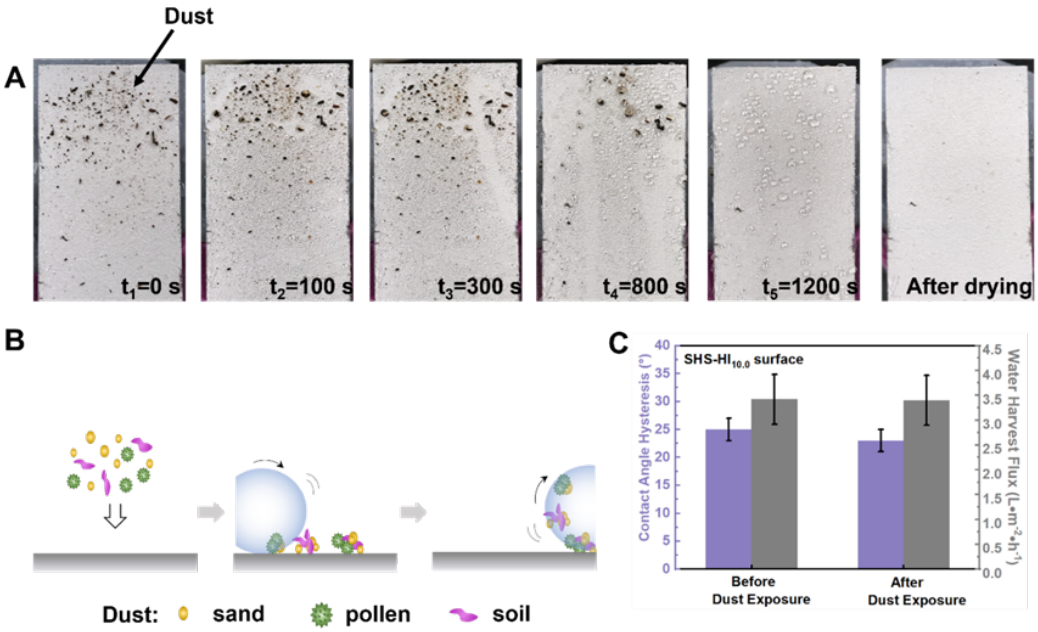

Figure 3.23 Dust removal by self-cleaning: A. Sequences photographs showing the fog deposited on the dust-polluted SHS-HI10.0 surface, B. Illustration showing the self-cleaning of the fog-harvesting surface, C. Contact angle hysteresis and water harvesting flux before and after dust exposure.

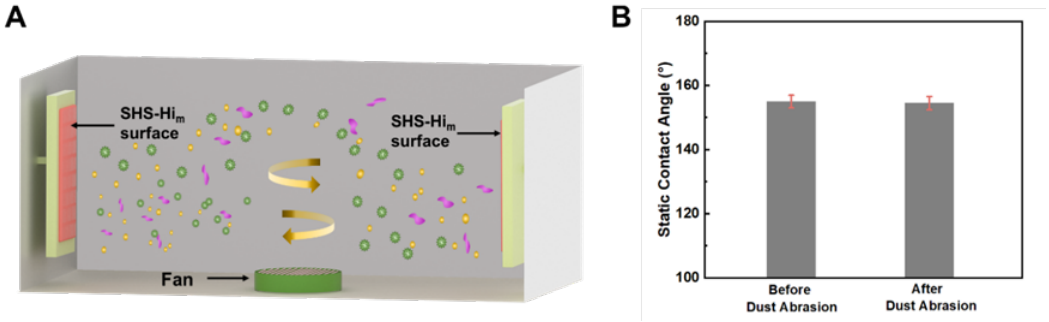

Figure 3.24 A. Dust strike and impinging Measurements B. Static water contact angle of SHS-$HI_{10.0}$ surface before and after dust abrasion.

To further demonstrate the steady-state water harvesting rate,[50,51] the SHS-$HI_{10.0}$ surface was tested in a standard testing chamber for 48 h. **Figure 3.19H** showed that the average water deposition rate remained constant at around as 3.363 L/m^2•h and the water harvesting performance remained fairly constant with similar deposition and drainage characteristic as that observed at the short-term test (**Figure 3.25**). The results confirmed that the surface would not succumb to flooding that destroyed the surface structure and reduce the water harvesting efficiency.[49] When the hydrophilic/superhydrophobic coating was applied on the mesh substrates, they performed an efficient water harvesting flux compared to other studies (**Figure 3.26**). Thus, in foggy weather conditions, incorporating a superhydrophobic surface with nanoscale hydrophilic topography would represent a highly promising strategy to enhance the water harvesting efficiency of existing water collection systems.

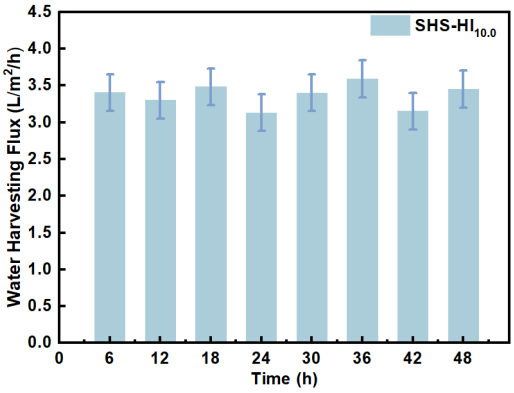

Figure 3.25 Water collection durability test on SHS-$HI_{10.0}$ surface. The water harvesting flux calculate every 6 hours

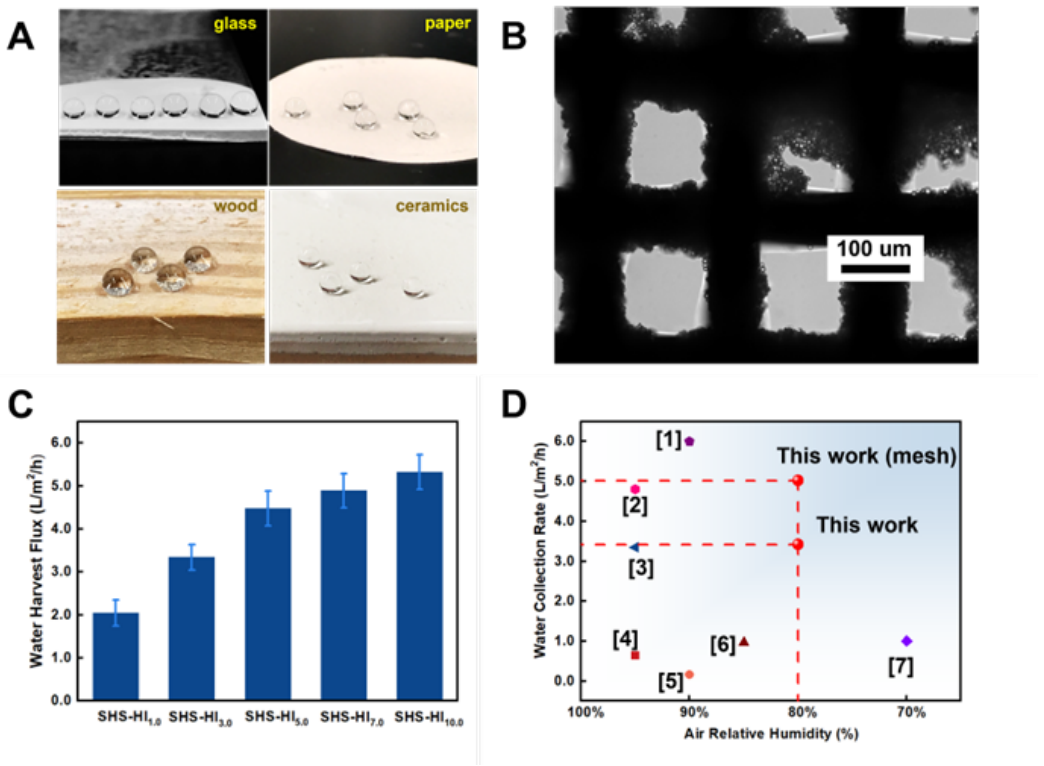

Figure 3.26 A. Superhydrophobic coatings on different substrates, B. The optical microscopic image of SHS-$HI_{10.0}$ coating onto stainless mesh, C. The water harvest flux on meshes coating with SHS-HI_m hydrophilic/superhydrophobic formulation, D. Water harvesting performance compared between this work and other published works[1–7].

3.6 Conclusion

In summary, we developed superhydrophobic surfaces with tunable hydrophilic nanodomains via a facile, sustainable and scalable approach. This nano-hydrophilic/superhydrophobic surfaces performed a stable high water harvesting efficiency through tunning the surface topography, balancing the trade-off between water deposition and transport, sustaining surface durability. Through experiments and modeling, we showed that the droplet deposition and removal rate could be manipulated by the hydrophilic nanodomains hydrophobicity and density. As a result of the continuous water capture on nanoscale hydrophilic patterns, the water collection rate was enhanced by more than 2-fold compared to lotus leaf-like superhydrophobic surfaces. We anticipated that our discovery of fundamentals in tunable water nucleation and scalable manufacturing technology will aid the development of water harvesting in drought-affected regions.

Chapter 4. Topographical design and Thermal-induced Organization of Interfacial Water Structure to Regulate the Wetting State of Surfaces

4.1 Introduction

Thermo-responsive polymer composites and coatings are a class of smart materials that find broad applications in wearable devices and drug delivery due to their switchable and programmable properties.[119] Particularly, the thermo-responsive behavior of polymers provides an effective strategy to design systems with tunable properties. These systems possess interesting physics associated with the conformational transition triggered by temperature that is still not completely understood.

Thus far, PNIPAM and $POEGMA_{188}$ are the two most widely studied thermo-responsive polymers due to their sharp thermal transition and their LCSTs being close to the body temperature. These transitions have been studied using many different techniques,[120] such as laser light scattering, fluorescence spectroscopy, turbidimetry, differential scanning calorimetry (DSC), infrared spectroscopy, nuclear magnetic resonance, and Raman spectroscopy, to understand the phase transition of thermo-responsive polymer in aqueous solutions. Two main conclusions were arrived from these experiments; coil-to-globule state of polymer and associated functional groups transition.[121] For thermal-responsive polymer grafted to bulk surfaces, the current understanding is that the wettability transition near the LCST depended on the exposed functional groups.[122] Nevertheless, the studies consistently claimed that the functionalized surface groups could only affect the water molecule directly in contact with or extremely close to (normally 1~2 nm) the interface.[123] Thus, fundamental understanding of how such short-range interactions influence the macroscopic wettability transition is necessary for the manipulation of the bulk surface wettability.

Lycopodium sporopollenin extine shell (L.SEC) microparticles have gained increasing attention for applications, such as drug carriers,[124] sensors, and soft robotics.[125] Owing to the unique morphology and versatile physical and chemical characteristics, L.SEC particles could be a good substrate for grafting thermo-responsive polymer brushes that offer us a flexible platform to investigate the polymer-water interactions. From the microscopic view, the grafting of thermo-responsive polymer brushes on rigid particles can enhance the structural stability that minimizes the aggregation of the polymer chains. Besides, the surface functionality of the L.SEC consisting of hemicellulose offers sufficient amounts of chemical reactive sites (hydroxyl groups) for the grafting of the polymer chains. Most importantly, these microparticles are naturally produced in plants, and hence they are renewable and abundant, are a good source of materials for a variety of applications. Herein, we prepared thermally-induced surfaces by grafting two representative thermo-responsive polymers, poly(N-isopropylacrylamide) (PNIPAM) and poly(oligoethylene glycol)methyl ether acrylate ($POEGMA_{188}$) onto pollen microparticles with uniform morphology and roughness to investigate the water-surface interaction at different length scale. We demonstrated that the temperature-dependent interfacial properties of the polymer grafted L.SEC particles are associated

with the interaction between interfacial water film and apolar/polar groups of the polymer brushes, as revealed by in situ Raman spectra and thermodynamic analysis. Additional rheological measurements suggested that the transformation of interfacial water structure near the polymer brushes can be amplified on each polymer grafted L.SEC particle due to the rearrangement of the hydrogen bonding network during the LCST transitions. The formation of distinct hydrogen bonding network at microscale on rough surfaces can effectively induce the bulk surface wettability transition, which can be elucidated by surface free energy calculations, 3D confocal microscopy imaging and liquid contact angles under different environmental conditions. This study provides fundamental insight and understanding into the relationship between the interfacial water structure and surface wettability transition. Furthermore, these findings offer a new route to design thermo-responsive colloids and surfaces (or other stimuli-responsive systems) for a wide range of applications, such as liquid-gated multiphase separation,[126] water purification and harvesting,[127] biomedical devices,[128] printing.[129]

4.2 Materials and method

Materials

Lycopodium clavatum pollen (Flinn Scientific Canada Inc.), Lotus pollen, N-Isopropylacrylamide, di(ethylene glycol) methyl ether methacrylate, cerium(IV) ammonium nitrate (CAN), potassium hydroxide, phosphoric acid, acetone, ethanol, Rhodamine B were used as received from Sigma-Aldrich. All chemicals were used without additional purification, unless stated otherwise. Milli-Q water (resistivity of 18.2 MΩ cm) was used to prepare the aqueous dispersions.

Preparation of Lycopodium sporopollenin extine shell (L.SEC)

Natural Lycopodium clavatum pollen grains were defatted to remove lips and intine materials yielding indestructible, ultra-tough, defatted pollen microcapsules. For this purpose, Lycopodium clavatum pollen granules (50 g) were refluxed in acetone (300 mL) for 3 h in a round-bottom flask under magnetic stirring (50°C, 350 rpm). The defatted pollen grains were recovered via vacuum filtration for intine materials extraction. This process involves pollen shell extraction and subsequent incubation in an alkaline medium, where the defatted pollen was treated with 10 wt vol%$^{-1}$ potassium hydroxide (KOH) at 80°C and stirred for 2 h to remove its internal cytoplasmic content. KOH-treated spores were next subjected to acidolysis by stirring them in 200 mL of 85% (w w^{-1}) phosphoric acid (H_3PO_4) at 60 °C for 3h. After the acid treatment, the spore solution was cooled, extensively washed with water, acetone and ethanol, and filtered. Finally, H_3PO_4-treated spores were dried at 60 °C for 24 h in an oven, and the weight of the final dried spores was measured L.SEC samples after each chemical treatment step were recovered for analysis. All the spores were stored at room temperature before their use in the experiments.

Preparation of thermal-responsive L.SEC-based superhydrophobic formulation

First, 100 mL of L.SEC (0.1 g) aqueous dispersion was mixed with 1.0 mL 70 wt% HNO_3 in a three-neck flask under magnetic stirring and degassed with nitrogen flow. The reaction was allowed to proceed under stirring in an ice bath for 30 min before the polymer grafting. Next, cerium (IV) ammonium nitrate (CAN) (0.05 g 0.10 mmol) was added to the reaction flask forming radical sites on the hydroxyl groups on L.SEC through the reduction of ceric ions. NIPAM monomer (1.13 g, 10.0 mmol) was introduced to initiate the polymerization and the solution was kept in an ice bath under slow magnetic stirring for a fixed time period (ranging from 1 h, 2 h, 3 h, 4 h, 6 h). Finally, the product was dialyzed against deionized water until the measured water conductivity remained constant. The reaction was repeated with various amounts of the CAN and NIPAM grafted moieties. The as-prepared PNIPAM modified L.SEC microparticles designated as PNm-g-L.SEC where m corresponds to monomer mass changing from 5, 10, 20, 40 mmol (initiator/monomer ratio-m is constant). For the polymerization of $POEGMA_{188}$ on L.SEC, $OEGMA_{188}$ monomer (1.88 g, 10.0 mmol) was introduced to initiate the polymerization (m: 2, 5, 10, 20, 40 mmol) and the solution was kept in an ice bath under slow magnetic stirring for a fixed time period. These $POEGMA_{188}$ modified L.SEC microparticles are denoted as POm-g-L.SEC, where m corresponds to the monomer mass changing from 5, 10, 20, 40 mmol.

Preparation of thermal-responsive L.SEC-based superhydrophobic surface

The L.SEC-based superwettable surfaces were constructed via the immobilization of polymer-L.SEC on an aluminum sheet. We sprayed the L.SEC powder on the aluminum sheet coated with an adhesive glue, where the surfaces were uniformly prepared, and the coating thickness was manipulated by adjusting the concentration of the formulation. The coated surface was vacuum dried, after which they were subjected to further analysis.

Characterization

The water/oil static and dynamic contact angle measurements were performed using the OCA 15 (Dataphysics). To measure the static contact angle, a sessile drop (5 μL) was dispensed onto the test surface with an auto-dosing system equipped with a 500 μL needle, and a side-view image was captured with the camera when the droplet was stabilized. To obtain an accurate value of the static contact angles, the captured image was further analyzed by the Image J analysis software. L.SECs were visualized and examined from optical microscopic images and videos captured using the Nikon LV ND microscope or Photron SA5 high-speed camera. The particle size was measured using Particle size analyzer (Anton Paar 1190) and Nano Zetasizer (Malvern ZS90) with temperature control system. The thermal responsive characteristics were evaluated by performing turbidimetric measurements on the Varian (Cary 100 Bio) UV–vis spectrometer equipped with a temperature controller and Micro-differential Scanning Calorimetry (DSC). Raman spectroscopy was conducted on LabRam HR800 confocal Raman microscope (HORIBA JobinYvon) with ×50 and x20 objective (excitation at 532 nm). The surface topography was characterized via scanning electron micrography (SEM) and confocal optical microscope (Olympus LEXT ols5000). Elemental

analyses were conducted using the energy dispersive X-ray spectroscopy (EDS-SEM), and XPS (Escalab 250XI, Thermo Scientific, USA). The rheological properties of the concentrated suspension were characterized in a Malvern Kinexus ultra+ rheometer with the cylindrical measuring system and a solvent trap to prevent water evaporation. The measured confocal (Zeiss LSM 510 Meta Laser Scanning Confocal Microscope (CLSM) image was shaped into a 3D image using ZEN 2009 analysis. The observation magnification was 40x/1.3 Water DIC, and an immersion objective lens was used, with the immersion medium being water.

4.3 Result and discussion

4.3.1 Polymer-L.SEC microparticles

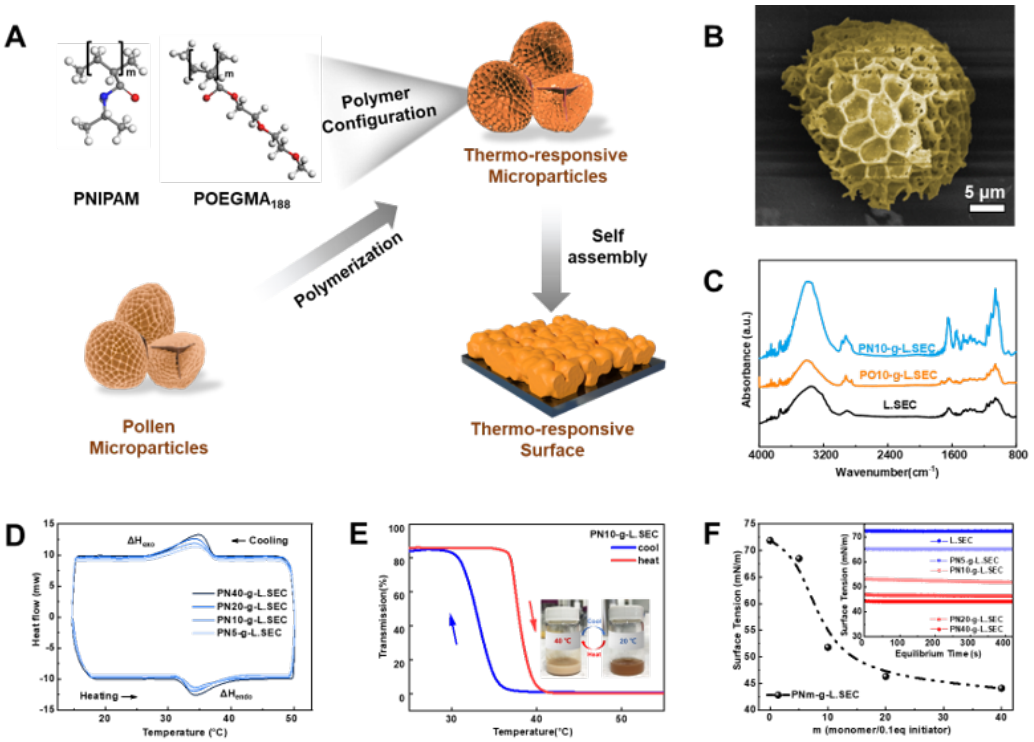

Figure 4.1 A. Schematic of preparation of thermo-responsive L.SEC particles and surfaces by grafting PNIPAM and $POEGMA_{188}$, B. SEM images of pristine L.SEC, C. FT-IR spectra of PN10-g-L.SEC, PO10-g-L.SEC and L.SEC, D. DSC measurement on PNm-g-L.SEC ranging the temperature from 15°C to 50°C with a scanning rate of 1°C/min, E. Turbidity change of PN10-g-L.SEC aqueous solution measured by UV-vis spectrophotometry, F. Surface tension of PNm-g-L.SEC detected by tensiometer.

The thermo-responsive L.SEC microparticles were synthesized by conducting cerium nitrate (CAN) free radical polymerization of N-isopropylacrylamide (NIPAM) and (oligoethylene glycol) methyl ether acrylate ($OEGMA_{188}$) in water (**Figure 4.1A**). Firstly, L.SEC microparticles with a tripartite structure decorated with honeycomb-like microridges (1~2 mm height and 200 nm width) on the external surface with uniform shape of 29.02 μm, were prepared via the KOH extraction process (**Figure 4.2**).[125] Notably, the hollow L.SEC with a large surface area offered a facile method to

control the external polymer layer architecture, consisting of polymer grafting density and chain length.[130] We manipulated these two factors by changing the monomer/initiator mass and polymerization time respectively. L.SECs were designated as PNm-g-L.SEC and POm-g-L.SEC respectively, where m corresponds to the molar ratio of the monomer to 0.1 eq of the initiator varying in 5, 10, 20, 40. A brown L.SEC powder was obtained and characterized by scanning electron microscopy (SEM), showing the surface morphology of PNm-g-L.SEC and POm-g-L.SEC featured with higher roughness nanostructure on micro-ridges owing to the polymer grafted canopy compared with pristine L.SECs (**Figure 4.1B**). Specifically, the architecture of the polymer grafted canopy of PNm-g-L.SEC particles transformed from a sparse to dense structure with high roughness nanostructure with the increasing grafting ratio (**Figure 4.3**). Moreover, the changes in the particle size were strongly associated with the polymer layer thickness as summarized in **Table 4.1**. For example, the size of PN-g-L.SEC increased from 30.51 μm to 31.62 μm as m increased from 5 to 40 mmol, corresponding with the epicuticular polymers covered the microridges on the outer surface becoming dense and increasing the thickness from 260.9 nm to 762.3 nm. POm-g-L.SEC showed a similar structural change as PNm-g-L.SEC. The induced structural and hydrophobicity change of modified L.SECs (PNm-g-L.SEC and POm-g-L.SEC) had a profound impact on the L.SEC-based thermo-responsive surfaces. Fourier transform infrared spectroscopy (FT-IR) further confirmed the successful grafting of PNIPAM and $POEGMA_{188}$ on the extine of L.SEC.[131] The IR spectrum of PN10-g-L.SEC displayed two characteristic peaks that confirmed the presence of amine groups, where the first band at 1650 cm^{-1} is associated with the N-C=O bond, while the absorption peak at 1550 cm^{-1} corresponds to the N-H bonds. The isopropyl groups (IP) were confirmed by the IR spectra over the range of 2500 to 4000 cm^{-1}. The peak at 2970 cm^{-1} was assigned to the antisymmetric and symmetric CH stretch of the methyl groups, while the peaks at around 2850 cm^{-1} and 2871 cm^{-1} were derived from the symmetric stretches of CH_2 and CH_3, respectively.[132] As shown in **Figure 4.1C**, PO10-g-L.SEC displayed the unique peak on 1740 cm^{-1}, which corresponds to the ester linkage between the methacrylate and oligoethylene glycol side chains of the $POEGMA_{188}$ graft brushes.[121] Further evidence on the successful polymerization of NIPAM and OEGMA from the surface is provided by X-ray photoelectron spectroscopic (XPS) elemental analyses, confirming that this layer contained organic molecules with the expected changes in the ratio of C-N bond on PNm-g-L.SEC surface and C–O bond on the POm-g-L.SEC surface. (Figure S3 and Table S1).[133]

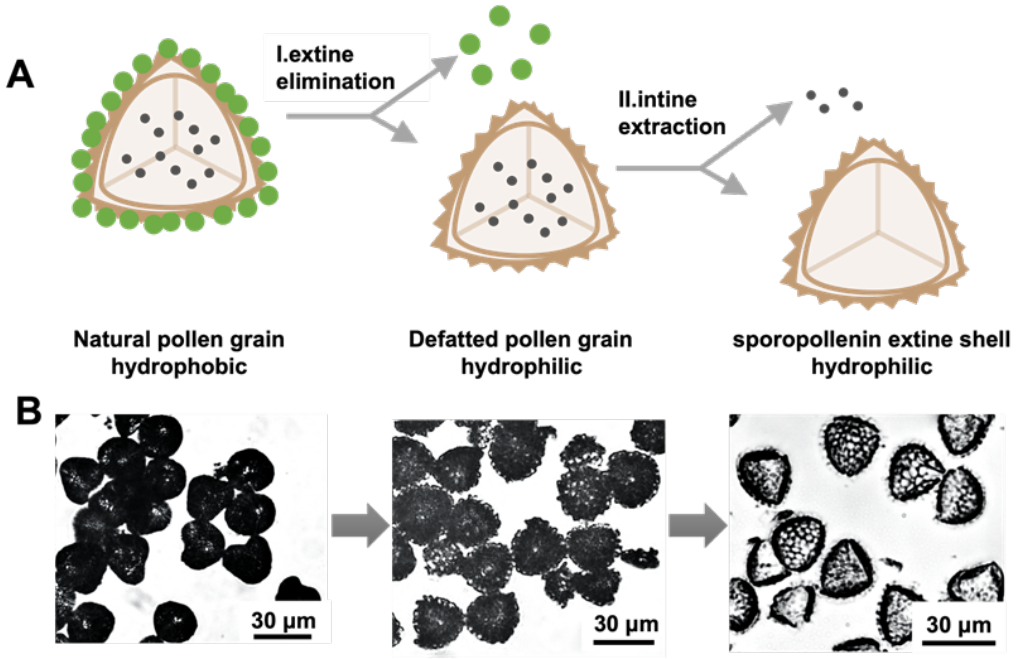

Figure 4.2 A. Schematic of transforming Lycopodium clavatum pollen into a hollow Lycopodium sporopollenin extine shell following the defatted and extraction process, B. The morphology changes of Lycopodium clavatum pollen during the defatted and extraction process were measured by optical microscope

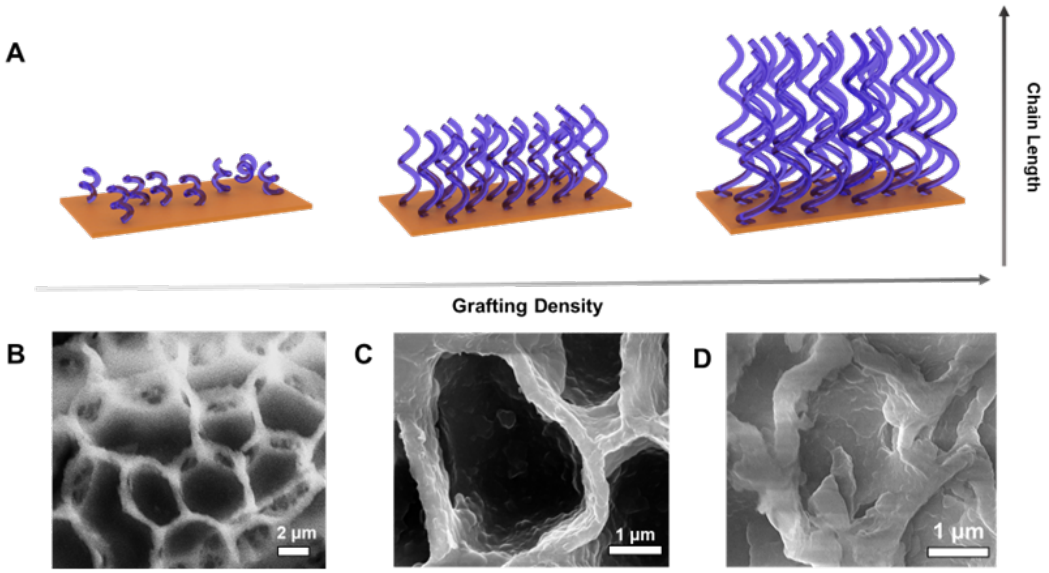

Figure 4.3 A. The PN-g-L.SEC and PO-g-L.SEC microparticles with different grafting density and chain length, SEM images of microridges on L.SEC outer surface: B. Pristine L.SEC, C. PN10-g-L.SEC, D. PN40-g-L.SEC

Table 4.1 Thickness of micro-ridges of modified L.SEC

Thickness of microridges \ Particles	m~5	m~10	m~20	m~40
PNm-g-L.SEC	260.9nm	402.3nm	582.8nm	762.3nm
POm-g-L.SEC	253.2nm	360.9nm	532.8nm	722.2nm

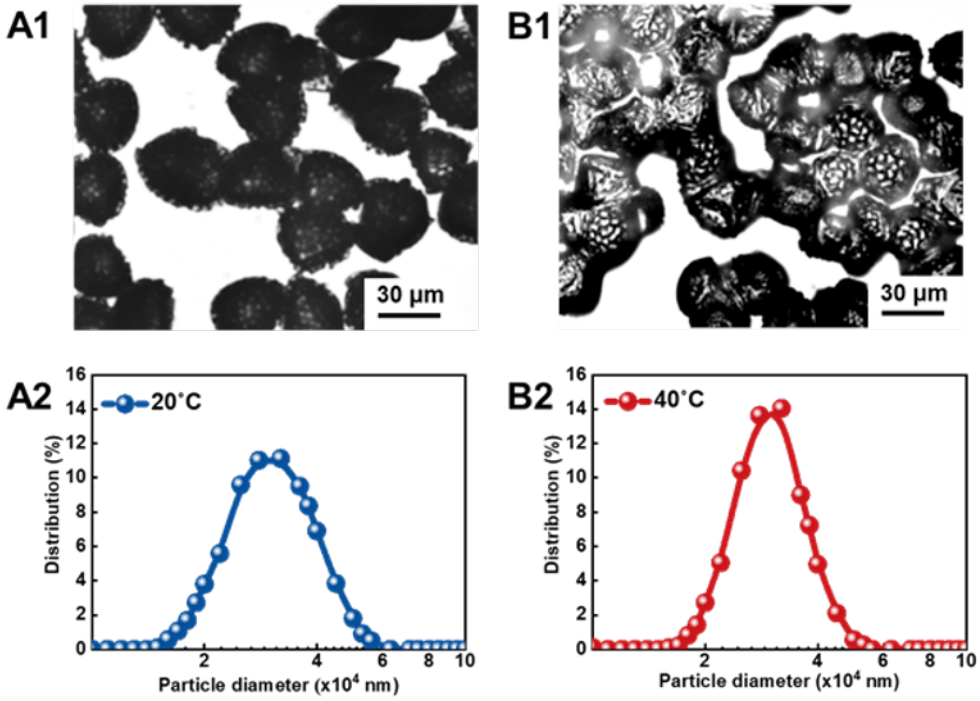

Figure 4.4 The shape changes and particle size change of PN10-g-L.SEC at different temperatures A. 20°C, B. 40°C

With regards to thermal responsive characteristics, the polymer conformational transition endowed the L.SEC with different interactions with water molecules that are dependent on the thermal characteristics, such as the lower critical solution temperature (LCST). The LCST driven by temperature was typically associated with the turbidity change, which could be measured by UV-vis spectrophotometry. **Figure 4.1E** reveals the LCST of PN10-g-L.SEC solutions at ~35.2°C, caused by the hydrophobic effect of the isopropyl groups (IP) and bound water around the amino (-NH_2) and carbonyl groups (-C=O). In addition, the phase transition of PNm-g-L.SEC was further investigated by differential scanning calorimetry (DSC) over consecutive heating/cooling cycles.[134] The LCST transition of the PNm-g-L.SEC revealed two different thermal processes as shown in **Figure 4.1D**, from the presence of a typical endothermic peak at ~35.8°C and an exothermic peak at ~36.2 °C of PN10-g-L.SEC. These thermal transitions were related to the dehydration of apolar groups (IP) and the interactions between polar groups and water molecules. Below the LCST, the

polymer chains are in a random coil conformation, with “water cages” around the IP and water molecules around or bonding with the NH_2 and C=O groups.[135] At temperatures above the LCST, the entropy of the polymer−water system dominated, which was unfavorable for the exothermic formation of hydrogen bonds. Thus, the water cages surrounding the IP groups were disrupted together with the bound water molecules that were released to increase their entropy and the polymers collapsed into a globular state.[136] The phase transition of PN10-g-L.SEC was evident from the inset of **Figure 4.1E** determined from the changes in the solution turbidity. PN10-g-L.SEC was well-dispersed in an aqueous solution with an average radius of 31.07 μm at 20°C, and the solution transformed into a turbid dispersion at 40°C that became water-insoluble and the suspension transformed into a brown opaque color, confirming that the side chain of grafted PNIPAM transformed into a collapsed globule and PN10-g-L.SEC with an average radius of 30.09 μm (**Figure 4.4**). The polymer chain conformational transition can be traced by the interfacial arrangement of these hydrophobic/hydrophilic segments on PN10-L.SEC, which was indicated by changes in the dynamic temperature-dependent surface tension and interfacial behavior between polar/apolar solvents. The dependence of the surface tension with changes in temperatures are displayed in **Figure 4.5**, where the γ_{LV} of PN10-g-L.SEC was 52.1 mN m^{-1} at 20°C and decreased to 38.7 mN m^{-1} at 40°C. The results demonstrated that the predominately strong hydrogen bonding interacting between water molecules with hydrophilic -NH_2 and -C=O groups at low temperature, while the exposure of a large amount of hydrophobic IP groups above the LCST decreased the surface tension. The surface tension of PN10-g-L.SEC was thermally responsive and reversible during the heating-and-cooling cycles, while the rearrangement of hydrophobic/hydrophilic groups induced by temperature could also be detected via the time dependent interfacial tension data (**Figure 4.6**).[5] With increasing temperature, the hydrophilic groups formed intramolecular interactions instead of hydrogen bonds with water, where the well-dispersed PN10-g-L.SEC particles in the water phase became hydrophobic and rearranged at the polar/apolar interface. This interfacial behavior of PN10-g-L.SEC resulted in the change of droplet shape, and the simulated value of the interfacial tension decreased around their LCST, which was consistent with the previous phase transition results.

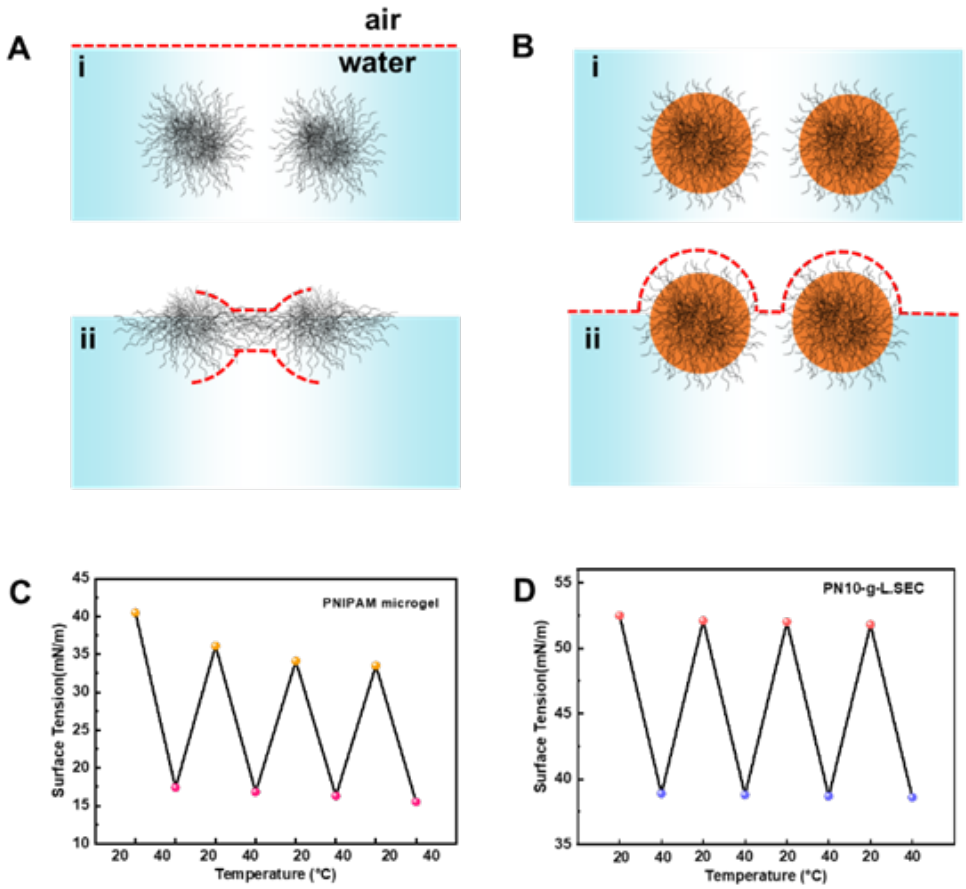

Figure 4.5 Schematic illustration of the adsorption kinetics at water-air interface: A. PNIPAM microgel, B. PN10-g-L.SEC, Surface tension variation of particles cycling between 40°C and 20°C: C. PNIPAM microgel, D. PN10-g-L.SEC

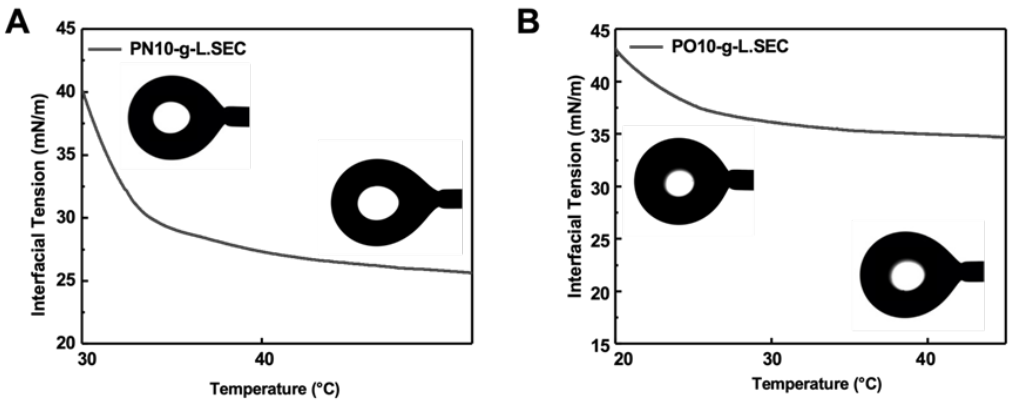

Figure 4.6 Interfacial tension measured by pendant drop method at the water/hexane interface: A. PN10-g-L.SEC, B. PO10-g-L.SEC

Moreover, different polymer chain structural arrangements were triggered by temperature, which could be deduced from surface tension. As a result, the equilibrium surface tension (γ_{LV}) of pure L.SEC aqueous solution was about 71.9 mN m^{-1}, which was close to pure water (72.8 mN m^{-1}).

With increasing grafting polymer ratio, the amounts of grafted polymers on L.SEC increased and the γ_{LV} decreased sharply from 68.3 mN m^{-1} to 44.1 mN m^{-1} for PN5-g-L.SEC and PN40-g-L.SEC, respectively (**Figure 4.1F**). The results demonstrated the amounts of grafted polymers as deduced from the grafting density and chain length at a low grafting ratio, where the IP groups on the side chain displayed a flat conformation on the pollen surface. However, at a high grafting ratio, the rearrangement of IP groups resulted in an extended and ordered chain conformation, that reduced water affinity. Besides, the polymer-L.SEC particle morphology could affect the adsorption at the air/water interface. To demonstrate this, we compared the interfacial behaviors between PN10-g-L.SEC microparticles and PNIPAM microgel, where the surface tension variation was recorded. As shown in Figure S2, the surface tension of PN10-g-L.SEC cycled over a smaller range (~ 12 ºC), and the process was reversible over several cycles, while surface tension of the PNIPAM soft microgel possessed a larger temperature range (~17-18 ºC), and the temperature decreased with each cycle. This is caused by the soft particles deforming and spreading over a larger interfacial area since they possessed a higher adsorption energy compared to rigid particles.[137] When two deformed microgels are forced into close proximity, their size and shape changed irreversibly resulting in a reduced surface tension after several cycling of between 20°C and 40°C. However, the polymer-L.SEC particles adsorb at the interface according to the Young–Dupré relationship,[138] endowing them with reversible chemical structural and morphological transition that further ensure a more flexible interaction between water and the stable interparticle interaction compared to the microgel. Therefore, the polymer-L.SEC particles are good candidates for the construction of thermo-responsive surfaces to achieve a tunable and reversible wettability transition.

To compare the influence of molecular structuring on the hydrophobic transition, POm-g-L.SEC were used as reference samples since their polymer chain transitions were different from PNIPAM. The LCST of PO10-g-L.SEC occurred in a reversible phase transition at ~26.9°C (**Figure 4.7**). Given the mechanism governing the phase transition, the polyethylene glycol (PEG) side chains were solubilized at low temperatures due to the extensive hydrogen bonding between the ether oxygen and water hydrogen atoms. When the temperature was increased beyond its LCST of 26.9°C, the polymer-polymer interaction became more thermodynamically favorable compared to polymer-water interaction, causing the PEG chains to collapse onto the methacrylate backbone forming an insoluble globule resulting in a turbid solution.[139] The hydrophobic methyl methacrylates (MMA) counterbalanced this hydrophilic character of oligo(ethylene glycol) (OEG) groups leading to a competitive hydrophobic effect. Besides, the LCST temperature of PNm-g-L.SEC were found, similarly to POm-g-L.SEC, to be relatively independent of polymer stereoregularity.

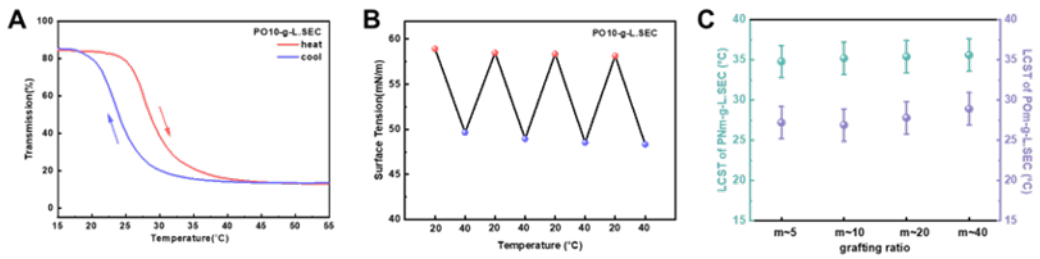

Figure 4.7 A. The LCST of PO10-g-L.SEC, B. surface tension variation of PO10-g-L.SEC cycling between 40°C and 20°C, C. LCSTs of PN-g-L.SEC and PO-g-L.SEC varying the grafting ratio

4.3.2 Temperature-dependent macroscopic surface wettability transformation

To gain a deep insight into the interactions between water and PNm-g-L.SEC and POm-g-L.SEC, we prepared surfaces with the L.SEC microparticles via self-assembly of the L.SEC microparticles onto a substrate. The combined hierarchical structure reinforced the surface hydrophobic transformation that highlighted the interaction between polymer chain and water molecules, providing a clear and visual picture to demonstrate the process.[140] The surface topography and roughness factor of the L.SEC-based surface, which were investigated by SEM and laser confocal microscopy. PN10-g-L.SEC surface possessed a porous network structure with a roughness factor (R_q) of 2.32 mm, where the green-yellow-red regions corresponded to the surface protrusions consisting of assembled L.SEC microparticles and blue regions represented the "valleys" between the protrusions (**Figure 4.8B and 4.8C**). The convex protrusions comprised of self-assembled L.SEC microparticles as indicated by the SEM image (**Figure 4.9**). Notably, this surface design strategy could amplify the molecular-level conformational transition for tunning the macroscopic surface characteristics.

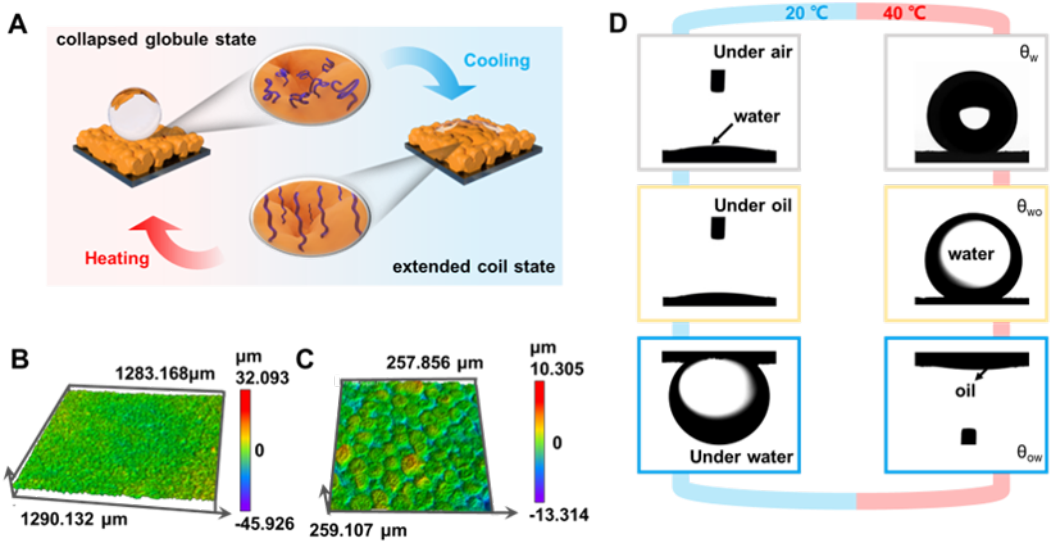

Figure 4.8 A. Illustration of surface wettability transition corresponding to the coil-to-globule transition driven by temperature, Surface topography of PN10-g-L.SEC surface measured by laser confocal microscopy: B. magnification 10X C. magnification 50X, D. Variation of contact angle on PN10-g-L.SEC surface under different environmental conditions.

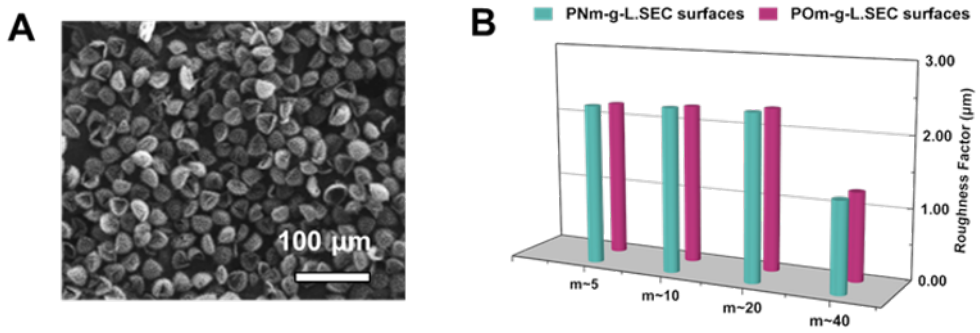

Figure 4.9 A. SEM images of PN10-g-L.SEC, B. Surface roughness factors of L.SEC-based surfaces

The surface wettability behavior is a key parameter to determine the relationship between water and substrate at the macroscale as characterized by contact angles. Since the surface conformation and structure influenced the water contact angle under air (θ_w), we separated the surfaces into three types for comparison. At a low grafting ratio of polymer (m~5 mmol), the grafted chain was randomly distributed on the L.SEC surface with low nanoscale roughness, resulting in insufficient functional groups on the outer surface yielding a mild response to temperature changes. As shown in **Figure 4.10A**, PN5-g-L.SEC surface was hydrophilic (θ_w~22°) regardless of the temperature, and the molecular conformation transition at the nanoscale could not alter the surface wettability at the macroscale.[141] Similar surface wettability characteristic was observed for PO5-g-L.SEC surfaces, **(Figure 4.10D)** showing hydrophilicity with θ_w of 22.4° (20 °C) and 22.1° (40 °C) at low grafting density, respectively. Notably, the grafting ratio on L.SEC was a key factor in determining the nano/microstructure of polymer-L.SEC, which further influenced the overall surface topography.

As for PN40-g-L.SEC surface (**Figure 4.9**), the surface roughness (R_q~1.28 mm) was reduced due to the high grafting ratio of polymer brushes that covered the L.SEC walls and microbridges. The result showed that the high grafting ratio of polymer altered the hierarchical nano/microstructure, where the increased nano roughness dramatically reduced the micro-roughness. In the case of PN40-g-L.SEC, the surface displayed a hydrophilic/hydrophobic with a θ_w of 54 ° at 20°C and 103° at 40 °C (**Figure 4.10C**). The reduced microstructure led to the hydrophilic/hydrophobic transition of PN40-g-L.SEC surface, which exhibited a similar trend as the flat polymer surface.[142] Here, with the enhanced nano/microstructure, the surface wettability transformation phenomenon was induced by the molecular structure, orientation, and restructuring of the polymer chain occurring at the water/PNIPAM interface driven by temperature. At low temperatures, C=O and N-H groups displayed strong hydrogen bonding with water molecules around the PNIPAM chains that impacted the air/PNIPAM/water interface. When the temperature exceeded the LCST, the polymer chains collapsed and the hydrophilic C=O and N-H groups interacted via hydrogen bonds while the exposed hydrophobic IP moieties near the surface of the collapsed chains contributed to the hydrophobicity of PN-g-L.SEC outer surface. In addition, based

on the theory of similarity-inter miscibility, hydrophobic groups (-CH_3) extended to the oil phase and the hydrophilic segments (-NH_2, C=O groups) extended towards the water phase. The orientation of the hydrophobic/hydrophilic moieties of the functional groups on the polymer brushes was confirmed by the oil CA under water ($\theta_{o/w}$) and the water CA under oil ($\theta_{w/o}$). PN40-g-L.SEC(20°C) surfaces were in a metastable state, possessing under-oil superhydrophobic ($\theta_{w/o}$~150.5°) and under-water oleophobic ($\theta_{o/w}$~151°) characteristics (**Figure 4.11**). **Figure 4.10F** shows the thermal switching between hydrophilic and hydrophobic states for the PO40-g-L.SEC surface, where the static θ_w oscillated between 22° at 20°C and 64° at 40°C. Although, this surface showed a similar thermal wettability transition from hydrophilic to hydrophobic, the molecular structural transformation of POm-g-L.SEC surfaces were different from PNm-g-L.SEC.

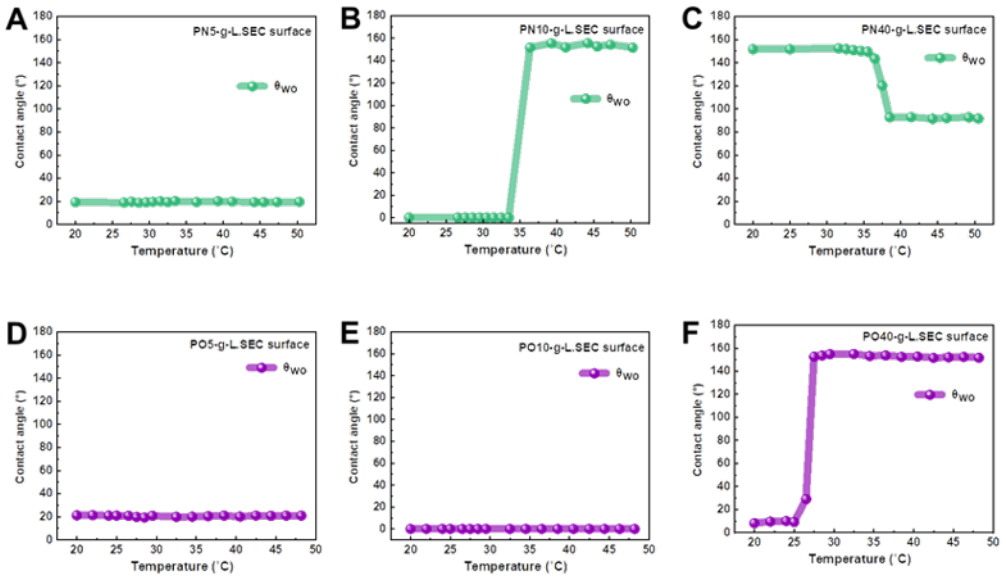

Figure 4.11 The variation of contact angle including water contact angle under oil: A.PN5-g-L.SEC, B. PN10-g-L.SEC, C. PN40-g-L.SEC, D. PO5-g-L.SEC, E. PO10-g-L.SEC, F. PO40-g-L.SEC.

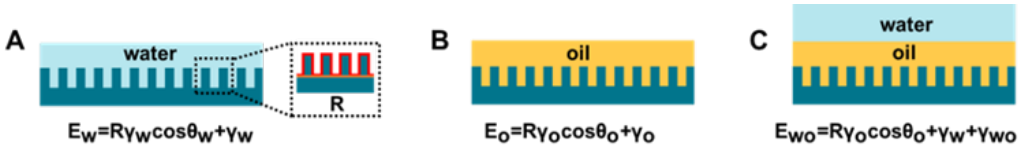

Figure 4.12. Illustration of interfacial energy measurement on polymer-L.SEC at different states: A. water-solid (E_w), B. hexane-solid (E_o), C. water-hexane-solid (E_{wo})

To elucidate the surface wettability generated by the hydrophobic/hydrophilic groups, the conformational transition of the polymer brushes on the L.SEC surfaces were analyzed by comparing the total interfacial energy of different wetting states (**Figure 4.12**).[30] We compared the total interfacial energies of L.SEC-based surfaces at different temperatures that were completely wetted by either water (E_w), or an arbitrary immiscible oil (hexane) (E_o) or without a fully wetted immiscible water floating on top (E_{wo}).[143] In addition, where θ_w and γ_w, θ_o and γ_o are

intrinsic CAs and surface tensions of water and hexane, respectively, while γ_{wo} corresponds to the surface energies of the water-hexane interface. R represents the roughness factor of the textured solid, which is defined as the ratio between the actual and projected areas of the surface. The surface was wetted preferentially by water or oil, and the conformational transition of hydrophobic and hydrophilic moieties on the PNIPAM and $POEGMA_{188}$ triggered by temperature could be estimated. For the PO40-g-L.SEC (20°C) surface, the comparison of interfacial energy ($E_w < E_o$ but $E_w > E_{wo}$) indicated that the surface would be preferentially wetted by water forming a stable water−solid interface and displayed hydrophilicity in oil and oleophobicity in water (**Table 4.3**). Under this wetting state, the ether oxygens of PEG on the exterior of the collapsed globules bonded with the water molecules. However, the interfacial energy indicated that the water-(PO40-g-L.SEC (40°C)) surface was thermodynamically unstable, whereas the experimental results showed that the PO40-g-L.SEC(40°C) surface exhibited an under-oil superhydrophilic ($\theta_{w/o}$~155.5°) and under-water superoleophobic ($\theta_{o/w}$ ~152.0°) characteristics. The under-oil superhydrophilic characteristics suggested that the hydrophobic moieties consisting of the methyl groups on the main chain of MMA favored the exterior environment and repelled water, resulting from the enhanced polymer-polymer interactions on PO40-g-L.SEC(40°C) surface. Besides, the under-water superoleophobic surface suggested that the hydrogen bonding between the side chain of $POEGMA_{188}$ and water persisted in forming a layer of water film that repelled oil preventing its infusion to the surface. Thus, the molecular conformational transition of POm-g-L.SEC system associated with the ether oxygens of PEG on the outer surface of the polymer chains bonded with water molecules below the LCST (26.9°C). Above the LCST, this balance was disrupted and the interaction between the side chain of $POEGMA_{188}$ and water was reduced, resulting in the enhanced polymer-polymer interactions over polymer-water interactions.

Table 4.3 Total interfacial energy calculation on PN40-g-L.SEC and PO40-g-L.SEC surfaces

surfaces	liquid A	liquid B	R (μm)	γA (mJ/N)	γB (mJ/N)	γAB (mJ/N)	θA (°)	θB (°)	ΔE_1(mJ/m²) =E_w-E_o	ΔE_2(mJ/m²) =E_w-E_{wo}	Stable Film? Theoretical	Stable Film? Experimental
PN40-g-L.SEC (20°C)	water	hexane	1.28	72.4	17.9	41.8	54.2	2.7	-73.1	23.2	Y/N	DL
	hexane	water	1.28	17.9	72.4	41.8	2.7	54.2	-10.4	-23.1	N	DL
PN40-g-L.SEC (40°C)	water	hexane	1.23	72.4	17.9	41.8	103.1	6.8	0.245	96.5	Y	Y
	hexane	water	1.23	17.9	72.4	41.8	6.8	103.1	-83.8	-96.5	N	N
PO40g-L.SEC (20°C)	water	hexane	1.25	72.4	17.9	41.8	23.3	1.5	-102.5	-6.25	N	N
	hexane	water	1.25	17.9	72.4	41.8	1.5	23.3	18.9	6.25	Y	Y
PO40-g-L.SEC (40°C)	water	hexane	1.18	72.4	17.9	41.8	64.7	3.1	-57.2	39.0	Y/N	DL
	hexane	water	1.18	17.9	72.4	41.8	3.1	64.7	-26.3	-39. 7	N	DL

"Y" indicates that liquid B can form a stable liquid film on the surface and is not replaced by liquid A. The surface has a strong affinity to liquid B.

"N" indicates that the liquid A−solid interface is more stable, and liquid B will be displaced by liquid A. The surface has a strong affinity to liquid A.

"DL" represents the under-liquid dual superlyophobic surfaces. The surface has affinity both to liquid A and B.

4.33 Mechanism investigation of interfacial water at multiple length scale and surface wettability transition

Although previous studies suggested that the surface wettability change was induced by the collapsed and extended state of the polymer chains, the associated water structure at the molecular interfaces needed to be determined. To better explore the macroscopic wettability phenomenon at the air/polymer-g-L.SEC/water interface, in situ Raman spectroscopy was used to investigate the changes in the structure and dynamics of water induced by the functional groups on the polymer chains.[144] Here, we present experimental evidence that revealed a similarity between the structure of water around the hydrophilic/hydrophobic groups and at macroscopic air/PN-g-L.SEC/water interfaces.

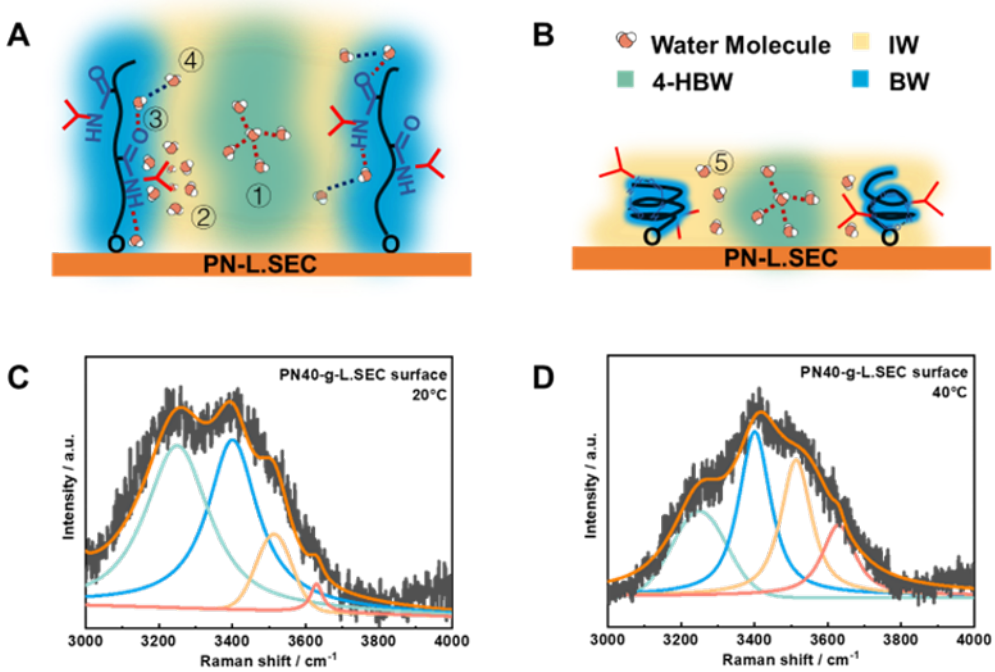

Figure 4.13 The water structure along PNIPAM polymer chain: A. below LCST, B. above LCST, The proportion of water ratio measured by Raman spectroscopy: C. PN40-g-L.SEC surface below LCST, D. PN40-g-L.SEC surface above LCST

Figure 4.13 shows a typical Raman spectrum of a fully prewetted and hydrated PN40-g-L.SEC surface over the temperature range from 20 °C to 40 °C. A broad Raman band extending from 3000 cm^{-1} to 4000 cm^{-1} is related to the vibration of hydrogen bonds in water, where the 3050, 3250, 3410, 3520, and 3630 cm^{-1} were assigned to different types of water structures. Gaussian fittings of the spectra showed that the O-H stretching band could be resolved into three distinct components, corresponding to three types of O-H stretching vibrations. The low wavenumber component of the 3250 cm^{-1} peak is associated with the vibration of 4-coordinate hydrogen-bonded water (4-HBW), which is attributed to free water with four hydrogen bonds (①) and -CH_3 surrounded by polyhedral

cages composed of tetrahedrally hydrogen-bonded water molecules (②).[135] Whereas the 3410 cm^{-1} is associated with the in-phase vibrations of water molecules captured by the C=O or N-H groups (③) of PNIPAM, which is regarded as bound water (BW). The high wavenumber components at 3520 and 3630 cm^{-1} correspond to the stretching of the weak or non-hydrogen bonded water molecules (④⑤), which is regarded as intermediate water (IW), reflecting the hydrophobic disordered water in the hydration shell.[101b] Note that the hydration-shell OH band possessed a different shape with changes in temperature ranging from 20 °C to 40 °C. At 20 °C, the resulting spectra revealed two small dangling (non-hydrogen-bonded) water OH peaks near 3520 cm^{-1} and 3630 cm^{-1} as well as two broad overlapping hydrogen-bonded OH features near 3250 cm^{-1} and 3410 cm^{-1}. Moreover, at 40 °C, the relative intensity of the Raman band near 3250 cm^{-1} decreased significantly whereas the high wavenumber components at 3520 and 3630 cm^{-1} showed a dramatic increase. The shift in the spectrum for water structure transformation was attributed to two stages in the polymer chain transition. On one hand, the C=O or N-H groups formed a strong hydrogen bond around water molecules at low temperatures, which was replaced by intramolecular interaction with each other that weakened the interaction with water molecules above the LCST. On the other hand, -CH_3 groups are surrounded by the hydrophobic hydration shells ("water cage") that resemble solid clathrate hydrates below the LCST, which were tetrahedral with fewer weak hydrogen bonds compared to bulk water. As the temperature increased to 40°C, the hydration shell transformed dramatically into a less-ordered and weaker H-bonded structure, accompanied by the peaks with a lower intensity of 3250 cm^{-1} and enhanced intensity near 3520 cm^{-1} and 3630 cm^{-1}. These results were observed for the PN40-g-L.SEC surface, where the phase transition of PNIPAM chains was accompanied by a water structure transformation.

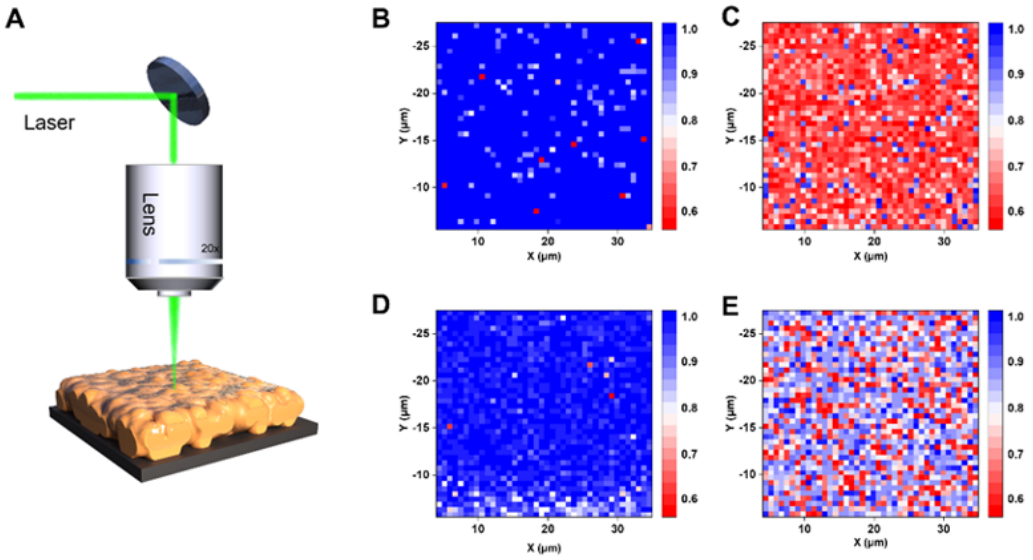

Figure 4.14 A. Illustration of temperature-dependent Raman spectroscopy, the water ratio of 4-HBW/BW changing with the temperature detected by Raman mapping (the ratio was measured at each pixel ranging from 0.6 to 1.0 that recorded as red to blue): B. PN40-g-L.SEC surface at 20°C, C. PN40-g-L.SEC surface at 40°C, D. PO40-g-L.SEC surface at 20°C, E. PO40-g-L.SEC surface at

40°C

A better description of the three types of water structures on the PN40-g-L.SEC surface can be described by comparing the proportion of O–H stretching vibrational band. Analysis of the results in **Figure 4.13C** and **4.13D** revealed that as the temperature was increased from 20 to 40°C, the proportion of 4-HBW decreased from 35.7% ± 1.5% to 21.1% ± 1.3%, BW varied between 36.8% ± 1.4% and 33.0% ± 1.3%, and IW increased from 27.5% ± 1.0% to 45.9% ± 1.2%. Since the proportion of 4-HBW and BW due to the disruption of the "water cage" surrounding -CH_3 and dehydration of C=O and -NH_2 respectively, we could compare the ratio of 4-HBW/BW to analyze these hydrophilic/hydrophobic orientation and transition around the LCST. Raman mappings on an area of 40*40 μm^2 clearly showed the changes of the hydrophilic/hydrophobic orientation and transition on the PN40-g-L.SEC surface at different temperatures (**Figure 4.14**). The signal contrast between 20°C and 40°C indicated that the ratio of 4-HBW/BW was higher at 20°C, revealing that the surface possessed more bound water and the hydrophilic C=O and -NH_2 groups assembled mainly at the air/PN-g-L.SEC/water interface. However, the ratio of 4-HBW/BW showed a dramatic drop over the whole area at 40°C, indicating that the water transformed into a less ordered and weaker hydrogen-bonded structure and the preferred exposure of hydrophobic -CH_3 groups rearranged at the interface.

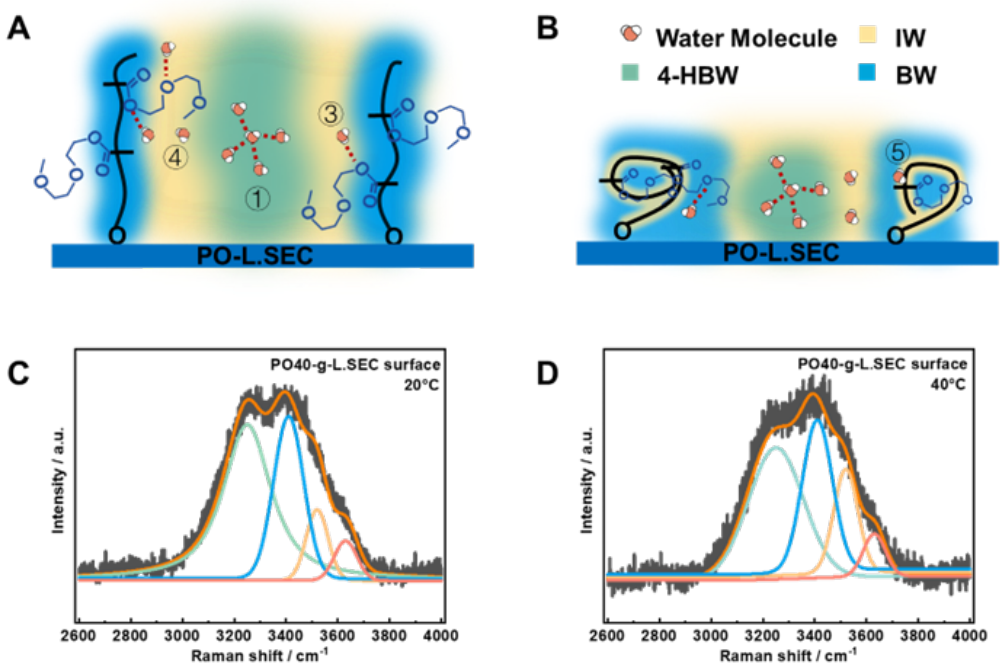

Figure 4.15 The water structure along POEGMA188 polymer chain: A. below LCST, B. above LCST, the proportion of water ratio measured by Raman spectroscopy: C. PO40-g-L.SEC surface below LCST, D. PO40-g-L.SEC surface above LCST

Furthermore, the O-H stretching spectra of PO40-g-L.SEC surface was selected to investigate the relationship between the water structure and polymer conformation. Theoretical predictions of the conformation of $POEGMA_{188}$ brushes possessed a hydrophobic main chain and hydrophilic side

chain. **Figure 4.15** shows the Raman spectra of PO40-g-L.SEC at 20°C and 40°C, and the proportion of 4-HBW decreased from 35.9% ± 1.3% to 28.7% ± 1.1%, BW varied between 37.8% ± 1.3 and 34.1% ± 1.3%, and IW increased from 26.3 to 37.2% ± 1.0%. Moreover, the ratio of 4-HBW/BW on PO40-g-L.SEC also showed lower fluctuations. These results confirmed that the $POEGMA_{188}$ comprised of a strong interaction between C-O and water and a weak hydrophobically hydration shell around the $-CH_3$ of the main chain. Additionally, the signal contrast on Raman mapping of PO40-g-L.SEC revealed that the change in the ratio of 4-HBW/BW was less than the PN40-g-L.SEC surface. Owing to the strong water affinity of C-O groups and chain structure, the IW layer occurred on the main chain with increasing temperature surrounded by a BW layer (**Figure 4.14**). Thus, the hydrophobic hydration shell was different from the "water cage" surrounding $-CH_3$ of PNIPAM that did not disappear with increasing temperature, resulting in a lower hydrophobic character of the $-CH_3$ groups.

The water structural variation occurred around the thermo-responsive polymer chains on a molecular level. However, as exhibited by the macroscopic evidence (wettability transformation), such a short-ranged interfacial effect determined the macroscale surface wettability transition when combined with the surface roughness. This could be attributed to the grafting of polymer brushes on the rigid and rough lycopodium pollen, where the water structure variation near the thermo-responsive polymer chain was optimum for a whole pollen particle due to the tendency of the water to maintain the integrity of its hydrogen bond network.[145] This phenomenon could be demonstrated by rheological analysis of concentrated pollen suspensions.

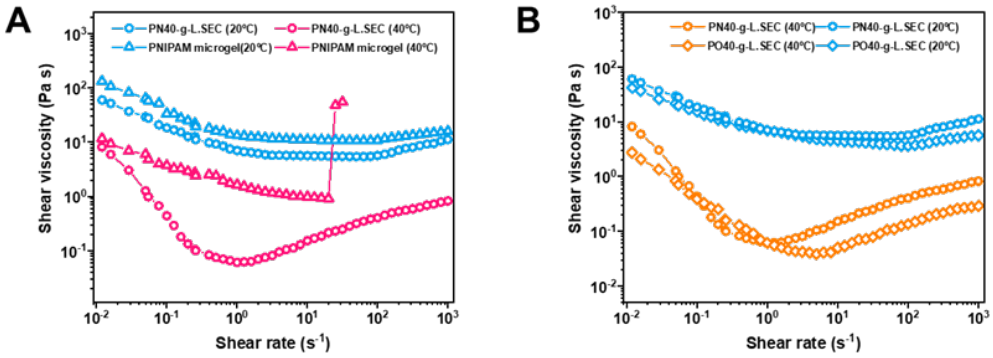

Figure 4.16 A. Rheological flow curves of PNIPAM microgel and PN40-g-L.SEC concentrated solution (volume fraction~51%) at 20 °C and 40 °C, B. Rheological flow curves of PN40-g-L.SEC and PO40-g-L.SEC concentrated solution (volume fraction~51%) at 20 °C and 40 °C

The dense suspensions with high volume fraction of particles were prepared near to the maximum packing volume fraction, and shear rheological measurements were performed.[146] In general, the rheological properties are extremely sensitivity to the interparticle interactions and hydration shell around the particles at the nanoscale. Due to the higher content of 4-coordinate hydrogen-bonded water (4-HBW) and bound water (BW) around the exposed and swollen polymer chain on PN40-g-L.SEC surface, their ordered hydrogen bond network[147] induced a stable and thick lubricating

hydration shell, which kept the particle surfaces separated until a critical load was exceeded resulting in the interpenetration of the brushes below the LCST (**Figure 4.16**). This stable lubrication layer would be disrupted at a high shear rate ($10^2 s^{-1}$), and the hydrodynamic rearrangement of the particles generated larger clusters of aggregated particles, leading to a smooth and reversible viscosity increase (continuous shear thickening in **4.16**).[148] Above the LCST, the interfacial water structure would be substantially altered, where more intermediate water structures are formed around the collapsed polymer chain disrupting the original tetrahedral hydrogen bond structure yielding a distorted and heterogeneous network brushes.[149] Thus, the thinner hydration shell and unstable hydrogen bond system would form at the interface, where the lubrication layer (hydration shell) could be readily disrupted under the hydrodynamic force that produced a higher viscosity signified by the shear thickening behavior. The changes in the rheological properties with temperature could also be observed for the dense PNIPAM microgel suspension. The shear stress would be suppressed, and discontinuous shear thickening occurred at temperatures exceeding the LCST (red open triangles of **Figure 4.16A**). The rheological profiles agreed with the prediction of recent molecular dynamics calculation and experiments.[146] The PO40-g-L.SEC displayed similar trend in the rheological behavior, where the shear thickening behavior was enhanced at high temperature. However, the conformational transition of $POEGMA_{188}$ brushes led to a lower amounts of intermediate water contents as determined by the Raman measurements. Therefore, it could still form stable hydrogen network between the PO40-g-L.SEC particles when compared with PN40-g-L.SEC at temperatures beyond the LCST, showing a smaller shear thickening enhancement. Besides, additional rheological experiments were conducted on another type of polymer grafted pollen microparticles (Lotus), where the Lotus pollen possessed a similar size but with a different surface roughness (**Figure 4.17**). Both the PN40-g-L.SEC and PN40-g-Lotus particles displayed temperature-dependent viscosity variations. However, above the LCST, PN40-g-L.SEC possessed a higher shear thickening effect compared to PN40-g-Lotus.[150] This is attributed to the rougher PN40-g-L.SEC particle with an enhanced proportion of polymer-water interface, leading to a larger heterogeneity of the water structures due to the increased density of intermediate water.[151]

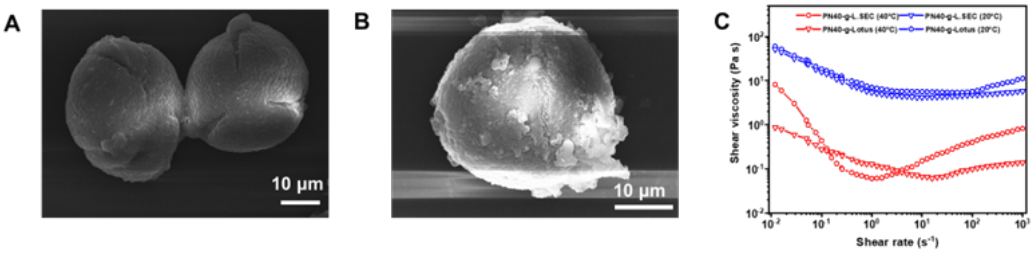

Figure 4.17 SEM images of lotus sporopollenin: A. before modification, B. after modification of PNIPAM designated as PN40-g-Lotus, C. Rheological flow curves of PN40-g-L.SEC and PN40-g-Lotus concentrated solution (volume fraction~51%) at 20 °C and 40 °C

Moreover, surface free energy (γ_s) was affected by the rearrangement of hydrophilic/hydrophobic

moieties, which is a key parameter to determine the wettability at the integrated air-liquid-solid interface. According to the Owens, Wendt, Rabel and Kaelble (OWRK) theory,[29] the surface free energy consisted of both polar (γ_s^p) and dispersive components (γ_s^d), where the two polar C=O, -NH_2 groups and apolar -CH_3 groups of PNIPAM contributed to γ_s^p and γ_s^d. **Table 4.4** provides a summary of the changes of surface free energy on PN-g-L.SEC and PO-g-L.SEC surfaces for the temperature at 20 °C and 40 °C. For PN40-g-L.SEC surface, when the temperature was increased from 20 to 40 °C, γ_s^p decreased from 15.8 mJ m^{-2} to 0.04 mJ m^{-2}, γ_s^d decreased from 39.5 mJ m^{-2} to 32.6 mJ m^{-2}, suggesting that the surface switched from hydrophilic to hydrophobic and γ_s of 55.2 mJ m^{-2} decreased to 32.6 mJ m^{-2}. It can be concluded that the surface free energy contributed to the increased hydrophobicity of the surface owing to the polar/apolar component's conformational transition.

Table 4.4 Surface free energy of PN-g-L.SEC and PO-g-L.SEC

	water	Methylene iodide	r_s^d	r_s^h	r_s
PN5-g-L.SEC(20°C)	22.2	5.3	39.4	32.6	72.0
PN5-g-L.SEC(40°C)	22.3	5.6	39.4	32.6	72.0
PN10-g-L.SEC(20°C)	3.1	0	38.8	37.4	76.2
PN10-g-L.SEC(40°C)	154.3	78.5	22.6	6.8	29.4
PN40-g-L.SEC(20°C)	54.2	23.3	39.5	15.8	55.2
PN40-g-L.SEC(40°C)	103.1	53.8	32.6	0.0	32.6
PO5-g-L.SEC(20°C)	22.4	5.2	39.5	32.5	72.0
PO5-g-L.SEC(40°C)	22.1	4.8	39.5	32.6	72.1
PO10-g-L.SEC(20°C)	2.1	0	38.8	37.4	76.2
PO10-g-L.SEC(40°C)	1.2	0	38.8	37.5	76.3
PO40-g-L.SEC(20°C)	23.3	6.6	39.4	32.2	71.6
PO40-g-L.SEC(40°C)	64.7	32.2	37.7	10.6	48.3

The temperature-dependent polymer conformational transition followed by the surrounding water structural transformation and surface free energy fluctuations, further impacted the water structure at a macroscopic air–water-solid interface. When the grafting ratio increased to a critical value, the surface could display a switchable wettability behavior driven by temperature that amplified the interaction modes between the water molecules and the polymer chain. We selected two representative states of PN10-g-L.SEC and PO10-g-L.SEC surfaces to illustrate the surface superhydrophobicity transformation. Interestingly, for the PN10-L.SEC surface with a R_q of 2.32 mm, the surface displayed a superhydrophobic/superhydrophilic change with a CA of 3.1 ° at 20 °C and 154.3° at 40 °C. The experimental results showed that the PN10-g-L.SEC (20°C) surfaces with under-water superoleophobic ($\theta_{o/w}$~151.5°) changed to $\theta_{o/w}$~1.4° at 40°C. This demonstrated that the hydrophilic moieties of PNIPAM brushes on PN10-g-L.SEC surface extended towards the water phase at 20°C. Above the LCST (at 40°C), the dehydration of hydrophobic groups induced the oil phase to displace the water phase on the surface. When the surface was prewetted by hexane, the IP interacted with hexane and repel water driven by solvation. Thus, the PN10-g-L.SEC surface

exposed more hydrophilic groups at low temperatures, which transformed into the hydrophobic groups at higher temperature. A large amount of hydrophobic groups (2 methyl/per unit) endowed the surface with a low surface free energy of 29.3 mJ m^{-2}, and in combination with the hierarchical structure, it produced the superhydrophobic characteristic as indicated by the CA above the LCST. A similar thermally switching between superhydrophobic and superhydrophilic was observed for the PN20-g-L.SEC surface (**Figure 4.18**). Additionally, the PN10-g-L.SEC surface possessed a rapid transformation between superhydrophilicity and superhydrophobicity as a single cycle took only several minutes, changing between 2º to 150º on PN10-g-L.SEC surface when the temperature cycled between 20°C and 40°C. This reversibility of the surface hydrophobicity remained after the sample was stored without special protection for more than three months, confirming that the polymer-L.SEC was robust and stable.

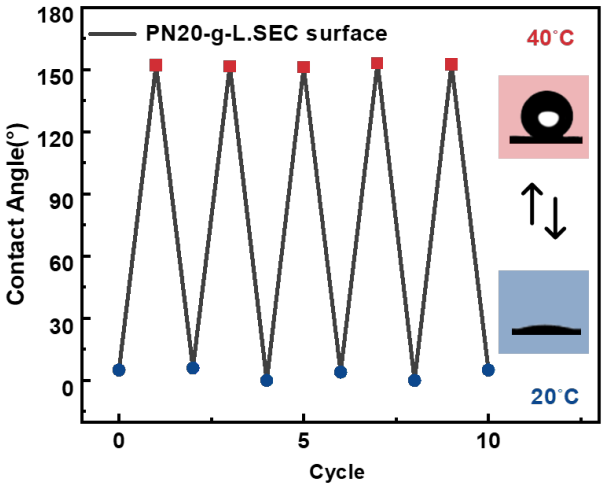

Figure 4.18 Thermally induced wettability transition of PN20-g-L.SEC surface cycling from 20°C to 40°C

Additionally, we observed that the PO10-g-L.SEC surface displayed superhydrophilic characteristics in contrast to PN10-g-L.SEC. The interfacial behavior at air/ $POEGMA_{188}$/water and the corresponding water affinity behavior was determined by the surface free energy of the hydrophobic MMA and hydrophilic OEG groups. Interestingly, the R_q was 2.25 mm for the PO10-g-L.SEC surfaces, where the CAs remained constant at 1° (20 °C) and 2° (40 °C) respectively, displaying superhydrophilicity without wettability transition. Below the LCST (26.9°C), the ether groups on PEG segments formed hydrogen bonds with water molecules. However, above the LCST, this balance was disrupted and the interaction between the side chain of $POEGMA_{188}$ and water decreased, resulting in the enhanced polymer–polymer interactions over polymer-water interactions. The $POEGMA_{188}$ chains collapsed into a globule conformation with the OEG chains/groups surrounding the hydrophobic MMA backbone yielding a less hydrophobic state (θ_i <90°), where the water repellent characteristic was less severe compared to PN10-g-L.SEC.[152] This phase

transition behavior led to a more hydrophobic of $POEGMA_{188}$ globules above the LCST compared to the solvated chains at low temperature, with the overall characteristics being somewhat hydrophilic. Since the OEG segments resided on the outer surface of the collapsed chains with a higher surface free energy, hence, the water droplets deposited on the PO10-g-L.SEC surface would spread with a low CA of 2°. These results confirmed the intrinsic hydrophilic characteristic of the polymer chain conformation together with the hierarchical structure controlling the surface wettability. To conclude, the thermally responsive switching between superhydrophobic and superhydrophilic state of PNm-g-L.SEC surfaces (m~10, 20) was observed due to the reduced low surface free energy caused by the hydrophobic IP moieties orientation at air/solid/water interface. In contrast, POm-g-L.SEC surfaces (m~10, 20) possessed a higher surface free energy due to the hydrophilic PEG segments being exposed to the interface resulting in a non-switchable wettability phenomenon.

To further confirm the mechanism of hydrophobic enhancement induced by the surface roughness and the interfacial water structure transformation, we imaged the 3D contact interface between the liquid droplet and the PN10-g-L.SEC surface at 20 and 40 ^{o}C via confocal laser microscopy. Below the LCST, the stable and ordered hydrogen bond network promoted the wetting of the microparticle surface by water molecules that also occupied the gap between the microparticles generating superhydrophilic domains as indicated in **Figure 4.19A**. The green dots (fluorescence-stained) persisted from the base substrate to the outer surface, demonstrating the fully wetted state. Above the LCST, the droplet contacts with the PN10-g-L.SEC surface revealed that the liquid baseline was suspended between particles, indicating a non-wetted state (**Figure 4.19B**). This observation further demonstrates that the more disordered water structure (intermediate water) caused by the polymer chain transition induced a weaker binding interaction resulting in a lower tendency to wet the surface. Thus, the liquid would not penetrate the air-pockets to fill the surface resulting in the observed superhydrophobic character of the substrate.

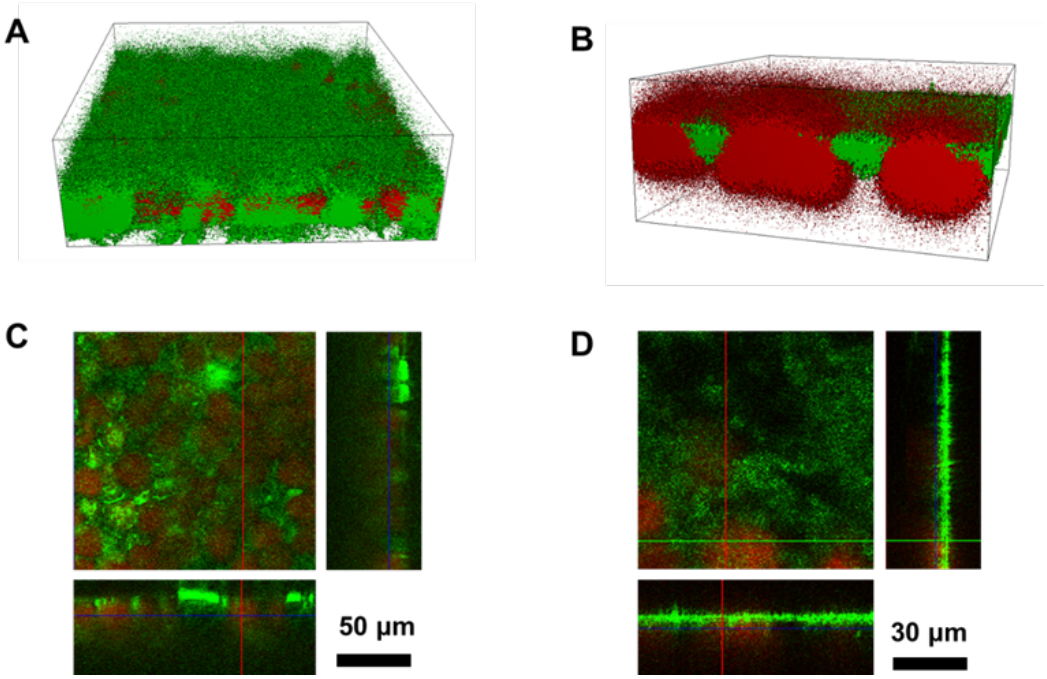

Figure 4.19 The interactions between water and PN10-g-L.SEC surface at different temperatures observed by confocal laser microscopy: A. 20℃, B.40℃, The three-phase contact line on PN10-g-L.SEC surface: C. 20℃, D.40℃, (L.SEC sporopollenin is autofluorescence and water is dye by Rhodamine B, where the z stack scope is 50 μm)

The molecular structure and chemical composition of PNIPAM and $POEGMA_{188}$ impacted the interaction between water molecules and polymer brushes, which controlled the hydrophobicity transition characteristics of the surface. Preferential exposure of the hydrophobic or hydrophilic moieties of the polymer-L.SEC altered the interfacial characteristics of the surrounding solvents (water or oil) and the surface, which could be used to manipulate the macroscopic wettability. Thus, these pollen-based thermo-responsive surfaces offer a novel design strategy to control the surface wettability transformation and exploited in various on-demand applications, such as emulsion separation. The switchable oil and water repellency driven by temperature can be conducted by alternately prewetting with water and oil, which gives the separation membrane the versatility to handle oil−water mixtures (**Figure 4.20**).

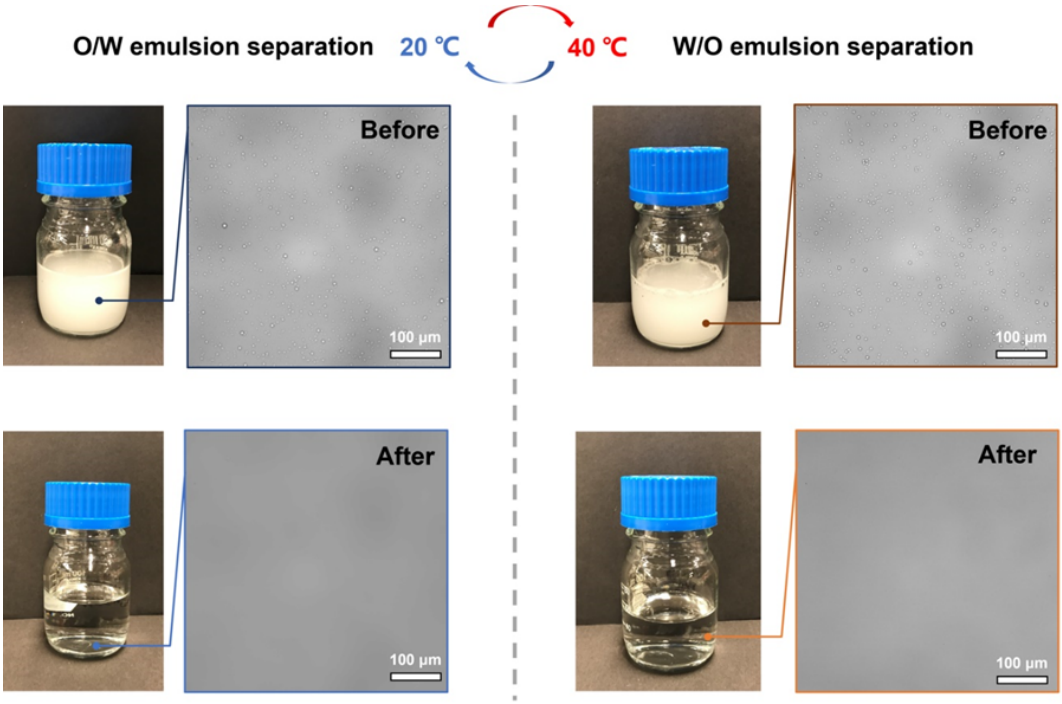

Figure 4.20 The potential application of PN10-g-L.SEC membrane applying for thermo-responsive emulsion separation and the optical images of the feed emulsion and filtrate

4.4 Conclusion

In summary, we studied the temperature-dependent interfacial properties on thermo-responsive surfaces. Specifically, we investigated the assemblies of microparticles grafted with two types of LCST polymers, PNIPAM and $POEGMA_{188}$, and correlated the interfacial water structure variation at multiple length scale with the wettability transition of integrated surface (formed by self-assembly of microparticles), as revealed by Raman measurements, supplementary rheology experiments and confocal microscopy. From the analysis at nanoscale and macroscale length scale, we concluded that the increased intermediate water (decreased bonded water structure) with combined surface roughness resulted in the enhanced hydrophobicity. This surface design strategy provides information that correlates the molecular-level conformational transition with the macroscopic surface wettability. Moreover, the knowledge and fundamental understanding derived from this study demonstrate the potential application of PNIPAM and $POEGMA_{188}$ by controlling the interfacial water structure at solid-liquid interface in other systems, such as biobased responsive surfaces.[153]

Chapter 5. Dual-Tunable Adhesion and Wetting Surface for Programmable Water Droplet Manipulation using Shape-Memory Plant Pollens

5.1 Introduction

Liquid manipulation on surfaces in a controllable manner have attracted increasing attention, offering numerous possible applications such as liquid transfer without mass loss[154], water harvesting[58], cell adhesion[155]. To optimize the controllable liquid manipulation, various artificial engineering superwettable surfaces have been developed because of their simplicity and efficiency. A particular interesting research area is to endow the surface with switchable adhesive status capable of manipulating the pinning and sliding of droplets in response to external stimuli, showing superior intelligence and controllability in smart devices.[1] In this regard, temperature, light, or electrically responsive surfaces offer a promising strategy to develop substrates or systems with precise control and low energy consumption.[2] However, the delayed response time to external stimuli remains a significant challenge for further improvement of these surfaces. To further advance the development of controllable liquid manipulation surfaces, it is necessary to explore surfaces that have a programmable response range, which are also highly sensitive to external signals.

Thermo-responsive polymers grafted onto surfaces and coatings offer a versatile approach to design materials with adjustable properties. However, the fixed LCST limits the surface to be widely used in different fields. To address this issue, incorporating comonomers shows promise to adjust the LCST behavior by altering the interfacial water structure around the polymer, resulting in an extended phase transition temperature. This imparts the thermo-responsive properties to match the unique temperature conditions of different applications.[156] Moreover, the orientation of the exposed functional groups at the interface has a significant influence on the wettability characteristics, such as contact angle, surface free energy, further affecting the response time.[5] Droplet dynamic behavior is another factor to describe the water manipulation property on surfaces, involving contact angle hysteresis (CAH) to demonstrate the friction force during droplet movement.[157] Notably, the adhesive and attractive forces of surfaces show potential for better characterizing droplet-surface interactions and provide guidance for the precise design of wettable surfaces.[158]

Plant-based sporopollenin microparticles extracted from pollen grains possess environmentally friendly properties and structural stability. The extine sporopollenin is known as the diamond of biopolymers and exhibits remarkable mechanical stability comparable to many carbon types and synthetic polymers.[159] However, previous studies have overlooked the hierarchical structure present on the extine surface, such as the pH-responsive shape-transform architecture found on the sunflower sporopollenin extine shell (SEC). There are largely untapped opportunities to explore the surface chemistry of the outer sporopollenin surface, where the hierarchical structural characteristic is a beneficial for constructing liquid-repellent surfaces.

Herein, we study the programmable thermo-responsive surface constructed using SECs to obtain superwettability transition and tunable adhesion status at various LCSTs. Specifically, by tethering

copolymers of N-isopropylacrylamide (NIPAM) with hydrophobic comonomer of N-tert-butylacrylamide (NtBA) on SEC microparticles, each building blocks of SEC features with temperature-dependent interfacial behaviors as revealed by thermodynamic analysis and interfacial tension. Additionally, rheological measurements illustrated that the hydrogen bonding network can be easily disrupted and rearranged with the addition of hydrophobic comonomer NtBA near the LCSTs. Furthermore, the polymer conformational transition driven by temperature combined with hierarchical and tunable roughness of the SEC prepared surfaces further influence the macroscopic surface wettability transformation as demonstrated on the water static and dynamic wettability measurements. To better understand the droplet-surface interaction, we investigated the influence of surface roughness and interfacial conformation on the surface adhesion under superhydrophobic state above the LCST using the micro-newton force measurements. Surface roughness reflects the active immerse force, while the interfacial conformation determines the attractive force that significantly impacts the adhesive force and dictate the droplet manipulation from pinning adhesion to sliding transfer. By tunning related parameters, we could achieve different interaction mechanisms with liquids according to the requirements of specific applications. For example, the surface with tunable adhesive force could be applied to droplet transfer without loss under specific temperature. While achieving fog harvesting enhancement, the surface feature with higher attractive force could be a good candidate to balance the trade-off between nucleation and transport. Besides, the concept described in this study shows a potential for the utilization of biobased thermal-responsive surface with tunable LCSTs for biomedical applications, like antibacterial and drug delivery, where such application has strict temperature requirement.

5.2 Materials and method

Chemicals and materials

Sunflower pollen (Flinn Scientific Canada Inc.), N-isopropylacrylamide (NIPAM), cerium (IV) ammonium nitrate, potassium hydroxide, phosphoric acid, acetone, ethanol, Rhodamine B and Nile Red were used as received from Sigma-Aldrich. All chemicals were used without additional purification, unless stated otherwise. Milli-Q water (resistivity of 18.2 MΩ·cm) was used to prepare the aqueous dispersions.

Preparation of surface-engineered sunflower sporopollenin extine shells (SECs)

Extraction of SECs Natural sunflower pollen grains were defatted to remove lips and intine materials yielding indestructible, ultra-tough, defatted pollen extine shells. For this purpose, sunflower pollen grains (50 g) were refluxed in acetone (300 mL) for 3 h in a round-bottom flask under magnetic stirring (50°C, 350 rpm). The defatted sunflower pollen grains were recovered via vacuum filtration for intine materials extraction. This process involves pollen shell extraction and subsequent incubation in an alkaline medium, where the defatted pollen was treated with 2M potassium hydroxide (KOH) at 80 °C and stirred for 2 h to remove its internal cytoplasmic content. KOH-treated spores were next subjected to neutralization, extensively washed with water, and

filtered. Finally, SECs after each chemical treatment step were recovered for analysis and stored at room temperature prior to their use in future experimentations.

SEC modified with thermo-responsive polymer layer First, 100 mL of SEC (0.1 g) aqueous dispersion was mixed with 1.0 mL 70 wt% HNO_3 in a three-neck flask under magnetic stirring and degassed with nitrogen flow. The reaction was allowed to proceed under stirring in an ice bath for 30 min prior to the polymer grafting. Next, cerium (IV) ammonium nitrate (CAN) (0.05 g 0.10 mmol) was added to the reaction flask forming radical sites on the hydroxyl groups of SEC through the reduction of ceric ion.[14] NIPAM monomer (1.13 g, 10.0 mmol) was introduced to initiate the polymerization and the solution was kept in an ice bath under slow magnetic stirring for 3h. Finally, the product was dialyzed against deionized water until the measured water conductivity remained constant. The reaction was repeated with various amounts of the NIPAM and NtBA grafted moieties. The as-prepared PNIPAM modified SEC microparticles designated as PNn-g-SECm, where n corresponding to the grafting molar ratio of PNIPAM to PNtBA (1:0, 8:2, 6:4, 4:6, 2:8) and recorded as PNI-g-SECm, PN8-g-SECm, PN6-g-SECm, PN4-g-SECm, PN2-g-SECm,

SECs engineered with adjustable topography To obtain structured samples, SECs were incubated in alkaline environment (2M KOH) for various incubation times (1, 3 or 5 h). The resulting pollen microparticle suspension was collected in the final centrifugation step followed by the supernatant removal, then stored for further utilization and characterization. The samples were designated as SECm, where m corresponding to incubation time ranging from 0, 1, 3, 5 and labelled as SEC0, SEC1, SEC3, SEC5.

Preparation of SEC-based superhydrophobic surface

The SEC-based superwettable surfaces were constructed via the immobilization of polymer-SEC on an aluminum sheet. We sprayed the SEC powder on the aluminum sheet coated with an adhesive glue, where the surfaces were uniformly formed, and the coating thickness was manipulated by adjusting the concentration of formulation. The coated surface was vacuum dried, after which they were used for further analysis.

Characterization

Surface Wettability Characterization

The water/oil static and dynamic contact angle measurements were performed using the OCA 15 (Dataphysics). To measure the static contact angle, a sessile drop (5 μL) was dispensed onto the test surface with an auto-dosing system equipped with a 500 μL needle, and side-view images or videos of the droplets were captured with a camera. To determine the accurate contact angles, the captured images were further analyzed by their Instant drop image evaluation software and Image J analysis software.

The surface adhesion force measurements were conducted via a tensiometer accompanied by a multi-axis sample stage. The force detected when using 5 μL droplet approaching and retracting from the surfaces at ~0.10 mm/s, while the droplet's size and shape were recorded by high-speed camera (IDS uEye camera). In addition, the adhesive force mapping was process in a point-by-point

force detection with the support of a multi-axis sample stage with a step size of 0.1 mm for an area 2.0 × 2.0 mm.

The contact line behaviors between water-solid surface were measured by confocal microscope (Zeiss LSM 510 Meta Laser Scanning Confocal Microscope (CLSM)) with ZEN 2009 analysis system. The observation magnification was 40x/1.3 Water DIC, and an immersion objective lens was used, with the immersion medium being water.

Topography Characterization

The shape and structure of SECs were visualized and examined from optical microscopic images and videos captured using the Nikon LV ND microscope or Photron SA5 high-speed camera. The surface topography was characterized via scanning electron micrographic (SEM) observations, confocal optical microscope (Olympus LEXT OLS5000). The particle size was measured using Particle size analyzer (Anton Paar 1190) and Nano Zetasizer (Malvern ZS90) with temperature control system.

Thermodynamic Characterization

The thermal responsive characteristics was evaluated by performing turbidimetric measurements on the Varian (Cary 100 Bio) UV–vis spectrometer equipped with a temperature controller and Micro-differential Scanning Calorimetry (DSC). The rheological properties of the concentrated suspension were characterized in a Malvern Kinexus ultra+ rheometer with the cylindrical measuring system and a solvent trap to prevent water evaporation.

5.3 Results and discussion

5.3.1 Designing Programmable SEC-based Surfaces

The design of programmable SEC-based surfaces through colloidal assembly of engineered SEC microparticles is illustrated in **Scheme 1**, taking advantages of the pH-responsive shape change of sunflower pollen and the surface composition transition induced by the grafted thermo-responsive polymer layers poly(NIPAM-co-NtBA). In this regard, this method allows for the creation of SEC-based surfaces that can be programmed to exhibit specific wettability properties.[5] First, the thermo-responsive polymer coating layers consisting of copolymers of NIPAM with hydrophobic comonomer of NtBA, endowed the surfaces with hydrophobic/hydrophilic wettability transition characteristics at the critical temperature. In addition, this temperature, referred to as LCST, could be adjusted by adjusting the grafting ratio of copolymer on each pollen particles, ranging from a large temperature gradient from 33°C to 14°C. Furthermore, in the fabrication of pollen-based surfaces, the hierarchical structures were derived through the self-assembly of the pollen and its inherent roughness characteristics. By combining hierarchical structures and thermo-responsive coatings, the surfaces are capable of undergoing superwettability transformation, exhibiting superhydrophobicity above their LCST and superhydrophilicity below their LCST. Particularly, the adhesion behaviors are significantly amplified on the modified superhydrophobic surfaces above LCST, and it is possible to control droplet behavior from a pinned state to a sliding state.

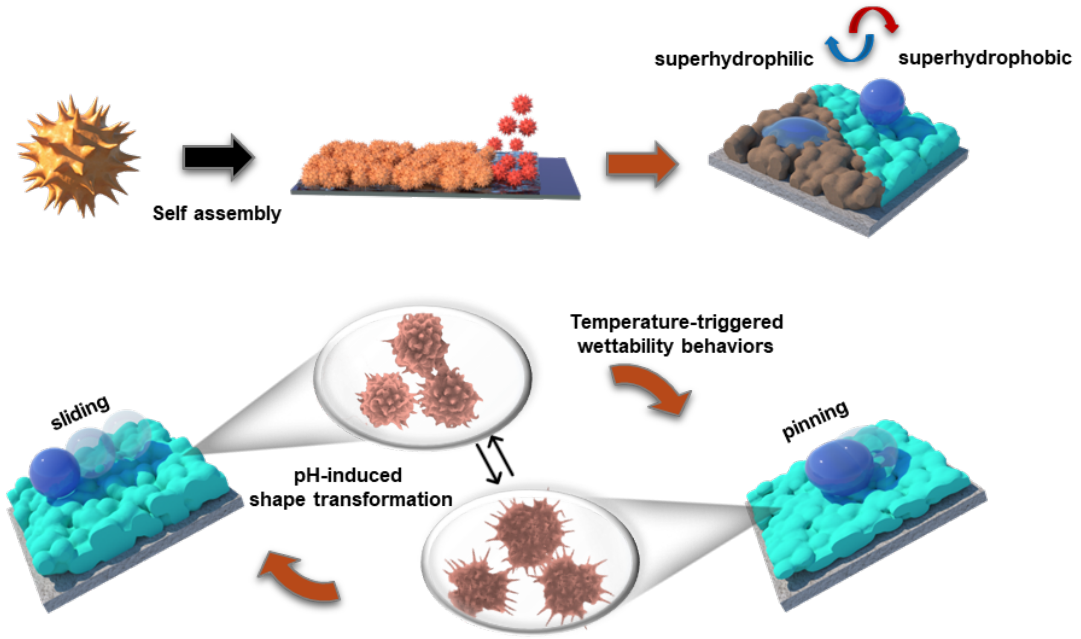

Scheme 5.1 Illustration of fabrication procedure of pollen-based surfaces using thermo-responsive polymer grafted SECs as building blocks, where the surface conformation could be tuned by comonomer grafting ratio and the topography could be altered by different pH incubation. The surface could achieve superhydrophobic/superhydrophobic wettability transition around its LCST, while exhibiting switchable adhesion properties involving droplet sliding on high roughness surface and pinning on low roughness surface.

Taking advantages of the abundance of hydroxyl groups on the outer surface of SECs after the extraction process[160], SECs were first initiated and grafted with thermo-responsive copolymers, poly(NIPAM-co-NtBA) (**Figure 5.1a**). By altering the comonomer grafting ratio, the distinct interfacial behaviors especially water molecule affinity and thermodynamic characteristics of PNn-g-SECm were demonstrated. SEM images revealed the architecture of the polymer grafted canopy of PNI-g-SEC0 with high roughness nanostructure. Further evidence on the successful polymerization of copolymer layer from the surface was provided by X-ray photoelectron spectroscopic (XPS) elemental analyses. The elemental composition of SEC0, PNI-g-SEC0, PN8-g-SEC0 were compared, confirming that this layer contained organic molecules with increased amount of C1s as the grafting ratio of comonomer was increased (**Figure 5.1b**) and the expected changes in the ratio of C-N, C-H, C-O bond on PNm-g-L.SEC surface[161]. High resolution spectra of C1s peak obtained from all the samples were found to be well-fitted by four types of peaks: 285.0 eV (C-C or C-H), 286.5 eV (C-O single bond) and 288.4 eV (O=C) and the new specific peaks corresponding to C-N bond (285.5 eV and 287.5 eV) as shown in **Figure 5.1c**. Fourier transform infrared spectroscopy (FT-IR) also confirmed the successful grafting of poly(NIPAM-co-NtBA) onto the extine of SEC. Specifically, the IR spectrum of PN8-g-SEC0 exhibited distinctive peaks indicating the existence of amine groups, where the peak observed at 1650 cm^{-1} was associated with

the N-C=O bond and the peak at 1550 cm^{-1} corresponded to the N-H bonds.[162] The peak observed at 2970 cm^{-1} was assigned to the symmetric and antisymmetric CH stretch of the methyl groups, whereas the peaks observed at around 2850 cm^{-1} and 2870 cm^{-1} were attributed to the symmetric stretches of CH_2 and CH_3, respectively. (**Figure 5.2a**). With regards to thermal responsive characteristics, the LCST behavior of modified SECs in aqueous solution was measured by the UV-vis spectrophotometry. As shown in **Figure 5.1d**, the PN-g-SEC0 solutions exhibited a change in transmittance around the critical temperature of 33.2°C, indicating the transition of the polymer chains from a random coil configuration to a globular conformation. Incorporating PNtBA into the polymer structure led to a reduction in the LCSTs, where the phase transition occurred rapidly at 28°C, 21°C, 17°C and 12°C for PN8-g-SEC0, PN6-g-SEC0, PN4-g-SEC0 and PN2-g-SEC0, respectively. Besides, the solution turbidity changed further providing clear evidence of the phase transition of PN8-g-SEC0. As such, PN8-g-SEC0 was well-dispersed in aqueous solution with a brown color at 10°C, and the solution transformed into a turbid dispersion at 30°C, while the suspension transformed into a yellow opaque dispersion. This result revealed that the phase transition of polymer brushes induced a rearrangement of the hydrophobic/hydrophilic groups, which subsequently impacted their dispersibility in water. Moreover, the changes in the interfacial tension (γ_{wo}) could serve as an effective indicator to verify the interfacial rearrangement of these groups. For instance, the γ_{wo} of PN4-g-L.SEC0 decreased from 39.8 mN m^{-1} to 27.9 mN m^{-1} with increasing temperature. The results demonstrated that that the exposure of hydrophobic methyl groups above the LCST induced the rearrangement of microparticles at the water-hexane interface, resulting in the simulated droplet shape transformation and a reduction in interfacial tension.[163] Under this condition, the predominately hydrogen bonding interaction between water molecules with $-NH_2$ and -C=O groups at low temperature was disrupted to form intramolecular H-bonding.[164] Additionally, the amount of hydrophobic groups on the side chain had a significant impact on the surface tension (γ_{lv}), as it altered the affinity of polymer shell with water molecule and the interfacial behavior of SECs.[165] As depicted in **Figure 5.1f**, the γ_{lv} of PN8-g-L.SEC0, PN6-g-L.SEC0, PN4-g-L.SEC0, PN2-g-L.SEC0 decreased sharply from 40.8 mN m^{-1}, 31.5 mN m^{-1}, 22.6 mN m^{-1} to 18.2 mN m^{-1} respectively. Conversely, PNI-g-L.SEC0 with a lower amount of hydrophobic methyl groups exhibited the highest γ_{lv} value of 59.6 mN m^{-1}.

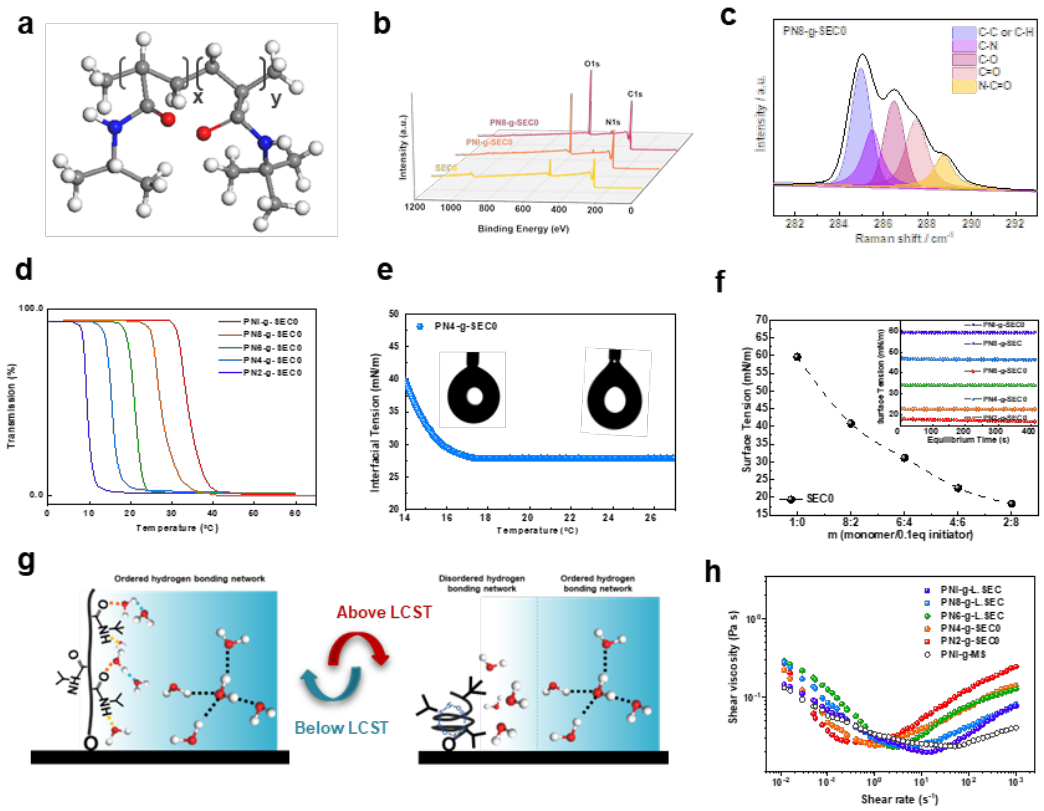

Figure 5.1 a. Illustration of molecular conformation of poly(NIPAM-co-NtBA), b. The hydrogen bonding network formed at the interface of SECs, c. XPS characterization of PNn-g-SEC0, d. C1s, e. LCSTs of PNn-g-SEC0 characterized by UV-vis spectroscopy, f. Interfacial tension between water/hexane of PN4-g-SEC0 measured by pendant drop method, g. Surface tension of PNn-g-SEC0 varying the comonomer grafting ratio, h. Rheological profiles of PNn-g-SEC0.

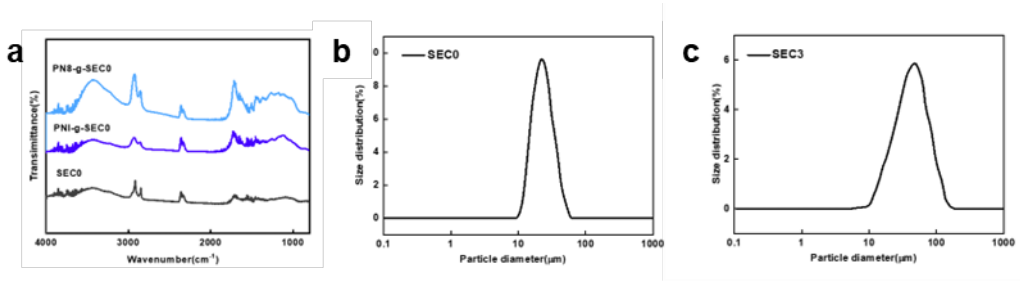

Figure 5.2 a. FT-IR spectrum of SEC0 and PNI-g-SEC0 Particle diameter of pollen microparticles:b. SEC0,c. SEC3

Moreover, the rheological profiles revealed the strength of hydrogen bonding network around polymer shell of SECs. When the temperature was raised to above the LCST, the interfacial water structure undergo a transformation, where the original tetrahedral hydrogen bond structure transformed into intermediate water structures around the collapsed polymer chains[5, 166] **(Figure 5.1g)**. This resulted in the formation of a distorted and heterogeneous hydrogen bonding network consisting of a hydration shell at the interface of SECs, which was susceptible to be disrupted under

hydrodynamic force yielding an increase in the viscosity.[167] As shown in **Figure 5.1h**, the shear stress would first be suppressed, which was then followed by the onset of shear thickening. It is worth noting that the strength of hydrogen bonding network was weakened with the introduction of hydrophobic comonomer (NtBA), which corresponded to the rapid occurrence of the shear thickening transition. An increase in the hydrophobicity of particles reduced the thickness of lubricant layer around the hydration shell, which could result in particle aggregation.[146, 168] This change increased the frictional force between the particles, which led to a stronger shear thickening phenomenon. Moreover, the roughness structure has a significant impact on shear thickening effect, attributing to the strong frictional force generated that could be disrupted the hydrogen bonding network with increasing temperature.[149] An example of this phenomenon was observed for the PNI-g-SEC0 that displayed a stronger shear thickening effect when compared to smooth microparticles PNI-g-SM. As a result, the rougher surface of the SEC particle resulting in an increased proportion of the polymer-water interface and more apolar groups exposed towards the outer surface, enabling the SECs with the high-sensitive water affinity transformation around the LCST.[169]

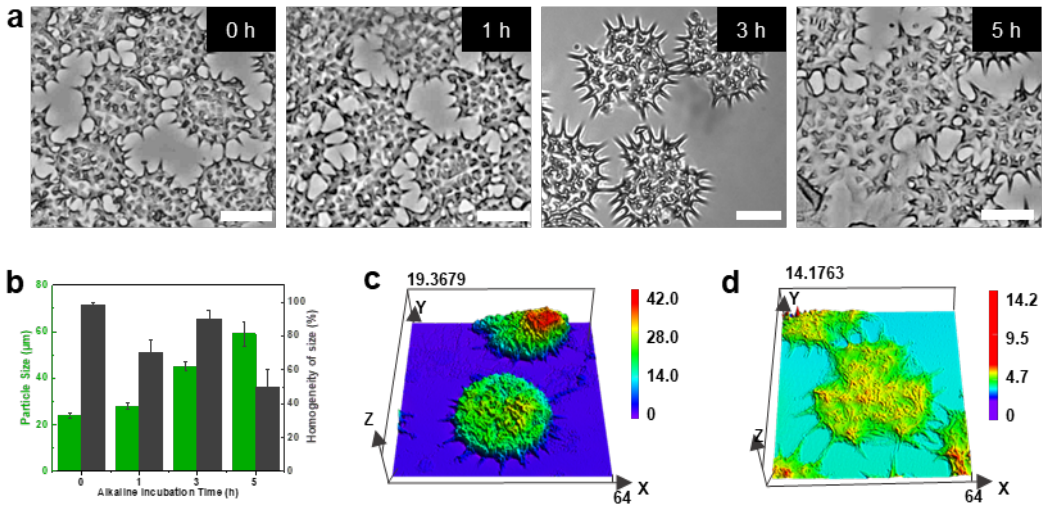

Figure 5.3 a. The morphology variation of SECs that incubated in alkaline environment (pH-12) at varying incubation times (0-SEC0, 1h-SEC1, 3h-SEC3, 5h-SEC5) observed by optical microscopy, b. Particle size and homogeneity of size corresponding to SECs, Structures and roughness factor of SECs characterized by laser confocal microscopic images: c. SEC0, d, SEC3.

Furthermore, we transformed defatted pollen grains into pliable, soft hollow microshells via alkaline incubation, as it used to adjust the surface topography with different roughness. The morphological variation of SECs with pH environment and incubation time changes was observed by optical microscopy, where 3D microspherical particles underwent extensive swelling when the incubation pH was changed from 2 to 12 (**Figure 5.3a**). During this process, the three apertures of the SECs began to open and stretch, while the 3D structure of the particles collapsed and flattened with the spiky external morphology. These unique shape changes were initiated by the chemical dissociation

of pectin that promoted the hydrolysis and expansion of the cellulose chains[125] (**Figure 5.3b**). Moreover, the shape transformation of SECs as a function of incubation time (1h, 3h, 5h), the SECs morphology was transformed from the spherical shape that swelled into 2D microsheets with three open apertures. After 1h incubation, some SECs re-organized into hexagon shape with three apertures, while some maintained their original shapes. The average particle size of SEC1 was 28 µm, while the homogeneity of particle size was determined to be 72%. In contrast to the defatted pollen particles, the pollen particles of SEC3 that were incubated in KOH for 3 hours exhibited a significant increase in size, swelling up to a diameter of 46 µm (**Figure 5.2b and 5c**). It is worth noting that the homogeneity of particle size was determined to be 90% although these particles experienced structural variation into hexagon shapes during hydration and flattening after natural drying, as shown in the laser confocal microscopic image in **Figure 5.3c** and **5.3d**. Particularly, the dry thickness decreased from 23.1 µm in SEC0 to 4.72 µm in SEC3, while the roughness factor of single pollen particle decreased from 1.85 µm in SEC0 to 0.227 µm in SEC3, indicating a significant change in the particle structure. Thus, owing to the unique and uniform structure, good mechanical strength, the swollen SEC3 and the original defatted SEC (SEC0) were selected as the two comparable building blocks for further surface construction. In addition, extended incubation of the pollen particles in KOH resulted in a significant decrease in their mechanical stiffness. This made them susceptible to swelling and irreversible structural re-organization during hydration, as was observed for SEC5 (**Figure 5.3a**).

5.3.2 Thermal Control of Wettability Transition of SEC-based Surfaces

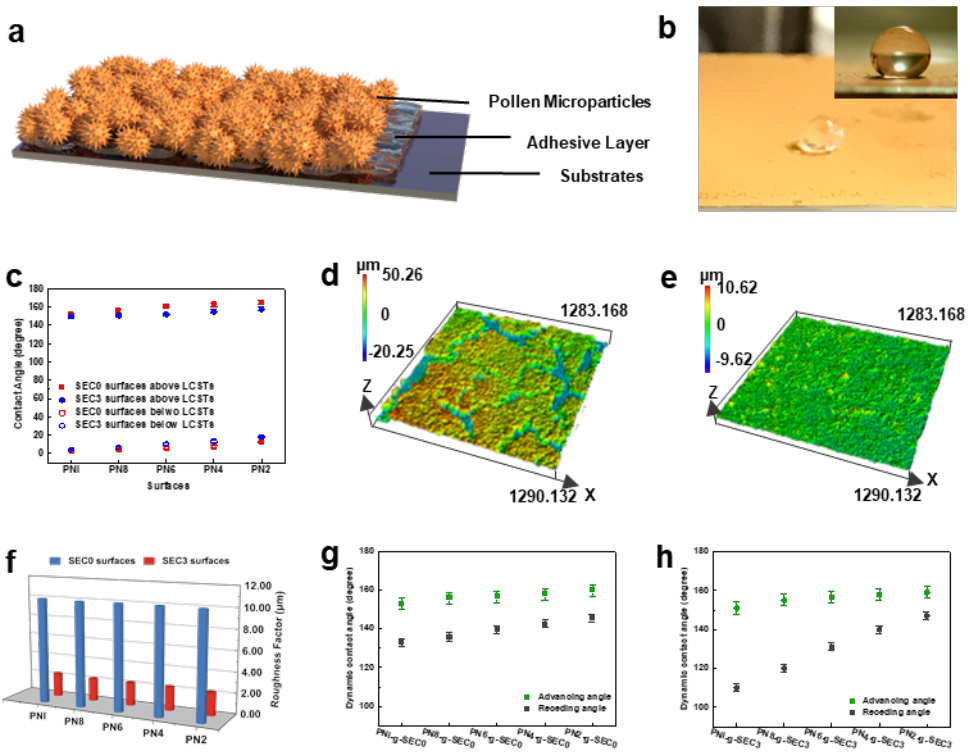

Figure 5.4 a. Surface topography of pollen-based surfaces, b. Digital images of PN8-g-SEC0 and

its wettability above LCST, c. Illustration of CAs on PNn-g-SECm surfaces around LCSTs, d. Surface roughness of PN8-g-SEC0 and PN8-g-SEC3 observed by laser confocal microscopy, Illustration of wettability characteristics of PNn-g-SECm surfaces: f. the roughness factors, g. ACAs and RCAs displayed on PNn-g-SEC0 above LCSTs, h. ACAs and RCAs displayed on PNn-g-SEC3 above LCSTs.

The hierarchical structures of SEC-based surfaces were fabricated via the self-assembly of modified SEC microparticles, which were sprayed onto aluminum sheet coated with an adhesive glue (**Figure 5.4a**). As shown in **Figure 5.4b**, the as-prepared coatings on the surfaces possessed a yellow-brown color that were robust when subjected to the wettability analyses. The temperature-dependent wettability characterization was performed by manipulating the surface (kept in a chamber) using a a thermal controller allowing for the rapid temperature adjustments to characterize the switchable wettability characteristics. In this regard, static water contact angles (CA) and surface free energy were first used to examine the wettability transition behaviors occurring on the pollen-based surface under various LCSTs. As shown in **Figure 5.4c**, PNI-g-SEC0 surface displayed a switchable wettability transition behavior that changed between the superhydrophilic and superhydrophobic state at around its LCST of 33.2°C. The static CA oscillated between 2 º to 151º on PN-g-SEC0 surface when the temperature cycled between 20°C and 40°C. It is worth noting that the PNI-g-SEC3 surface with a similar composition to PNI-g-SEC0 surface but varying in hierarchical structure could achieve superhydrophobic/superhydrophilic wettability transformation as well. However, the smooth polymer-grafted surfaces could only achieve hydrophobic/hydrophilic wettability state transformation when subjected to the critical temperature. As observed from **Figure 5.5,** we fabricated the poly(NIPAM-co-NtBA) copolymer-tethered smooth surface (PNm-g-SS) to study their intrinsic CAs. Among them, PN2-g-SS surface exhibited the most hydrophobic character with a CA of 78° above its LCST of 9.5°C but it could not attain the hydrophobic state (< 90°). Moreover, the PN8-g-SEC0, PN6-g-SEC0, PN4-g-SEC0, PN2-g-SEC0 also showed superhydrophilic to superhydrophobic state transition (**Figure 5.4c**). However, with the increasing amounts of hydrophobic comonomer the hydrophobicity of the surface was enhanced. Above its LCSTs, the CAs increased from 151º to 162º corresponding to PN8-g-SEC0 surfaces and PN2-g-SEC0 surfaces. Besides, the PNn-g-SECm surface possessed a rapid transformation between superhydrophilicity and superhydrophobicity since a single cycle took only several minutes, while the thermally switching could cycle more than 10 cycles. Furthermore, the temperature signal used to trigger this wettability transformation could be controllede by adjusting the comonomer grafting ratio. It is evident that obtaining a state of superwettability required the presence of both suitable surface topography and composition.

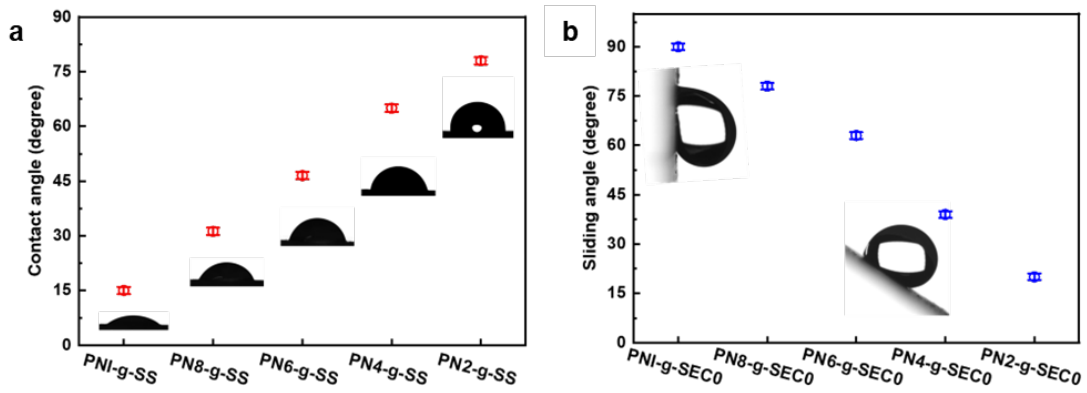

Figure 5.5 a. Contact angles measured on copolymer grafting onto the flat substrates, b. Sliding angles measured on PNn-g-SEC0 surfaces

The pH-dependent shape change displayed by surface-anchored elastomeric SECs could be harnessed to modulate surface topography to tune the dynamic surface wettability. Confocal laser microscopy was used to visualize the roughness of the surface topography of the pollen-based surfaces (**Figure 5.4d and 5.4e**), where the green-yellow-red areas corresponded to the height of the protrusions on surfaces formed by the assembly of SEC microparticles and the blue regions represented the vacancies between the protrusions. Besides, the surface topography of the pollen-based surfaces was evaluated by quantifying the roughness factor (R_q) (**Figure 5.4f**). For example, PN8-g-SEC0 exhibited a high R_q of 10.32 μm, while the surface of PN8-g-SEC3 showed a significant reduction in R_q to 2.21 μm. This distinctive surface features were attributed to the unique shape of single pollen microparticles and their assembled porous network structure, which had a significant impact on the droplet-surface interactions.[170] In particular, we performed the dynamic wettability characterization on the surface above its LCST, such as contact angle hysteresis (CAH), sliding angle to enable an effective comparison of the droplet behavior on superhydrophobic surfaces. As depicted in **Figure 5.4g**, the PN8-g-SEC0 surface exhibited a low CAH of 20° due to the high advancing contact angle (ACA) of 156±2° and a low receding contact angle (RCA) of 136±2°. Conversely, the lower surface roughness factor led to a significant increase in the CAH, as evidenced by the PN8-g-SEC3 surface exhibiting a large CAH of 35°. This is due to the reduction in air pockets on the surface, which increased the interacting area between the water and surface, resulting in higher frictional force that hindered droplet movement.[12]

In addition, with the enhancement of hydrophobicity of the polymer shell, the receding contact angle gradually increased, corresponding to the RCAs of PN8-g-SEC3, PN6-g-SEC3, PN4-g-SEC3 of 109°, 123°, 137°, respectively. As a result, the surface modified with a larger amount of hydrophobic comonomer exhibited a reduction in the contact angle hysteresis (CAH), with PN4-g-SEC3 displaying a CAH value of 18°. With further increase in the hydrophobicity/hydrophilic monomer ratio, the PN2-g-SEC3 surface displayed a lower CAH of 15±2°. The results indicated that the surfaces with more exposed hydrophobic groups (methyl group on the side chain of PNAIPAM, PNtBA) at the three-phase line encountered a higher energy barrier that needed to be

overcome, especially when the droplet contact line began to migrate from the adjacent pillars.[171] Similarly, the CAH values of PNn-g-SEC0 surfaces exhibited a decreasing trend as the hydrophobicity of the polymer shell was increased (**Figure 5.5h**). Besides, there was a good agreement between the changes in CAHs and sliding angle (SA) on these surfaces (**Figure 5.5b**). Surfaces with a higher degree of roughness, such as PNm-g-SEC0, exhibited smaller SAs. As the hydrophobicity of the grafted polymer layer on the surface increased, the surface exhibited a lower frictional force and a reduction in the surface area, ranging from 90°±1° to 20°±1°. Conversely, the PNm-g-SEC3 series of surfaces with lower roughness displayed higher SAs, with droplets adhering to the PN-g-SEC3 surface when it was tilted upwards. Besides, there was a noticeable difference in the surface adhesion forces between these two surfaces, and this will be elaborated in the subsequent section.

2.3 Modulating Adhesion on SEC-Based Surfaces

To enhance our understanding of the water-solid surface interaction, we conducted measurements and calculations of the adhesive force (F_{ad}) of the pollen-based surfaces. **Figure 5.6a** illustrates the tensile adhesion measurements performed through the touch-sensitive approach, where the force detected during the water droplet touch-retract cycle and the accompanying deformation of the water droplet shape were recorded. In particular, the starting point of the droplet suspended on the cantilever and was far from the PN-g-SEC0 surface, which was recorded as z=1.0 mm and F=0, indicating no force acting on it. As the droplet started to move downward, an attractive snap-in force was observed (F_a) when the bottom of the droplet was closed to the SEC-based surface.[172] Following this step, we applied an external force to bring the droplet into contact with the hierarchical structures and varied the immersion depths at 0.10 mm, 0.20 mm, 0.30 mm (z recorded as negative values). The rough structure of the surface generated a resistance force (F_r) to the droplet, preventing it from wetting the surface, as indicated by the different shape changes of the droplet. Upon retraction, the pull-off force increased until it reached the maximum adhesion force, F_{ad} = 79.4 μN required for complete detachment from the surface (**Figure 5.6b**).

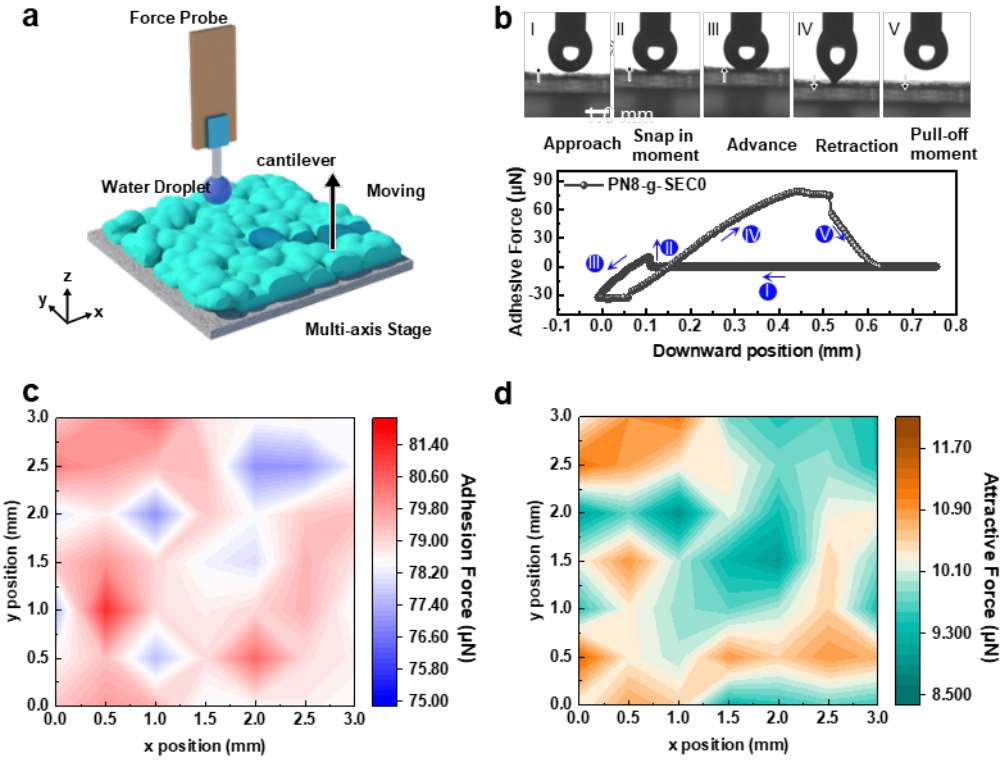

Figure 5.6 a. Schematic illustration of adhesion force measurements on the surface, **b.** The procedure of measuring and recording the adhesion force on surface, **c.** Adhesion force mapping on PN8-g-SEC0, **d.** Attractive force mapping on PN8-g-SEC0.

Moreover, we performed a point-by-point adhesive force mapping on different regions of the surface to record the micrometer-scale wetting variations on surfaces and examine the distribution of the adhesive forces. The surface adhesion force mapping for PN8-g-SEC0 and PN8-g-SEC3 surfaces with an area of 3.0 × 3.0 cm and the measurements were recorded at points with a spacing of 1.0 mm. Based on the surface adhesion mapping results, we observed that PN8-g-SEC0 had a uniform force distribution across the surface, with a value of 79.4 μN (**Figure 5.6c**). In contrast, the attractive force mapping results indicated that PN8-g-SEC0 exhibited a relatively consistent surface adhesive force of 27.6 μN, which was proportional to the adhesive force (**Figure 5.6d**).

Furthermore, the interaction forces comprising the attractive and resistant force were investigated to gain deeper insights into the relationship between the surface and droplet manipulation characteristics. As shown in **Figure 5.6b**, the droplet was observed to be attracted towards the surface and experienced a snap-in moment before coming into contact with the surface at z=0. This finding suggested that the attractive force exerted by the surface was sufficiently strong to capture the water droplet at a specific distant. To better utilize this force in droplet manipulation, we exploited the influence of surface roughness and conformation on the strength of F_a. SEC0 and SEC3-fabricated surfaces represented two typical surfaces with distinct topography. The hierarchical structures were assembled by modified SECs, as evidenced by SEM images that clearly depicted the comparative structured surfaces. In **Figure 5.7a**, it could be observed that PN8-g-SEC0

exhibited a highly rough surface structure, where the original defatted SEC0 shaped with a spherical 3D structure possessed vertical spiky spines (1~2 mm height and 200 nm width). On the other hand, PN8-g-SEC3 had a flattened surface structure, with 2D pollen microsheets tightly adhering to each other. Interestingly, there were no significant difference in the attractive force between these two types of surfaces when the grafted polymer composition was similar. For example, PN8-g-SEC0 possessed an attractive force of 10.8 μN, while the attractive force of PN8-g-SEC3 surfaces was 10.3 μN (**Figure 5.7d** and **5.7e**).

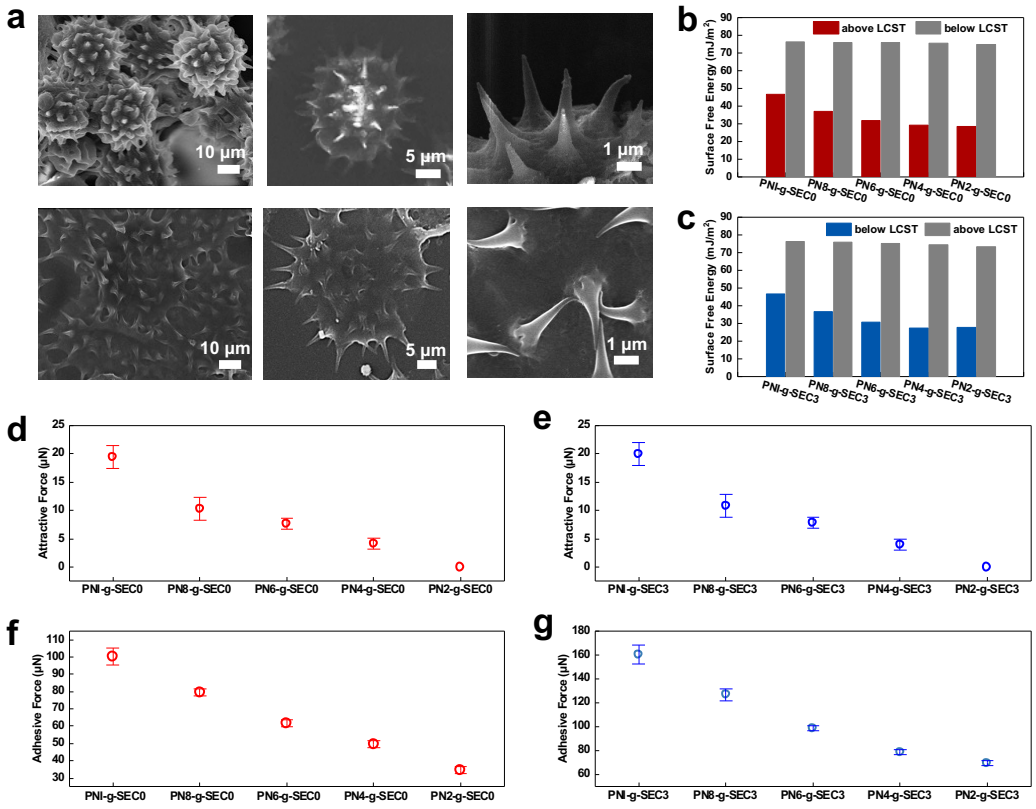

Figure 5.7 a. Structure of SECs involving fabricated surface, each pollen microparticles and spiky spines: SEC0 (top) and SEC3 (bottom) b. Surface free energy of PNn-g-SECm below LCSTs, c. Surface free energy of PNn-g-SECm above LCSTs, Adhesive forces measured under superhydrophobic states: d. PNn-g-SEC0, e. PNn-g-SEC3, Attractive forces measured under superhydrophobic states: d. PNn-g-SEC0, e. PNn-g-SEC3.

The adhesion force on these two series of surfaces differed significantly, as shown in **Figure 5.7f** and **5.7g**. The PN8-g-SEC0 surface, with highly rough structures, had an adhesion force of 79.4 μN. In contrast, the PN8-g-SEC3 surface with low roughness, exhibited higher water affinity possessed a higher adhesion force of up to 127.1 μN. In addition, similar phenomena were observed in other surfaces of varying grafting compositions, where rough structures led to lower surface adhesion. Specifically, the adhesion forces measured on PNI-g-SEC0, PN6-g-SEC0, PN4-g-SEC0, and PN2-g-SEC0 surfaces, with values of 100.3 μN, 61.7 μN, 49.5 μN, and 34.6 μN, respectively. As compared to SEC3-fabricated surfaces, the adhesion forces detected on PNI-g-SEC3, PN6-g-SEC3,

PN4-g-SEC3, and PN2-g-SEC3 surfaces, with values of 160.4 μN, 98.7 μN, 79.2 μN, and 69.9 μN, respectively. This phenomenon could be attributed to the air cushion generated between the microparticles that acts as a hydrophobic medium and adsorb some of the pressure from the water droplet.[173] As a result, the contact line on high-roughness surfaces decreased, leading to a lower surface adhesion.

The surface conformation played a key role on magnitude of the attractive forces, as clearly shown in **Figure 5.7d** that different F_a of PNI-g-SEC0, PN8-g-SEC0, PN6-g-SEC0, and PN4-g-SEC0 were recorded with values of 19.4 μN, 10.3 μN, 7.7 μN and 4.13 μN, respectively. As the hydrophobicity of the grafted polymer coating on surfaces increased, the droplet shape exhibited slight changes and the movement of the contact line was reduced.[174] When the surface coating possessed high hydrophobicity, such as PN2-g-SEC0 surface, the attractive force could not be detected as the values were smaller than micronewton.[175] This attributed to the interfacial free energy of surfaces, which had an impact on the attractive force between water droplet and polymer coatings.[176] To examine the orientation and rearrangement of the polymer chain's functional groups at the water/PNIPAM interface, we conducted a comparison of the total interfacial energies of pollen-based surfaces at different temperatures using polar (water) and nonpolar (hexane) solvents, which could be calculated using the WORK model[29, 162] (**Table 5.1**). The surface free energy of the PNI-g-SEC0 surface was higher, at 46.8 mJ/m^2, due to the large amounts of hydrophilic groups. In contrast, the addition of the hydrophobic comonomer NtBA resulted in a reduction in the surface free energy for PN8-g-SEC0, PN6-g-SEC0, PN4-g-SEC0 and PN2-g-SEC0 surfaces, with values of 37.0, 31.8, 29.1, and 28.5 mJ/m^2, respectively. That is to say, the orientation of the hydrophobic methyl moieties at the interface reduced the surface free energy and generated a large energy barrier between the droplet-air-polymer interface, which in turn resulted in the smaller attractive forces observed on these surfaces.[177]

Table 5.1 Calculation of Surface free energy

Surfaces	water	Methylene iodide	γ_s^d	γ_s^p	γ_s
PNI-g-SEC0(below LCST)	3.5	0	38.81	37.34	76.1852
PNI-g-SEC0(above LCST)	150	58.5	36.2	10.6	46.8
PN8-g-sec0(below LCST)	5	0	38.83	37.21	76.04
PN8-g-sec0(above LCST)	151	69	28.82	8.24	37.06
PN6-g-SEC0(below LCST)	6.3	0	38.86	37.05	75.91
PN6-g-SEC0(above LCST)	152	75	24.75	7.05	31.8
PN4-g-SEC0(below LCST)	7.5	0	38.89	36.88	75.77
PN4-g-SEC0(above LCST)	155	79	22.29	6.81	29.1
PN2-g-SEC0(below LCST)	12.5	2	39.03	35.86	74.89
PN2-g-SEC0(above LCST)	158	80.6	21.43	7.05	28.48
PNI-g-SEC3(below LCST)	4	0	38.81	37.3	76.1852
PNI-g-SEC3(above LCST)	152	59.6	35.68	10.94	46.62
PN8-g-SEC3(below LCST)	6.3	0	38.86	37.06	75.92
PN8-g-SEC3(above LCST)	156	78.6	22.62	7.12	29.74
PN6-g-SEC3(below LCST)	10.2	2	38.94	36.4	75.34
PN6-g-SEC3(above LCST)	161	81	21.33	7.52	28.85
PN4-g-SEC3(below LCST)	13.5	3.2	39.03	35.62	74.65
PN4-g-SEC3(above LCST)	163	83	20.15	7.35	27.5
PN2-g-SEC3(below LCST)	18.2	6.8	39.01	34.28	73.29
PN2-g-SEC3(above LCST)	165	86.5	18.1	6.79	24.89

On the other hand, the surface roughness played an important role in controlling the droplet behaviors that contributed to the differences in the F_{ad}. For instance, the PNn-g-SEC3 surfaces exhibited larger adhesive forces ranging from 160.4 μN to 69.9 μN, which were higher than PNn-g-SEC0. In order to demonstrate the droplet-surface interactions, we investigated the water-resistance forces on surfaces under external forces by adjusting the immersion depth during the touch-retraction measurement process.[158a] PN2-g-SEC0 and PN2-g-SEC3 were utilized to eliminate the impact of the resistance force (F_r) on the subsequent immersion process. It was clearly shown in **Figure 5.8b** that a larger droplet shape change occurred at the touching stage and the droplet tended to advance at a long distance on the surface, due to less air pockets embedded within the PN2-g-SEC3 surface. The force generated on the PN2-g-SEC0 surface was smaller of 33.1μN (**Figure 5.8c**), when compared to the force generated on the PN2-g-SEC3 surface determined to be 22.5 μN (**Figure 5.8f**). At this time, similar force curves were observed on both surfaces during the touch-retraction process at an immersion depth of 0.10 mm, confirming the hypothesis of the hierarchical structures, where F_r behaved as a function of F_{ad}.[178] Thus, the surfaces with higher water resistance and a larger F_r were attributed to the presence of air cushions within the hierarchical structures.[179]

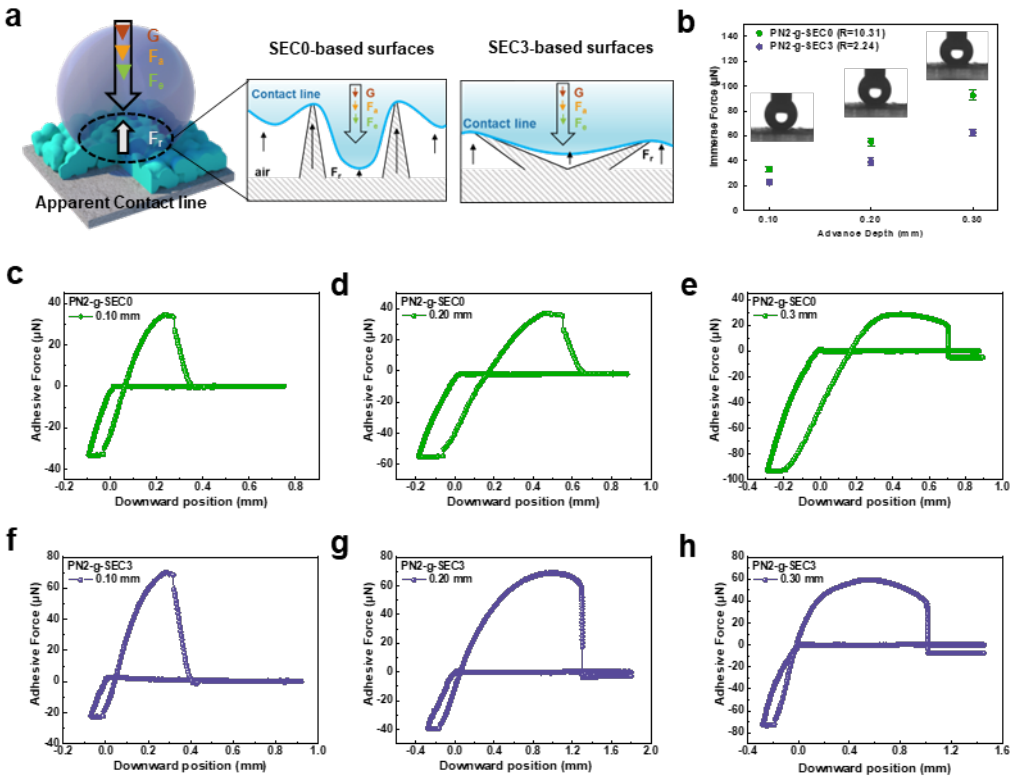

Figure 5.8 a. Schematic illustration of the attractive force variation and force changes varying the immerse depth, **b.** Force changes varying the immerse depth on PN2-g-SEC0 and PN2-g-SEC3, The interaction forces between droplet and surfaces varying the immerse depth on PN2-g-SEC0: **c.**0.10 mm, **d.** 0.20 mm, **e.** 0.30 mm, The interaction forces between droplet and surfaces varying the immerse depth on PN2-g-SEC0: **f.** 0.10 mm, **g.** 0.20 mm, **h.** 0.30 mm.

As the immersion depth was increased to 0.20 mm, PN2-g-SEC0 possessed the same value of F_{ad} but the F_r was increased to 55.2 μN (**Figure 5.8d**). Under an external force, the droplet changed shape and the contact line advanced. As shown in **Figure 5.8e**, when the surface advanced to z=-0.30 mm, the hierarchical structure of PN2-g-SEC0 responded to prevent the water spreading on the surface and responded with the highest water-resistance force(F_r ~ 92.5 μN). [180] However, due to the excessive local pressure, the droplet could not maintain its original spherical shape and retained a water layer on the surface.[181] The final F_{ad} corresponded to the droplet mass when the cantilever leaved the surface, however it did not correspond to the surface adhesion force. In contrast to the PN2-g-SEC0 surface, the droplet could not be completely extracted from the surface when the cantilever was at z=-0.20 mm, and left some residual water droplet that adhered to the PN2-g-SEC3 surface (**Figure 5.8g**). The value of F_r on PN2-g-SEC3 increased slightly to 39.2 μN as the water had penetrated into the structures resulting to an increase in the wetted contact area. Likewise, during the detachment process, the droplet was forced to make contact with a larger area on the surface when the immersion depth was 0.30 mm and could not be fully retracted due to the friction. (**Figure 5.8h**). The results revealed a strong correlation between F_r and surface structures that were

associated with the surface composition that impacted the strength of surface adhesion.[182] Moreover, it was observed that the adhesive forces of the surface displayed a similar trend with the CAHs. As the proportion of hydrophobic comonomers in the grafted polymer coating on the surface increased, the values of F_{ad}, CAH, and S_a also increased, resulting in sliding behaviors [183] (**Figure 5.9**).

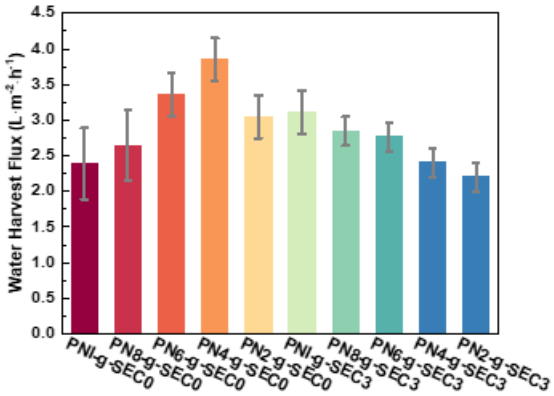

Figure 5.9 Illustration of water harvest flux measured on PNn-g-SEC0 and PNn-g-SEC3 surfaces.

2.4 Droplet Manipulation Performance

To evaluate the droplet manipulation capacity of our constructed surface, the droplet transfer from the different surfaces was tested and monitored. With the temperature controller, the droplet could easily transfer from the low adhesive surface to higher adhesive surface without any residual water remaining on the surface. For example, PN2-g-SEC0 could deliver tiny droplet (2 μL) to PN4-g-SEC0 without leaving any residual water. To demomstrate the cyclic reproducibility of the detacement process, the water transfer processes were measured over 10 cycles under cyclic temperature variation. The results confirmed the potential of the tunable and reversible wettable surfaces for droplet manipulation technologies.[184] Furthermore, the PN4-g-SEC3 displayed a high performance in water harvesting with a water harvesting flux of 3.85 L/m^2/h (**Figure 5.9**). Specifically, the attractive force enhanced the droplet nucleation process when tiny droplets approached the surface, with minimal or no occurrence of droplet re-entrainment phenomena.[20] The surface could achieve water transport with an average droplet self-removal size of 675 μm since the surface with low CAH reduced the resistance for sliding.[58]

5.4 Conclusions

In summary, we studied the thermo-responsive surfaces with programmable wettability and adhesion transformation properties to facilitate the development of controllable droplet manipulation. By controlling the comonomer grafting ratio and morphology of the sunflower pollen microparticles, the surfaces exhibited superhydrophilic/superhydrophobic transformations with varying LCSTs. Particularly, the surface under the superhydrophobic state could adjust its water attraction and adhesive properties in a controllable manner. With the introduction of hydrophobic

comonomers, the surfaces exhibited a lower water attractive force due to the weak hydrogen bonding network and lower interfacial free energy. Moreover, the surfaces roughness determined the water-resistance force generated on the surface, especially when droplet movement was induced by external force or pressure. Compared to surfaces fabricated with SEC microsheets, the high-roughness surface prepared using SEC microspheres displayed stronger water resistance endurance due to the air cushion beneath the spiky structures. The surface adhesion was influenced by the co-operative functions of the water attractive and water-resistance forces. These investigations demonstrated the potential of utilizing the unique characteristics of these surfaces for controllable droplet transferring on programmable wettability sites, as well as for effective droplet deposition and transport in water harvesting applications.

Chapter 6. Boosting Solar-Driven Water Evaporation through Selective Water Gating Enabled by Thermo-Responsive Sporopollenin

6.1 Introduction

Freshwater scarcity is becoming a global concern, necessitating the development of effective water collection and purification technologies.[185] More recently, interfacial solar-driven evaporation has emerged as a sustainable method for generating clean water using solar energy. Unlike traditional solar evaporation that requires heating the bulk water, interfacial solar-driven evaporation achieves heat localization to achieve improved solar energy utilization.[186] However, the low efficiency of the water-thermal management hinders the water generation rate in different solar evaporation systems. [187]

Porous materials like sponges and foams are commonly employed in solar-driven water evaporators, leveraging capillary forces to provide sufficient water supply through interconnected pores. However, the excess water retained within the porous materials due to capillary forces reduces the evaporation rate and diminishes the solar thermal energy efficiency. Recent studies have proposed a simple approach to address these challenges by reducing the diameter of the water supply channel, confirming the feasibility of implementing a better water management and control by confining the evaporation process within a thin water layer.[127b, 188] Besides, the separated-layered evaporator can improve the water evaporation rate by decoupling the water supply and evaporation sections in the foam.[189] In addition to the reduced water transport content due to smaller channels, the continuous water transport in the sponge is challenging, as maintaining the upward water transport and associated water saturation in the sponge is inevitable under these conditions. Thus, special control of the water supply should be included in the solar water evaporator. Thus, innovative approaches to enhance controllable water management and maximize solar energy utilization in interfacial solar-driven evaporation systems are necessary and intensive research efforts are actively being pursued.

In this study, we successfully fabricated a solar driven water evaporator (SDWE) using nickel foam as the substrate and incorporated two key components: the interfacial polydopamine nanosphere-assembled layer (PDA) and the bottom thermo-responsive sporopollenin-engineering layer (PNm-g-SEC). The SDWEs design enables the continuous and controllable water transport using a porous PDA coating layer incorporated in the water channels. Additionally, the incorporation of thermo-responsive pollen microparticles within the foam serves as a solid water gating system, enabling the passage of thin water while preventing bulk water from flooding the pore structure of the foam during the evaporation process. By optimizing the ratio of these two regions, the SDWEs achieved high performance in the evaporation rate with desirable water supply and reduced evaporation enthalpy. The bilayer design also facilitates an efficient thermal energy management, where the PDA layer enhances the light absorption and the hollow microcapsule structure of SEC serves as a thermal insulation layer. Therefore, this unique SDWE design yielded a high solar-vapor

conversion performance, with a vapor generation rate of up to 3.58 kg m^{-2} h^{-1} and 93.9% solar-to-vapor efficiency under 1 sun irradiation. Furthermore, the SDWE demonstrated its effectiveness in solar-driven seawater desalination, contaminated water purification, and removal of heavy metal ions. These properties endow the SDWE with recyclability, anti-salt-accumulation characteristic, and scalability for practical applications that further contribute to its potential as an efficient solar-driven evaporation system.

6.2 Materials and method

Materials

Lycopodium clavatum pollen (Flinn Scientific Canada Inc.), Nickel foam, N-isopropylacrylamide, Cerium (IV) ammonium nitrate, potassium hydroxide, phosphoric acid, acetone, ethanol, ammonia solution (28-30%), Rhodamine B, potassium iodide were used as received from Sigma-Aldrich. All the chemicals were used without additional purification, unless stated otherwise. Milli-Q water (resistivity of 18.2 MΩ cm) was used to prepare the aqueous dispersions.

Fabrication of Bilayer-structured Solar Evaporator (SDWEs)

Preparation of PNm-g-SEC microparticles

Briefly, we prepared sunflower sporopollenin (SEC) via alkaline extraction method and modified its outer surface with monomer of N-Isopropylacrylamide (NIPAM) via free radical polymerization.[5] Following the previous study, we first treated the defatted pollen with 10 wt% potassium hydroxide (KOH) at 80°C and stirred for 2 h to remove its internal cytoplasmic content. KOH-treated pollens were next subjected to acidolysis in 85% phosphoric acid (H_3PO_4) and then extensively washed with ethanol and water for further synthesis. Next, the surface modification of SEC microparticles was conducted under nitrogen environment, where cerium (IV) ammonium nitrate (CAN) (0.05 g 0.10 mmol) was added to the reaction flask forming radical sites on SEC through the reduction of ceric ions under magnetic stirring in an ice bath for 30 min for pre-synthesis. Next, NIPAM monomer (1.13 g, 10.0 mmol) was introduced to initiate the polymerization. Finally, the product was dialyzed against deionized water until the measured water conductivity remained constant. The as-prepared PNIPAM modified SEC microparticles designated as PNm-g-SEC where m corresponds to monomer mass changing from 5, 10, 20 mmol (initiator/monomer ratio-m is constant).

Preparation of PDA@NiF foams

Firstly, the nickel foam (NiF) with dimensions of 5 cm × 5 cm ×10 mm was washed with acetone, ethanol and immersed in 1 M hydrochloric acid (HCl) for 1 h to remove the oxide layer. The treated NiF foam was then immersed in a 150 mL water/ethanol solution (v:v=2:1) and ammonia aqueous solution (NH_4OH, 0.75 mL, 28-30%) was added dropwise to the mixture under mild stirring at room temperature for 30 min. Dopamine hydrochloride (0.5 g) was dissolved in deionized water (10 mL) and injected into the above mixture solution. The color of this solution immediately turned to brown and gradually changed to dark brown. The reaction was allowed to proceed for 3 h. The foams coated with PDA layers (p-PDA*)* were obtained and washed with water three times to remove

unreacted chemicals. As for the reference samples, NiF foam coated with smooth PDA layers (s-PDA) were prepared by changing reaction environment in the water-ammonia solution, while roughness PDA layer (r-PDA) was fabricated in water-ammonia solution at 55°C.

Fabrication of SDWE evaporators

The SDWE evaporators were fabricated using conventional dip-coating methods. PDA@NiF foams were immersed in specific depth of the PNm-g-SEC solution that was controlled by a variable speed motor-driven height positioning unit of DCAT 15. Then, the PNm-g-SEC microparticles were adhered to the foam and vacuum dried for the solar water evaporation test. This series of solar evaporator designated as SDWEs, while s-SDWE, r-SDWE and p-SDWE refers to the evaporator with the distinct structure of PDA layer, respectively.

Solar water evaporation experiments

The water evaporation performance experiments were conducted in the laboratory using a solar simulator (AbetTech, M-LS Rev B) with a simulated solar flux of 1,000 W m^{-2} (1 sun). The samples were cut into cubes and mounted onto a polystyrene thermal insulating foam (surface area~5 cm×5 cm; thickness~10 mm). The size of the samples was carefully aligned with the solar illumination and absorber surface, preventing additional light falling onto the non-sample region to avoid additional solar-thermal heating. Besides, the distance between the solar simulator and the evaporator was set to 20 cm. The water container along with the sample was placed on a sensitive electronic weighing balance (Radwag SMB-60/AS 60/220.R2) to measure the mass of the water with time with a sampling rate of 1 data point per second. In this regard, the evaporation rate was quantified by correlating it with the mass loss/change (Δm) of water. Simultaneously, the temperature changes were recorded by mounting two K-type thermocouples at different positions (z), where one was mounted onto the top surface of the foam (z=10.0 mm) and the second thermocouple was installed at the bottom of the foam (z=0 mm). These thermocouples were connected to an electronic data logger for temperature monitoring, while thermal images of the absorber surface and bulk water were recorded using an infrared camera (FLIR TG167).

Before illuminating the set-up, the evaporation rate under the dark condition was measured for 1 h and used as a reference for self-evaporation. Then, the loss in water mass, with and without the p-SDWEs, were recorded for the calculation of the evaporation rate. The solar-illuminated evaporation rate was determined by subtracting the dark-condition evaporation rate. All the evaporation rates were measured after stabilization under 1 sun for 10 min.

Other Characterizations

Particle Morphology and Surface Topography Characterizations

The shape and structure of SECs were visualized and examined using scanning electron microscope (SEM) and supplementary optical microscopic images and videos captured using the Nikon LV ND microscope. The particle size was measured using particle size analyzer (Anton Paar 1190) and Nano Zetasizer (Malvern ZS90) with a temperature control system. The as-prepared SEC surface topography was characterized by a confocal laser microscope (Olympus LEXT OLS5000).

Thermodynamic Characterization

The thermal responsive characteristics was evaluated by performing turbidimetric measurements on the Varian (Cary 100 Bio) UV–vis spectrometer equipped with a temperature controller and Micro-differential Scanning Calorimetry (DSC). The rheological properties of the concentrated suspension were characterized using Malvern Kinexus ultra+ rheometer with the cylindrical measuring system and a solvent trap to prevent water evaporation.

Surface Wettability Characterization

The water/oil static and dynamic contact angle measurements were conducted via sessile drop methods using the OCA 15 device (Dataphysics). For the measurement of the static contact angle, a 5 μL volume micro droplet was dispensed onto the test surface using an auto-dosing system equipped with a 500 μL needle. Side-view images or videos of the droplet behaviors were captured using a high-speed camera (IDS uEye camera), while the analysis system recorded the time-dependent contact angles and incorporating Image J analysis software for the results analysis.

The surface adhesion force measurements were conducted in a tensiometer with the accompanied a multi-axis sample stage. In particular, the adhesion force variation was measured by the force probe while approaching and retracting a 3 μL droplet from the surfaces at an approximate speed of 0.05 mm/s, while the droplet's size and shape were recorded by a high-speed camera.

Liquid transport characterization

Aqueous liquids containing fluorescent dye (Rhodamine B, < 0.01 wt %) were introduced into the SDWE foam. Liquids were injected by driving the liquid through the capillary using a syringe pump with micromanipulator mounted on the confocal microscope. The fluoresce-dyed water was dropped on one side of the foam and recorded water movement on specific area under time-series mode and z-stack mode.

The interfacial behaviors between water-air-solid surface were characterized by a confocal microscope (Zeiss LSM 510 Meta Laser Scanning Confocal Microscope) under the time-series frame mode and z-stack mode to distinguish the three phases. During the testing process, water-immersion objective lens were used with the observation magnification of 40x/1.3 water DIC.

6.3 Results and discussion

6.3.1 Design of the solar driven water evaporator (SDWE)

Scheme 6.1 illustrates the construction units and working principles of the designed solar water evaporator. Our solar evaporator, namely SDWEs, comprises two essential components modified on nickel foam, namely the interfacial polydopamine nanosphere-assembled layer (PDA) and the bottom thermo-responsive sporopollenin-engineering layer (PNm-g-SEC). The bilayer structures work synergistically to enhance the solar water generation performance by balancing the trade-offs between water transport rate and light-to-heat energy consumption during the water phase-transition evaporation process. Specifically, the introduction of porous PDA coating layer along the skeleton enabled the continuous water supply of controllable and varying amounts. By incorporating the thermo-responsive pollen microparticles on the bottom side in contact with seawater, PNm-g-SEC

particles performed as a solid gate to guide the thin water passing through the hydrophilic microchannel that effectively block the flow of large amounts of bulk water through the external microchannels originating from the pore of the foam. This switch-like behaviors induced the selective and directional water supply that reduce the excessive heat absorption during the evaporation process. Moreover, the distinctive textures originating from the bilayer design rationalize the thermal energy management. The low thermal diffusivity of PDA combined with the porous topographical texture enhance the light absorption, while the hollow microcapsule structure of SEC with trapped air pockets serves as an effective heat resistance layer to reduce the thermal dissipation. Thus, when exposed to sunlight, the encapsulation black layer could efficiently achieve an optimal photothermal conversion efficiency, raising the temperature gradient and maintaining a stable high temperature within the system to further improve the evaporation performance.

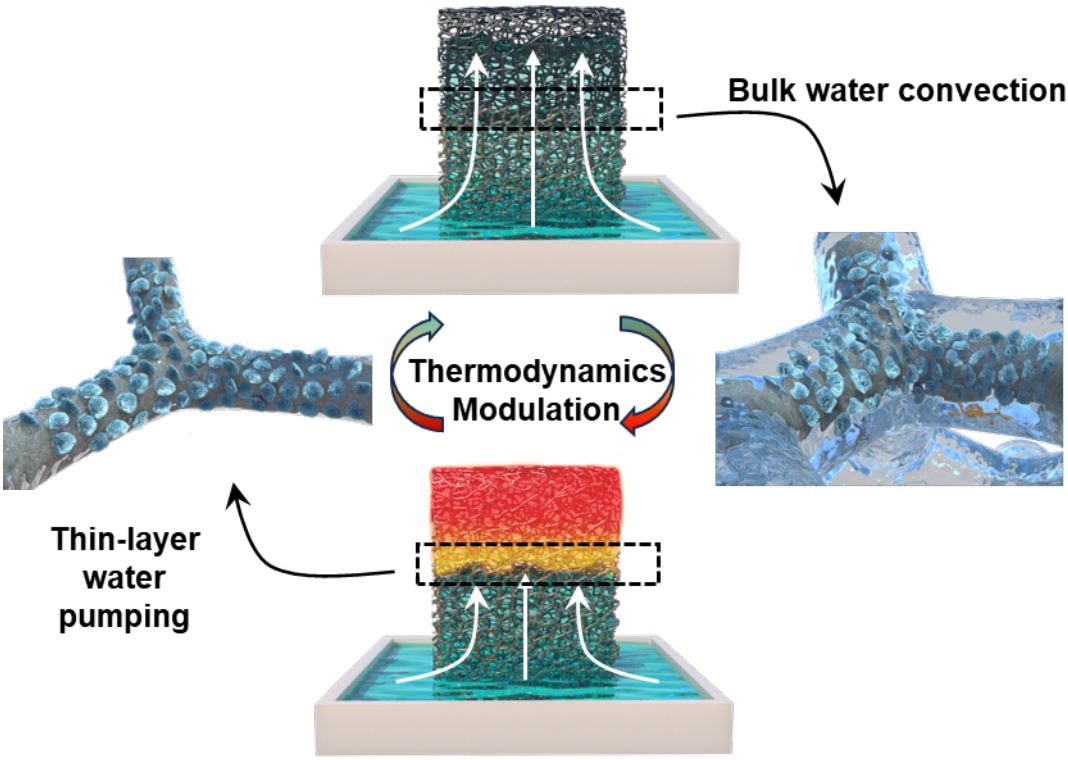

Scheme 6.1 Illustration of working principles of SDWEs

The fabrication of p-SDWE foam was conducted in two steps, as schematically shown in **Figure 6.1a**. First, p-PDA nanospheres were first deposited onto the porous nickel foam (NiF) with pore size (≈200 μm) using in-situ polymerization method.[190] As shown in **Figure 6.1b,** the color of NiF transitioned from silver grey to black after being modified with an adherent p-PDA layer, which simultaneously endowed the foam with a remarkable light absorption characteristic. The PDA coating layer on the substrate served as a thin water transport layer, while the top section of the

evaporator also functioned as the photothermal layer. Subsequently, the incorporation of thermo-responsive sporopollenin onto the bottom section of evaporator was achieved by a facile dip-coating process.[87] The p-PDA@NiF was dipped into PNm-g-SEC solution at a certain immerse depth, where the bottom skeleton of the foam coated with PNm-g-SEC turned into dark brown after vacuum drying. Owing to the unique temperature-dependent water affinity, PNm-g-SEC decorated at the bottom section served as the water-transport gating layer to enable the selective thin water supply (**Figure 6.1c**).

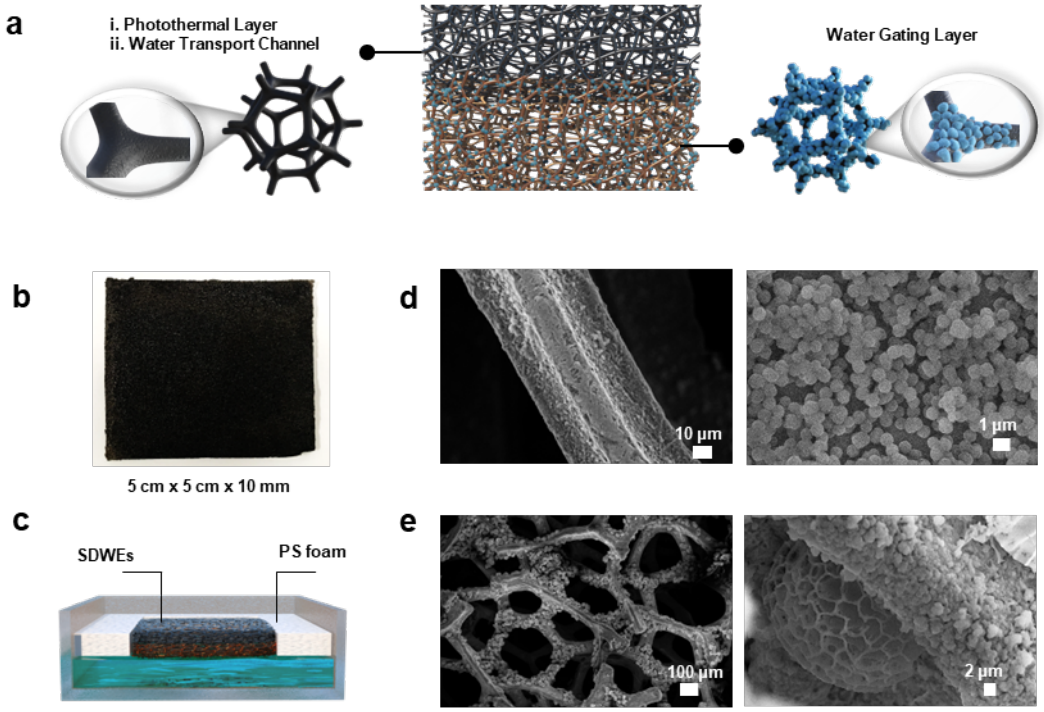

Figure 6.1 a. Shematic illustration of the fabrication procedure of bilayer-structured evaporator, **b.** Digital images of evaporator, **c.** The structure design of evaporator localized at the water-air interface, SEM images of p-PDA coating layer: **d.** The porous structure of foam skeleton, **e.** p-PDA nanospheres, SEM images of water-transport gating layer **f.** The skeleton decorated with PNm-g-SEC microparticles, **g.** The interaction between PNm-g-SEC microparticles and PDA layer.

Specifically, monodispersed PDA spheres grew on the skeleton of the foam in water-ethanol-ammonia mixed solvents at room temperature. By adjusting the water-ethanol solvent reactive conditions, various morphologies of PDA layers were produced according to the Hansen solubility parameters[191], designated as smooth PDA layer (s-PDA), roughness PDA layer (r-PDA) and porous PDA layer (p-PDA), respectively. The p-PDA nanospheres, with a diameter of 520 nm, assembled into micro clusters and assembled into interconnected channels as demonstrated in scanning electron microscopic image (SEM) of **Figure 6.1d**, which introduced onto the skeleton with porous structures and facilitated water transport. s-PDA samples featured with the flat topography and r-PDA samples displayed a continuous bumpy microstructure with large PDA clusters (**Figure 6.2**).

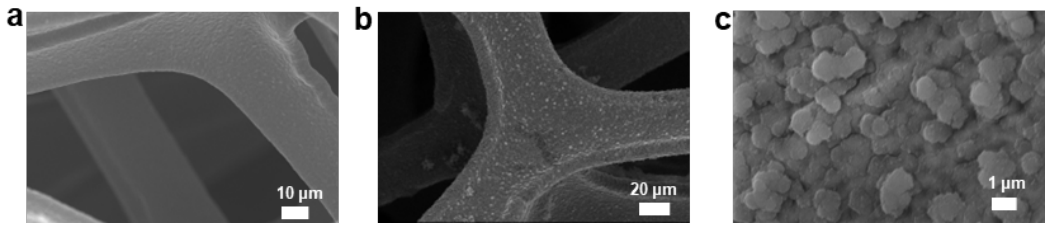

Figure 6.2 The morphology of PDA layer: **a.** s-PDA, **b.** r-PDA, **c.** The PDA cluster on r-PDA layer.

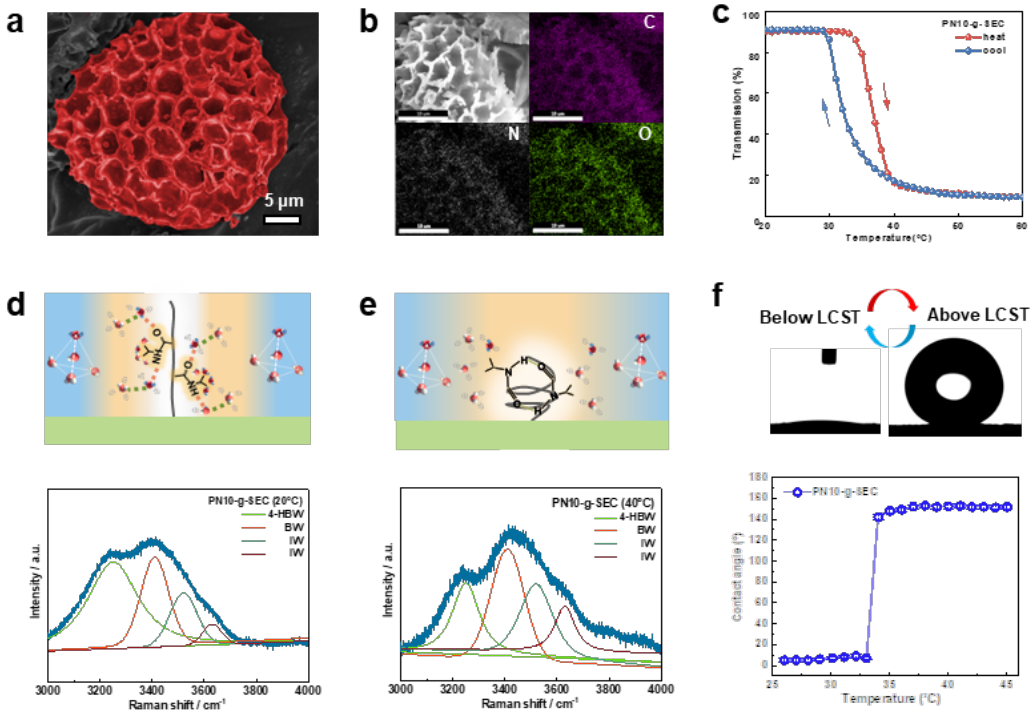

Figure 6.3 a. SEM images of PN10-g-SEC microparticles, **b.** EELS mapping images of PN10-g-SEC microparticles, **c.** LCST behaviors of PN10-g-SEC confirmed by UV-vis spectrophotometry, Interfacial water structure along polymer-grafted layer of PN10-g-SEC measured by Raman spectroscopy**: d.** below LCST, **e.** above LCST, **f.** Water contact angle changes driven by LCST.

Moreover, the water-transport gating layer was fabricated by coating thermo-responsive sporopollenin (PNm-g-SEC) onto the foam skeleton as shown by the SEM images of **Figure 6.1e.** The coated PNm-g-SEC was prepared by grafting sunflower sporopollenin with N-isopropylacrylamide (NIPAM) via free radical polymerization under nitrogen environment. SEM images of **Figure 6.3a** revealed the morphology of PN10-g-SEC, exhibiting triangular shapes decorated with microridges, and the polymer grafted canopy on PN10-g-SEC particles featured with high roughness nanostructure. Additionally, the particle size analysis confirmed the successful preparation of PN10-g-SEC paricles with a uniform size distribution of ~26.9 μm (**Figure 6.4a**). As shown in **Figure 6.3b**, the electron energy-loss spectroscopy (EELS) elemental mapping images showed that the C, N, and O elements were uniformly distributed within the PN10-g-SEC microparticles. Successful PNIPAM-grafted layer was further characterized by X-ray photoelectron

spectroscopic (XPS) elemental analyses, demonstrating the presence of organic molecules with the expected changes in the ratio of N-C bond on the surface of PN10-g-SEC[192] (**Figure 6.4c and Table 6-1**). Besides, Fourier transform infrared (FTIR) spectrum confirmed the presence of amino groups, where the peak at 1650 cm^{-1} was associated with the N-C=O bond and the absorption peak at 1550 cm^{-1} corresponded to the N-H bonds[193] (**Figure 6.4b**). In addition to the thermal responsive characteristics, the polymer conformational transition of PNm-SEC was confirmed by UV-vis spectrophotometry and **Figure 6.3c** displayed the lower critical solution temperature (LCST) of PNm-g-SEC with a LCST of 33.2°C. This LCST behaviors allowed for the rearrangement of functional groups, where the hydrophobic isopropyl groups exposed at the interface of the polymer coating, resulting to the reduced water affinity. Moreover, the related hydrophilicity of PNm-g-SEC was determined by the conformation of interfacial water structure, which was investigated by comparing the proportion of O–H stretching vibrational band using Raman spectrum. As shown in **Figure 6.3d**, the broad Raman band of PN10-g-SEC extending from 3000 cm^{-1} to 4000 cm^{-1} indicated the vibration of hydrogen bonds in water. Within this range, the 3250 cm^{-1} peak corresponded to free water with four hydrogen bonds (①) and -CH_3 groups surrounded by polyhedral cages composed of tetrahedrally hydrogen-bonded water molecules (②), which is known as 4-coordinate hydrogen-bonded water (4-HBW). The peak at 3410 cm^{-1} represents the in-phase vibrations of water molecules captured by the C=O or N-H groups (③), which is referred to as bound water (BW). Besides, the peaks at 3520 and 3630 cm^{-1} correspond to the stretching of weakly or non-hydrogen bonded water molecules (④⑤), known as intermediate water (IW), indicating the presence of hydrophobic disordered water in the hydration shell[194]. At 20°C, the higher ratio suggested that the PN10-g-L.SEC surface had a larger amount of bound water, with the hydrophilic C=O and -NH_2 groups predominantly positioned at the air/PN-g-L.SEC/water interface. Conversely, the spectrum displayed a significant reduction in the 4-HBW/BW ratio at 40°C, indicating that the water underwent a transformation into a less ordered and weaker hydrogen-bonded structure, while the hydrophobic -CH_3 groups rearranged and exposed at the interface[5] (**Figure 6.3e**). Taking advantage of this characteristic together with the hierarchical structure on the outer surface of SEC, we obtained the thermo-responsive surfaces with switchable wettability transition as illustrated in our previous reported study[5]. By adjusting the polymer grafting density, we successfully obtained pollen microparticles with hydrophilic/hydrophobic transition states displayed on PN20-g-SEC surfaces (**Figure 6.4f**) and the constructed PN10-g-SEC surfaces exhibited remarkable superhydrophobic/superhydrophilic wettability transition characteristics. The water contact angles (θ_w) observed on the surface assembled with PN10-g-SEC particles underwent a transition, switching from 2° at 20°C to 153° at 35°C, clearly demonstrating the potential for effective water management (**Figure 6.3f**).

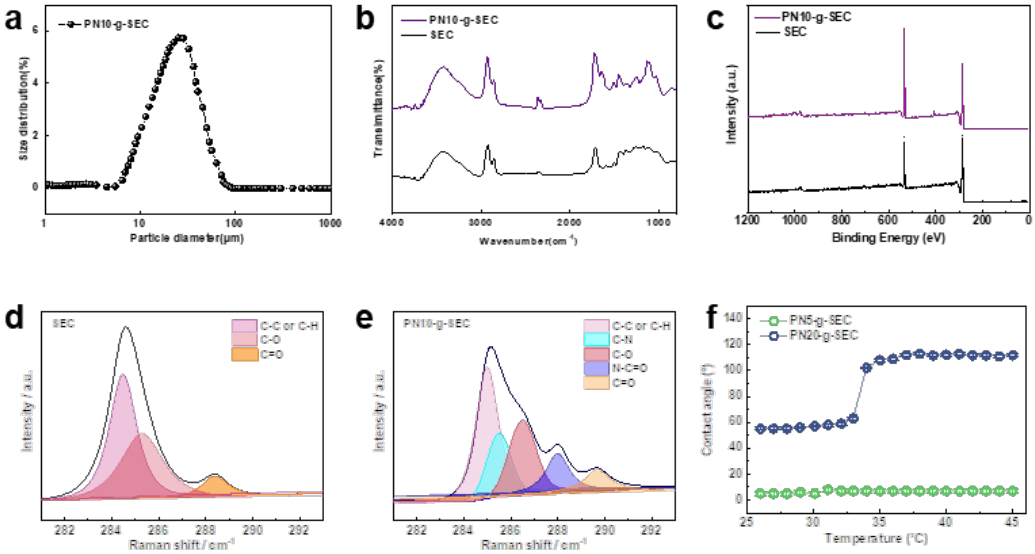

Figure 6.4 a. Particle Size of PN10-g-SEC, **b.** FT-IR spectrum of SEC and PN10-g-SEC, **c.** XPS spectrum of PN10-g-SEC and SEC, **d.** C1s fitting spectra of SEC, **e.** C1s fitting spectra of PN10-g-SEC, **f.** Contact angle variation of PN5-g-SEC and PN20-g-SEC under different temperature

6.3.2 Water and energy management in the HNGs

Under constant solar illumination (1 kW m^{-2}), solar vapor generation performance of the SDWEs (5 cm*5 cm area, 1.0 cm thickness) was recorded by mass change of evaporated water and temperature distribution of SDWEs with time evolution (**Figure 6.5a**). It is obvious that the vapor generation using the SDWEs was more efficient than pure water without SDWEs under identical illumination conditions. The water evaporation rates were calculated from the slope of mass change curves. Under 1 sun illumination, p-SDWE achieved the highest rate up to 3.58 kg m^{-2} h^{-1} among all SDWEs samples, which was 1.3, 2.2 and 5.2 times that for s-SDWE, r-SDWE and pure water, respectively (**Figure 6.6a**). These results revealed that p-SDWE has an optimized water transport channel and economical energy consumption.

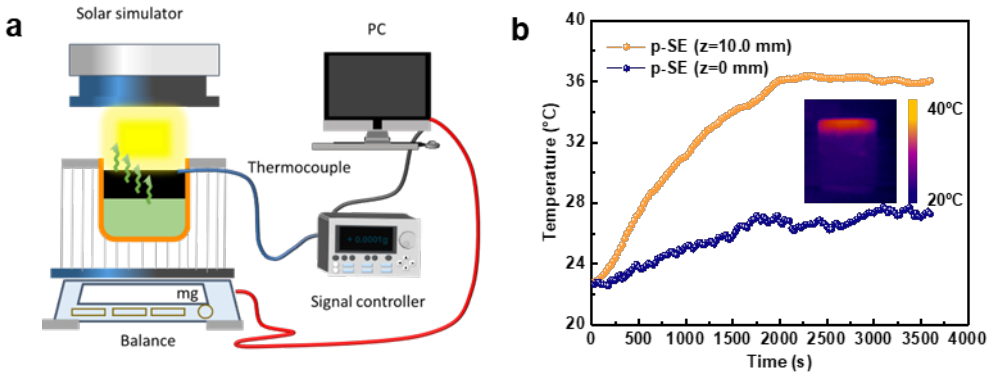

Figure 6.5 a. The set-up for measuring the solar evaporation performance, **b.** The surface temperature and ambient water temperature of p-SE (p-PDA coated nickel foam without bottom SEC layer)

Photothermal effect and thermal conductivity of the foam

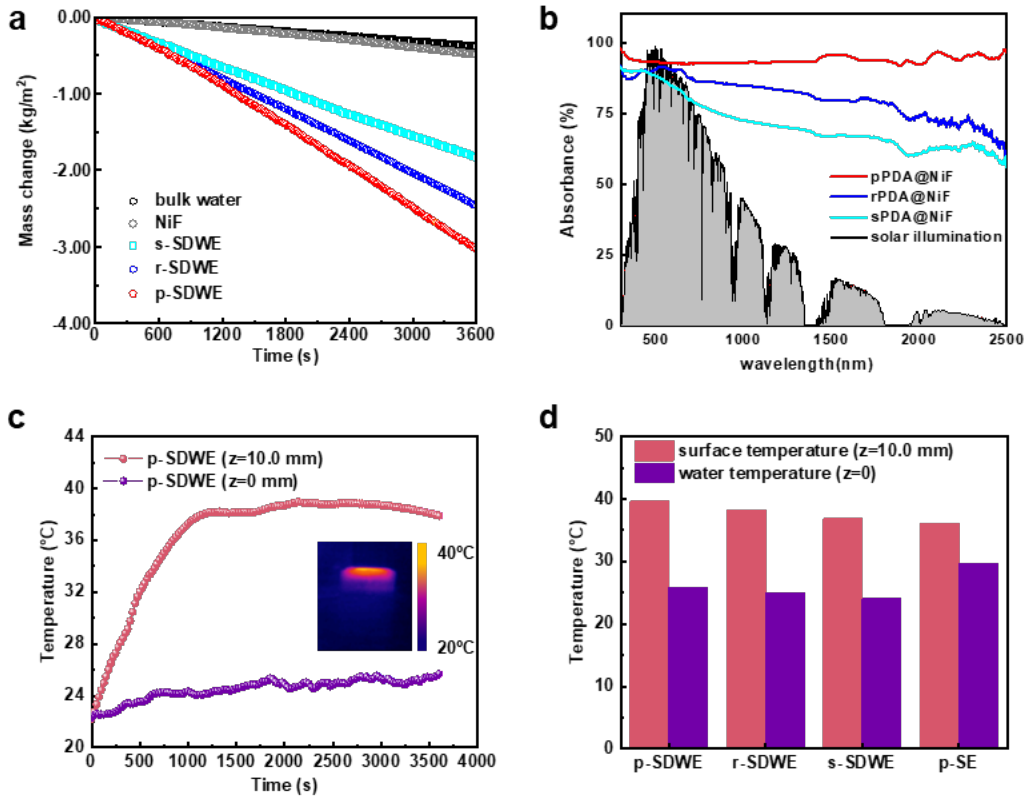

Figure 6.6 a. Mass change of water over time of the SDWE foams under one sun solar illumination, **b.** UV-vis-NIR diffuse reflection spectra of the PDA-coated NiF in the wavelength range of 250 to 2500 nm, **c.** Surface temperature variations of PDA-coated NiFs, **d.** Temperature gradient of SDWE foams characterized by infrared thermal images under one sun solar irradiation.

An efficient photothermal layer and companied with a heat insulation layer enabled the localized surface heating on the evaporator while alleviating unexpected heat conduction to the surrounding environment, which is one key factor for improving the solar evaporation rate. **Figure 6.6b** exhibited the UV-visible–near-infrared (UV-vis-NIR) absorbance spectra of the PDA@NiF foams with varied the structure of PDA layer (s-PDA, r-PDA, p-PDA). The p-PDA displayed stronger and broader solar absorption (~93.6%) with low reflectance over a wide wavelength range (from 250 to 2000 nm), compared with the lower sunlight absorption capacity of s-PDA and r-PDA. As further verified by the IR thermal images and temperature profiles in **Figure 6.6c**, the surface temperature of p-PDA increased rapidly and reached a plateau at around 39.6°C, while the temperature of bulk water only increased slightly. Furthermore, the surface temperature of p-SDWE showed a higher temperature increase compared to the solar evaporator with an s-PDA layer (38.1°C) and an r-PDA layer (36.9°C) under identical light irradiation condition. The results indicated that the closely packed nanospheres along the sidewalls of the interconnected pore in NiF could achieve an efficient and broadband solar absorption, attributing to the hierarchical porous structure with induced strong diffuse reflection[195] Considering the increase in topographical texture with effective phonon

scattering and low thermal diffusivity in PDA (0.08 W m^{-1} K^{-1}), the thermal energy dissipation must be much slower than the accumulation, which rationalized the high photothermal conversion.

Moreover, the convective heat loss of solar absorber to air cannot be ignorable, thus the heat insulation layer is a key factor in achieving thermal localization. The hollow structure of SEC with trapped air pockets is a good candidate as a heat resistance layer, resulting from the low thermal conductivity of air.[100] In the thermal steady state, the surface temperature showed more than 13.7 °C higher than the bottom water temperature (25.9°C). From the results in **Figure 6.5b**, the solar evaporator (p-SDWE) acted as a controlled sample by removing the SEC layer, resulting in a lower surface temperature increase of approximately 36.2°C and ultimately raising the bottom water temperature to 27.4°C. That was attributed to the strong thermal localization of hollow PN10-g-SEC layer, which effectively reduced excess convection heat losses to the water beneath. Therefore, the introduction of PN10-g-SEC layer within the SDWEs could maintain the lower temperature fluctuations and reduced the heat loss, revealing the potential improvement of evaporation rate for outdoor operation.

Selective and directional water transport of thermo-responsive interfacial layer

A solar evaporator with controllable water management enables the continuous water supply while alleviating the excess energy consumption during water-vapor phase transition, which is desirable for achieving higher evaporation rate. Our SDWEs serve as a flexible and novel approach to manage water transport via an internal structure design that utilizes selective and directional water transport.

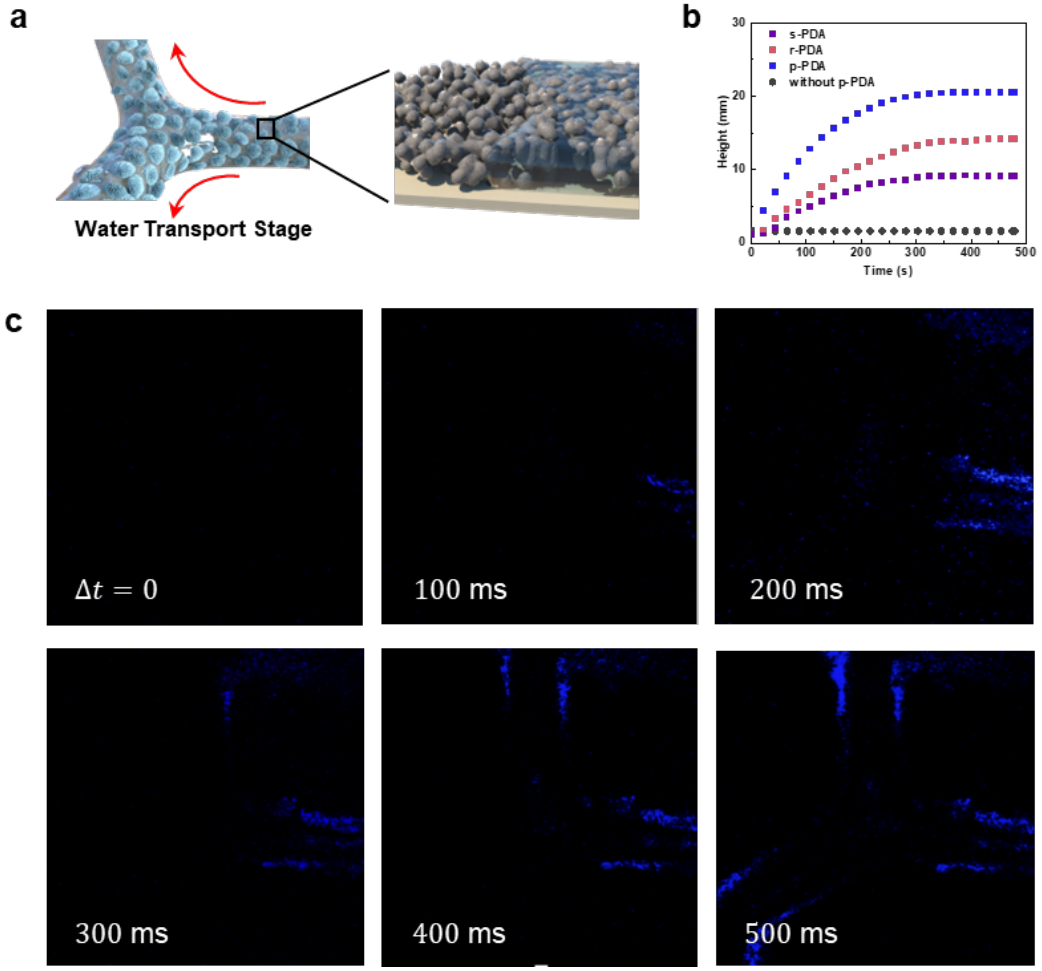

Figure 6.7 a. Schematic illustration of water transport within switchable channel of SDWEs, **b.** Water transport rate along PDA layer varying different structures, **c.** Confocal microscopic images of thin water transport along PDA@NiF

The continuous water supply from seawater to the evaporator layer is a prerequisite for the optimal vaporization of water. As we know, Ni foam itself has many interconnected pores that can generate capillary forces, which is one of the driving forces necessary for vertical transport of liquid water. Therefore, we designed porous PDA coating layers on the skeleton of NiF as water wicking layer that produced narrow water-transport channels within the interconnected pores of NiF and the pore generated by the PDA nanospheres (**Figure 6.7a**). Notably, the water transport rate is affected by different factors, such as the topography, and the water affinity of the channel. We first investigated the influence of topography of PDA layer on the water transport rates of three types of coating surfaces (s-PDA, r-PDA, p-PDA). To simplify the water management configurations, three different PDA coated nickel plates were used to compare the vertical water transport rates. These plates were positioned upright in a water-filled environment, and the changes in the water height were captured using a high-speed camera. As shown in **Figure 6.7b**, water could be rapidly transported upward on the p-PDA surface with a water transport rate of up to 10.0 mm/s. In contrast, the s-PDA and r-PDA surfaces, the rate of water transport was limited to 0.7 mm/s and 2.10 mm/s respectively. While

water cannot be keep transported upward on the plate without the PDA layer, it could only attain a certain height associated with the capillary action.[115] Additionally, the water transport rate was independent of the thickness of the PDA layer, but it had an impact on the evaporation rate, where thicker water layers displayed lower evaporation efficiency, while ultra-thin water layers led to salt accumulation[196] (**Figure 6.8**). This phenomenon was induced by distinct capillary force generated during the water pumping process, where water pumping on p-PDA surface utilized the roughness structure of the wall and closed capillary force.

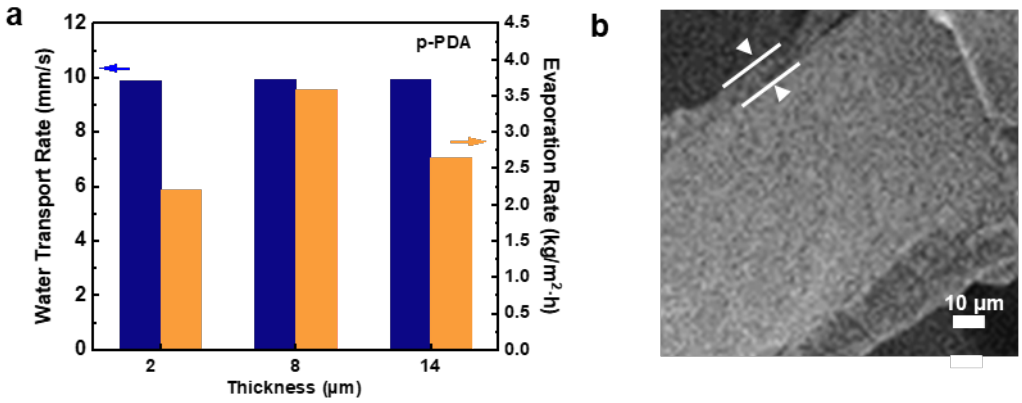

Figure 6.8 a. Illustration of the water transport rate and evaporation rate in varying PDA layers, **b.** The thickness of p-PDA layer on PN10-g-SEC

In addition to the topography and diameter of the channel, the water affinity also played an important role in the capillary force that was reflected by the water transport rates.[197] The wettability characteristics of the PDA surface were key factors controlling the interaction of water and the surfaces that were described by the water contact angle, surface free energy and adhesive force. **Figure 6.9** shows that the water contact angle of p-PDA surface was 4° and was superhydrophilic, where water could easily spread (1 s) and penetrated the coating layer in 2.5 s. r-PDA possessed higher hydrophilicity with a water contact angle (CA) of 12.5±1° compared to s-PDA layer with a CA of 32.1±1°. In addition, the surface free energies calculated based on Owens, Wendt, Rabel and Kaelble (OWRK) theory demonstrated the surface attractive force towards polar/non-polar surfaces[29]. Specifically, p-PDA surface with 72.3 mJ m^{-2} possessed a higher affinity towards water compared to the other two surfaces, where the r-PDA and s-PDA surfaces possessed a value of 70.1 mJ m^{-2} and 67.6 mJ m^{-2}, respectively.[29]

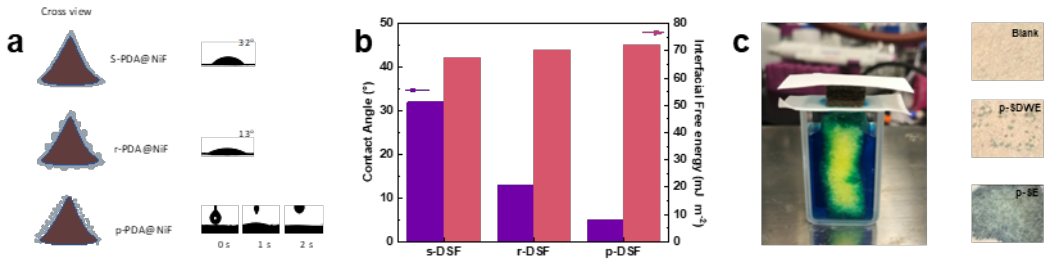

Figure 6.9 a. Ilustration of water affinity and its corresponding contact angles of PDA layers on the structure, **b.** Contact angle and interfacial free energy of s-PDA, r-PDA and p-PDA layers, c. The phase of water pumping using different p-SE and p-SDWE

Furthermore, the channels generated among the agminated PDA nanospheres was much smaller than the pores of the sponges, thus the capillary force generated by the channels among PDA was much higher than that in the pores of the sponges. This meant that water preferred to transport upward as an ultra-thin layer by the microchannels among PDA, even faster than the pores of the sponge itself. To illustrate this concept, we introduced fluorescent-dyed into the foams and tracked their motion using time series-confocal microscopy. As visualized in **Figure 6.7c**, the water phase (blue signal) preferential adhere to the skeleton of the PDA@NiF and flow rapidly along the entire framework. The water layer within the PDA@NiF coating was determined to have a thickness of 5 to 8 μm. The results illustrated that porous PDA layer have strong water affinity and capillary force, which could achieve directional ultrathin water transport. Apart from the capillary force, the pressure drop induced by evaporation also facilitated the flow of liquid.

Block bulk water after the exposure of sunlight

Since the capillary force generated by the pores of the foam itself is one of the driving forces for pumping water from bottom to the top surface, flooding of water in the foam is inevitable. In this situation, the solar energy is wasted to heat the excess bulk water, resulting in lower solar-driven water evaporation rates. An efficient water management is desirable for maintaining a high solar steam generation. The introduction of thermo-responsive PN10-g-SEC microparticles serves as a gating layer for water transport. When the foam was placed under the solar illumination, the temperature of the bottom section was increased to above the LCST and its hydrophobic character repelled the water. Thus, the water only flow along the microchannel and cannot not pass through the macrochannels of the foam itself.[198] Thus, this could effectively block the bulk water without sacrificing the continuous water supply.

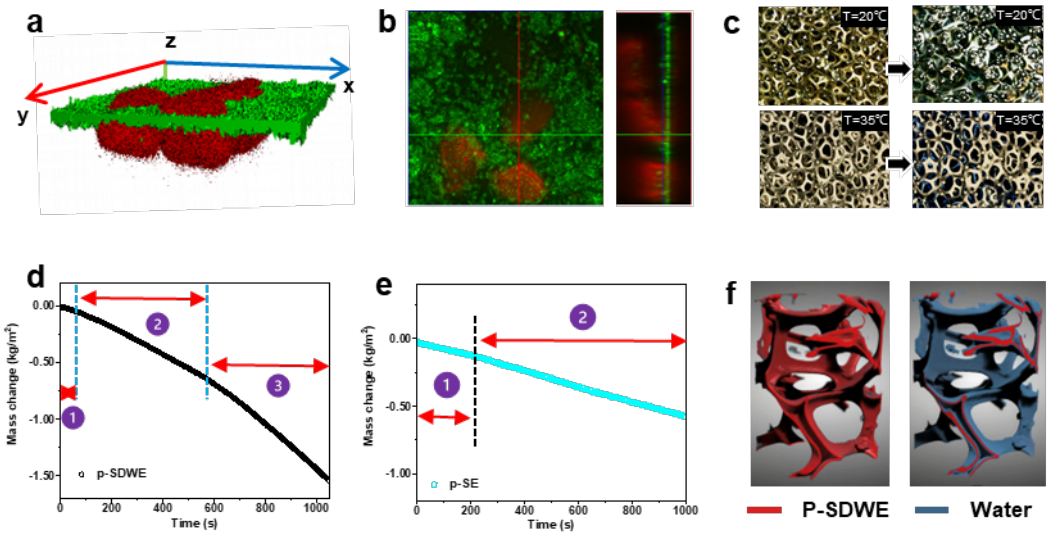

Figure 6.10 a. The contact line between pollen surface-air-water observed by confocal laser microscopy, b. The cross view of pollen -air-water interface observed by confocal laser microscopy, **c.** Water pumping driven by different temperature captured by microscopy, **d.** Mass change of water generated by p-SDWE under 1 sun irradiation, **e.** Mass change of water generated by p-SE under 1 sun irradiation, **f.** Thin water layer measured by Micro-CT

To further confirm the water-solid surface interaction, we imaged the 3D interface in contact between the liquid droplet and integrated PN10-g-SEC surface using the confocal laser microscopy at different temperatures.[199] The green section (fluorescence-stained) is represented as the water phase in the confocal images, while the red section is associated with PN10-g-SEC microparticles (**Figure 6.10a**). At the temperature below the LCST, the green section was observed from the base substrate to the outer surface, illustrating the droplet tendency to fully wet the micro-particle surface and fill the gap between the microparticles. In contrast, if the droplet contacted with the PN10-g-SEC surface at a higher temperature (above LCST), we could observe the liquid baseline suspended between particles, indicating a non-wetted state. This result demonstrated that the temperature could

readily switch the droplet-surface interaction and drive the water transport along the preferred channel. As a proof on the blocking of the bulk water, we characterized the water blocking characteristic of the PN10-g-SEC layer during the solar steam generation, by recording the pumped water states using an optical microscope. The p-SDWE were placed onto the dyed water, and the water transport upwards within the pore and along the skeleton was recorded. Water easily pumped up via the capillary force generated by the pores of the Ni foam, where the dyed water filled the foam without solar illumination (**Figure 6.10b**). In contrast, under the solar illumination, a thin water layer along the skeleton of p-SDWE was observed on the topside where the water layer was indicated by the light dot but it did not block the pores of evaporator layer. Thus, this temperature-dependent wettability transition characteristics endowed the PN10-g-SEC as a smart gate that could switch off the water transport channel within the pores of the foam during the evaporation process. Simultaneously, a pH-test paper, functioning as a color indicator, was placed on the upper surface of the foams within the water supply device as shown in **Figure 6.9c**. The color reaction of the pH-test paper was then monitored and recorded. After 5 s, no color change was observed from the paper on the NiF, while blue clusters can be observed on the p-SE. After 5 s, no color change was observed from the paper on the NiF, while blue clusters can be observed on the p-SE. These results indicated that water rapidly transport from bottom to the top surface through the macrochannels present within the pores of the foam material itself. However, distinct from the water transport phenomenon, abundant blue dots were observed in the first stage of the p-SDWE and followed by the blue clusters. Owing to the high surface free energy and voids among the hierarchical structure, the water could easily wet the PDA nanospheres to form continuous liquid bridges on p-PDA. Consequently, closed capillary force generated in p-PDA surface displayed fast water wicking at the thin water layer.[200] The ability to manipulate the water affinity has a significant impact on both the quantity and rate of water supply, consequently playing a crucial role in the water evaporation process.

6.3.3 Mechanism for high-efficiency solar water evaporation

In general, the evaporation rate was calculated using the overall mass change once the temperature approached a steady state (pre-heating for ~10 min). To examine the water transport behavior for the whole process, we recorded the water loss under transient conditions, enabling the comparison of the evaporation rates. The mass change of water within the SDWE was observed to possess three distinct stages, as depicted in **Figure 6.10d**. The initial stage involved the light-to-heat conversion and transfer, where natural water evaporation occurred.[102] Following this process, as the bulk water filled the pores, evaporation occurred throughout the entire foam at a rate of 1.2 kg m^{-2} h^{-1}. These two stages are referred to as the response period of SDWEs over a time period of around 400 s, which the evaporation rate was typically calculated from this point. The foam exhibited high evaporation rate of 3.8 kg m^{-2} h^{-1}, where this third stage proceeded with the supply of thin water. Conversely, the foam lacking the PNm-g-SEC gating layer (p-SE) demonstrated lower efficiency in solar evaporation despite its rapid response (**Figure 6.10e**). In comparison, the average

evaporation rate of p-SDWE was 3.58 kg m^{-2} h^{-1}, which was even higher than the evaporation rate of p-SE. The results demonstrated that the thin water layer promoted the water pumping and evaporation process.

To examine the mechanism of enhanced water evaporation by SDWEs, water transport driven by temperature gradient, water-vapor phase transformation and energy conversion at solid-liquid interface were analyzed. The thickness of the water layer directly impacted the amount of thermal energy required for the liquid water-to-vapor transition during the water evaporation process. Micro-CT with a resolution of 500 nm was first utilized to quantify the thickness of water on the SDWEs.[201] The foam with the water supply systems was sealed and placed in the sample room, and the obtained 2D images and 3D reconstruction models at different positions were recorded. The KI solution was used as a contrast agent for better observation of the different phases.[202] As shown in **Figure 6.10f**, the inner phase of red section was assigned to the sponge skeleton and the blue phase corresponds to the water phase. According to the CT scanning, no water filled the pores of the sponge itself, which further confirmed that the ultrathin water layer was generated within the whole sponge.[203] For the cross view of water phase, the calculated thickness of water ranged from 5.7 to 7.9 μm, and the average thickness was about 6.8 μm (**Figure 6.11**). The reduced thickness of water layer not only enhanced the water transport rate, but also impacted the evaporation process and its associated evaporation entropy. When water molecules were confined within a microchannel, they tended to escape from the surface as small clusters rather than individual molecules. As a result, the evaporation of water in this confined state led to a lower equivalent evaporation enthalpy (~1080 J g^{-1}) compared to the conventional latent heat of bulk water[101b] (**Figure 6.12**). This characteristic of thin water layer transport within the foam could effectively mitigate the unnecessary heat required for vaporization.[38a]

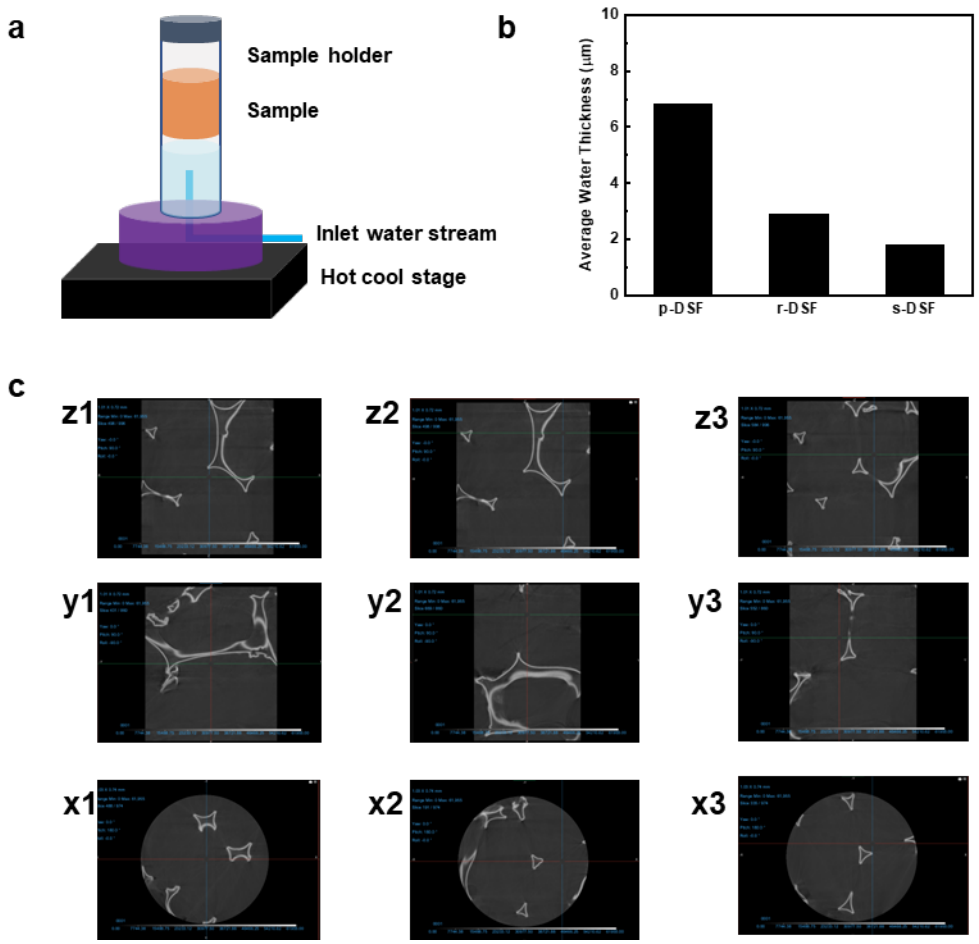

Figure 6.11 a. Thin water layer characterization conducted by Micro-CT, **b.** Water thickness within s-SDWE, r-SDWE and p-SDWE, **c.** Cross view of water layer observed in p-SDWE

We measured the evaporation enthalpy of water in the SDWEs using the differential scanning calorimeter (DSC). The vaporization enthalpy measurements were conducted by placing the saturated foam in an open aluminum crucible and subjected to a linear heating rate of 5 K/min under a nitrogen flow rate of 20 mL/min, within a temperature range of 20 to 180 °C. The effective specific heat capacity was calculated by comparing the heat flow of the measured samples with that of the standard sample. As shown in **Figure 6.12**, a sharp peak was observed for pure water, followed by a significant reduction in the heat flow signal, indicating immediate water evaporation.[204] However, the heat flow signals were different in all the tested SDWE samples, and the peaks were much broader and smaller than that of pure water. The measured enthalpy of water was 2420 J/g, which was close to the theoretical value of 2450 J/g, indicating the accuracy of our measurements. The vaporization enthalpy of water within the p-SDWE was significantly lower than that of pure water, attributable to the influence of the hydrogel network on the evaporation process.

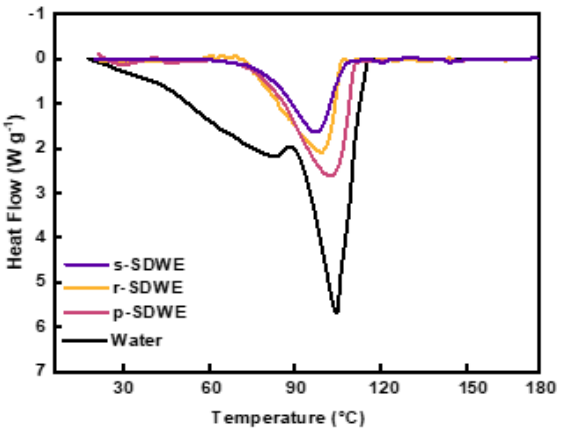

Figure 6.12 Thermograms of pure water and SDWEs.

To determine the vaporization enthalpy, the evaporation enthalpy of water within SDWE was measured. Specifically, water and SDWE samples with the same surface area were placed together in a closed container along with a supersaturated potassium carbonate solution, creating a stabilized relative humidity (RH) under room temperature.[127b] The equivalent evaporation enthalpy (h_{eq}) of water in the SDWEs could be estimated by vaporizing water with the same power input (U_{in}), using the equation (6-1):

$$U_{in} = h_{eq}\, m_0 = h_{vap} m_g \qquad (6\text{-}1)$$

where h_{vap} is the evaporation enthalpy and m_0 is the mass change of bulk water, while mg corresponds to the mass change of the sample. The evaporation rate of water and the calculated h_{eq} are shown in **Figure 6.12**, where h_{eq} was 1930 J g^{-1} for p-SDWE, was found to be significantly lower compared to bulk water.

Table 6.1 Equivalent evaporation Enthalpy of Water and SDWEs

enthalpy (J g^{-1})	s-SDWE	r-SDWE	p-SDWE	water
DSC	1610	1780	1930	2420
vaporization test	1032	1050	1080	

The design in obtaining an ultrathin water layer in the SDWE contributed to achieving high energy efficiency. The energy efficiency(η) was calculated using the following equation $\eta = mh_v/(C_{opt}P_0)$. Specifically, m represents the net evaporation rate and while h_v denotes the evaporation enthalpy of the water in the SDWE. The optical parameters assigned in the equation are referred to P_0 for the solar irradiation power and C_{opt} for the optical concentration.[49] As shown in **Figure 6.13b**, the p-SDWE achieved an energy efficiency of ≈93.9% under one sun, which was higher than the other two evaporator (s- SDWE and r- SDWE). This enhancement could be attributed to the incorporation

of a switchable microchannel, which minimized the heat loss to the water phase, resulting in only a 1.9% convection loss and a conduction heat loss of approximately 1.86% of the total received energy. The energy loss during the entire process could be attributed to four main factors: conduction, radiation, convection, and reflection.[49] Each heat loss parameters were calculated as follows:

$$Q_{conduction} = Cm\Delta T \quad (6.2)$$

where $Q_{conduction}$ refers to the heat energy transfer from the evaporator to bulk water, C was the specific heat capacity of pure water (4.2 kJ kg^{-1} K^{-1}), m was the weight of water and ΔT is the temperature change of bulk water under one sun irradiation within 3600 s. Therefore, the conduction heat loss of the evaporator was ~1.86% under 1 sun irradiation.

$$Q_{radiation} = \varepsilon A\sigma(T_s^4 - T_0^4) \quad (6.2)$$

where ε corresponding to the emissivity (assumed to be 1), A was the evaporator area (5.0 x 5.0 cm^2), and σ was the Stefan-Boltzmann constant (5.669 × 10^{-8} $Wm^{-2}K^{-4}$), T_s is associated with the temperature of the evaporator surface, T_0 was the ambient water temperature. The surface radiation heat loss accounts for ~2.84% of the total energy received.

$$Q_{convection} = hA(T_s - T_0) \quad (6.3)$$

where h was the convection heat transfer coefficient (5 W m^{-2} K^{-1}). The convection heat loss made up for 1.9% of the total received energy.

The measured average reflection loss of p-SDWE over the broad solar spectrum (200–2000 nm) was ~6.4%. Therefore, the sum of calculated energy losses was 13.0% under 1 sun illumination. Besides, the hydrophilic nature of the p-PDA layer reduced the heat transfer resistance at the interface, leading to improved heat transfer and facilitating the formation of a vaporized core. Thus, the p-SDWE showed a high-performance of solar-driven water evaporation.

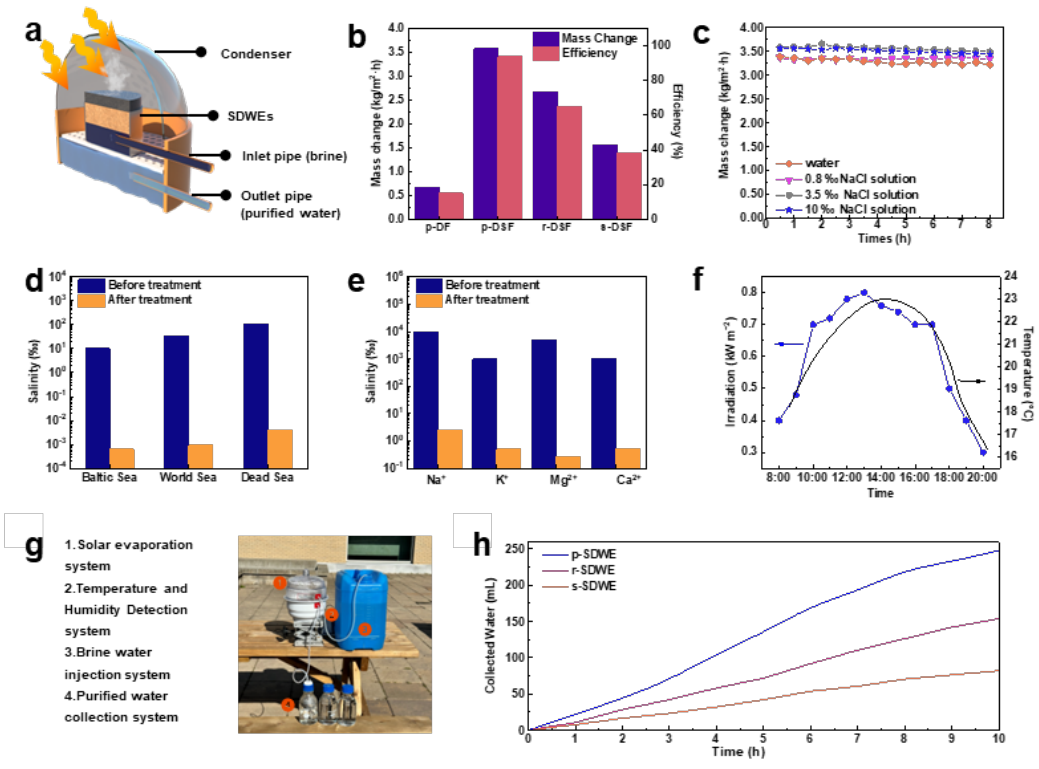

Figure 6.13 a. Schematic illustration of solar-driven water evaporation, **b.** Evaporation rate and efficiency generated by SDWEs, **c.** Evaporation rate under salt solution, **d.** The salinities of three artificial seawater samples before and after desalination using p-SDWE. **e.** Measured concentrations of four primary ions in an actual seawater sample before and after desalination, **f.** Solar radiation recorded over time on a sunny day from 08:00 to 20:00, **g**. A prototype solar water purification system simulating the practical water purification equipment, **h.** The amount of purified water during 12 h of outdoor solar desalination

6.3.4 Laboratory and outdoor solar desalination

To further evaluate the long-term water generation performance, the continuous solar evaporation performance of the SDWE was test in a standard testing chamber for 6 hours under one sun irradiation (**Figure 6.13a**). The evaporation rate of p-SDWE remained constant at 3.58 kg m^{-2} h^{-1} and the water generation rate achieved up to 3.02 kg m^{-2} h^{-1}, which was constant with similar deposition and drainage characteristic that was similar to the observed at the short-term test (**Figure 6.13b**). The results confirmed that the surface would not succumb to flooding that could destroy the surface structure and reduce the water harvesting efficiency. The continuous solar desalination performance of the SDWE was also evaluated using simulated seawater with specific salinity (g of dissolved salt per kg seawater (‰)), including Baltic sea (8‰), world ocean (35‰), and Dead Sea (100‰), under one sun irradiation.[205] As shown in **Figure 6.13c**, there was no visible salt crystal appeared on the top surface of the foam after the 6 h continuous illumination due to the confined convection flow. Besides, the average evaporation rate for seawater (0.8 wt%) remained as high as 3.56 kg m^{-2} h^{-1}. After the solar desalination, the salinities of different simulated seawater samples decreased correspondingly (**Figure 6.13d**), which was far below the WHO and EPA drinking water standard. Moreover, the concentration of Na^+, Mg^{2+}, Ca^{2+}, and K^+ was significantly reduced by orders of magnitude after solar desalination (**Figure 6.13e**). Even when the solar irradiation reached 5 kW m^{-2}, the occurrence of salt crystal could be resolved by the natural convection through the large pore size of the SDWE during the night. The introduction of flexible water transport channel could enable its recyclability and anti-salt-accumulation characteristic[206].

To demonstrate the possibility of continuous water generation, we conducted an outdoor experiment using the homemade solar evaporator system. A solar water purification prototype based on the optimized evaporator system was placed on the roof of the Engineering 3 at the University of Waterloo campus (**Figure 6.13g**). The experiment was conducted from 08:00 to 20:00 under natural sunlight with an average solar heat flux of ~0.72 KW m^{-2}. In this setup, a SDWE sample with a diameter of ~10 cm x10 cm and thickness of 1 cm was floated in a water container, and the container was insulated by a thermal insulation made of polystyrene foam to minimize heat loss. The evaporated water condensed on a transparent condenser that was modified with an omniphobic lliquid-like coating[77b], avoiding light path occlusion and scattering (**Figure 6.14**). Additionally, an automatic water supply and pumping system were implemented using gravity, eliminating the need for external energy input. As shown in **Figure 6.13e**, the p-SDWE could achieve an average water

evaporation rate of 3.14 kg m^{-2} h^{-1} and water purification rate of ~2.48 L m^{-2} h^{-1}. Besides, the surface temperature of SDWE approached the peak temperature of around 50°C in the thermal steady state. The temperature difference exhibited between SDWE and surrounding environment illustrated the localized heat supported by the photothermal layer of PDA and good thermal insulation of the SEC layer. These findings suggested that the p-SDWE evaporator exhibited great potential as a cost-effective solution to enhance the performance of solar-driven water generation on a practical and large scale.

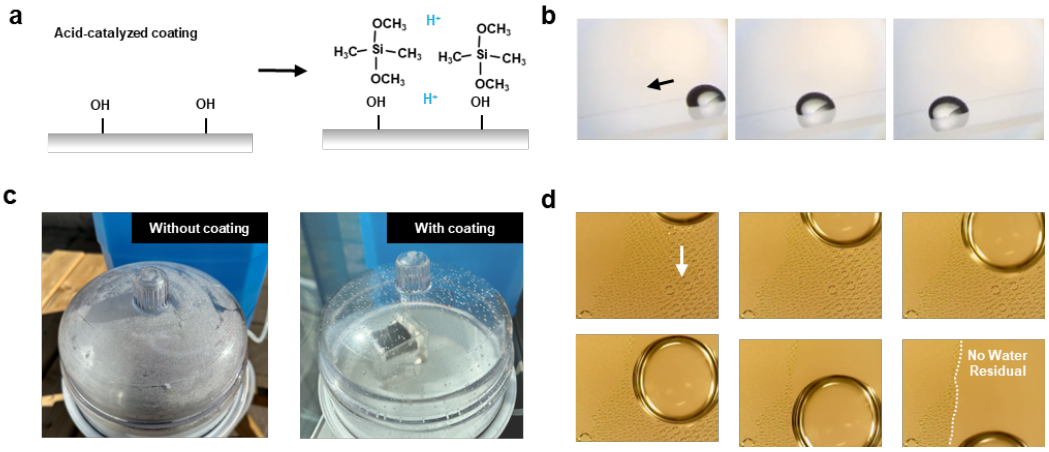

Figure 6.14 a. Preparation of omniphobic liquid-like coating, **b.** Time-sequence images illustrating water slide on the omniphobic liquid-like coated glass substrate at a tilted angle of 10°, **c.** Illustration of condenser applied in SDWE system with omniphobic liquid-like coating, **d.** Droplet movement during evaporation process observed by microscope.

6.4 Conclusions

We have successfully fabricated a solar evaporator (SDWE) with bilayer structure that enabled the continuous thin water supply and efficient thermal energy management. Taking advantage of the thermo-responsive layer, the water transport channel was switchable to allow for the passage of thin water within the inner microchannel. This water gating mechanism endowed the evaporator with a high solar-vapor conversion performance due to the thin water required low latent heat during evaporation compared to ther bulk water. With the optimization of solar-driven water generation system, the solar evaporator could achieve a high vapor generation rate of up to 3.58 kg m^{-2} h^{-1} and 93.9% solar-to-vapor efficiency under 1 sun irradiation. Furthermore, the SDWE demonstrated its potential in solar-driven seawater desalination, contaminated water purification, and heavy metal ions removal. These findings provide fundamentals understandings to the water transport and phase-transition at the evaporated interface, offering opportunities for the advancement of solar evaporator design.

Chapter 7 Conclusions and Recommendation for Future Studies

7.1 Conclusions

In this thesis, approaches to rationally engineer sustainable superwettable surfaces were successfully implemented for efficient water manipulation. In Chapter 3, a unique superhydrophobic surface with tunable nanoscale hydrophilicity was constructed by structured Pickering emulsions. Preferential exposure of cellulose nanocrystal's outer surface and wax microspheres accelerated the droplet deposition allowing for the manipulation of droplet mobility. Appropriate tunning of the wetting characteristics of the surfaces, optimizing the hydrophobicity and density of the water affinity nanodomains enhanced the water deposition rate without the sacrifice of water transport rate, achieving an optimal water harvesting flux of 3.402 L/m^2/h for a plate and 5.02 L/m^2/h for a mesh. This nano-hydrophilic/superhydrophobic surfaces performed a stable high water harvesting efficiency through tunning the surface topography, balancing the trade-off between water deposition and transport, sustaining surface durability. As a result of the continuous water capture on nanoscale hydrophilic patterns, more than a 2-fold enhancement in the water collection rate was achieved compared to lotus leaf-like superhydrophobic surfaces.

Through external environmental stimuli, we investigated the temperature-dependent interfacial properties on thermo-responsive surfaces at multi-scale level and presented a fundamental design strategy to develop thermo-responsive surfaces with tunable wettability. Specifically, we investigated the assembly of microparticles grafted with two types of LCST polymers, PNIPAM and POEGMA188, and correlated the interfacial water structure variation at multiple length scale with the wettability transition of the integrated surface, as revealed by Raman measurements, supplementary rheology experiments and confocal microscopy. From the analysis at nanoscale and macroscale length scale, we concluded that the increased intermediate water (decreased bonded water structure) with combined surface roughness resulted in the enhanced hydrophobicity. This surface design strategy provided information that correlated the molecular-level conformational transition with the macroscopic surface wettability. Moreover, the knowledge and fundamental understanding derived from this study demonstrated the potential application of PNIPAM and POEGMA188 by controlling the interfacial water structure at solid-liquid interface in other systems, such as biobased responsive surfaces.

Building upon the study in Chapter 4, we examined the thermo-responsive surfaces with programmable adhesive transformation characteristics to facilitate the development of the controllable droplet manipulation. By controlling the comonomer grafting ratio and morphology of sunflower pollen microparticles, the surfaces exhibited superhydrophilic/superhydrophobic transformations under flexible LCSTs. Particularly, the surface under superhydrophobic state could alter its water attractive and adhesive properties in a controllable manner. With the introduction of hydrophobic comonomers, the surfaces exhibited lower water attractive force due to the weak hydrogen bonding network and lower interfacial free energy. Moreover, the surfaces roughness

determined the water-resistance force generated on the surface, especially when droplet movement was controlled by external force or pressure. Compared to surfaces fabricated with SEC microsheets, the high-roughness surface produced from SEC microspheres exhibited stronger water resistance endurance due to the air cushion beneath the spiky structures. The surface adhesion was influenced by the cooperative functions of the water attractive and water-resistance forces. These investigations demonstrated the potential of utilizing the unique characteristics of these surfaces for controllable droplet transport on programmable wettability sites, as well as for the effective droplet deposition and transport in water harvesting applications.

Based on the study of switchable wettability characteristics of pollen microparticles in Chapter 4 and Chapter 5, we designed a bilayer-structured solar evaporator (SDWE) with bilayer structure that enabled the continuous thin water supply and efficient thermal energy management. Taking advantage of the thermo-responsive layer, the water transport channel was switchable and only allowed for the passage of thin water within the inner microchannels. This water gating mechanism endowed the evaporator with high solar-vapor conversion performance, attributing to the thin water that required low latent heat during evaporation compared to bulk water. With the optimization of solar-driven water generation system, the solar evaporator could achieve a high vapor generation rate of up to 3.58 kg m^{-2} h^{-1} and 93.9% solar-to-vapor efficiency under 1 sun irradiation. Furthermore, the SDWE demonstrated its potential in solar-driven seawater desalination, contaminated water purification, and heavy metal ions removal. These findings generated improved understanding into water transport and phase-transition at the evaporated interface, offering opportunities for the advancement of solar evaporator design.

7.2 Recommended Future Work

Based on the studies conducted in this thesis, the following recommendations are proposed for future study.

Surface Design

a. Despite the large number of biomimetic surfaces being designed, there is still a lack of clear design guidance to accomodate different demands in dynamic water management. By exploring the fundamental mechanism of each process combined with simulated theoretical tools, such as artificial intelligence, machine learning and materiomics, a useful strategy in guiding the exploration and design of new functional materials/structures can be advanced.

b. Moreover, biomimicry surface engineering offers new insights into the production of intelligent water harvesting systems on demand, by combining nature and synthetic analogues to create self-organizing, self-powered, self-sustained and self-evolving structures. Ultimately, the designs of biomimetic material/structures could manipulate water or vapor under dynamic conditions.

c. Apart from the advanced properties, the durability and self-cleaning of the superhydrophobic surface need further improvement to enable long-term and continuous utilization.

Sustainable Water Harvesting and Manipulation System Development

a. The toxicity and biocompatibility of materials for constructing superwettable surfaces should be considered, particularly in water harvesting devices where the safety of collected water is directly affected. The construction of hierarchical air-trapped microstructure on substrates and the coating of surfaces with low surface energy materials, such as fluoropolymers or organic siloxanes could achieve excellent water repellent properties. Although these surfaces display good performance in water collection, fluoride-based materials are harmful to the environment and human. Thus, a series of novel and sustainable materials should be explored and exploited, such as cellulose nanocrystals, biocompatible polymers, etc.

b. The current fabrication methods have many restrictions and large-scaled production of water harvesting and purification devices is challenging. The intricate bioinspired structure required for water harvesting typically demands complex technologies, leading to increased costs and high energy consumption. To enable large-scale utilization, it is crucial to develop facile, low-cost, and highly efficient water harvesting technologies that can overcome these challenges and be readily implemented on a practical scale.

c. The understanding of the underlying water management mechanism of these natural organisms and utilizing the mechanisms to achieve controllable water capture/transport can promote the development of water harvesting system. With considerable efforts to bridge the gaps between the state-of-the-art water harvesting systems and its practical utilizations, this technology can be optimized to balance efficiency, cost, scalability, stability, and adaptability so that the commercial application of this technology can be realized.

Letters of Copyright Permission

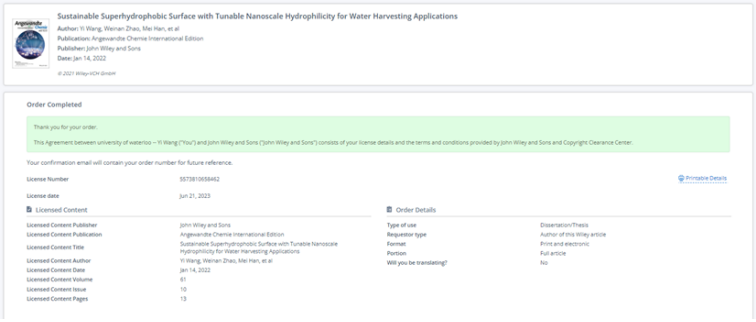

Sustainable Superhydrophobic Surface with Tunable Nanoscale Hydrophilicity for Water Harvesting Applications

Author: Yi Wang, Weinan Zhao, Mei Han, et al
Publication: Angewandte Chemie International Edition
Publisher: John Wiley and Sons
Date: Jan 14, 2022

© 2021 Wiley-VCH GmbH

Order Completed

Thank you for your order.

This Agreement between university of waterloo -- Yi Wang ("You") and John Wiley and Sons ("John Wiley and Sons") consists of your license details and the terms and conditions provided by John Wiley and Sons and Copyright Clearance Center.

Your confirmation email will contain your order number for future reference.

License Number	5573810658462
License date	Jun 21, 2023

Printable Details

Licensed Content

Licensed Content Publisher	John Wiley and Sons
Licensed Content Publication	Angewandte Chemie International Edition
Licensed Content Title	Sustainable Superhydrophobic Surface with Tunable Nanoscale Hydrophilicity for Water Harvesting Applications
Licensed Content Author	Yi Wang, Weinan Zhao, Mei Han, et al
Licensed Content Date	Jan 14, 2022
Licensed Content Volume	61
Licensed Content Issue	10
Licensed Content Pages	13

Order Details

Type of use	Dissertation/Thesis
Requestor type	Author of this Wiley article
Format	Print and electronic
Portion	Full article
Will you be translating?	No

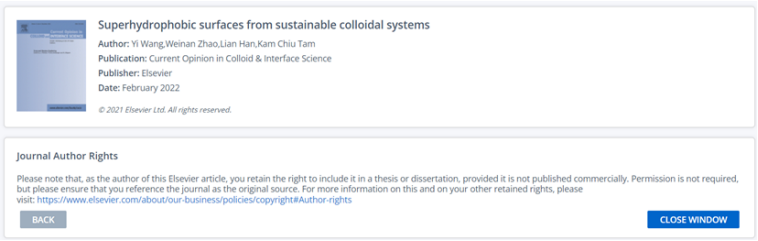

Superhydrophobic surfaces from sustainable colloidal systems

Author: Yi Wang,Weinan Zhao,Lian Han,Kam Chiu Tam
Publication: Current Opinion in Colloid & Interface Science
Publisher: Elsevier
Date: February 2022

© 2021 Elsevier Ltd. All rights reserved.

Journal Author Rights

Please note that, as the author of this Elsevier article, you retain the right to include it in a thesis or dissertation, provided it is not published commercially. Permission is not required, but please ensure that you reference the journal as the original source. For more information on this and on your other retained rights, please visit: https://www.elsevier.com/about/our-business/policies/copyright#Author-rights

BACK CLOSE WINDOW

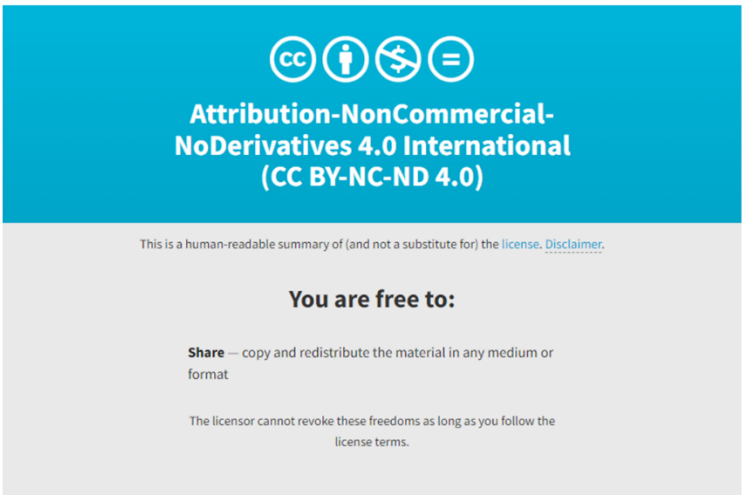

Attribution-NonCommercial-NoDerivatives 4.0 International (CC BY-NC-ND 4.0)

This is a human-readable summary of (and not a substitute for) the license. Disclaimer.

You are free to:

Share — copy and redistribute the material in any medium or format

The licensor cannot revoke these freedoms as long as you follow the license terms.

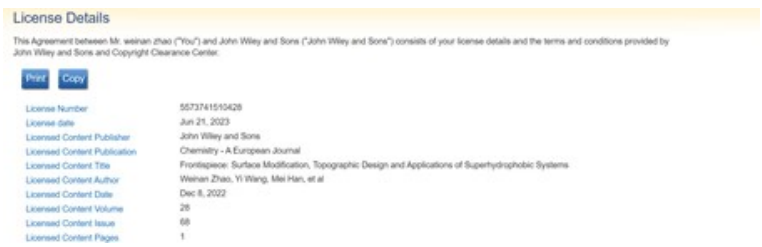

License Details

This Agreement between Mr. weinan zhao ("You") and John Wiley and Sons ("John Wiley and Sons") consists of your license details and the terms and conditions provided by John Wiley and Sons and Copyright Clearance Center.

Print Copy

License Number	5573741510428
License date	Jun 21, 2023
Licensed Content Publisher	John Wiley and Sons
Licensed Content Publication	Chemistry - A European Journal
Licensed Content Title	Frontispiece: Surface Modification, Topographic Design and Applications of Superhydrophobic Systems
Licensed Content Author	Weinan Zhao, Yi Wang, Mei Han, et al
Licensed Content Date	Dec 8, 2022
Licensed Content Volume	28
Licensed Content Issue	68
Licensed Content Pages	1

References

1. Li, A., Li, H., Li, Z., Zhao, Z., Li, K., Li, M. & Song, Y. Programmable droplet manipulation by a magnetic-actuated robot. *Science Advances* **6**, eaay5808 (2020).
2. Sun, L., Bian, F., Wang, Y., Wang, Y., Zhang, X. & Zhao, Y. Bioinspired programmable wettability arrays for droplets manipulation. *Proceedings of the National Academy of Sciences* **117**, 4527-4532 (2020).
3. Liu, Y., Zhao, L., Lin, J. & Yang, S. Electrodeposited surfaces with reversibly switching interfacial properties. *Science Advances* **5**, eaax0380 (2019).
4. Wenzel, R.N. Resistance of solid surfaces to wetting by water. *Industrial & Engineering Chemistry* **28**, 988-994 (1936).
5. Cassie, A.B.D. & Baxter, S. Wettability of porous surfaces. *Transactions of the Faraday Society* **40**, 546-551 (1944).
6. Wang, Y., Zhao, W., Han, M., Guan, L., Han, L., Hemraj, A. & Tam, K.C. Sustainable Superhydrophobic Surface with Tunable Nanoscale Hydrophilicity for Water Harvesting Applications. *Angewandte Chemie International Edition* **61**, e202115238 (2022).
7. Schutzius, T.M., Jung, S., Maitra, T., Graeber, G., Köhme, M. & Poulikakos, D. Spontaneous droplet trampolining on rigid superhydrophobic surfaces. *Nature* **527**, 82-85 (2015).
8. Wang, Y., Zhao, W., Han, L. & Tam, K.C. Superhydrophobic surfaces from sustainable colloidal systems. *Current Opinion in Colloid & Interface Science* **57**, 101534 (2022).
9. Zhang, X., Sun, L., Wang, Y., Bian, F., Wang, Y. & Zhao, Y. Multibioinspired slippery surfaces with wettable bump arrays for droplets pumping. *Proceedings of the National Academy of Sciences* **116**, 20863-20868 (2019).
10. Meng, J., Yang, G., Liu, L., Song, Y., Jiang, L. & Wang, S. Cell adhesive spectra along surface wettability gradient from superhydrophilicity to superhydrophobicity. *Science China Chemistry* **60**, 614-620 (2017).
11. Huhtamäki, T., Tian, X., Korhonen, J.T. & Ras, R.H.A. Surface-wetting characterization using contact-angle measurements. *Nature Protocols* **13**, 1521-1538 (2018).
12. Butt, H.-J., Roisman, I.V., Brinkmann, M., Papadopoulos, P., Vollmer, D. & Semprebon, C. Characterization of super liquid-repellent surfaces. *Current Opinion in Colloid & Interface Science* **19**, 343-354 (2014).
13. Gao, N., Geyer, F., Pilat, D.W., Wooh, S., Vollmer, D., Butt, H.-J. & Berger, R. How drops start sliding over solid surfaces. *Nature Physics* **14**, 191-196 (2018).
14. Zhou, W.-l., Wu, T., Du, Y., Zhang, X.-h., Chen, X.-c., Li, J.-b., Xie, H. & Qu, J.-p. Efficient fabrication of desert beetle-inspired micro/nano-structures on polypropylene/graphene surface with hybrid wettability, chemical tolerance, and passive anti-icing for quantitative fog harvesting. *Chemical Engineering Journal* **453**, 139784 (2023).
15. Roth-Nebelsick, A., Ebner, M., Miranda, T., Gottschalk, V., Voigt, D., Gorb, S., Stegmaier, T., Sarsour, J., Linke, M. & Konrad, W. Leaf surface structures enable the endemic Namib desert grass Stipagrostis sabulicola to irrigate itself with fog water. *Journal of The Royal Society*

Interface **9**, 1965-1974 (2012).

16. Zheng, Y., Bai, H., Huang, Z., Tian, X., Nie, F.-Q., Zhao, Y., Zhai, J. & Jiang, L. Directional water collection on wetted spider silk. *Nature* **463**, 640-643 (2010).
17. Chen, H., Ran, T., Gan, Y., Zhou, J., Zhang, Y., Zhang, L., Zhang, D. & Jiang, L. Ultrafast water harvesting and transport in hierarchical microchannels. *Nature Materials* **17**, 935-942 (2018).
18. Gurera, D. & Bhushan, B. Passive water harvesting by desert plants and animals: lessons from nature. *Philosophical Transactions of the Royal Society A: Mathematical, Physical and Engineering Sciences* **378**, 20190444 (2020).
19. Parker, A.R. & Lawrence, C.R. Water capture by a desert beetle. *Nature* **414**, 33-34 (2001).
20. Masrahi, Y.S. Glochids microstructure and dew harvesting ability in Opuntia stricta (Cactaceae). *Journal of King Saud University - Science* **32**, 3307-3312 (2020).
21. Zhang, S., Chi, M., Mo, J., Liu, T., Liu, Y., Fu, Q., Wang, J., Luo, B., Qin, Y., Wang, S. & Nie, S. Bioinspired asymmetric amphiphilic surface for triboelectric enhanced efficient water harvesting. *Nature Communications* **13**, 4168 (2022).
22. Comanns, P., Esser, F.J., Kappel, P.H., Baumgartner, W., Shaw, J. & Withers, P.C. Adsorption and movement of water by skin of the Australian thorny devil (Agamidae: Moloch horridus). *Royal Society Open Science* **4**, 170591 (2017).
23. Elbaum, R., Gorb, S. & Fratzl, P. Structures in the cell wall that enable hygroscopic movement of wheat awns. *Journal of Structural Biology* **164**, 101-107 (2008).
24. Feng, S., Zhu, P., Zheng, H., Zhan, H., Chen, C., Li, J., Wang, L., Yao, X., Liu, Y. & Wang, Z. Three-dimensional capillary ratchet-induced liquid directional steering. *Science* **373**, 1344-1348 (2021).
25. Chen, C., Kuang, Y. & Hu, L. Challenges and Opportunities for Solar Evaporation. *Joule* **3**, 683-718 (2019).
26. Dawson, C., Vincent, J.F.V. & Rocca, A.-M. How pine cones open. *Nature* **390**, 668-668 (1997).
27. Xu, N., Hu, X., Xu, W., Li, X., Zhou, L., Zhu, S. & Zhu, J. Mushrooms as Efficient Solar Steam-Generation Devices. *Advanced Materials* **29**, 1606762 (2017).
28. Ma, Z., Liu, X., Xu, X., Liu, L., Yu, B., Maluk, C., Huang, G., Wang, H. & Song, P. Bioinspired, Highly Adhesive, Nanostructured Polymeric Coatings for Superhydrophobic Fire-Extinguishing Thermal Insulation Foam. *ACS Nano* **15**, 11667-11680 (2021).
29. Fowkes, F.M. ATTRACTIVE FORCES AT INTERFACES. *Industrial & Engineering Chemistry* **56**, 40-52 (1964).
30. Owens, D.K. & Wendt, R.C. Estimation of the surface free energy of polymers. *Journal of Applied Polymer Science* **13**, 1741-1747 (1969).
31. Wong, T.-S., Kang, S.H., Tang, S.K.Y., Smythe, E.J., Hatton, B.D., Grinthal, A. & Aizenberg, J. Bioinspired self-repairing slippery surfaces with pressure-stable omniphobicity. *Nature* **477**, 443-447 (2011).
32. Scanlon, B.R., Fakhreddine, S., Rateb, A., de Graaf, I., Famiglietti, J., Gleeson, T., Grafton, R.Q., Jobbagy, E., Kebede, S., Kolusu, S.R., Konikow, L.F., Long, D., Mekonnen, M., Schmied, H.M., Mukherjee, A., MacDonald, A., Reedy, R.C., Shamsudduha, M., Simmons, C.T., Sun, A.,

Taylor, R.G., Villholth, K.G., Vörösmarty, C.J. & Zheng, C. Global water resources and the role of groundwater in a resilient water future. *Nature Reviews Earth & Environment* **4**, 87-101 (2023).

33. Huang, X., Mandal, J., Xu, J. & Raman, A.P. Passive freezing desalination driven by radiative cooling. *Joule* **6**, 2762-2775 (2022).
34. Mauter, M.S. & Fiske, P.S. Desalination for a circular water economy. *Energy & Environmental Science* **13**, 3180-3184 (2020).
35. Hanikel, N., Prévot, M.S. & Yaghi, O.M. MOF water harvesters. *Nature Nanotechnology* **15**, 348-355 (2020).
36. Yu, Z., Zhu, T., Zhang, J., Ge, M., Fu, S. & Lai, Y. Fog Harvesting Devices Inspired from Single to Multiple Creatures: Current Progress and Future Perspective. *Advanced Functional Materials* **32**, 2200359 (2022).
37. Yue, H., Zeng, Q., Huang, J., Guo, Z. & Liu, W. Fog collection behavior of bionic surface and large fog collector: A review. *Advances in Colloid and Interface Science* **300**, 102583 (2022).
38. Liu, X., Beysens, D. & Bourouina, T. Water Harvesting from Air: Current Passive Approaches and Outlook. *ACS Materials Letters* **4**, 1003-1024 (2022).
39. Lord, J., Thomas, A., Treat, N., Forkin, M., Bain, R., Dulac, P., Behroozi, C.H., Mamutov, T., Fongheiser, J., Kobilansky, N., Washburn, S., Truesdell, C., Lee, C. & Schmaelzle, P.H. Global potential for harvesting drinking water from air using solar energy. *Nature* **598**, 611-617 (2021).
40. Tu, Y., Wang, R., Zhang, Y. & Wang, J. Progress and Expectation of Atmospheric Water Harvesting. *Joule* **2**, 1452-1475 (2018).
41. Zhao, F., Guo, Y., Zhou, X., Shi, W. & Yu, G. Materials for solar-powered water evaporation. *Nature Reviews Materials* **5**, 388-401 (2020).
42. Pang, Y., Zhang, J., Ma, R., Qu, Z., Lee, E. & Luo, T. Solar–Thermal Water Evaporation: A Review. *ACS Energy Letters* **5**, 437-456 (2020).
43. Zhang, W., Jin, Y., Yang, S., Zhang, H. & Wang, Z. Bioinspired Topological Surfaces for Mitigating Water, Thermal and Energy Crises. *Accounts of Materials Research* **3**, 199-212 (2022).
44. Li, J., Li, J., Sun, J., Feng, S. & Wang, Z. Biological and Engineered Topological Droplet Rectifiers. *Advanced Materials* **31**, 1806501 (2019).
45. Arzt, E., Quan, H., McMeeking, R.M. & Hensel, R. Functional surface microstructures inspired by nature – From adhesion and wetting principles to sustainable new devices. *Progress in Materials Science* **120**, 100823 (2021).
46. Lu, W., Ong, W.L. & Ho, G.W. Advances in harvesting water and energy from ubiquitous atmospheric moisture. *Journal of Materials Chemistry A* (2023).
47. Zhang, W., Wang, D., Sun, Z., Song, J. & Deng, X. Robust superhydrophobicity: mechanisms and strategies. *Chemical Society Reviews* **50**, 4031-4061 (2021).
48. Chen, F., Wang, Y., Tian, Y., Zhang, D., Song, J., Crick, C.R., Carmalt, C.J., Parkin, I.P. & Lu, Y. Robust and durable liquid-repellent surfaces. *Chemical Society Reviews* **51**, 8476-8583 (2022).

49. Chen, L., Huang, S., Ras, R.H.A. & Tian, X. Omniphobic liquid-like surfaces. *Nature Reviews Chemistry* **7**, 123-137 (2023).
50. Cho, H.J., Preston, D.J., Zhu, Y. & Wang, E.N. Nanoengineered materials for liquid–vapour phase-change heat transfer. *Nature Reviews Materials* **2**, 16092 (2016).
51. Ma, J., Sett, S., Cha, H., Yan, X. & Miljkovic, N. Recent developments, challenges, and pathways to stable dropwise condensation: A perspective. *Applied Physics Letters* **116**, 260501 (2020).
52. Zhang, M., Zheng, Z., Zhu, Y., Zhu, Z., Si, T. & Xu, R.X. Combinational biomimetic microfibers for high-efficiency water collection. *Chemical Engineering Journal* **433**, 134495 (2022).
53. Jiang, J., Gao, J., Zhang, H., He, W., Zhang, J., Daniel, D. & Yao, X. Directional pumping of water and oil microdroplets on slippery surface. *Proceedings of the National Academy of Sciences* **116**, 2482-2487 (2019).
54. Boylan, D., Monga, D., Shan, L., Guo, Z. & Dai, X. Pushing the Limit of Beetle-Inspired Condensation on Biphilic Quasi-Liquid Surfaces. *Advanced Functional Materials* **33**, 2211113 (2023).
55. Ejeian, M. & Wang, R.Z. Adsorption-based atmospheric water harvesting. *Joule* **5**, 1678-1703 (2021).
56. Zhou, X., Lu, H., Zhao, F. & Yu, G. Atmospheric Water Harvesting: A Review of Material and Structural Designs. *ACS Materials Letters* **2**, 671-684 (2020).
57. Tao, P., Ni, G., Song, C., Shang, W., Wu, J., Zhu, J., Chen, G. & Deng, T. Solar-driven interfacial evaporation. *Nature Energy* **3**, 1031-1041 (2018).
58. Liu, S., Li, S. & Lin, M. Understanding Interfacial Properties for Enhanced Solar Evaporation Devices: From Geometrical to Physical Interfaces. *ACS Energy Letters*, 1680-1687 (2023).
59. Jung, Y., Ahn, J., Kim, J.-S., Ha, J.-H., Shim, J., Cho, H., Oh, Y.S., Yoon, Y.-J., Nam, Y., Oh, I.-K., Jeong, J.-H. & Park, I. Spherical Micro/Nano Hierarchical Structures for Energy and Water Harvesting Devices. *Small Methods* **6**, 2200248 (2022).
60. Venkatesan, H., Chen, J., Liu, H., Liu, W. & Hu, J. A Spider-Capture-Silk-Like Fiber with Extremely High-Volume Directional Water Collection. *Advanced Functional Materials* **30**, 2002437 (2020).
61. Liu, Y., Zhai, H., Li, X., Yang, N., Guo, Z., Zhu, L., Gao, C., Hou, Y. & Zheng, Y. High efficient fog-water harvesting via spontaneous swallowing mechanism. *Nano Energy* **96**, 107076 (2022).
62. Bai, H., Zhao, T., Wang, X., Wu, Y., Li, K., Yu, C., Jiang, L. & Cao, M. Cactus kirigami for efficient fog harvesting: simplifying a 3D cactus into 2D paper art. *Journal of Materials Chemistry A* **8**, 13452-13458 (2020).
63. Li, C., Yu, C., Zhou, S., Dong, Z. & Jiang, L. Liquid harvesting and transport on multiscaled curvatures. *Proceedings of the National Academy of Sciences* **117**, 23436-23442 (2020).
64. Dai, X., Sun, N., Nielsen, S.O., Stogin, B.B., Wang, J., Yang, S. & Wong, T.-S. Hydrophilic directional slippery rough surfaces for water harvesting. *Science Advances* **4**, eaaq0919 (2018).
65. Feng, R., Song, F., Xu, C., Wang, X.-L. & Wang, Y.-Z. A Quadruple-Biomimetic surface for spontaneous and efficient fog harvesting. *Chemical Engineering Journal* **422**, 130119 (2021).

66. Yu, Z., Zhang, J., Li, S., Zhou, Z., Qin, Z., Liu, H., Lai, Y. & Fu, S. Bio-inspired Copper Kirigami Motifs Leading to a 2D–3D Switchable Structure for Programmable Fog Harvesting and Water Retention. *Advanced Functional Materials* **33**, 2210730 (2023).
67. Wang, Y., Zhao, W., Han, M., Guan, L., Han, L., Hemraj, A. & Tam, K.C. Sustainable Superhydrophobic Surface with Tunable Nanoscale Hydrophilicity for Water Harvesting Applications. *Angew. Chem. Int. Ed.* **61**, e202115238 (2022).
68. Song, J., Hou, Y., Sudersan, P., Lam, C.W.E., Poulikakos, D., Butt, H.-J. & Yeung, K.L. Inhibition of condensation-induced droplet wetting by nano-hierarchical surfaces. *Chemical Engineering Journal* **460**, 141761 (2023).
69. Yoon, J., Ryu, M., Kim, H., Ahn, G.-N., Yim, S.-J., Kim, D.-P. & Lee, H. Wet-Style Superhydrophobic Antifogging Coatings for Optical Sensors. *Advanced Materials* **32**, 2002710 (2020).
70. Laney, S.K., Michalska, M., Li, T., Ramirez, F.V., Portnoi, M., Oh, J., Thayne, I.G., Parkin, I.P., Tiwari, M.K. & Papakonstantinou, I. Delayed Lubricant Depletion of Slippery Liquid Infused Porous Surfaces Using Precision Nanostructures. *Langmuir* **37**, 10071-10078 (2021).
71. Monga, D., Guo, Z., Shan, L., Taba, S.A., Sarma, J. & Dai, X. Quasi-Liquid Surfaces for Sustainable High-Performance Steam Condensation. *ACS Applied Materials & Interfaces* **14**, 13932-13941 (2022).
72. Wilke, K.L., Antao, D.S., Cruz, S., Iwata, R., Zhao, Y., Leroy, A., Preston, D.J. & Wang, E.N. Polymer Infused Porous Surfaces for Robust, Thermally Conductive, Self-Healing Coatings for Dropwise Condensation. *ACS Nano* **14**, 14878-14886 (2020).
73. Yamauchi, Y., Tenjimbayashi, M., Samitsu, S. & Naito, M. Durable and Flexible Superhydrophobic Materials: Abrasion/Scratching/Slicing/Droplet Impacting/Bending/Twisting-Tolerant Composite with Porcupinefish-Like Structure. *ACS Applied Materials & Interfaces* **11**, 32381-32389 (2019).
74. Adera, S., Alvarenga, J., Shneidman, A.V., Zhang, C.T., Davitt, A. & Aizenberg, J. Depletion of Lubricant from Nanostructured Oil-Infused Surfaces by Pendant Condensate Droplets. *ACS Nano* **14**, 8024-8035 (2020).
75. Peppou-Chapman, S., Hong, J.K., Waterhouse, A. & Neto, C. Life and death of liquid-infused surfaces: a review on the choice, analysis and fate of the infused liquid layer. *Chemical Society Reviews* **49**, 3688-3715 (2020).
76. Fazle Rabbi, K., Ho, J.Y., Yan, X., Ma, J., Hoque, M.J., Sett, S. & Miljkovic, N. Polydimethylsiloxane-Silane Synergy enables Dropwise Condensation of Low Surface Tension Liquids. *Advanced Functional Materials* **32**, 2112837 (2022).
77. Huang, S., Li, J., Liu, L., Zhou, L. & Tian, X. Lossless Fast Drop Self-Transport on Anisotropic Omniphobic Surfaces: Origin and Elimination of Microscopic Liquid Residue. *Advanced Materials* **31**, 1901417 (2019).
78. Zhang, L., Guo, Z., Sarma, J. & Dai, X. Passive Removal of Highly Wetting Liquids and Ice on Quasi-Liquid Surfaces. *ACS Applied Materials & Interfaces* **12**, 20084-20095 (2020).
79. Shi, Y., Ilic, O., Atwater, H.A. & Greer, J.R. All-day fresh water harvesting by microstructured

hydrogel membranes. *Nature Communications* **12**, 2797 (2021).

80. Haechler, I., Park, H., Schnoering, G., Gulich, T., Rohner, M., Tripathy, A., Milionis, A., Schutzius, T.M. & Poulikakos, D. Exploiting radiative cooling for uninterrupted 24-hour water harvesting from the atmosphere. *Science Advances* **7**, eabf3978 (2021).
81. Ho, J.Y., Rabbi, K.F., Khodakarami, S., Sett, S., Wong, T.N., Leong, K.C., King, W.P. & Miljkovic, N. Ultrascalable Surface Structuring Strategy of Metal Additively Manufactured Materials for Enhanced Condensation. *Advanced Science* **9**, 2104454 (2022).
82. Liu, L., Liu, S., Schelp, M. & Chen, X. Rapid 3D Printing of Bioinspired Hybrid Structures for High-Efficiency Fog Collection and Water Transportation. *ACS Applied Materials & Interfaces* **13**, 29122-29129 (2021).
83. Zhang, L., Sun, J., Han, P., Qi, G., Gao, D., Che, J., Tao, S. & Wang, Y. Wettability-Patterned Meshes for Efficient Fog Collection Enabled by Polymer-Assisted Laser Sintering. *ACS Applied Polymer Materials* **5**, 614-624 (2023).
84. Zhang, L., Guo, Z., Sarma, J., Zhao, W. & Dai, X. Gradient Quasi-Liquid Surface Enabled Self-Propulsion of Highly Wetting Liquids. *Advanced Functional Materials* **31**, 2008614 (2021).
85. Suh, Y., Lee, J., Simadiris, P., Yan, X., Sett, S., Li, L., Rabbi, K.F., Miljkovic, N. & Won, Y. A Deep Learning Perspective on Dropwise Condensation. *Advanced Science* **8**, 2101794 (2021).
86. Ma, Z., Ai, J., Shi, Y., Wang, K. & Su, B. A Superhydrophobic Droplet-Based Magnetoelectric Hybrid System to Generate Electricity and Collect Water Simultaneously. *Advanced Materials* **32**, 2006839 (2020).
87. Buddingh, J.V., Hozumi, A. & Liu, G. Liquid and liquid-like surfaces/coatings that readily slide fluids. *Progress in Polymer Science* **123**, 101468 (2021).
88. Wang, L. & McCarthy, T.J. Covalently Attached Liquids: Instant Omniphobic Surfaces with Unprecedented Repellency. *Angewandte Chemie International Edition* **55**, 244-248 (2016).
89. Ma, J., Zheng, Z., Hoque, M.J., Li, L., Rabbi, K.F., Ho, J.Y., Braun, P.V., Wang, P. & Miljkovic, N. A Lipid-Inspired Highly Adhesive Interface for Durable Superhydrophobicity in Wet Environments and Stable Jumping Droplet Condensation. *ACS Nano* **16**, 4251-4262 (2022).
90. Ren, J., Liu, Q., Pei, Y., Wang, Y., Yang, S., Lin, S., Chen, W., Ling, S. & Kaplan, D.L. Bioinspired Energy Storage and Harvesting Devices. *Advanced Materials Technologies* **6**, 2001301 (2021).
91. Lu, H., Shi, W., Guo, Y., Guan, W., Lei, C. & Yu, G. Materials Engineering for Atmospheric Water Harvesting: Progress and Perspectives. *Advanced Materials* **34**, 2110079 (2022).
92. Wang, M., Sun, T., Wan, D., Dai, M., Ling, S., Wang, J., Liu, Y., Fang, Y., Xu, S., Yeo, J., Yu, H., Liu, S., Wang, Q., Li, J., Yang, Y., Fan, Z. & Chen, W. Solar-powered nanostructured biopolymer hygroscopic aerogels for atmospheric water harvesting. *Nano Energy* **80**, 105569 (2021).
93. Hanikel, N., Pei, X., Chheda, S., Lyu, H., Jeong, W., Sauer, J., Gagliardi, L. & Yaghi, O.M. Evolution of water structures in metal-organic frameworks for improved atmospheric water harvesting. *Science* **374**, 454-459 (2021).
94. Yilmaz, G., Meng, F.L., Lu, W., Abed, J., Peh, C.K.N., Gao, M., Sargent, E.H. & Ho, G.W.

Autonomous atmospheric water seeping MOF matrix. *Science Advances* **6**, eabc8605 (2020).

95. Ni, F., Qiu, N., Xiao, P., Zhang, C., Jian, Y., Liang, Y., Xie, W., Yan, L. & Chen, T. Tillandsia-Inspired Hygroscopic Photothermal Organogels for Efficient Atmospheric Water Harvesting. *Angewandte Chemie International Edition* **59**, 19237-19246 (2020).
96. Zhang, Y., Wu, L., Wang, X., Yu, J. & Ding, B. Super hygroscopic nanofibrous membrane-based moisture pump for solar-driven indoor dehumidification. *Nature Communications* **11**, 3302 (2020).
97. Hanikel, N., Prévot, M.S., Fathieh, F., Kapustin, E.A., Lyu, H., Wang, H., Diercks, N.J., Glover, T.G. & Yaghi, O.M. Rapid Cycling and Exceptional Yield in a Metal-Organic Framework Water Harvester. *ACS Central Science* **5**, 1699-1706 (2019).
98. LaPotin, A., Zhong, Y., Zhang, L., Zhao, L., Leroy, A., Kim, H., Rao, S.R. & Wang, E.N. Dual-Stage Atmospheric Water Harvesting Device for Scalable Solar-Driven Water Production. *Joule* **5**, 166-182 (2021).
99. Xu, J., Li, T., Yan, T., Wu, S., Wu, M., Chao, J., Huo, X., Wang, P. & Wang, R. Ultrahigh solar-driven atmospheric water production enabled by scalable rapid-cycling water harvester with vertically aligned nanocomposite sorbent. *Energy & Environmental Science* **14**, 5979-5994 (2021).
100. Yang, J., Zhang, X., Qu, H., Yu, Z.G., Zhang, Y., Eey, T.J., Zhang, Y.-W. & Tan, S.C. A Moisture-Hungry Copper Complex Harvesting Air Moisture for Potable Water and Autonomous Urban Agriculture. *Advanced Materials* **32**, 2002936 (2020).
101. Song, Y., Xu, N., Liu, G., Qi, H., Zhao, W., Zhu, B., Zhou, L. & Zhu, J. High-yield solar-driven atmospheric water harvesting of metal–organic-framework-derived nanoporous carbon with fast-diffusion water channels. *Nature Nanotechnology* **17**, 857-863 (2022).
102. Li, R., Shi, Y., Wu, M., Hong, S. & Wang, P. Improving atmospheric water production yield: Enabling multiple water harvesting cycles with nano sorbent. *Nano Energy* **67**, 104255 (2020).
103. Ma, D., Huang, X., Zhang, Y., Wang, L. & Wang, B. Metal-organic frameworks: Synthetic methods for industrial production. *Nano Research* (2023).
104. Zheng, Z., Nguyen, H.L., Hanikel, N., Li, K.K.-Y., Zhou, Z., Ma, T. & Yaghi, O.M. High-yield, green and scalable methods for producing MOF-303 for water harvesting from desert air. *Nature Protocols* **18**, 136-156 (2023).
105. Lyu, T., Wang, Z., Liu, R., Chen, K., Liu, H. & Tian, Y. Macroporous Hydrogel for High-Performance Atmospheric Water Harvesting. *ACS Applied Materials & Interfaces* **14**, 32433-32443 (2022).
106. Lei, C., Guo, Y., Guan, W., Lu, H., Shi, W. & Yu, G. Polyzwitterionic Hydrogels for Efficient Atmospheric Water Harvesting. *Angewandte Chemie International Edition* **61**, e202200271 (2022).
107. Guo, Y., Guan, W., Lei, C., Lu, H., Shi, W. & Yu, G. Scalable super hygroscopic polymer films for sustainable moisture harvesting in arid environments. *Nature Communications* **13**, 2761 (2022).
108. Zhang, C., Liang, H.-Q., Xu, Z.-K. & Wang, Z. Harnessing Solar-Driven Photothermal Effect

toward the Water–Energy Nexus. *Advanced Science* **6**, 1900883 (2019).

109. Kuang, Y., Chen, C., He, S., Hitz, E.M., Wang, Y., Gan, W., Mi, R. & Hu, L. A High-Performance Self-Regenerating Solar Evaporator for Continuous Water Desalination. *Advanced Materials* **31**, 1900498 (2019).
110. Xu, N., Li, J., Wang, Y., Fang, C., Li, X., Wang, Y., Zhou, L., Zhu, B., Wu, Z., Zhu, S. & Zhu, J. A water lily–inspired hierarchical design for stable and efficient solar evaporation of high-salinity brine. *Science Advances* **5**, eaaw7013 (2019).
111. Lei, Z., Zhu, S., Sun, X., Yu, S., Liu, X., Liang, K., Zhang, X., Qu, L., Wang, L. & Zhang, X. A Multiscale Porous 3D-Fabric Evaporator with Vertically Aligned Yarns Enables Ultra-Efficient and Continuous Water Desalination. *Advanced Functional Materials* **32**, 2205790 (2022).
112. Tian, C., Liu, J., Ruan, R., Tian, X., Lai, X., Xing, L., Su, Y., Huang, W., Cao, Y. & Tu, J. Sandwich Photothermal Membrane with Confined Hierarchical Carbon Cells Enabling High-Efficiency Solar Steam Generation. *Small* **16**, 2000573 (2020).
113. Fan, X., Yang, Y., Shi, X., Liu, Y., Li, H., Liang, J. & Chen, Y. A MXene-Based Hierarchical Design Enabling Highly Efficient and Stable Solar-Water Desalination with Good Salt Resistance. *Advanced Functional Materials* **30**, 2007110 (2020).
114. Li, C., Cao, S., Lutzki, J., Yang, J., Konegger, T., Kleitz, F. & Thomas, A. A Covalent Organic Framework/Graphene Dual-Region Hydrogel for Enhanced Solar-Driven Water Generation. *Journal of the American Chemical Society* **144**, 3083-3090 (2022).
115. Zhang, L., Li, X., Zhong, Y., Leroy, A., Xu, Z., Zhao, L. & Wang, E.N. Highly efficient and salt rejecting solar evaporation via a wick-free confined water layer. *Nature Communications* **13**, 849 (2022).
116. Yang, K., Pan, T., Dang, S., Gan, Q. & Han, Y. Three-dimensional open architecture enabling salt-rejection solar evaporators with boosted water production efficiency. *Nature Communications* **13**, 6653 (2022).
117. Xia, Y., Hou, Q., Jubaer, H., Li, Y., Kang, Y., Yuan, S., Liu, H., Woo, M.W., Zhang, L., Gao, L., Wang, H. & Zhang, X. Spatially isolating salt crystallisation from water evaporation for continuous solar steam generation and salt harvesting. *Energy & Environmental Science* **12**, 1840-1847 (2019).
118. Zeng, J., Wang, Q., Shi, Y., Liu, P. & Chen, R. Osmotic Pumping and Salt Rejection by Polyelectrolyte Hydrogel for Continuous Solar Desalination. *Advanced Energy Materials* **9**, 1900552 (2019).
119. Xu, K., Wang, C., Li, Z., Wu, S. & Wang, J. Salt Mitigation Strategies of Solar-Driven Interfacial Desalination. *Advanced Functional Materials* **31**, 2007855 (2021).
120. Zou, M., Zhang, Y., Cai, Z., Li, C., Sun, Z., Yu, C., Dong, Z., Wu, L. & Song, Y. 3D Printing a Biomimetic Bridge-Arch Solar Evaporator for Eliminating Salt Accumulation with Desalination and Agricultural Applications. *Advanced Materials* **33**, 2102443 (2021).
121. Yang, H., Sun, Y., Peng, M., Cai, M., Zhao, B., Li, D., Liang, Z. & Jiang, L. Tailoring the Salt Transport Flux of Solar Evaporators for a Highly Effective Salt-Resistant Desalination with High Productivity. *ACS Nano* **16**, 2511-2520 (2022).

122. Chen, C., Zhou, L., Yu, J., Wang, Y., Nie, S., Zhu, S. & Zhu, J. Dual functional asymmetric plasmonic structures for solar water purification and pollution detection. *Nano Energy* **51**, 451-456 (2018).
123. Wang, F., Xu, N., Zhao, W., Zhou, L., Zhu, P., Wang, X., Zhu, B. & Zhu, J. A high-performing single-stage invert-structured solar water purifier through enhanced absorption and condensation. *Joule* **5**, 1602-1612 (2021).
124. Deng, W., Fan, T. & Li, Y. Water wave vibration-promoted solar evaporation with super high productivity. *Nano Energy* **92**, 106745 (2022).
125. Xu, Z., Zhang, L., Zhao, L., Li, B., Bhatia, B., Wang, C., Wilke, K.L., Song, Y., Labban, O., Lienhard, J.H., Wang, R. & Wang, E.N. Ultrahigh-efficiency desalination via a thermally-localized multistage solar still. *Energy & Environmental Science* **13**, 830-839 (2020).
126. Wang, W., Aleid, S., Shi, Y., Zhang, C., Li, R., Wu, M., Zhuo, S. & Wang, P. Integrated solar-driven PV cooling and seawater desalination with zero liquid discharge. *Joule* **5**, 1873-1887 (2021).
127. Ma, W., Lu, T., Cao, W., Xiong, R. & Huang, C. Bioinspired Nanofibrous Aerogel with Vertically Aligned Channels for Efficient Water Purification and Salt-Rejecting Solar Desalination. *Advanced Functional Materials* **n/a**, 2214157 (2023).
128. Singh, S.C., ElKabbash, M., Li, Z., Li, X., Regmi, B., Madsen, M., Jalil, S.A., Zhan, Z., Zhang, J. & Guo, C. Solar-trackable super-wicking black metal panel for photothermal water sanitation. *Nature Sustainability* **3**, 938-946 (2020).
129. Xu, C., Gao, M., Yu, X., Zhang, J., Cheng, Y. & Zhu, M. Fibrous Aerogels with Tunable Superwettability for High-Performance Solar-Driven Interfacial Evaporation. *Nano-Micro Letters* **15**, 64 (2023).
130. Wang, H.-D., Xue, C.-H., Guo, X.-J., Liu, B.-Y., Ji, Z.-Y., Huang, M.-C. & Jia, S.-T. Superhydrophobic porous film for daytime radiative cooling. *Applied Materials Today* **24**, 101100 (2021).
131. Xing, H., Song, Y., Xu, H., Chen, S., Li, K., Dong, L., Wang, B., Xue, J. & Lu, Y. A Magneto-Heated Silk Fibroin Scaffold for Anti-Biofouling Solar Steam Generation. *Small* **n/a**, 2206189 (2023).
132. Li, T., Wu, M., Xu, J., Du, R., Yan, T., Wang, P., Bai, Z., Wang, R. & Wang, S. Simultaneous atmospheric water production and 24-hour power generation enabled by moisture-induced energy harvesting. *Nature Communications* **13**, 6771 (2022).
133. Russell, T.P. Surface-Responsive Materials. *Science* **297**, 964-967 (2002).
134. Dubovik, A.S., Kuznetsov, D.V., Grinberg, N.V., Grosberg, A.Y. & Tanaka, T. Studies of the Thermal Volume Transition of Poly(N-isopropylacrylamide) Hydrogels by High-Sensitivity Differential Scanning Microcalorimetry. 2. Thermodynamic Functions. *Macromolecules* **33**, 8685-8692 (2000).
135. Monosmith, W.B. & Walrafen, G.E. Temperature dependence of the Raman OH-stretching overtone from liquid water. *The Journal of Chemical Physics* **81**, 669-674 (1984).
136. Liu, M., Leroux, J.-C. & Gauthier, M.A. Conformation–function relationships for the comb-

shaped polymer pOEGMA. *Progress in Polymer Science* **48**, 111-121 (2015).

137. Okada, K., Miura, Y., Chiya, T., Tokudome, Y. & Takahashi, M. Thermo-responsive wettability via surface roughness change on polymer-coated titanate nanorod brushes toward fast and multi-directional droplet transport. *RSC Advances* **10**, 28032-28036 (2020).
138. Zhao, Z., Ning, Y., Jin, X., Ben, S., Zha, J., Su, B., Tian, D., Liu, K. & Jiang, L. Molecular-Structure-Induced Under-Liquid Dual Superlyophobic Surfaces. *ACS Nano* **14**, 14869-14877 (2020).
139. Potroz, M.G., Mundargi, R.C., Gillissen, J.J., Tan, E.-L., Meker, S., Park, J.H., Jung, H., Park, S., Cho, D., Bang, S.-I. & Cho, N.-J. Plant-Based Hollow Microcapsules for Oral Delivery Applications: Toward Optimized Loading and Controlled Release. *Advanced Functional Materials* **27**, 1700270 (2017).
140. Zhao, Z., Hwang, Y., Yang, Y., Fan, T., Song, J., Suresh, S. & Cho, N.-J. Actuation and locomotion driven by moisture in paper made with natural pollen. *Proceedings of the National Academy of Sciences* **117**, 8711-8718 (2020).
141. Hou, X., Hu, Y., Grinthal, A., Khan, M. & Aizenberg, J. Liquid-based gating mechanism with tunable multiphase selectivity and antifouling behaviour. *Nature* **519**, 70-73 (2015).
142. Chen, C., Liu, M., Zhang, L., Hou, Y., Yu, M. & Fu, S. Mimicking from Rose Petal to Lotus Leaf: Biomimetic Multiscale Hierarchical Particles with Tunable Water Adhesion. *ACS Applied Materials & Interfaces* **11**, 7431-7440 (2019).
143. Zhao, F., Zhou, X., Shi, Y., Qian, X., Alexander, M., Zhao, X., Mendez, S., Yang, R., Qu, L. & Yu, G. Highly efficient solar vapour generation via hierarchically nanostructured gels. *Nature Nanotechnology* **13**, 489-495 (2018).
144. Xu, X., Ozden, S., Bizmark, N., Arnold, C.B., Datta, S.S. & Priestley, R.D. A Bioinspired Elastic Hydrogel for Solar-Driven Water Purification. *Advanced Materials* **33**, 2007833 (2021).
145. Qing, G., Zhao, X., Gong, N., Chen, J., Li, X., Gan, Y., Wang, Y., Zhang, Z., Zhang, Y., Guo, W., Luo, Y. & Liang, X.-J. Thermo-responsive triple-function nanotransporter for efficient chemo-photothermal therapy of multidrug-resistant bacterial infection. *Nature Communications* **10**, 4336 (2019).
146. Zhao, Z., Kumar, J., Hwang, Y., Deng, J., Ibrahim Mohammed Shahrudin, B., Huang, C., Suresh, S. & Cho, N.-J. Digital printing of shape-morphing natural materials. *Proceedings of the National Academy of Sciences* **118**, e2113715118 (2021).
147. Jiao, Y., Tibbits, A., Gillman, A., Hsiao, M.-S., Buskohl, P., Drummy, L.F. & Vaia, R.A. Deformation Behavior of Polystyrene-Grafted Nanoparticle Assemblies with Low Grafting Density. *Macromolecules* **51**, 7257-7265 (2018).
148. Sun, B., Lin, Y., Wu, P. & Siesler, H.W. A FTIR and 2D-IR Spectroscopic Study on the Microdynamics Phase Separation Mechanism of the Poly(N-isopropylacrylamide) Aqueous Solution. *Macromolecules* **41**, 1512-1520 (2008).
149. Cho, E.C., Lee, J. & Cho, K. Role of Bound Water and Hydrophobic Interaction in Phase Transition of Poly(N-isopropylacrylamide) Aqueous Solution. *Macromolecules* **36**, 9929-9934 (2003).

150. Harrison, R.H., Steele, J.A.M., Chapman, R., Gormley, A.J., Chow, L.W., Mahat, M.M., Podhorska, L., Palgrave, R.G., Payne, D.J., Hettiaratchy, S.P., Dunlop, I.E. & Stevens, M.M. Modular and Versatile Spatial Functionalization of Tissue Engineering Scaffolds through Fiber-Initiated Controlled Radical Polymerization. *Advanced Functional Materials* **25**, 5748-5757 (2015).

151. Yang, H., Zhu, H., Hendrix, M.M.R.M., Lousberg, N.J.H.G.M., de With, G., Esteves, A.C.C. & Xin, J.H. Temperature-Triggered Collection and Release of Water from Fogs by a Sponge-Like Cotton Fabric. *Advanced Materials* **25**, 1150-1154 (2013).

152. Davis, J.G., Gierszal, K.P., Wang, P. & Ben-Amotz, D. Water structural transformation at molecular hydrophobic interfaces. *Nature* **491**, 582-585 (2012).

153. Kolberg, A., Wenzel, C., Hackenstrass, K., Schwarzl, R., Rüttiger, C., Hugel, T., Gallei, M., Netz, R.R. & Balzer, B.N. Opposing Temperature Dependence of the Stretching Response of Single PEG and PNiPAM Polymers. *Journal of the American Chemical Society* **141**, 11603-11613 (2019).

154. Rey, M., Law, A.D., Buzza, D.M.A. & Vogel, N. Anisotropic Self-Assembly from Isotropic Colloidal Building Blocks. *Journal of the American Chemical Society* **139**, 17464-17473 (2017).

155. Guzmán, E., Martínez-Pedrero, F., Calero, C., Maestro, A., Ortega, F. & Rubio, R.G. A broad perspective to particle-laden fluid interfaces systems: from chemically homogeneous particles to active colloids. *Advances in Colloid and Interface Science* **302**, 102620 (2022).

156. Lutz, J.-F., Akdemir, Ö. & Hoth, A. Point by Point Comparison of Two Thermosensitive Polymers Exhibiting a Similar LCST: Is the Age of Poly(NIPAM) Over? *Journal of the American Chemical Society* **128**, 13046-13047 (2006).

157. Liu, M., Wang, S. & Jiang, L. Nature-inspired superwettability systems. *Nature Reviews Materials* **2**, 17036 (2017).

158. Wang, D., Sun, Q., Hokkanen, M.J., Zhang, C., Lin, F.-Y., Liu, Q., Zhu, S.-P., Zhou, T., Chang, Q., He, B., Zhou, Q., Chen, L., Wang, Z., Ras, R.H.A. & Deng, X. Design of robust superhydrophobic surfaces. *Nature* **582**, 55-59 (2020).

159. Sun, T., Wang, G., Feng, L., Liu, B., Ma, Y., Jiang, L. & Zhu, D. Reversible Switching between Superhydrophilicity and Superhydrophobicity. *Angewandte Chemie International Edition* **43**, 357-360 (2004).

160. Wang, Y., Di, J., Wang, L., Li, X., Wang, N., Wang, B., Tian, Y., Jiang, L. & Yu, J. Infused-liquid-switchable porous nanofibrous membranes for multiphase liquid separation. *Nature Communications* **8**, 575 (2017).

161. Smith, J.D., Cappa, C.D., Drisdell, W.S., Cohen, R.C. & Saykally, R.J. Raman Thermometry Measurements of Free Evaporation from Liquid Water Droplets. *Journal of the American Chemical Society* **128**, 12892-12898 (2006).

162. Giovambattista, N., Debenedetti Pablo, G. & Rossky Peter, J. Enhanced surface hydrophobicity by coupling of surface polarity and topography. *Proceedings of the National Academy of Sciences* **106**, 15181-15185 (2009).

163. Miyazaki, M., Fujii, A., Ebata, T. & Mikami, N. Infrared spectroscopic evidence for protonated

water clusters forming nanoscale cages. *Science* **304**, 1134-1137 (2004).

164. Hsu, C.-P., Mandal, J., Ramakrishna, S.N., Spencer, N.D. & Isa, L. Exploring the roles of roughness, friction and adhesion in discontinuous shear thickening by means of thermo-responsive particles. *Nature Communications* **12**, 1477 (2021).
165. Chen, L., He, X., Liu, H., Qian, L. & Kim, S.H. Water Adsorption on Hydrophilic and Hydrophobic Surfaces of Silicon. *The Journal of Physical Chemistry C* **122**, 11385-11391 (2018).
166. Cheng, X., McCoy Jonathan, H., Israelachvili Jacob, N. & Cohen, I. Imaging the Microscopic Structure of Shear Thinning and Thickening Colloidal Suspensions. *Science* **333**, 1276-1279 (2011).
167. Shin, S. & Willard, A.P. Water's Interfacial Hydrogen Bonding Structure Reveals the Effective Strength of Surface–Water Interactions. *The Journal of Physical Chemistry B* **122**, 6781-6789 (2018).
168. James, N.M., Han, E., de la Cruz, R.A.L., Jureller, J. & Jaeger, H.M. Interparticle hydrogen bonding can elicit shear jamming in dense suspensions. *Nat Mater* **17**, 965-970 (2018).
169. Guzmán, E., Tajuelo, J., Pastor, J.M., Rubio, M.Á., Ortega, F. & Rubio, R.G. Shear rheology of fluid interfaces: Closing the gap between macro- and micro-rheology. *Current Opinion in Colloid & Interface Science* **37**, 33-48 (2018).
170. Tang, J., Berry, R.M. & Tam, K.C. Stimuli-Responsive Cellulose Nanocrystals for Surfactant-Free Oil Harvesting. *Biomacromolecules* **17**, 1748-1756 (2016).
171. Dhyani, A., Wang, J., Halvey Alex, K., Macdonald, B., Mehta, G. & Tuteja, A. Design and applications of surfaces that control the accretion of matter. *Science* **373**, eaba5010 (2021).
172. Zhang, Q., Bai, X., Li, Y., Zhang, X., Tian, D. & Jiang, L. Ultrastable Super-Hydrophobic Surface with an Ordered Scaly Structure for Decompression and Guiding Liquid Manipulation. *ACS Nano* **16**, 16843-16852 (2022).
173. Cui, H., Wang, W., Shi, L., Song, W. & Wang, S. Superwettable Surface Engineering in Controlling Cell Adhesion for Emerging Bioapplications. *Small Methods* **4**, 2000573 (2020).
174. Chen, F., Lu, G., Yuan, H., Li, R., Nie, J., Zhao, Y., Shu, X. & Zhu, X. Mechanism and regulation of LCST behavior in poly(hydroxypropyl acrylate)-based temperature-sensitive hydrogels. *Journal of Materials Chemistry A* **10**, 18235-18247 (2022).
175. Tan, Y., Yang, J., Li, Y., Li, X., Wu, Q., Fan, Y., Yu, F., Cui, J., Chen, L., Wang, D. & Deng, X. Liquid-Pressure-Guided Superhydrophobic Surfaces with Adaptive Adhesion and Stability. *Advanced Materials* **34**, 2202167 (2022).
176. Daniel, D., Lay, C.L., Sng, A., Jun Lee, C.J., Jin Neo, D.C., Ling, X.Y. & Tomczak, N. Mapping micrometer-scale wetting properties of superhydrophobic surfaces. *Proceedings of the National Academy of Sciences* **116**, 25008-25012 (2019).
177. Liimatainen, V., Vuckovac, M., Jokinen, V., Sariola, V., Hokkanen, M.J., Zhou, Q. & Ras, R.H.A. Mapping microscale wetting variations on biological and synthetic water-repellent surfaces. *Nature Communications* **8**, 1798 (2017).
178. Hwang, Y., Sadhu, A., Shin, S., Leow, S., Zhao, Z., Deng, J., Jackman, J., Kim, M., Wong, L. &

Cho, N. An Intrinsically Micro-/Nanostructured Pollen Substrate with Tunable Optical Properties for Optoelectronic Applications. *Advanced materials (Deerfield Beach, Fla.)* **33**, e2100566 (2021).

179. Fan, T.-F., Park, S., Shi, Q., Zhang, X., Liu, Q., Song, Y., Chin, H., Ibrahim, M.S.B., Mokrzecka, N., Yang, Y., Li, H., Song, J., Suresh, S. & Cho, N.-J. Transformation of hard pollen into soft matter. *Nature Communications* **11**, 1449 (2020).
180. Mendoza, D.J., Ayurini, M., Browne, C., Raghuwanshi, V.S., Simon, G.P., Hooper, J.F. & Garnier, G. Thermoresponsive Poly(N-isopropylacrylamide) Grafted from Cellulose Nanofibers via Silver-Promoted Decarboxylative Radical Polymerization. *Biomacromolecules* **23**, 1610-1621 (2022).
181. Pan, Y., Huang, S., Li, F., Zhao, X. & Wang, W. Coexistence of superhydrophilicity and superoleophobicity: theory, experiments and applications in oil/water separation. *Journal of Materials Chemistry A* **6**, 15057-15063 (2018).
182. Guan, X., Liu, Y., Wan, Z., Steve Tse, Y.-L. & Ngai, T. Non-covalent reconfigurable microgel colloidosomes with a well-defined bilayer shell. *Chemical Science* **13**, 6205-6216 (2022).
183. Harrer, J., Rey, M., Ciarella, S., Löwen, H., Janssen, L.M.C. & Vogel, N. Stimuli-Responsive Behavior of PNiPAm Microgels under Interfacial Confinement. *Langmuir* **35**, 10512-10521 (2019).
184. Tavagnacco, L., Zaccarelli, E. & Chiessi, E. Modeling Solution Behavior of Poly(N-isopropylacrylamide): A Comparison between Water Models. *The Journal of Physical Chemistry B* **126**, 3778-3788 (2022).
185. Chen, X., Yang, T., Kataoka, S. & Cremer, P.S. Specific Ion Effects on Interfacial Water Structure near Macromolecules. *Journal of the American Chemical Society* **129**, 12272-12279 (2007).
186. Wang, Y.-H., Zheng, S., Yang, W.-M., Zhou, R.-Y., He, Q.-F., Radjenovic, P., Dong, J.-C., Li, S., Zheng, J., Yang, Z.-L., Attard, G., Pan, F., Tian, Z.-Q. & Li, J.-F. In situ Raman spectroscopy reveals the structure and dissociation of interfacial water. *Nature* **600**, 81-85 (2021).
187. Ye, Y., Shangguan, Y., Song, Y. & Zheng, Q. Influence of charge density on rheological properties and dehydration dynamics of weakly charged poly(N-isopropylacrylamide) during phase transition. *Polymer* **55**, 2445-2454 (2014).
188. Wilson, J.F., Zahradník, B., Šrom, O., Jaquet, B., Hassouna, F., Hrdlička, Z., Kosek, J. & Šoóš, M. Study of the Shear-Thinning Effect between Polymer Nanoparticle Surfaces during Shear-Induced Aggregation. *Industrial & Engineering Chemistry Research* **60**, 10654-10665 (2021).
189. James, N.M., Han, E., de la Cruz, R.A.L., Jureller, J. & Jaeger, H.M. Interparticle hydrogen bonding can elicit shear jamming in dense suspensions. *Nat. Mater.* **17**, 965-970 (2018).
190. Zhao, W., Wang, Y., Han, M., Xu, J. & Tam, K.C. Surface Modification, Topographic Design and Applications of Superhydrophobic Systems. *Chemistry – A European Journal* **28**, e202202657 (2022).
191. Qiao, S., Li, S., Li, Q., Li, B., Liu, K. & Feng, X.-Q. Friction of Droplets Sliding on

Microstructured Superhydrophobic Surfaces. *Langmuir* **33**, 13480-13489 (2017).

192. Sariola, V. Analytical Expressions for Spring Constants of Capillary Bridges and Snap-in Forces of Hydrophobic Surfaces. *Langmuir* **35**, 7129-7135 (2019).
193. Wang, D., Jiang, Y., Zhu, Z., Yin, W., Asawa, K., Choi, C.-H. & Drelich, J.W. Contact Line and Adhesion Force of Droplets on Concentric Ring-Textured Hydrophobic Surfaces. *Langmuir* **36**, 2622-2628 (2020).
194. Daniel, D., Timonen, J.V.I., Li, R., Velling, S.J., Kreder, M.J., Tetreault, A. & Aizenberg, J. Origins of Extreme Liquid Repellency on Structured, Flat, and Lubricated Hydrophobic Surfaces. *Physical Review Letters* **120**, 244503 (2018).
195. Hokkanen, M.J., Backholm, M., Vuckovac, M., Zhou, Q. & Ras, R.H.A. Force-Based Wetting Characterization of Stochastic Superhydrophobic Coatings at Nanonewton Sensitivity. *Advanced Materials* **33**, 2105130 (2021).
196. Tian, Y., Ina, M., Cao, Z., Sheiko, S.S. & Dobrynin, A.V. How To Measure Work of Adhesion and Surface Tension of Soft Polymeric Materials. *Macromolecules* **51**, 4059-4067 (2018).
197. Rezayi, T., Entezari, M.H. & Moosavi, F. The variation of surface free energy of Al during superhydrophobicity processing. *Chemical Engineering Journal* **322**, 181-187 (2017).
198. Zhang, Z., Wang, W., Korpacz, A.N., Dufour, C.R., Weiland, Z.J., Lambert, C.R. & Timko, M.T. Binary Liquid Mixture Contact-Angle Measurements for Precise Estimation of Surface Free Energy. *Langmuir* **35**, 12317-12325 (2019).
199. Zhang, Z., Shen, W., Lin, L., Wang, M., Li, N., Zheng, Z., Liu, F. & Cao, L. Vertically Transported Graphene Oxide for High-Performance Osmotic Energy Conversion. *Adv Sci (Weinh)* **7**, 2000286 (2020).
200. Teisala, H. & Butt, H.-J. Hierarchical Structures for Superhydrophobic and Superoleophobic Surfaces. *Langmuir* **35**, 10689-10703 (2019).
201. Sun, Y., Li, Y., Dong, X., Bu, X. & Drelich, J.W. Spreading and adhesion forces for water droplets on methylated glass surfaces. *Colloids and Surfaces A: Physicochemical and Engineering Aspects* **591**, 124562 (2020).
202. Al-Sharafi, A., Yilbas, B.S., Sahin, A.Z. & Al-Qahtani, H. Droplet stretching between hydrophobic and hydrophilic plates: Droplet fluid heating. *International Communications in Heat and Mass Transfer* **120**, 105010 (2021).
203. Sun, Q., Lin, S., Wang, D., Li, Y., Yang, J. & Deng, X. In situ tunable droplet adhesion on a super-repellent surface via electrostatic induction effect. *iScience* **24**, 102208 (2021).
204. Beitollahpoor, M., Farzam, M. & Pesika, N.S. Determination of the Sliding Angle of Water Drops on Surfaces from Friction Force Measurements. *Langmuir* **38**, 2132-2136 (2022).
205. Venkateshan, D.G. & Tafreshi, H.V. Modelling droplet sliding angle on hydrophobic wire screens. *Colloids and Surfaces A: Physicochemical and Engineering Aspects* **538**, 310-319 (2018).
206. Wang, H., Zhang, Z., Zheng, J., Zhao, J., Liang, Y., Li, X. & Ren, L. Multifunctional superhydrophobic surface with dynamically controllable micro/nanostructures for droplet manipulation and friction control. *Chemical Engineering Journal* **417**, 127944 (2021).

207. He, C., Liu, Z., Wu, J., Pan, X., Fang, Z., Li, J. & Bryan, B.A. Future global urban water scarcity and potential solutions. *Nature Communications* **12**, 4667 (2021).
208. Liu, S., Li, S. & Lin, M. Understanding Interfacial Properties for Enhanced Solar Evaporation Devices: From Geometrical to Physical Interfaces. *ACS Energy Letters* **8**, 1680-1687 (2023).
209. Ding, T., Zhou, Y., Ong, W.L. & Ho, G.W. Hybrid solar-driven interfacial evaporation systems: Beyond water production towards high solar energy utilization. *Materials Today* **42**, 178-191 (2021).
210. Wang, Z., Wu, X., He, F., Peng, S. & Li, Y. Confinement Capillarity of Thin Coating for Boosting Solar-Driven Water Evaporation. *Advanced Functional Materials* **31**, 2011114 (2021).
211. Yu, Z., Gu, R., Zhang, Y., Guo, S., Cheng, S. & Tan, S.C. High-flux flowing interfacial water evaporation under multiple heating sources enabled by a biohybrid hydrogel. *Nano Energy* **98**, 107287 (2022).
212. Wang, Y., Zhao, W., Han, M., Xu, J., Zhou, X., Luu, W., Han, L. & Tam, K.C. Topographical Design and Thermal-Induced Organization of Interfacial Water Structure to Regulate the Wetting State of Surfaces. *JACS Au* **2**, 1989-2000 (2022).
213. Zou, Y., Chen, X., Yang, P., Liang, G., Yang, Y., Gu, Z. & Li, Y. Regulating the absorption spectrum of polydopamine. *Science Advances* **6**, eabb4696 (2020).
214. Qin, J., Wang, X., Jiang, Q. & Cao, M. Optimizing Dispersion, Exfoliation, Synthesis, and Device Fabrication of Inorganic Nanomaterials Using Hansen Solubility Parameters. *ChemPhysChem* **20**, 1069-1097 (2019).
215. Bluestein, B.M., Reed, J.A. & Canavan, H.E. Effect of substrate storage conditions on the stability of "Smart" films used for mammalian cell applications. *Applied Surface Science* **392**, 950-959 (2017).
216. Wei, J., Yu, H., Liu, H., Du, C., Zhou, Z., Huang, Q. & Yao, X. Facile synthesis of thermo-responsive nanogels less than 50 nm in diameter via soap- and heat-free precipitation polymerization. *Journal of Materials Science* **53**, 12056-12064 (2018).
217. Shin, D., Hwang, J. & Jhe, W. Ice-VII-like molecular structure of ambient water nanomeniscus. *Nature Communications* **10**, 286 (2019).
218. Prodan, E., Radloff, C., Halas, N.J. & Nordlander, P. A Hybridization Model for the Plasmon Response of Complex Nanostructures. *Science* **302**, 419-422 (2003).
219. Zhou, L., Tan, Y., Wang, J., Xu, W., Yuan, Y., Cai, W., Zhu, S. & Zhu, J. 3D self-assembly of aluminium nanoparticles for plasmon-enhanced solar desalination. *Nature Photonics* **10**, 393-398 (2016).
220. Liu, G., Chen, T., Xu, J., Yao, G., Xie, J., Cheng, Y., Miao, Z. & Wang, K. Salt-Rejecting Solar Interfacial Evaporation. *Cell Reports Physical Science* **2**, 100310 (2021).
221. Li, Y., Alibakhshi, M.A., Zhao, Y. & Duan, C. Exploring Ultimate Water Capillary Evaporation in Nanoscale Conduits. *Nano Letters* **17**, 4813-4819 (2017).
222. Lv, C., Varanakkottu, S.N. & Hardt, S. Liquid plug formation from heated binary mixtures in capillary tubes. *Journal of Fluid Mechanics* **889**, A15 (2020).
223. Wilking, J.N., Zaburdaev, V., De Volder, M., Losick, R., Brenner, M.P. & Weitz, D.A. Liquid

transport facilitated by channels in Bacillus subtilis biofilms. *Proceedings of the National Academy of Sciences* **110**, 848-852 (2013).

224. Olanrewaju, A., Beaugrand, M., Yafia, M. & Juncker, D. Capillary microfluidics in microchannels: from microfluidic networks to capillaric circuits. *Lab on a Chip* **18**, 2323-2347 (2018).

225. Hunter, L. & Dewanckele, J. Evolution of Micro-CT: Moving from 3D to 4D. *Microscopy Today* **29**, 28-34 (2021).

226. Kratz, J., Galvez-Hernandez, P., Pickard, L.R., Belnoue, J. & Potter, K. Lab-based in-situ micro-CT observation of gaps in prepreg laminates during consolidation and cure. *Composites Part A: Applied Science and Manufacturing* **140**, 106180 (2021).

227. Takeya, S., Muraoka, M., Muromachi, S., Hyodo, K. & Yoneyama, A. X-ray CT observation and characterization of water transformation in heavy objects. *Physical Chemistry Chemical Physics* **22**, 3446-3454 (2020).

228. Zheng, Q., Zhang, Y., Montazerian, M., Gulbiten, O., Mauro, J.C., Zanotto, E.D. & Yue, Y. Understanding Glass through Differential Scanning Calorimetry. *Chemical Reviews* **119**, 7848-7939 (2019).

229. Xiao, P., He, J., Ni, F., Zhang, C., Liang, Y., Zhou, W., Gu, J., Xia, J., Kuo, S.-W. & Chen, T. Exploring interface confined water flow and evaporation enables solar-thermal-electro integration towards clean water and electricity harvest via asymmetric functionalization strategy. *Nano Energy* **68**, 104385 (2020).

230. Wu, L., Dong, Z., Cai, Z., Ganapathy, T., Fang, N.X., Li, C., Yu, C., Zhang, Y. & Song, Y. Highly efficient three-dimensional solar evaporator for high salinity desalination by localized crystallization. *Nature Communications* **11**, 521 (2020).